ANALYTICAL AND EXPERIMENTAL STUDY OF A MOTION AMPLIFICATION DAMPER FOR IMPROVING ENERGY DISSIPATION CAPACITY OF PRECAST POST-TENSIONED STRUCTURAL SYSTEMS

by

Ahmet Ata Kulaksızoğlu

B.S., Civil Engineering, Istanbul Technical University, 2008

M.S., Civil Engineering, Boğaziçi University, 2011

Submitted to the Institute for Graduate Studies in
Science and Engineering in partial fulfillment of
the requirements for the degree of
Doctor of Philosophy

Graduate Program in Civil Engineering

Boğaziçi University

2023

ABSTRACT

ANALYTICAL AND EXPERIMENTAL STUDY OF A MOTION AMPLIFICATION DAMPER FOR IMPROVING ENERGY DISSIPATION CAPACITY OF PRECAST POST-TENSIONED STRUCTURAL SYSTEMS

Seismic design approach for structures is rapidly evolving towards low-damage design, with the aim of limiting structural damage in members in addition to providing sufficient strength. Precast post-tensioned concrete is a construction system which is very efficient in limiting seismic structural damage because of two phenomena. The earthquake resistance of the structure is provided by connecting precast members with post-tensioning tendons, which are designed to remain elastic subjected to seismic effects. In addition, the gap opening mechanism allows the structural damage to occur locally in specially designed joints. These aspects unique to precast post-tensioned concrete, however, reduce the hysteretic energy dissipation capacity of the structures, which in other systems exist due to plastic hinging of structural members. To enhance energy dissipation capacity of this system, various external dampers have been proposed in the literature. Majority of these dampers are metallic yielding or translational friction dampers, which work with the principle of relative translational displacement. In this study, an external damper which works with rotational friction mechanism due to relative rotation between friction surfaces is proposed. The contribution of damper to the energy dissipation capacity is increased by amplifying relative rotations between surfaces by way of geometric disposition of the damper mechanism. Analytical and experimental studies were conducted and it was concluded that the proposed damper had significant contribution to energy dissipation capacity of precast post-tensioned systems and novel aspects that distinguishes it from previously proposed dampers.

ÖZET

ÖNÜRETİMLİ ARDGERMELİ YAPI SİSTEMLERİNİN ENERJİ SÖNÜMLEME KAPASİTESİNİ ARTTIRMAK İÇİN TASARLANMIŞ BİR HAREKET BÜYÜTME SÖNÜMLEYİCİSİNİN ANALİTİK VE DENEYSEL ÇALIŞMASI

Deprem mühendisliği yaklaşımı, yeterli taşıma gücü sağlamaya ilave olarak, elemanlardaki yapısal hasarı minimum seviyeye indirmeyi hedefleyen düşük hasarlı tasarım ilkesine doğru evrilmektedir. Önüretimli ardgermeli beton sistemler, sahip oldukları iki özellik sebebi ile, yapısal deprem hasarının sınırlanması açısından çok avantajlıdır. Yapının deprem dayanımı, önüretimli elemanlar ve bu elemanları birbirine bağlayan ardgerme halatları ile sağlanır. Bu halatlar deprem yükleri altında elastik davranacak şekilde tasarlanır. Buna ilave olarak, kiriş-kolon birleşimlerinde meydana gelen boşluk açılma mekanizması, yapısal hasarın özel olarak tasarlanmış düğüm noktasında meydana gelmesine sebep olur. Önüretimli ardgermeli sistemlere özgü bu özellikler, bu yapıların, diğer yapısal sistemlerde plastik mafsallaşma ile oluşan histeretik enerji sönümleme kapasitesini azaltır. Bu sistemlerin enerji sönümleme kapasitesini arttırmak için literatürde bazı sönümleyiciler önerilmiştir. Önerilen bu sönümleyicilerin çoğunluğu, yatay göreli deplasman ilkesi ile çalışan metalik akma ya da sürtünme bazlı sönümleyicilerdir. Bu çalışmada, birbirlerine göreli olarak dönen sürtünme yüzeylerinin oluşturduğu bir sönümleyici önerilmiştir. Bu sönümleyicinin yapının enerji sönümleme kapasitesine olan katkısı, geometrik yerleşiminin etkisi ile göreli dönmeleri büyüterek artar. Analitik ve deneysel çalışmalar yapılmış ve önerilen sönümleyicinin önüretimli ardgermeli yapı sistemlerinin enerji sönümleme kapasitelerini önemli ölçüde arttırdığı ve daha önce önerilen sönümleyicilere göre avantajları olduğu sonucuna varılmıştır.

TABLE OF CONTENTS

ACKNOWLEDGEMENTS . . . iii
ABSTRACT . . . iv
ÖZET . . . v
LIST OF FIGURES . . . viii
LIST OF TABLES . . . xvi
LIST OF SYMBOLS . . . xviii
LIST OF ACRONYMS/ABBREVIATIONS . . . xxi
1. INTRODUCTION . . . 1
1.1. General . . . 1
1.2. Literature Survey . . . 3
1.2.1. Precast Post-Tensioned Concrete As a Low-Damage Seismic System 3
1.2.2. An Overview of Passive Energy Dissipation Devices . . . 9
1.2.3. External Dampers for Precast Post-tensioned Structures . . . 11
1.3. Problem Statement and the Proposed Damper . . . 19
2. EXPERIMENTAL STUDIES . . . 23
2.1. Experiment Setup . . . 23
2.2. Test Parameters . . . 25
2.3. Test Results . . . 30
2.3.1. Response Parameters . . . 30
2.3.2. Summary of Test Results . . . 31
2.3.3. Force-Displacement Histories . . . 34
2.3.4. Force Capacity . . . 41
2.3.5. Initial Stiffness . . . 42
2.3.6. Area of the Hysteresis Loop . . . 43
2.3.7. System Adequacy of the Damper Mechanism . . . 44
2.3.8. Condition of Prototype Damper Mechanism Components after the Test . . . 57
3. NUMERICAL STUDIES . . . 59
3.1. Principles and Verification of Numerical Model of the Damper Mechanism 59

3.2. Sub-Assembly Level Analyses 70
3.2.1. Principles and Verification of Numerical Model 70
3.2.2. Sub-assembly Analysis Parameters 75
3.2.3. Force-Drift Ratio Plots 80
3.2.4. Force Capacity 83
3.2.5. Relative Energy Dissipation Ratio 87
3.2.6. Post-Tensioning Tendon Stresses 90
3.2.7. Damper Forces 93
3.3. Frame-Level Analyses 95
3.3.1. Principles and Verification of Numerical Model 99
3.3.2. Frame Analysis Parameters 100
3.3.3. Base Shear 101
3.3.4. Energy Dissipation Parameters 104
3.3.5. Post-Tensioning Tendon Forces 105
3.3.6. Damper Forces 111
3.4. Time-History (Dynamic) Analyses 116
4. ANALYTICAL MODEL 124
4.1. Analytical Model of the Damper 124
4.2. Analytical Model of the Sub-Assembly 128
5. SUMMARY AND CONCLUSIONS 133
REFERENCES 136
APPENDIX A: DAMPER DESIGN 143
APPENDIX B: COPYRIGHTS FOR FIGURES 147

LIST OF FIGURES

Figure 1.1. Performance Zones Specified by Turkish Seismic Code [3]. 2

Figure 1.2. Precast Post-Tensioned Concrete Frame Joint [5]. 4

Figure 1.3. Hybrid joint tested in NIST in 1993 [6]. 4

Figure 1.4. Four types of connections tested by Priestley et al. [7]. 6

Figure 1.5. Condition of the connections after being subjected to seismic effect by Priestley et al. [7]. 7

Figure 1.6. Prototype frame tested by Kato et al. [8]. 7

Figure 1.7. Hysteretic response of a) reinforced concrete b) precast post-tensioned concrete [9]. 8

Figure 1.8. An overview of passive energy dissipation devices by Symans et al. [23]. 10

Figure 1.9. Friction damper proposed by Pall [24]. 11

Figure 1.10. Friction damper proposed by Mualla [25]. 12

Figure 1.11. Toggle-brace dampers by Constantinou et al. [41]. 13

Figure 1.12. The specimens tested by Ozden and Ertas [48]. 14

Figure 1.13. The hysteresis plots of specimens tested by Ozden and Ertas [48]. 14

Figure 1.14. Damper proposed by Kurama and Morgen [21]. 15

Figure 1.15. Dampers tested by Marriott et al. [50]. 16

Figure 1.16. Hysteretic response of the dampers tested by Marriott et al. [50]. . 16

Figure 1.17. Damper proposed by Yano et al. [18]. 17

Figure 1.18. Hysteretic response of the damper proposed by Yano et al. [18]. . 17

Figure 1.19. Damper proposed by Li et al. [51]. 18

Figure 1.20. Cyclic response of damper proposed by Li et al. [51]. 18

Figure 1.21. Damper proposed by Wang et al. [52]. 19

Figure 1.22. The proposed damper. 20

Figure 1.23. a) Translational friction mechanism, b) Metallic yielding mechanism and c) proposed (rotational friction) mechanism with amplified damping. 21

Figure 1.24. Kinematic analysis demonstrating motion amplification effect. . . 22

Figure 2.1. Experiment setup. 23

Figure 2.2. Parts used in the prototype damper mechanism. 24

Figure 2.3. Dimensions of the prototype damper mechanism. (All units are in mm) 25

Figure 2.4. Test parameters of the prototype damper mechanism. 26

Figure 2.5. Displacement protocol applied to the prototype damper mechanism. 27

Figure 2.6. Response parameters. 30

Figure 2.7. Force-displacement plots for Group 1 tests. 35

Figure 2.8. Force-displacement plots for Group 2 tests. 36

Figure 2.9. Force-displacement plots for Group 3 tests. 37

Figure 2.10. Force-displacement plots for Group 4 tests. 38

Figure 2.11. Force-displacement plots for Group 5 tests. 39

Figure 2.12. Force-displacement plots for Group 6 tests. 40

Figure 2.13. Force capacity results for tests. 42

Figure 2.14. Results of average initial stiffness for tests. 43

Figure 2.15. Results of area of the hysteresis loop for tests. 44

Figure 2.16. Initial stiffness values calculated for all cycles of Group 1 tests. . . 45

Figure 2.17. Initial stiffness values calculated for all cycles of Group 2 tests. . . 46

Figure 2.18. Initial stiffness values calculated for all cycles of Group 3 tests. . . 47

Figure 2.19. Initial stiffness values calculated for all cycles of Group 4 tests. . . 48

Figure 2.20. Initial stiffness values calculated for all cycles of Group 5 tests. . . 49

Figure 2.21. Initial stiffness values calculated for all cycles of Group 6 tests. . . 50

Figure 2.22. Area of the hysteresis loop values calculated for all cycles of Group 1 tests. 51

Figure 2.23. Area of the hysteresis loop values calculated for all cycles of Group 2 tests. 52

Figure 2.24. Area of the hysteresis loop values calculated for all cycles of Group 3 tests. 53

Figure 2.25. Area of the hysteresis loop values calculated for all cycles of Group 4 tests. 54

Figure 2.26. Area of the hysteresis loop values calculated for all cycles of Group 5 tests. 55

Figure 2.27. Area of the hysteresis loop values calculated for all cycles of Group 6 tests. 56

Figure 2.28. Aluminum alloy friction disks after the experiment. 57

Figure 2.29. Damper bolts after the experiment. 58

Figure 2.30. Damper plate friction surface experiment. 58

Figure 3.1. Modeling principles for the damper mechanism. 60

Figure 3.2. Determination of μ for Test 27. 61

Figure 3.3. Comparison of experimental and numerical results for Group 1 tests. 64

Figure 3.4. Comparison of experimental and numerical results for Group 2 tests. 65

Figure 3.5. Comparison of experimental and numerical results for Group 3 tests. 66

Figure 3.6. Comparison of experimental and numerical results for Group 4 tests. 67

Figure 3.7. Comparison of experimental and numerical results for Group 5 tests. 68

Figure 3.8. Comparison of experimental and numerical results for Group 6 tests. 69

Figure 3.9. Numerical modeling principles for Ertas sub-assembly for verification. 71

Figure 3.10. Concrete model used in OpenSEES. 72

Figure 3.11. Stress-strain curve for prestressing steel. 73

Figure 3.12. Experiment sub-assembly of Ertas used for verification of numerical modeling principles [54]. 74

Figure 3.13. Comparison of a) Numerical results and b) Experiment results for Ertas sub-assembly [54]. 75

Figure 3.14. Sub-assembly used in numerical analyses. 76

Figure 3.15. Drift ratio protocol applied to the sub-assembly. 78

Figure 3.16. Relative energy dissipation ratio β. 79

Figure 3.17. Force vs. drift ratio plots for sub-assembly 0 through 9. 81

Figure 3.18. Force vs. drift ratio plots for sub-assembly 10 through 21. 82

Figure 3.19. Force capacity vs. drift ratio plots. 84

Figure 3.20. Force capacity vs. relative energy dissipation ratio plots. 88

Figure 3.21. Comparison for β at 1.00% and 4.00% drift ratios for SU8. 90

Figure 3.22. Post-tensioning stress vs. drift ratio plots for sub-assembly 0 through 9. 91

Figure 3.23. Post-tensioning stress vs. drift ratio plots for sub-assembly 10 through 21. 92

Figure 3.24. Damper force vs. drift ratio plots for sub-assembly 0 through 9. . 93

Figure 3.25. Damper force vs. drift ratio plots for sub-assembly 10 through 21. 94

Figure 3.26. Plan of the prototype building and section of the analyzed frame. 96

Figure 3.27. Damper configurations for investigated frames. 96

Figure 3.28. Details for damper mechanism used in frame analyses. 98

Figure 3.29. Numerical modeling principles for the frames. 99

Figure 3.30. Comparison of frame results for a) Morgan and Kurama [21] b) this study. 100

Figure 3.31. Equivalent viscous damping ξ_{eq}. 101

Figure 3.32. Base shear vs roof drift plots for the frames. 103

Figure 3.33. Post-tensioning forces for F_0. 107

Figure 3.34. Post-tensioning forces for F_{st}. 108

Figure 3.35. Post-tensioning forces for $F_{20D\text{-}1/4}$. 109

Figure 3.36. Post-tensioning forces for $F_{40D\text{-}1/4}$. 110

Figure 3.37. Post-tensioning forces for $F_{40D\text{-}1/8}$. 111

Figure 3.38. Damper force F_d. 112

Figure 3.39. Damper forces for F_{st}. 112

Figure 3.40. Damper forces for $F_{20D\text{-}1/4}$. 113

Figure 3.41. Damper forces for $F_{40D\text{-}1/4}$. 114

Figure 3.42. Damper forces for $F_{40D\text{-}1/8}$. 115

Figure 3.43. Acceleration history and elastic spectra for Coyote Lake, Düzce and Erzincan earthquakes. 118

Figure 3.44. Acceleration history and elastic spectra for Imperial Valley, Kobe and Loma Prieta earthquakes. 119

Figure 3.45. Scaling of acceleration histories of earthquakes. 120

Figure 4.1. Analytical model for the damper. 125

Figure 4.2. Verification of analytical model for the damper. 126

Figure 4.3. Initial angle vs. total relative rotation plot for fixed axial displacement of one end of the mechanism. 127

Figure 4.4. Damper “lock” position. 127

Figure 4.5. Plot of the initial angle at which damper locks itself for imposed u_{max}. 128

Figure 4.6. Analytical model. 129

Figure 4.7. Beam-column joint equilibrium. 130

Figure 4.8. Vector loop for upper damper unit. 131

Figure 4.9. Vector loop for lower damper unit. 131

Figure 4.10. Verification of sub-assembly analytical model. 132

Figure A.1. Internal forces acting on the damper. 143

Figure A.2. Internal forces acting on the damper plate for maximum tensile force case. 145

Figure A.3. Anchorage of damper to precast column. 146

Figure B.1. Copyrights obtained from PCI 147

Figure B.2. Copyrights obtained from Engineering Structures 147

LIST OF TABLES

Table 2.1. Test parameters 27

Table 2.2. Test results 31

Table 3.1. Coefficient of friction (μ) and T_{fr} values 62

Table 3.2. Parameters for sub-assembly tests 77

Table 3.3. Force capacity F_{sa} for sub-assemblies 83

Table 3.4. Relative energy dissipation ratio β for sub-assemblies 87

Table 3.5. Analysis parameters for investigated frames 97

Table 3.6. Base shear values 101

Table 3.7. Energy dissipation values for frames 104

Table 3.8. Natural vibration periods (T_N) of the frames 116

Table 3.9. Earthquakes used in time-history analyses 117

Table 3.10. Comparison of story drifts (%) 120

Table 3.11. Maximum story drifts for F_0 (%) 121

Table 3.12. Maximum story drifts for F_{st} (%) 121

Table 3.13. Maximum story drifts for $F_{40D-1/8}$ (%) 122

Table 3.14. Base shear values (kN) obtained from dynamic analyses 122

LIST OF SYMBOLS

A_{ps}	Cross-sectional area of post-tensioning tendons
A_{so}	Area related to stiffness for calculation of equivalent viscous damping
c_c	Depth of concrete compressive block for analytical model
d	Diameter of bolt torque
d_b	Depth of beam
e_{ps}	Eccentricity of post-tensioning tendons from mid-height of the beam
E_a	Elasticity Modulus of aluminum alloy used in friction disks
E_b	Elasticity Modulus of connection bolts used in damper mechanism
E_s	Elasticity Modulus of steel used in damper mechanism
$E_D(t)$	Energy dissipated by viscous damping
$E_I(t)$	Energy input to the structure from the time earthquake excitation has begun
$E_K(t)$	Kinetic energy of the mass
$E_S(t)$	Recoverable strain energy of the system
$E_Y(t)$	Energy dissipated by yielding
f_{ya}	Yield strength of aluminum alloy used in friction disks
f_{yb}	Yield strength of connection bolts used in damper mechanism
f_{ys}	Yield strength of steel used in damper mechanism
f_{ua}	Ultimate strength of aluminum alloy used in friction disks
f_{ub}	Ultimate strength of connection bolts used in damper mechanism
f_{up}	Ultimate strength of prestressing steel
f_{us}	Ultimate strength of steel used in damper mechanism
F_1	Force at negative drift ratio for calculation of relative energy dissipation ratio

F_2	Force at positive drift ratio for calculation of relative energy dissipation ratio
$F(t)$	The vertical reaction of the prototype damper mechanism at time t
F_c	Concrete compressive force reaction for analytical model
F_d	Force reaction at damper mechanism
F_{max}	Maximum force capacity of damper mechanism measured at experiment (equal to force measured at positive displacement amplitude)
F_{min}	Force measured at damper experiment at negative displacement amplitude
F_{sa}	Force reaction for sub-assembly analyses
F_{pt}	Force at post-tensioning tendons
k_{eff}	Initial stiffness of damper mechanism
$k_{eff,ave}$	Average initial stiffness of damper mechanism
K	Coefficient for connection bolt
L_c	Length of column
M_{beam}	Moment acting on beam for analytical model
M_{col}	Moment acting on column for analytical model
M_d	Design moment acting on the damper plate
M_{jo}	Moment acting on joint for analytical model
N_{blt}	Normal force at connection bolt
N_d	Design normal force acting on the damper plate
p	Pressure acting on damper joint interface
r_1	Inner radius of damper mechanism joints
r_2	Outer radius of damper mechanism joints
$T_{blt,m}$	Bolt torque applied at the middle joint of the damper
$T_{blt,tb}$	Bolt torque applied at the top and bottom joints of the damper
T_{fr}	Friction torque at joint of damper
$T_{fr,j}$	Friction torque at joint j of damper

u_{max}	The positive amplitude of the deformation protocol applied in the test
u_{min}	The negative amplitude of the deformation protocol applied in the test (equal to positive amplitude)
u_{sa}	Displacement at top column joint for sub-assembly analyses
$u(t)$	The displacement applied to the prototype damper mechanism at time t
W_D	Area of hysteresis loop for damper mechanism
$W_{D,ave}$	Average area of hysteresis loop for damper mechanism
μ	Coefficient of friction between friction disk and steel plate at damper joint
δ_{sa}	Drift ratio for sub-assembly analyses
δ_{fr}	Drift ratio for frame analyses
Δ_j	Relative rotation at joint j of damper
β	Relative energy dissipation ratio
ξ_{eq}	Equivalent viscous damping ratio
σ_{pt}	Stress at post-tensioning tendons
ϕ_{col}	Curvature of column for analytical model
ϕ_{beam}	Curvature of beam for analytical model
θ_i	Initial angle of the damper
θ_{jo}	Joint rotation for analytical model
θ'_1	Negative drift ratio calculated according to initial stiffness for relative energy dissipation ratio
θ'_2	Positive drift ratio calculated according to initial stiffness for relative energy dissipation ratio

LIST OF ACRONYMS/ABBREVIATIONS

CD	Controlled Damage Level
CP	Collapse Prevention Level
LD	Limited Damage Level
F_0	Frame with no damper used
F_{st}	F_0 strengthened with dampers
$F_{20D-1/4}$	Frame with 20 dampers and similar yield capacity with F_0 with target β of 0.250
$F_{40D-1/4}$	Frame with 40 dampers and similar yield capacity with F_0 with target β of 0.250
$F_{40D-1/8}$	Frame with 40 dampers and similar yield capacity with F_0 with target β of 0.125
OpenSEES	Opensource Earthquake Engineering Software
SU	Sub-assembly

1. INTRODUCTION

1.1. General

Hardy Cross, a pioneer in structural engineering and developer of the Cross Method, once said "strength is essential and otherwise unimportant", stressing on the fact "that if a structure is not sufficiently strong, it makes little difference what other attributes it has" [1]. Since then, another attribute, not less important than strength, was adopted in structural engineering.

Modern structural earthquake engineering approach focuses on two major phenomena: Providing sufficient strength to resist loads due to earthquake and providing sufficient ductility to be able to undergo inelastic deformations without failing in a brittle manner. Due to the economically infeasible nature of designing structures to remain elastic especially in large earthquakes, inelastic behaviour is permitted, one might even say encouraged. This inelastic behaviour, in turn, manifests itself in the form of structural damage. For a structure subjected to an earthquake excitation, this concept can be illustrated with the energy balance equation which is expressed as

$$E_I(t) = E_K(t) + E_D(t) + E_S(t) + E_Y(t), \tag{1.1}$$

where the $E_Y(t)$ term represents the hysteretic energy dissipated by yielding of the structure [2]. In reinforced concrete and emulative precast concrete structures, this occurs by the mechanisms of yielding of rebar steel and cracking of concrete, which causes residual deformations and structural damage. In modern specifications for earthquake design, this structural damage is permitted to occur except for a group of structures with high importance factors. However, limits are defined for the damage levels according to the probability of exceedance of the earthquake event in the location the structure is to be built.

Turkish Seismic Code [3] specifies four performance zones to evaluate seismic performance of structures: Limited Damage Zone, Marked Damage Zone, Advanced

Damage Zone and Collapse Zone. Boundaries between these zones define Limited Damage (LD) Level, Controlled Damage (CD) Level and Collapse Prevention (CP) Level, respectively. This concept is illustrated in Figure 1.1.

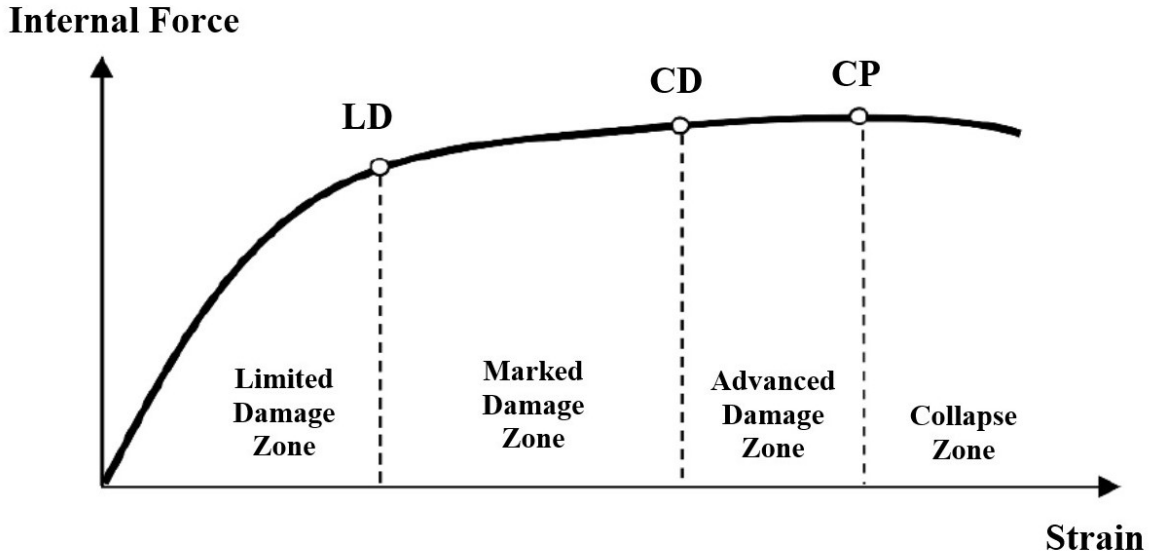

Figure 1.1. Performance Zones Specified by Turkish Seismic Code [3].

In most cases, buildings are required to remain within Controlled Damage Level for earthquake excitations with a probability of exceedance of 10% in 50 years, which is the design earthquake level in Turkish Seismic Code. Turkish Seismic Code defines Controlled Damage as the level which corresponds to 75% of the limit parameters that are defined for Collapse Prevention Level. In other words, strain demands on rebar steel and concrete extreme compressive fiber and plastic rotation demand for the relevant hinge is allowed to reach 75% of those that would put the building in Collapse Zone. Furthermore, some structural members are allowed to be in Advanced Damage Zone provided their percentage within the story do not exceed defined limits [3].

These definitions for structural damage levels are meaningful to structural engineers. However, from the standpoint of functionality of the building or to the ears of people who will occupy the building, they are not clear. Federal Emergency Management Agency of the US (FEMA) describes Life Safety Level, which can be interpreted as equivalent to Controlled Damage Level of Turkish Seismic Code, as buildings that

"may be beyond economical repair", with "some residual strength and stiffness left in all stories" and "some permanent drift". In addition for reinforced concrete frames, it indicates "extensive damage to beams, spalling of cover and shear cracking for ductile columns, joint cracks" [4].

1.2. Literature Survey

1.2.1. Precast Post-Tensioned Concrete As a Low-Damage Seismic System

The aforementioned definitions directly indicate situations which can either make repair economically impossible or cause serious obstructions to the functionality of the building after the earthquake, which is a significant problem especially for industrial buildings in which productivity is vital. The need to overcome this problem triggered emergence of Low-Damage Seismic Systems, which by definition exhibit minimum/repairable damage in specially-designed localized regions.

One of the most superior seismic systems in terms of low damage is Precast Post-tensioned Concrete, in which precast concrete structural members are connected using post-tensioning tendons at the site. Precast concrete beams are almost always pre-stressed individually, to resist the internal forces they are subjected to. Gravitational and lateral loads are resisted by a system which is governed by a gap-opening mechanism that occurs at the joints. This mechanism imposes strain demands on post-tensioning tendons which are the primary source of load resistance. (Figure 1.2 [5]) Post-tensioning tendons can be unbonded in which case there is no bonding of the strands to the member sections. They can alternatively be bonded by means of grout injection which provides bonding to member sections. The tendons can span the entire frame or they can be anchored to anchorages left in precast beams along the span.

Experimental studies on precast post-tensioned concrete systems were initiated at National Institute of Standards and Technology (NIST) of USA in 1987 [6]. 1/3 scale models for interior beam column joints incorporating mild steel at top and bottom fibers of the beam and post-tensioning tendons at mid-height were subjected to cyclic

inelastic loading. These type of connections were named 'hybrid connections', referring to the fact that the behaviour is the result of contributions from both the mild steel and post-tensioning tendons. Figure 1.3 illustrates one of the types of joints tested in the program.

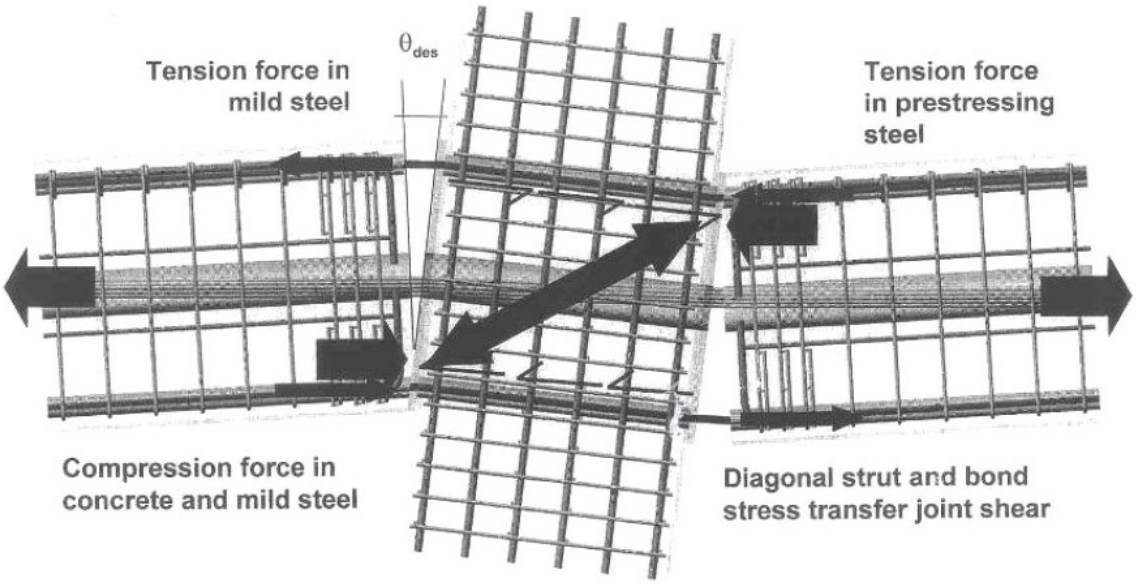

Figure 1.2. Precast Post-Tensioned Concrete Frame Joint [5].

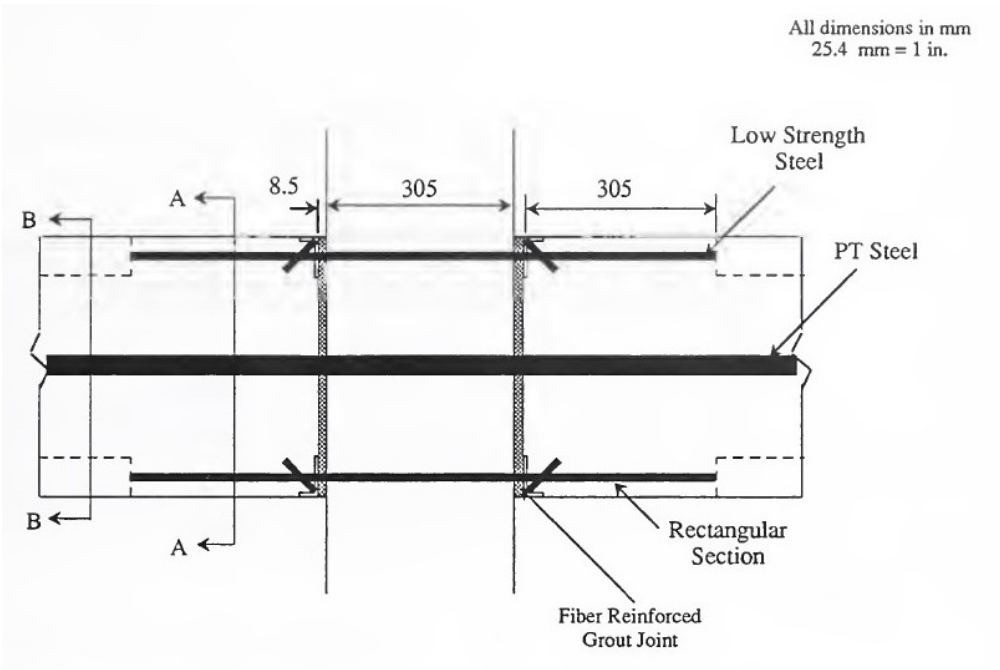

Figure 1.3. Hybrid joint tested in NIST in 1993 [6].

Priestley et al. conducted tests on a five-story precast post-tensioned building incorporating four types of connections in 1999 [7]. In hybrid post-tensioned connection, unbonded post-tensioning strands were used at mid-height. Mild steel rebars were placed at top and bottom parts of the connection to enhance flexural strength and energy dissipation capacity. These rebars were partially unbonded to limit strain demands. The pretensioned connection consisted of only unbonded post-tensioning strands placed at mid-height of connection and no additional mild steel. In the TCY-gap connection, bottom part was clamped to the column by threaded post-tensioning bars. Mild steel rebars were placed at top part of the connection to yield alternatively in tension and compression. TCY connections consisted of mild steel rebars at top and bottom parts to emulate a conventional reinforced concrete connection with equal reinforcement. These connections are shown in Figure 1.4.

The prototype building was subjected to shake-table tests and response of the aforementioned four connection types were investigated [7]. Priestley et al. observed that at seismic demands more than twice the design drift level, hybrid connections and pretensioned connections performed excellently, exhibiting minor damage concentrated at the fiber grout joint interface. In TCY gap and TCY connections, sliding of the beam along the interface, along with the fracture of some mild steel rebars were observed. It is important to note that although TCY gap connections performed relatively worse, the overall damage exhibited by the hybrid and posttensioned connections at drift levels reaching 4.50% was significantly smaller than what would be expected from a conventional reinforced concrete building. The conditions of the connections subjected to more than twice the design earthquake level are shown in Figure 1.5.

In 2000, Kato et al. conducted dynamic tests on a prototype precast post-tensioned frame, which is shown in Figure 1.6 [8]. The frame consisted of unbonded post-tensioning strands running through the ducts in the beams and columns and anchored at both ends of the frame. The structural damage manifested itself as minor cracks around the joint even for 4.00% story drift, and it was concluded that the frame showed sufficient seismic performance including in large drift demands. They also observed that the frame did not have significant hysteretic damping capacity.

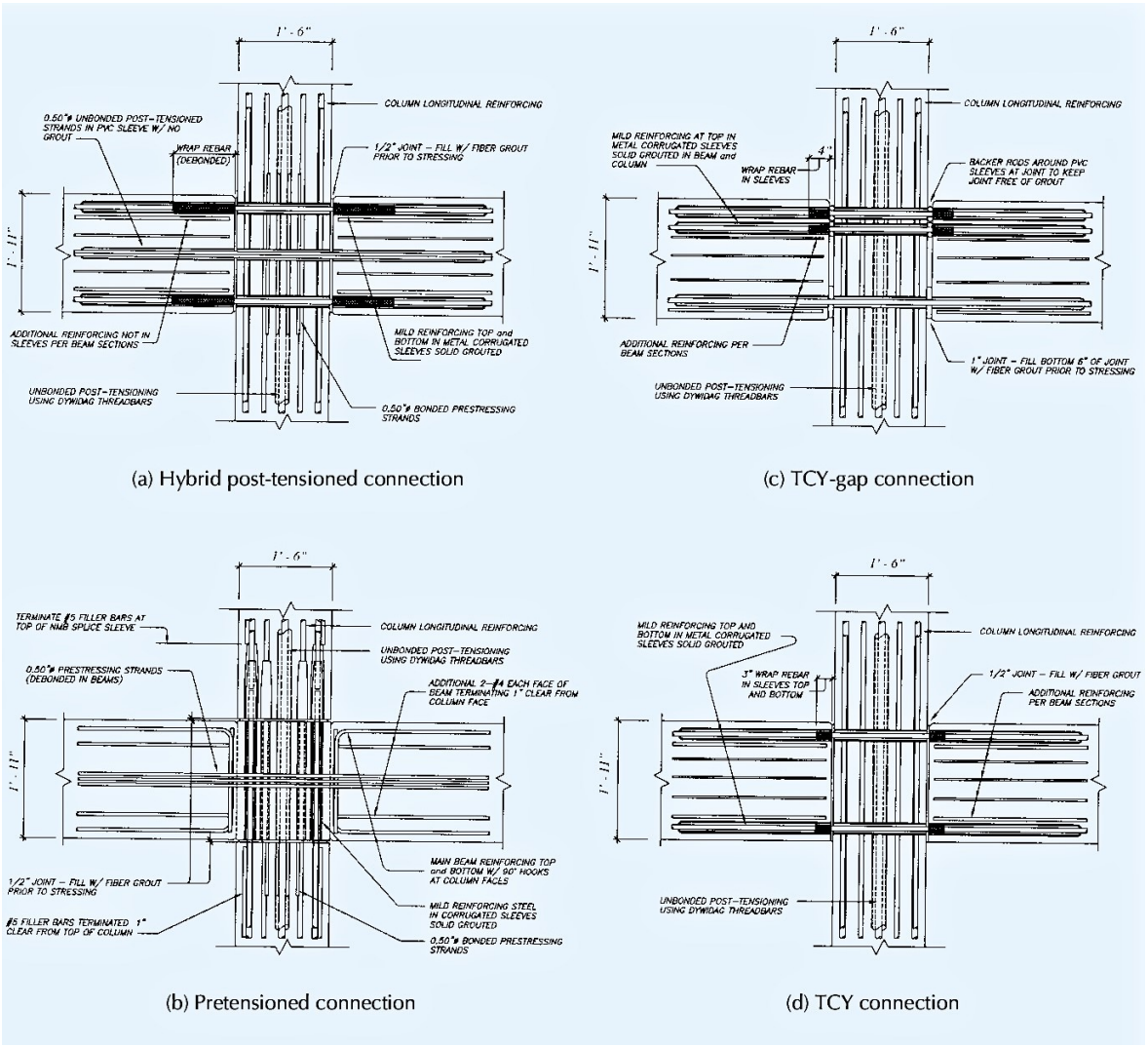

Figure 1.4. Four types of connections tested by Priestley et al. [7].

As the results of the initial research studies show, precast post-tensioned concrete structural systems show superior performance even in very severe seismic conditions in terms of structural damage and structural integrity. Specifically, the structural damage is minor and concentrated around the specially designed joint interface. Furthermore, the post-tensioning strands are designed to remain elastic under design seismic effects, which causes the structure to self-center after the earthquake. However, this advantageous aspect comes with lack of hysteretic energy dissipation capacity, which is inherent in many structural systems. This phenomenon is illustrated in Figure 1.7, which shows ideal hysteretic responses and damage states for reinforced concrete and precast post-tensioned specimens tested by Wada et al. [9].

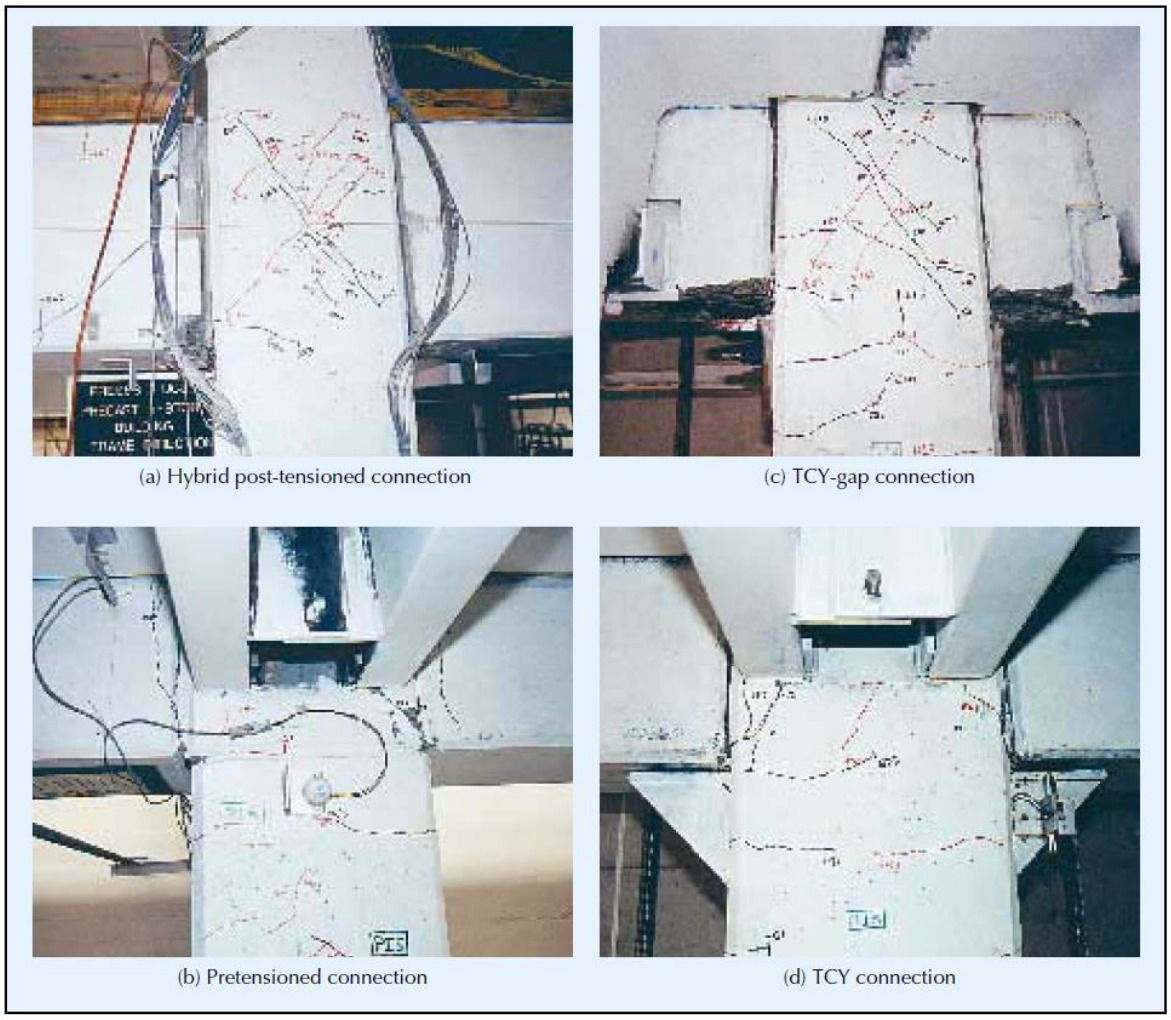

Figure 1.5. Condition of the connections after being subjected to seismic effect by Priestley et al. [7].

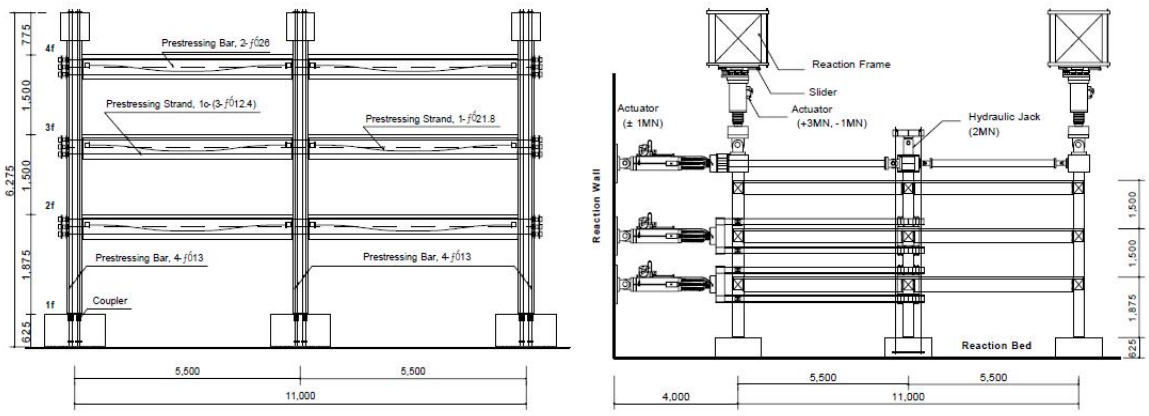

Figure 1.6. Prototype frame tested by Kato et al. [8].

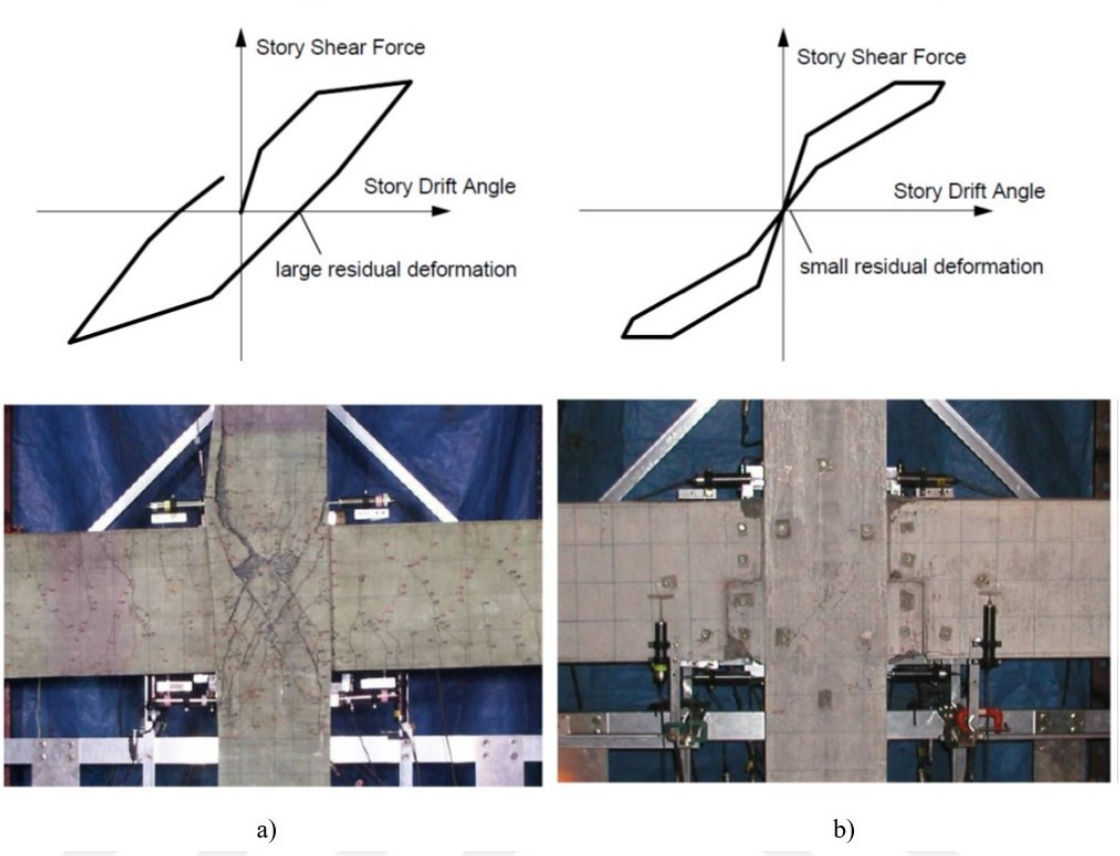

Figure 1.7. Hysteretic response of a) reinforced concrete b) precast post-tensioned concrete [9].

The interior beam column joints shown in Figure 1.7 are subjected to ±4.00% drift demand. As can be observed, the reinforced concrete joint exhibits significant structural damage, particularly in the joint panel area and the plastic hinging of the column. However, the precast post-tensioned joint looks intact and only local concrete spalling is seen at top and bottom parts of the interface. The structural damage is a manifestation of hysteretic (yielding) response of the reinforced concrete specimen which can be observed in the drift-story shear force plot. The area enclosed by the hysteresis curve is large, hence hysteretic energy dissipation. For the precast post-tensioned specimen, however, there is very limited area enclosed by the hysteresis loop. Although this results in very small residual deformation and self-centering capacity, it also means very limited hysteretic energy dissipation capacity. This limitation in hysteretic energy dissipation capacity results in increase of seismic drift demands on precast post-tensioned concrete structures. To enhance energy and force capacity, passive energy dissipation

devices (external dampers) to be implemented on these structures have been proposed in literature.

1.2.2. An Overview of Passive Energy Dissipation Devices

Extensive research has been made about passive energy dissipation devices, alternatively known as external dampers. These dampers are classified as viscous fluid dampers [10–12], viscoelastic solid dampers [13–15], metallic yielding dampers [16–18] and friction dampers [19–22]. A summary of these dampers is illustrated by Symans et al. and is shown in Figure 1.8 [23].

Viscous fluid dampers consist of a tube filled with a fluid, which is generally silicone-based. The resistance to the flow of this fluid through the orifices of the tube when the piston is excited is the source of damping. Viscoelastic solid dampers work with the principle of shear deformation of a viscoelastic material, generally elastomeric rubber pad, which is due to the relative displacement of the steel plates to which it is attached. Metallic yield dampers are those in which the damper yields in a cyclic manner and contributes to the energy dissipation capacity of the structure by way of hysteretic damping. Friction dampers dissipate energy by way of relative sliding or rotation between two or more surfaces. Figure 1.9 shows Pall friction damper [19], in which brake lining pads move relative to the steel plates to which they are attached and this mechanism dissipates energy via friction.

Another type of friction damper is proposed by Mualla and is shown in Figure 1.10 [25–31]. This damper consists of steel plates and special friction pads that are placed at their connections. At these connections, clamping force is applied by way of a torque wrench at the end of the bolt that connects the members. The damper is placed in a chevron brace and when the frame is displaced, the steel plates rotate relative to each other and the friction mechanism at the joint dissipates energy. At these dampers, the friction mechanism occurs at the middle joint between the plates, which are connected to the chevron brace at their opposite ends with hinged connections.

	Viscous Fluid Damper	Viscoelastic Solid Damper	Metallic Damper	Friction Damper
Basic Construction			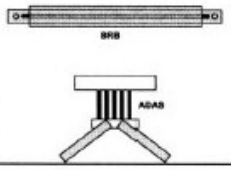	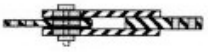
Idealized Hysteretic Behavior	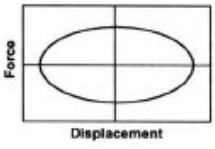	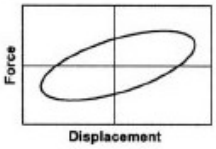	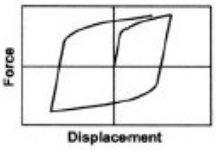	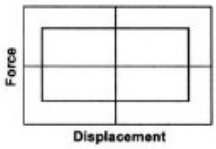
Idealized Physical Model	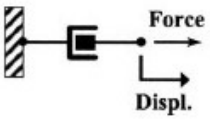	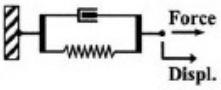	Idealized Model Not Available	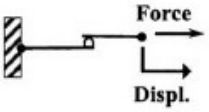
Advantages	- Activated at low displacements - Minimal restoring force - For linear damper, modeling of damper is simplified. - Properties largely frequency and temperature-independent - Proven record of performance in military applications	- Activated at low displacements - Provides restoring force - Linear behavior, therefore simplified modeling of damper	- Stable hysteretic behavior - Long-term reliability - Insensitivity to ambient temperature - Materials and behavior familiar to practicing engineers	- Large energy dissipation per cycle - Insensitivity to ambient temperature
Disadvantages	- Possible fluid seal leakage (reliability concern)	- Limited deformation capacity - Properties are frequency and temperature-dependent - Possible debonding and tearing of VE material (reliability concern)	- Device damaged after earthquake; may require replacement - Nonlinear behavior; may require nonlinear analysis	- Sliding interface conditions may change with time (reliability concern) - Strongly nonlinear behavior; may excite higher modes and require nonlinear analysis - Permanent displacements if no restoring force mechanism provided

Figure 1.8. An overview of passive energy dissipation devices by Symans et al. [23].

Experiments were conducted on a rotational friction damper that consists of two side plates and friction mechanism on the multiple surfaces between them with varying parameters [32]. Numerical studies were conducted to investigate the behavior of a quadrilateral damper with rotational friction mechanism on all corners and a diagonal

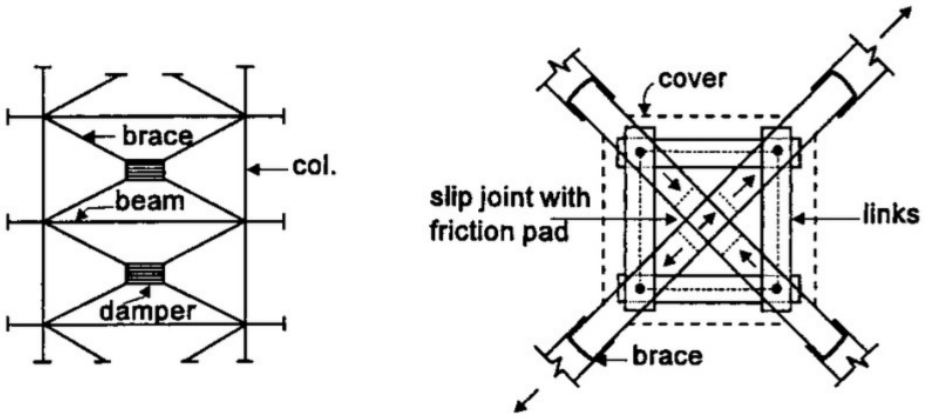

Figure 1.9. Friction damper proposed by Pall [24].

spring in between two of the corners [33]. Experiments conducted on a prototype frame incorporating rotational frictional dampers with two side plates placed on the ends of two chevron braces symmetrical to the vertical axis proved the effectiveness of such rotational dampers and indicated that the performance of the damper is significantly enhanced by optimizing the geometry [34]. Analytical and experimental studies were also conducted on alternative rotational frictional damper designs [35–40].

Toggle-brace dampers are those which are placed in a geometrical composition that amplifies the displacements imposed on the system by the earthquake [41–47]. Examples of such dampers as illustrated by Constantinou et al. [41] are shown in Figure 1.11.

1.2.3. External Dampers for Precast Post-tensioned Structures

The most extensively studied supplemental enery dissipation option for precast post-tensioned concrete structures is mild steel rebar. In this kind of connection, post-tensioning strands are placed at mid-height of the beam to limit seismic strain demands and ensure elastic behaviour. To enhance moment capacity and to add hysteretic damping, mild steel rebars are placed at top and bottom parts of the connection. When the structure is subjected to an earthquake event, a gap opens at the joint, which increases the strain in the mild steel rebars and the post-tensioning strands. The

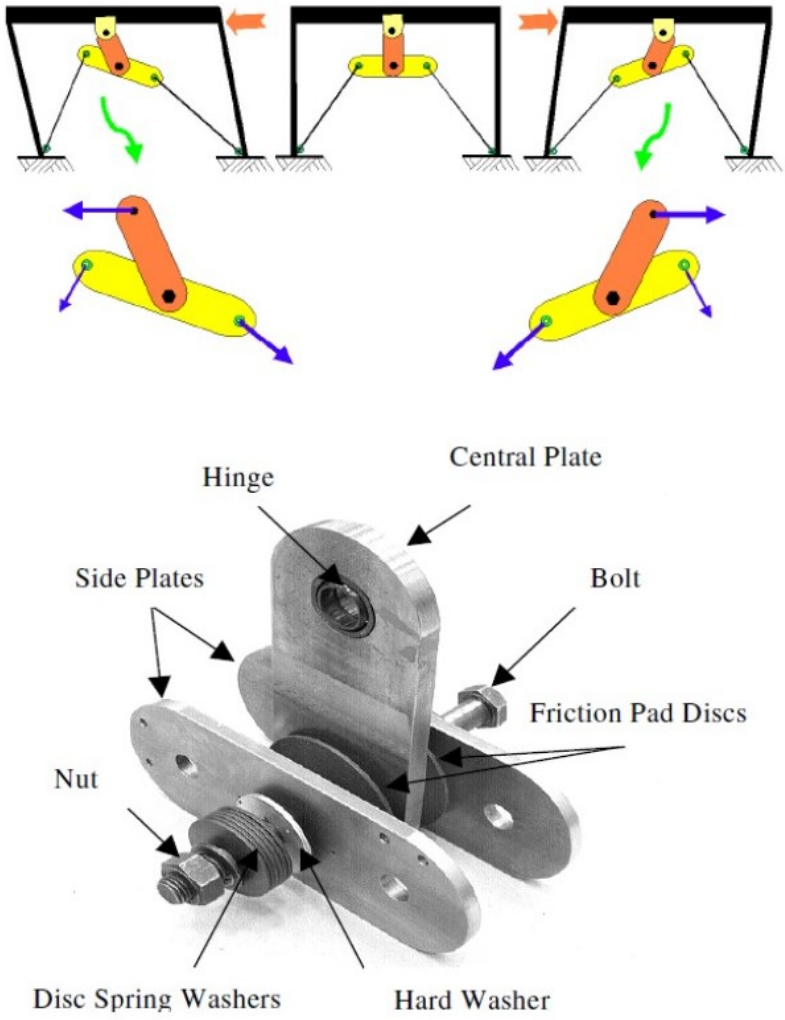

Figure 1.10. Friction damper proposed by Mualla [25].

post-tensioning strands are designed to remain elastic whereas the rebars are designed to yield. This yielding of rebars contributes to both the moment and energy dissipation capacity. Examples of interior beam-column joints using mild steel rebar at top and bottom parts of the connection can be seen in Figure 1.2 and Figure 1.4a. This type of connection is also called "hybrid" connection, implying the combined contribution of mild steel rebar and post-tensioning strands to force and energy dissipation capacity.

Ozden and Ertas conducted tests on an exterior precast post-tensioned beam-column joint specimen, shown in Figure 1.12, studying the effect of different percentages of mild steel rebar used in the hybrid connection [48]. They tested specimens with 65%, 50%, 30%, 10% and 0% contribution of mild steel rebar to moment capacity of the

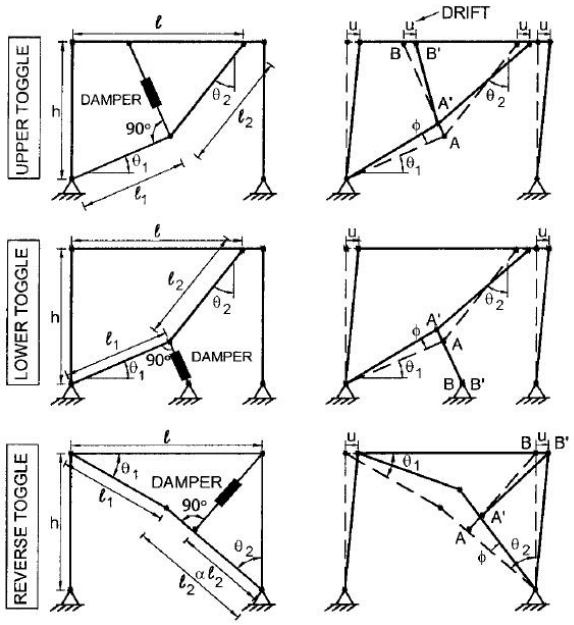

Figure 1.11. Toggle-brace dampers by Constantinou et al. [41].

joint, and labeled them PTM65, PTM50, PTM30, PTM10 and PTM0, respectively. The specimens were subjected to a displacement protocol up to ±4.00% drift. The load-drift plots for PTM0, PTM30 and PTM60 are shown in Figure 1.13.

As can be seen from the plots, as the contribution of mild steel rebar increases, the area of the hysteresis loop, which is an indicator of energy dissipation capacity, increases significantly. This area is negligibly small for PTM0, which confirms the limited energy dissipation capacity of precast post-tensioned structures. However, it can also be observed that there is also no residual deformation even after ±4.00% drift, due to the self-centering effect of strands. For PTM30 and PTM60, the enclosed area is much larger, indicating a significant increase in hysteretic energy dissipation. The residual deformation for PTM60, however, is very large. It is very important to note here that the advantage of supplemental hysteretic energy dissipation by mild steel rebars is offset by residual deformations and the need to replace the yielded rebars after the earthquake. For this reason, Ozden and Ertas proposed that 20% to 30% mild steel rebar is optimum amount to balance energy dissipation and self-centering ability.

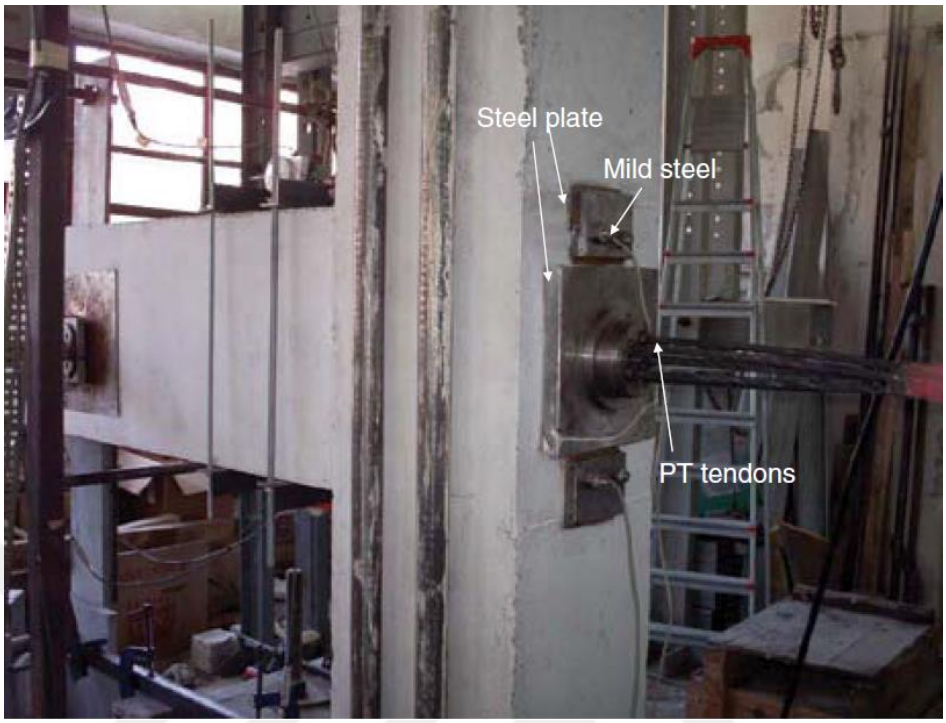

Figure 1.12. The specimens tested by Ozden and Ertas [48].

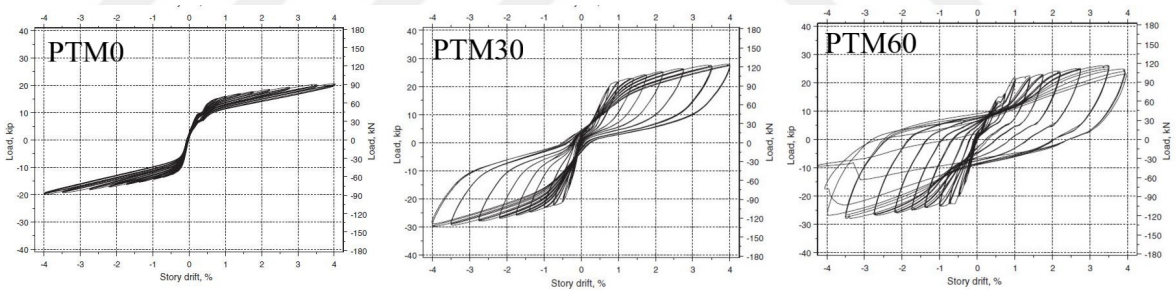

Figure 1.13. The hysteresis plots of specimens tested by Ozden and Ertas [48].

Kurama and Morgen proposed an external friction damper that is placed at top and bottom parts of the joint [49]. The damper, which is shown in Figure 1.14, works with principle of translational friction mechanism which occurs between surfaces moving relative to eachother as the gap at the joint opens and closes. They made 55 tests with alternating friction disk material, beam depth, number of post-tensioning strands, average initial post-tensioning stress and nominal damper normal force. They observed that the proposed damper was the primary source of energy dissipation, and can be designed to increase the relative energy dissipation ratio well above the minimum requirement, which cannot be satisfied for precast post-tensioned joints without

the dampers. The dampers also contributed significantly to the moment capacity, providing beams with smaller depths equal moment capacity with beams with large depths. It is also important to point out that one of the observations of the tests was that the cyclic degradation of specimens with dampers were smaller than specimens without dampers. This indicates a more reliable performance particularly for large seismic demands, where post-yield stiffness degradation can be a problem.

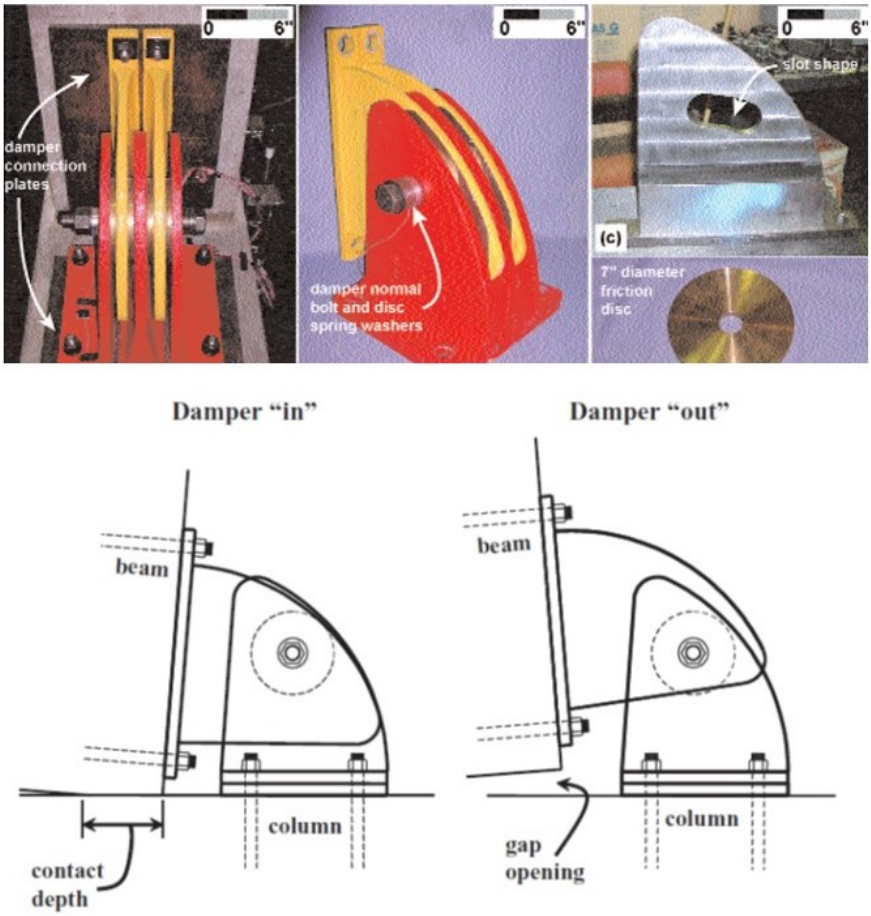

Figure 1.14. Damper proposed by Kurama and Morgen [21].

Marriott et al. tested precast post-tensioned walls with external mild steel dampers, viscous dampers and a combination of these, which are shown in Figure 1.15 [50]. They applied dynamic testing protocol to four specimens, consisting of a specimen without any external damper, a specimen with 4 viscous dampers, a specimen with 4 viscous dampers plus 2 mild steel dampers and a specimen with 2 mild steel dampers. These specimens were labeled HY_{0MS-0V}, HY_{0MS-4V}, HY_{2MS-4V} and HY_{2MS-0V}, respectively. The dampers, of which nonlinear response is shown in Figure 1.15, were

individually tested and their performances were deemed to be "extremely well". The flag-shaped hysteretic responses shown in Figure 1.16 indicate an improvement in energy dissipation capacity by use of viscous and/or mild steel dampers. However, it can be observed that, although the self-centering behaviour is preserved, the energy dissipation capacity provided by the proposed dampers is limited.

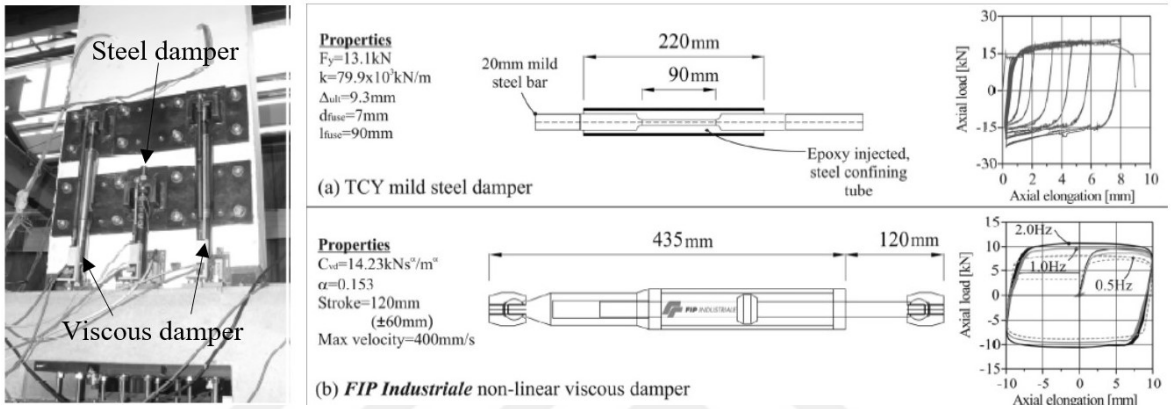

Figure 1.15. Dampers tested by Marriott et al. [50].

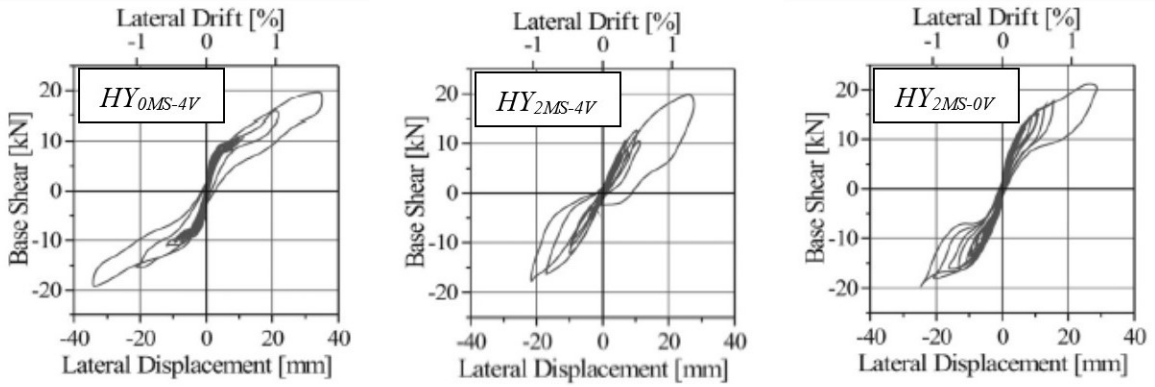

Figure 1.16. Hysteretic response of the dampers tested by Marriott et al. [50].

Yano et al. tested external metallic yielding steel dampers with anti-buckling restraints on precast post-tensioned walls, as shown in Figure 1.17 [18]. The test setup consisted of a precast post-tensioned beam rotated 90 degrees and steel dampers placed at both sides to utilize the gap opening mechanism that occurs when the specimen is displaced. To prevent buckling of dampers, they were placed inside buckling-restraining tubes. The cyclic response of the specimen with and without damper is shown in Figure 1.18. It can be seen that the steel damper provides additional energy dissipation,

albeit very limited one. It should be also noted here that since the damper is yielding by nature, it is necessary to replace it after the earthquake event.

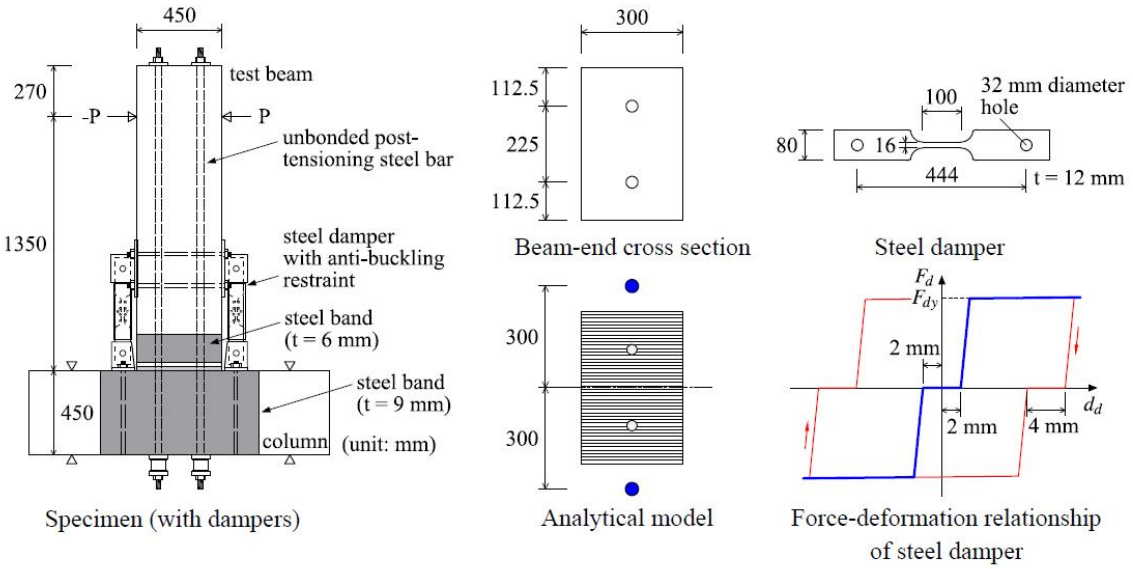

Figure 1.17. Damper proposed by Yano et al. [18].

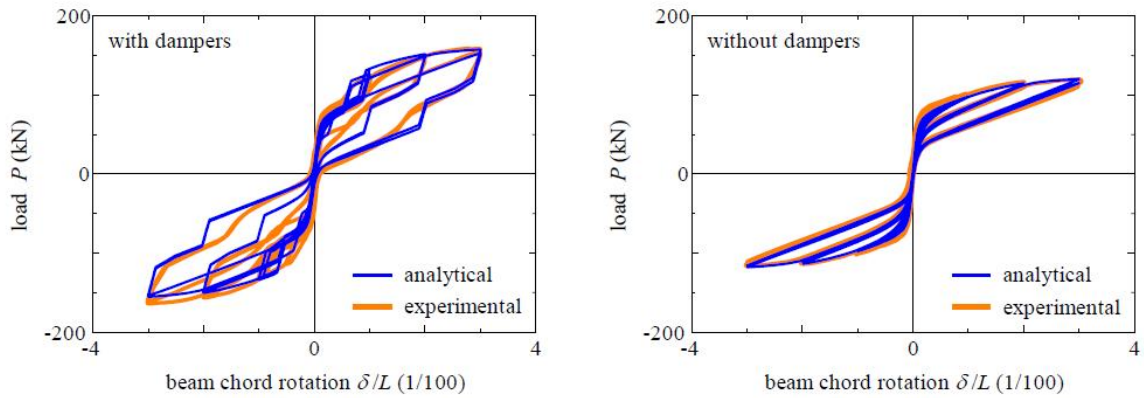

Figure 1.18. Hysteretic response of the damper proposed by Yano et al. [18].

Li et al. conducted tests on a metallic yielding damper to be used in beam-column joints of precast post-tensioned structures [51]. This damper is shown in Figure 1.19. The drift-force plot for this damper is shown in Figure 1.20. The nonlinear cyclic response of this metallic yielding damper shows that although it enhances energy dissipation capacity, it compromises the self centering aspect of precast post-tensioned concrete systems significantly.

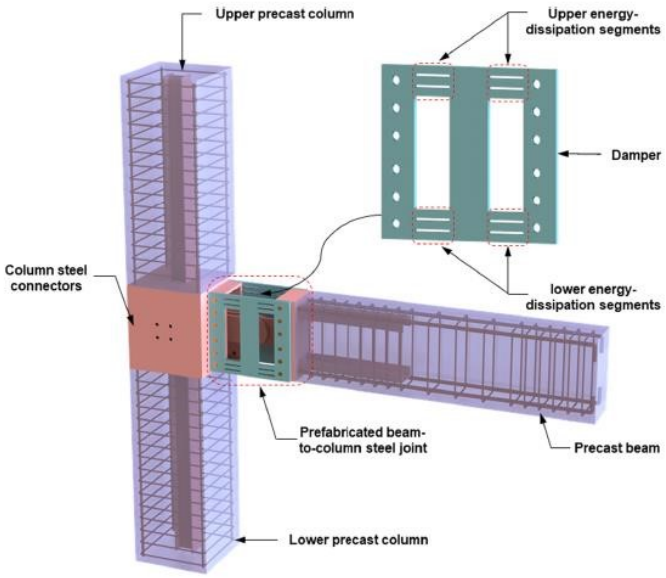

Figure 1.19. Damper proposed by Li et al. [51].

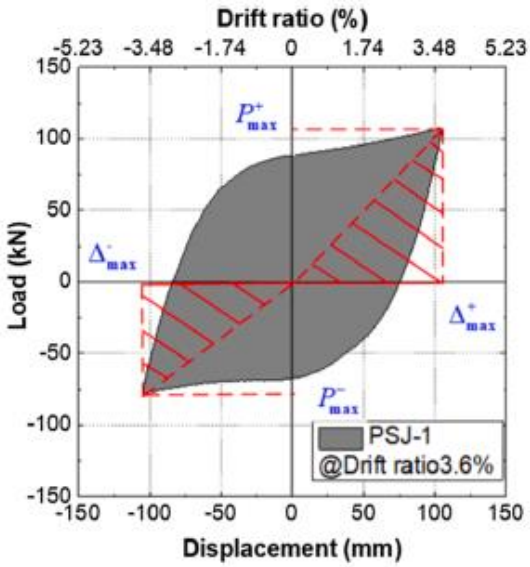

Figure 1.20. Cyclic response of damper proposed by Li et al. [51].

Wang et al. proposed and conducted tests on a metallic yielding damper to be placed to beam-column joints [52], which is shown in Figure 1.21 along with the hysteretic response.

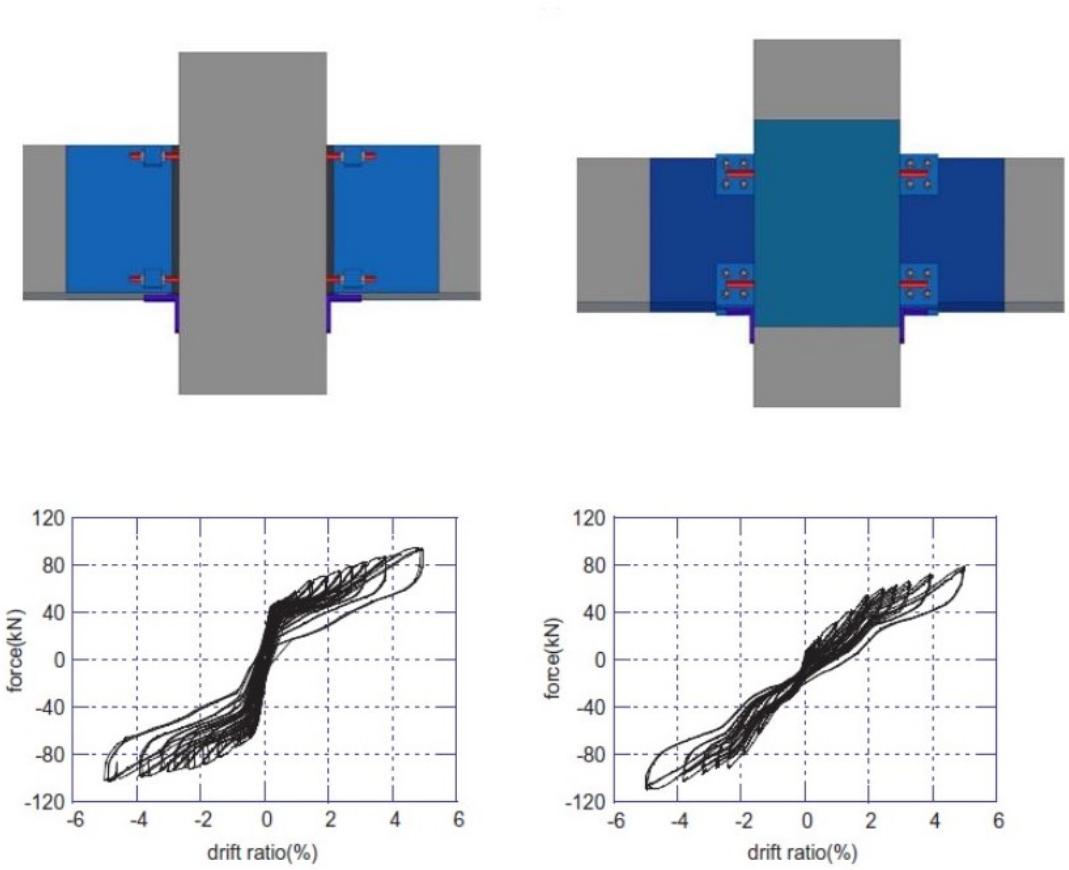

Figure 1.21. Damper proposed by Wang et al. [52].

1.3. Problem Statement and the Proposed Damper

Precast post-tensioned concrete structural systems, due to the lack of hysteretic damping phenomenon that is inherent in many structural systems, have very low energy dissipation capacity. This causes seismic displacement demands on such structures to be larger. Although mild steel rebars placed at top and bottom parts of the beam have been proposed, these are not feasible because it is very difficult to reach and replace them after an earthquake.

For this reason, external energy dissipation devices are developed in literature and outlined in previous parts of this document. These devices work with metallic yielding, translational friction or viscous damping. All of these mechanisms rely on either translational displacement or translational velocity. However, the gap opening

at beam-column joints of precast post-tensioned structures that triggers these translational movements are not in large amplitude.

This study proposes an external damper that is placed at top and bottom parts of beam-column joints. The damper consists of steel plates with friction disks placed in between at the joints. Clamping force is applied to the joints by way of a torque wrench at the end of bolts. When the structure is subjected to an earthquake event, the gap opening that occurs at beam-column joint causes the steel plates to rotate relative to each other. The friction mechanism that exists at the joints dissipate energy. As it is demonstrated in this research, when the initial angle of the damper mechanism is small, it amplifies the gap opening displacement and utilizes the relative rotations due to this amplification to contribute to energy dissipation capacity of the structure. Details of the proposed damper are shown in Figure 1.22. A comparison of the proposed damper mechanism with the alternative mechanisms is shown in Figure 1.23.

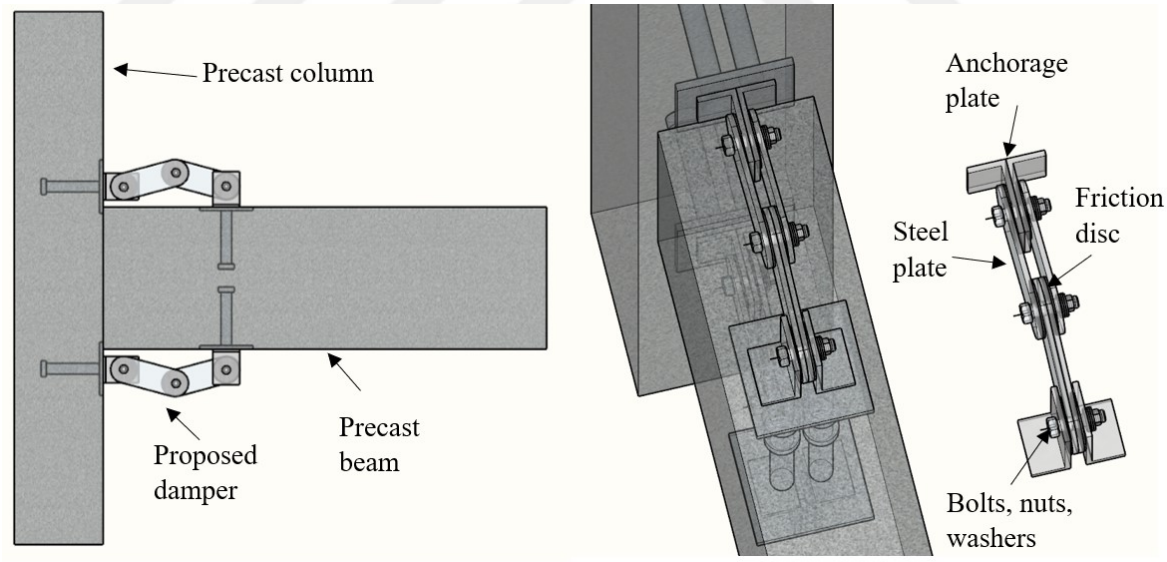

Figure 1.22. The proposed damper.

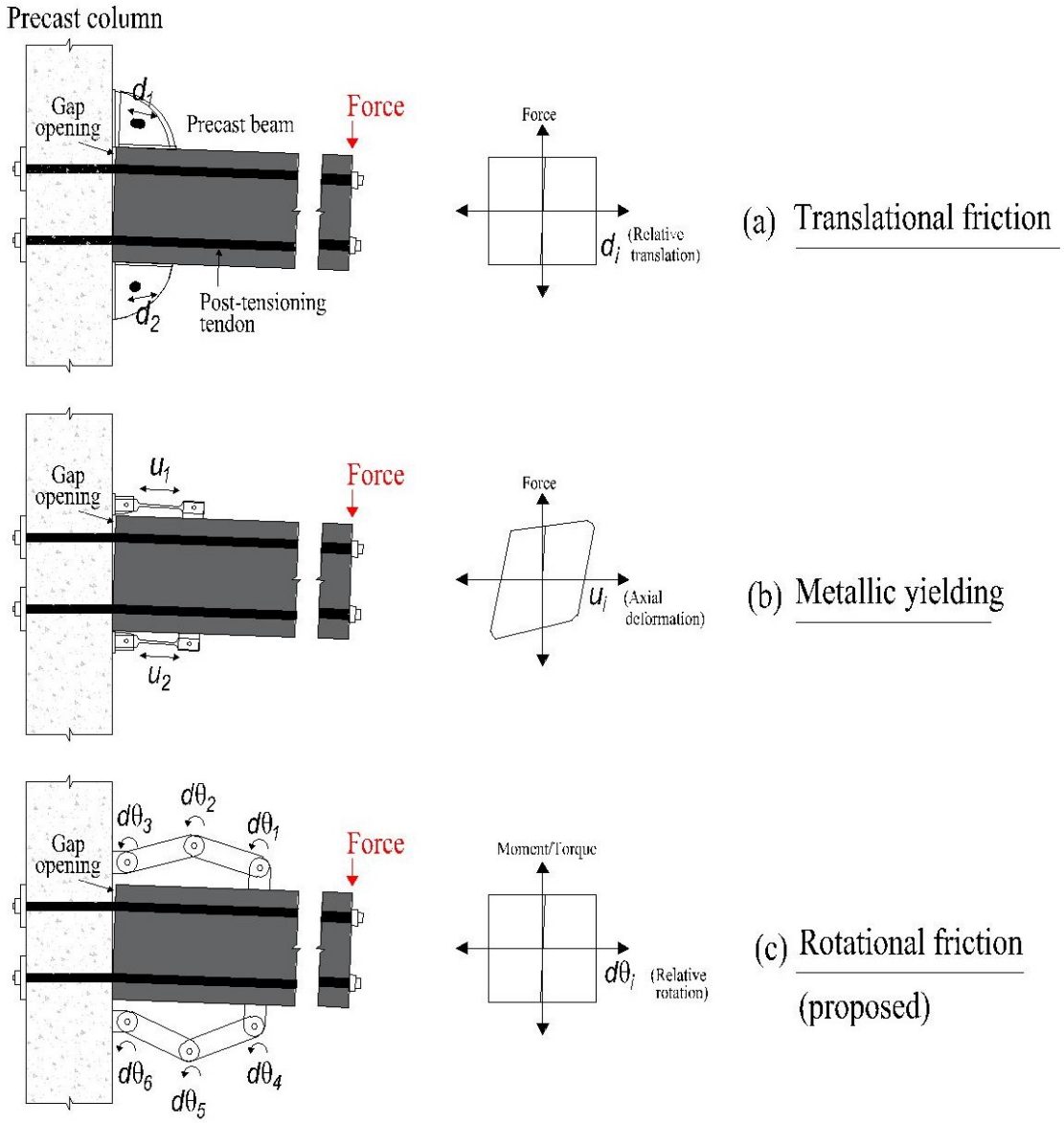

Figure 1.23. a) Translational friction mechanism, b) Metallic yielding mechanism and c) proposed (rotational friction) mechanism with amplified damping.

A kinematic study performed on a precast post-tensioned beam-column joint specimen with the proposed damper that demonstrates the motion amplification effect is shown in Figure 1.24. As can be observed, as the initial angle decreases, the relative rotation between surfaces exponentially increases. Since friction damping is directly correlated to relative rotation, the amplification effectively increases the damper performance.

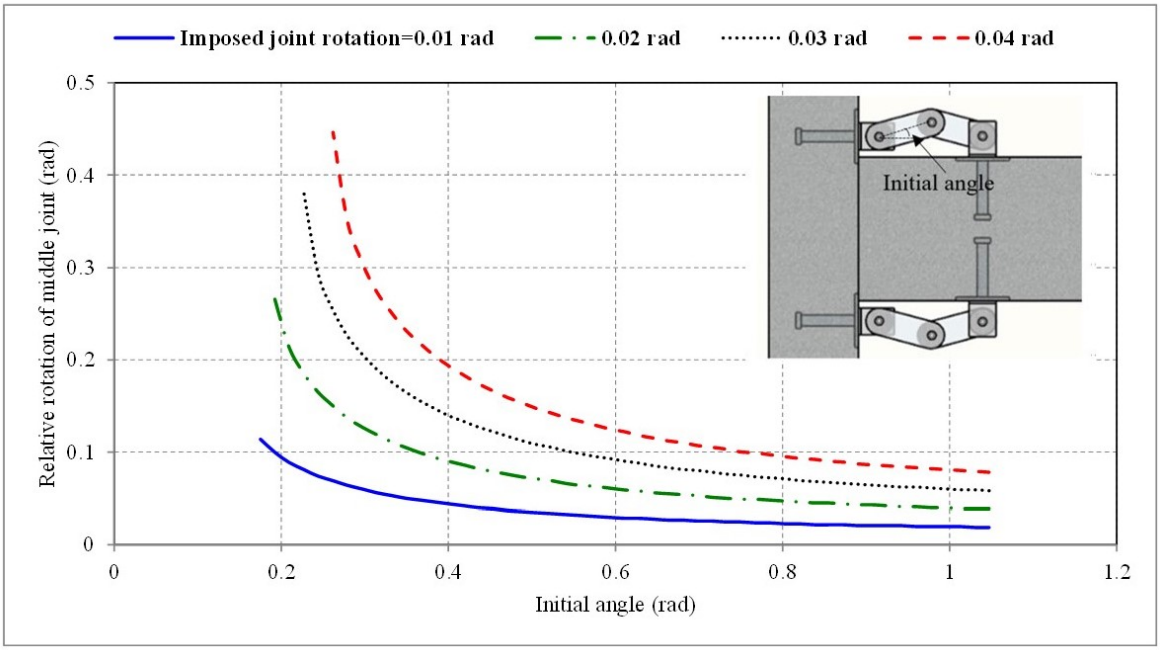

Figure 1.24. Kinematic analysis demonstrating motion amplification effect.

There are several novel aspects of the proposed damper. One of them is that previously proposed rotational dampers do not utilize the amplification mechanism due to small initial angle. The toggle-brace dampers which utilize this mechanism are placed inside braces, which occupy significant space inside the building. However, the damper described in this thesis is a compact mechanism that is placed at the joint and does not occupy space. Another novel aspect is that the friction mechanism exists at all joints of the mechanism, rather than only the middle joint. For rotational dampers that have been studied throughout literature, only the middle joint has friction.

The damper mechanism is also proposed to contribute to the force capacity of the system significantly, hence enabling a substantial reduction in materials which are the primary sources of force capacities of structural systems, particularly post-tensioning tendons for structures investigated in this thesis.

2. EXPERIMENTAL STUDIES

2.1. Experiment Setup

In order to investigate the behaviour of the proposed damper under cyclic loading, experiments were conducted using a servo-hydraulic testing machine. The prototype damper mechanism consisted of two identical sets of dampers placed symmetrically to prevent eccentric loading applied to the machine. The damper mechanism was rotated 90 degrees since the machine was able to apply loads in a vertical manner. The test setup is shown in Figure 2.1.

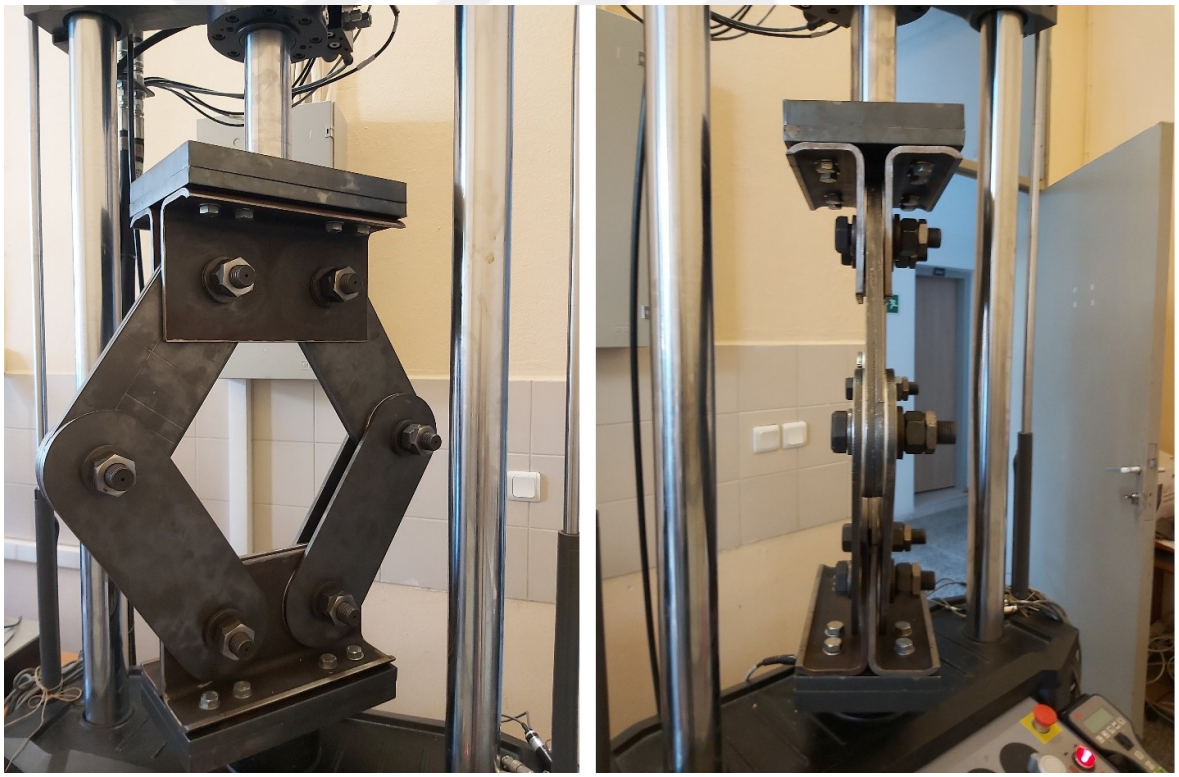

Figure 2.1. Experiment setup.

Figure 2.2 shows the parts used in the prototype damper mechanism. In one unit of dampers, four steel plates (P6), two at top and two at bottom were used. At the joints that connects these plates, aluminum alloy friction pads (D) were placed. Bolts (C1) were used to connect the plates and to apply clamping force. Disk springs (Y) were used to ensure uniform stress under cyclic loading. Nuts and counter-nuts (S)

were also used to prevent stress loss in the interface. The prototype was anchored to the test machine using rectangular plates (P1-P4) and bolts (C2-C3). The connection between anchorage plates and damper plates was established by way of steel corner members (P5).

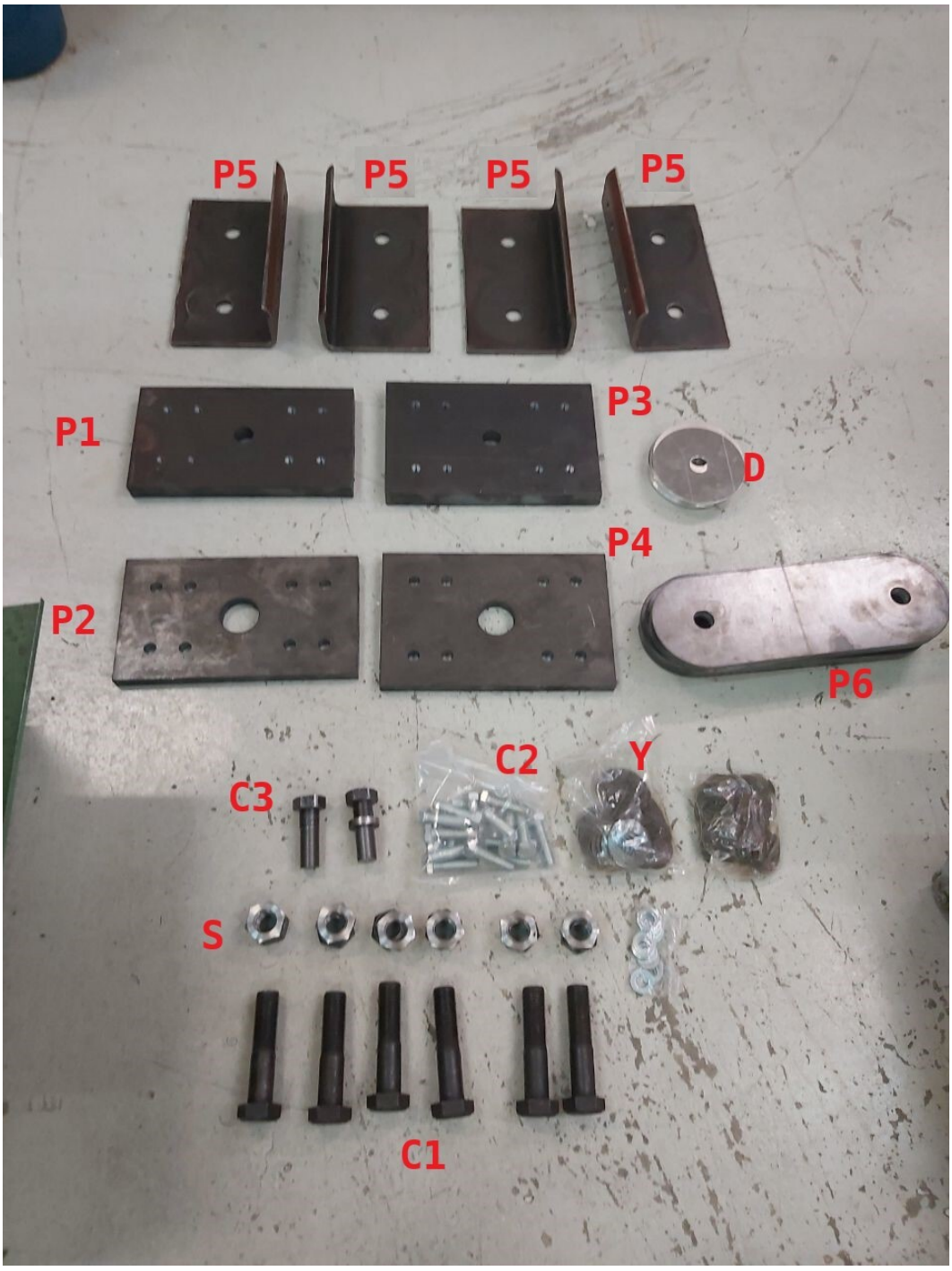

Figure 2.2. Parts used in the prototype damper mechanism.

The damper and anchorage plates were plasma cut from St37 grade steel (f_{ys}=300MPa, f_{us}=370MPa, E_s=200GPa). The friction disks were laser cut from 6061 aluminum alloy (f_{ya}=275MPa, f_{ua}=310MPa, E_a=68GPa). The M30 bolts and nuts were 8.8 grade (f_{yb}=640MPa, f_{ub}=800MPa, E_b=200GPa)

The prototype damper mechanism dimensions are shown in Figure 2.3.

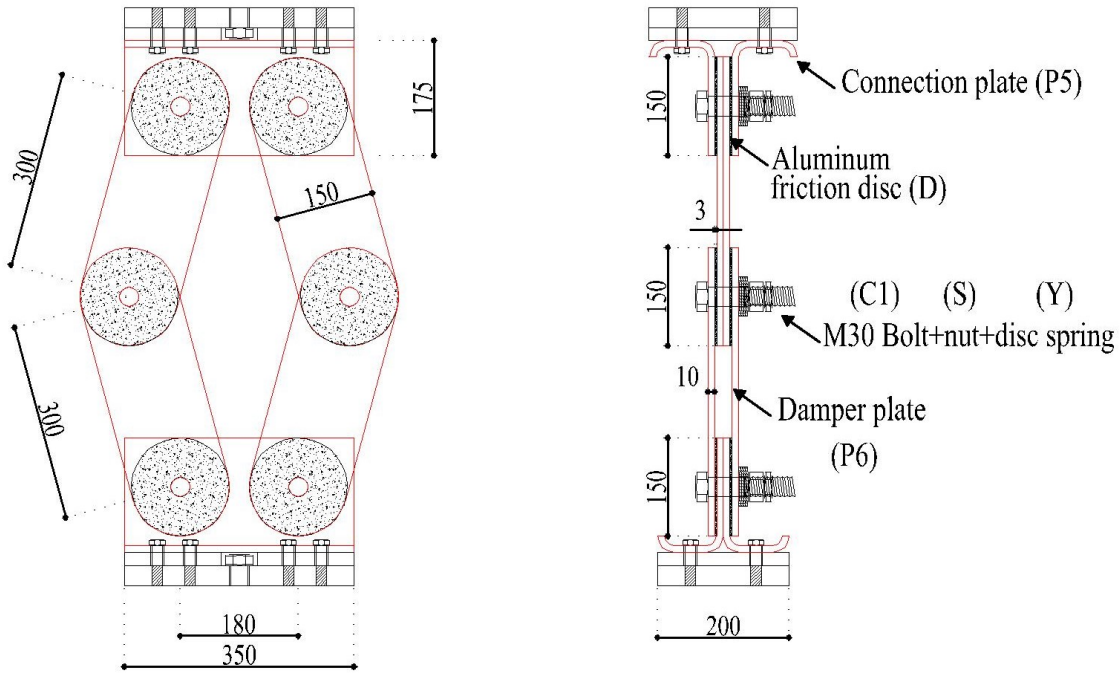

Figure 2.3. Dimensions of the prototype damper mechanism. (All units are in mm)

2.2. Test Parameters

A total of 48 tests were conducted to investigate the response of the proposed damper mechanism with various parameters. These parameters, which are shown in Figure 2.4, are as follows:

- θ_i is the initial angle of the damper (30, 22.5, 15 degrees)
- $T_{blt,m}$ is the bolt torque applied at the middle joint of the damper (25, 50, 100 Nm)
- $T_{blt,tb}$ is the bolt torque applied at top and bottom joints of the damper (0, 25,

50, 100 Nm)

- u_{max} is the amplitude of the deformation protocol applied in the test (5, 15, 25 mm)

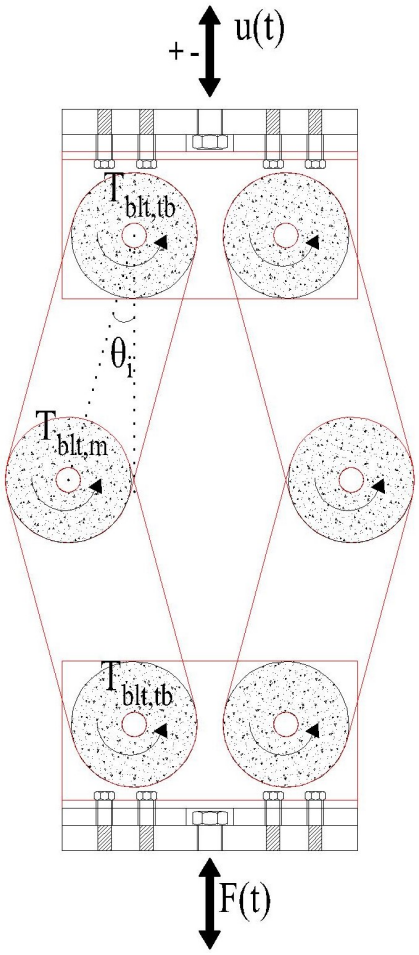

Figure 2.4. Test parameters of the prototype damper mechanism.

The response of the prototype damper mechanism was measured in terms of the vertical force reaction that is read at load cell at the bottom of the test machine $F(t)$ for the displacement amplitude $u(t)$ at time t.

The experiments were conducted according to the specifications of FEMA-356, which requires "each device shall be loaded with 20 fully reversed in the displacement of the energy dissipation device" [4]. The cyclic displacement protocol $u(t)$ shown in Figure 2.5 consisting of 30 cycles of triangular waves with frequencies 0.5 Hz or 1 Hz and displacement amplitudes of 5mm, 15mm and 25mm was applied at the top of the

damper mechanism in the vertical direction in compliance with FEMA-356 and the force-displacement response of the damper (u vs. F) was recorded.

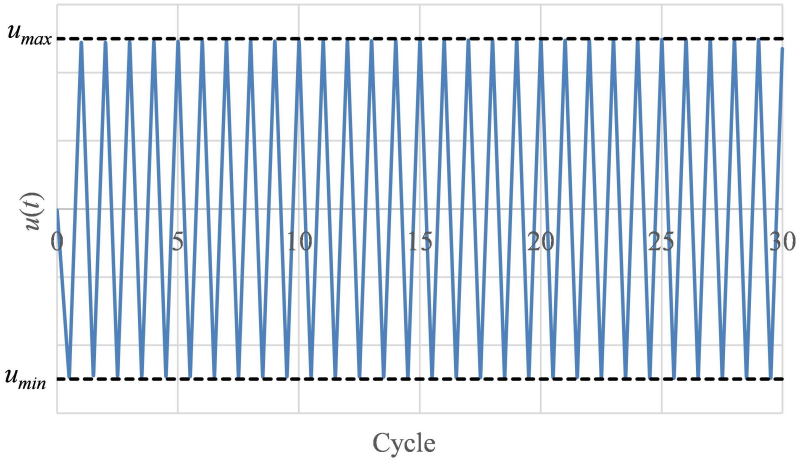

Figure 2.5. Displacement protocol applied to the prototype damper mechanism.

The tests were grouped according to the bolt torque applied to middle joint $T_{blt,m}$ and the bolt torque applied to top and bottom joints $T_{blt,tb}$. In odd numbered groups $T_{blt,tb}$=0 and $T_{blt,m}$ is equal to 25 Nm, 50 Nm and 100 Nm for Groups 1, 3 and 5, respectively. Furthermore, in the even numbered groups $T_{blt,m}$=$T_{blt,tb}$ and the torque values are 25 Nm, 50 Nm and 100 Nm for Groups 2, 4 and 6, respectively. The test parameters are listed in Table 2.1.

Table 2.1. Test parameters

Test	θ_i	$T_{blt,m}$	$T_{blt,tb}$	u_{max}	f	Group
	rad	Nm	Nm	mm	Hz	
1	30	25	0	5	1	1
2	30	25	0	15	1	
3	30	25	0	25	0.5	
4	22.5	25	0	5	1	
5	22.5	25	0	15	1	
6	22.5	25	0	25	0.5	
7	15	25	0	5	1	
8	15	25	0	15	1	

Table 2.1. Test parameters (cont.)

Test	θ_i	$T_{blt,m}$	$T_{blt,tb}$	u_{max}	f	Group
	rad	Nm	Nm	mm	Hz	
9	30	25	25	5	1	2
10	30	25	25	15	1	
11	30	25	25	25	0.5	
12	22.5	25	25	5	1	
13	22.5	25	25	15	1	
14	22.5	25	25	25	0.5	
15	15	25	25	5	1	
16	15	25	25	15	1	
17	30	50	0	5	1	3
18	30	50	0	15	1	
19	30	50	0	25	0.5	
20	22.5	50	0	5	1	
21	22.5	50	0	15	1	
22	22.5	50	0	25	0.5	
23	15	50	0	5	1	
24	15	50	0	15	1	
25	30	50	50	5	1	4
26	30	50	50	15	1	
27	30	50	50	25	0.5	
28	22.5	50	50	5	1	
29	22.5	50	50	15	1	
30	22.5	50	50	25	0.5	
31	15	50	50	5	1	
32	15	50	50	15	1	

Table 2.1. Test parameters (cont.)

Test	θ_i	$T_{blt,m}$	$T_{blt,tb}$	u_{max}	f	Group
	rad	Nm	Nm	mm	Hz	
33	30	100	0	5	1	5
34	30	100	0	15	1	
35	30	100	0	25	0.5	
36	22.5	100	0	5	1	
37	22.5	100	0	15	1	
38	22.5	100	0	25	0.5	
39	15	100	0	5	1	
40	15	100	0	15	1	
41	30	100	100	5	1	6
42	30	100	100	15	1	
43	30	100	100	25	0.5	
44	22.5	100	100	5	1	
45	22.5	100	100	15	1	
46	22.5	100	100	25	0.5	
47	15	100	100	5	1	
48	15	100	100	15	1	

2.3. Test Results

2.3.1. Response Parameters

The response of the prototype damper mechanism was evaluated according to the response parameters specified by FEMA-356 [4], along with the force-displacement history of the tests. Figure 2.6 shows an example force-displacement plot to help better explain these response parameters. In the plot, u_{max} and u_{min} are positive and negative amplitudes of the vertical displacements applied to the prototype damper mechanism, respectively. These two values are equal with opposite directions. F_{max} and F_{min} are force reactions measured corresponding to these amplitudes, respectively.

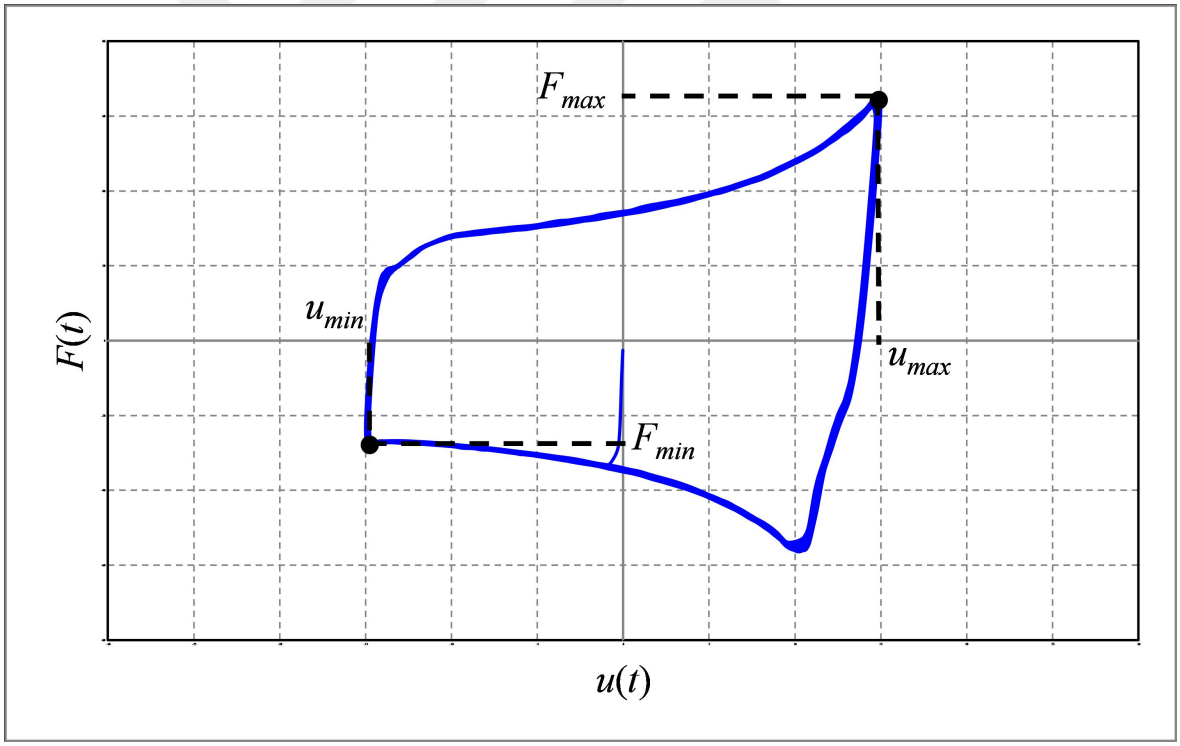

Figure 2.6. Response parameters.

The three response parameters according to which damper performance was evaluated are force capacity F_{max}, effective stiffness k_{eff} and area enclosed by hysteresis loop W_D.

The force capacity of the damper mechanism F_{max} is the maximum force reaction measured at the bottom of the damper throughout the 30 full cycles of displacement protocol. It is theoretically the larger value of F_{max} and absolute value of F_{min}. However, due to amplification effect of the damper mechanism which is demonstrated in the following chapters of this document, maximum force acting on the damper is always equal to F_{max}, because a positive displacement for the damper means a decrease in the damper angle, which increases the force capacity exponentially, as shown in Figure 2.6.

The initial stiffness of the damper mechanism k_{eff} as specified by Federal Emergency Management Agency [4] is expressed as

$$k_{eff} = \frac{|F_{max}| + |F_{min}|}{|u_{max}| + |u_{min}|}. \tag{2.1}$$

The area enclosed by one complete cycle of the force-displacement response for the damper mechanism, W_D, is a measure of hysteretic damping provided by the mechanism.

2.3.2. Summary of Test Results

Test results are summarized in Table 2.2. Results are classified in six groups according to parameters.

Table 2.2. Test results

Test	θ_i	$T_{blt,m}$	$T_{blt,tb}$	u_{max}	f	F_{max}	$k_{eff,ave}$	$W_{D,ave}$	Group
	rad	Nm	Nm	mm	Hz	kN	kN/m	kNmm	
1	30	25	0	5	1	3.6	715	54	1
2	30	25	0	15	1	4.3	255	187	
3	30	25	0	25	0.5	4.6	149	313	
4	22.5	25	0	5	1	4.8	898	71	
5	22.5	25	0	15	1	5.6	297	230	
6	22.5	25	0	25	0.5	6.5	185	396	
7	15	25	0	5	1	7.7	1301	103	
8	15	25	0	15	1	13.5	563	379	

Table 2.2. Test results (cont.)

Test	θ_i	$T_{blt,m}$	$T_{blt,tb}$	u_{max}	f	F_{max}	$k_{eff,ave}$	$W_{D,ave}$	Group
	rad	Nm	Nm	mm	Hz	kN	kN/m	kNmm	
9	30	25	25	5	1	5.7	1142	95	2
10	30	25	25	15	1	6.4	393	318	
11	30	25	25	25	0.5	6.9	239	546	
12	22.5	25	25	5	1	8.0	1537	127	
13	22.5	25	25	15	1	9.0	526	422	
14	22.5	25	25	25	0.5	11.1	342	747	
15	15	25	25	5	1	13.7	2407	199	
16	15	25	25	15	1	21.6	987	692	
17	30	50	0	5	1	7.3	1444	114	3
18	30	50	0	15	1	8.2	512	401	
19	30	50	0	25	0.5	8.8	306	688	
20	22.5	50	0	5	1	10.4	1959	151	
21	22.5	50	0	15	1	11.4	663	529	
22	22.5	50	0	25	0.5	13.9	426	911	
23	15	50	0	5	1	17.6	3051	229	
24	15	50	0	15	1	28.7	1255	859	
25	30	50	50	5	1	9.5	1908	154	4
26	30	50	50	15	1	10.5	661	517	
27	30	50	50	25	0.5	11.2	398	889	
28	22.5	50	50	5	1	13.3	2581	209	
29	22.5	50	50	15	1	16.3	937	740	
30	22.5	50	50	25	0.5	20.0	614	1302	
31	15	50	50	5	1	24.6	4402	349	
32	15	50	50	15	1	41.4	1867	1247	

Table 2.2. Test results (cont.)

Test	θ_i	$T_{blt,m}$	$T_{blt,tb}$	u_{max}	f	F_{max}	$k_{eff,ave}$	$W_{D,ave}$	Group
	rad	Nm	Nm	mm	Hz	kN	kN/m	kNmm	
33	30	100	0	5	1	8.4	1717	132	5
34	30	100	0	15	1	9.7	593	464	
35	30	100	0	25	0.5	10.4	364	799	
36	22.5	100	0	5	1	12.8	2450	183	
37	22.5	100	0	15	1	15.1	863	668	
38	22.5	100	0	25	0.5	18.5	558	1151	
39	15	100	0	5	1	20.9	3744	269	
40	15	100	0	15	1	34.7	1523	1020	
41	30	100	100	5	1	17.9	3585	284	6
42	30	100	100	15	1	20.1	1252	985	
43	30	100	100	25	0.5	22.2	768	1678	
44	22.5	100	100	5	1	25.8	5056	392	
45	22.5	100	100	15	1	30.8	1749	1344	
46	22.5	100	100	25	0.5	36.8	1131	2325	
47	15	100	100	5	1	44.2	7730	571	
48	15	100	100	15	1	65.0	3103	2027	

2.3.3. Force-Displacement Histories

Force-displacement histories of tests for Group 1 through Group 6 are shown in Figure 2.7 through Figure 2.12. As can be observed, the shapes of force-displacement plots for the proposed damper mechanism deviate from the rectangular shape pertaining to most friction dampers in the literature. This is due to the effect of decreasing initial angle θ_i on the response of the damper mechanism. For example, comparing plots of Test 45 (θ_i=22.5 degrees) and Test 48 (θ_i=15 degrees), it can be seen that as the displacement u increases in the positive (upwards) direction, the force reaction F increases in an exponential manner. The same can be observed for Test 5 vs. Test 8, Test 13 vs. Test 16, Test 21 vs. Test 24, Test 29 vs. Test 32 and Test 37 vs. Test 40. This exponential behaviour does not happen in the negative (direction), when the angle θ increases. Furthermore, an decrease of initial angle in the same amount from 30 degrees to 22.5 degrees does not have the same effect on the damper response (e.g. Test 42 vs Test 45). This is a significant demonstration of the amplification effect of small initial angle θ_i.

Another point worth noting in the force-displacement plots is the slight relaxation in stiffness of the damper mechanism when the displacement is reversed after reaching maximum amplitude in positive direction. This phenomenon, which is most clearly observed for cases in which θ_i is 15 degrees and u_{max} is 15 mm (Tests 8, 16, 24, 32, 40 and 48), is due to the gap between the bolt and the hole in the plates and friction pads. This gap is unavoidable since it is practically impossible to drill the holes without tolerance in production. However, it can also be observed that the stiffness of the damper is very swiftly preserved and the degradation effect is negligible since the gap is very small.

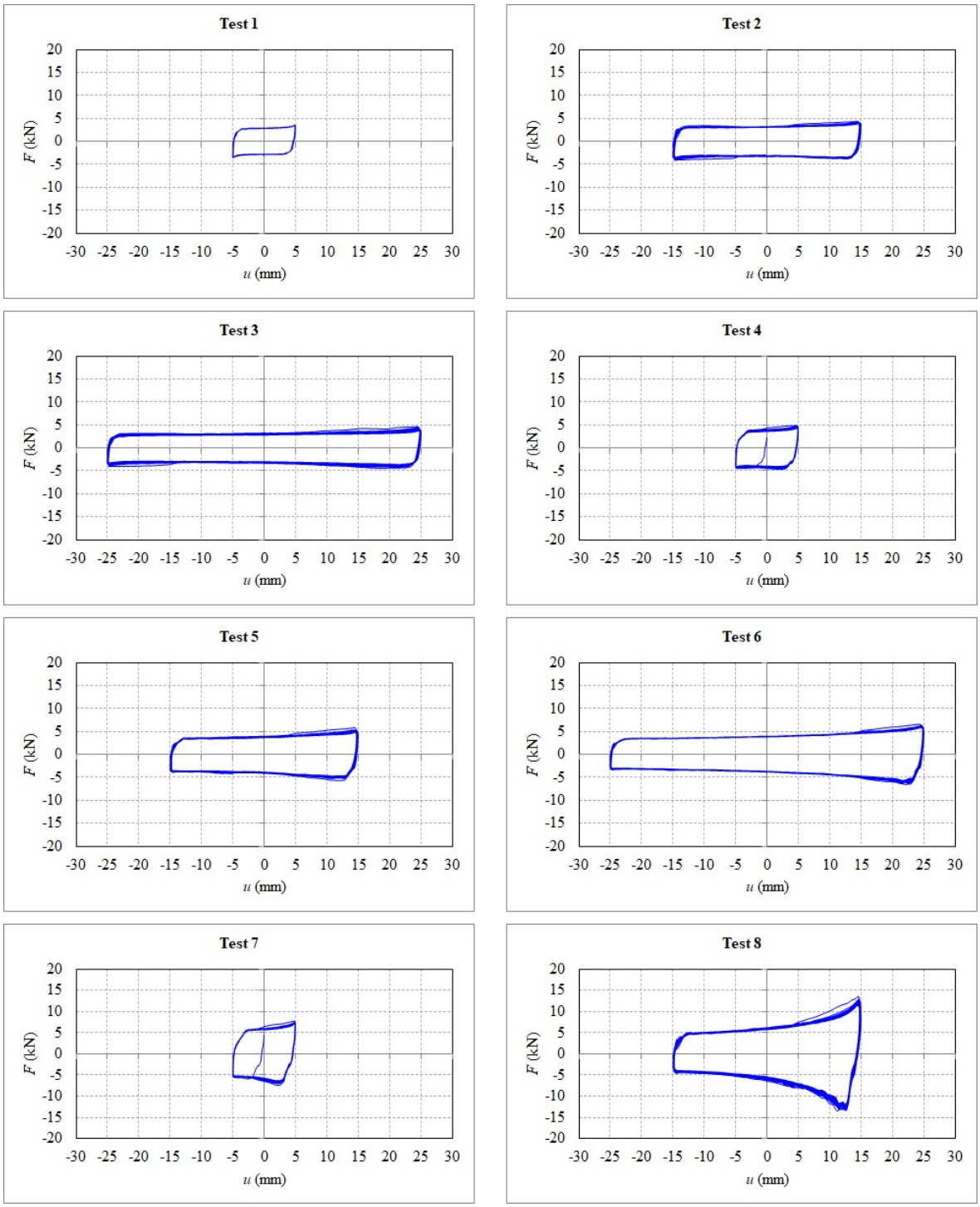

Figure 2.7. Force-displacement plots for Group 1 tests.

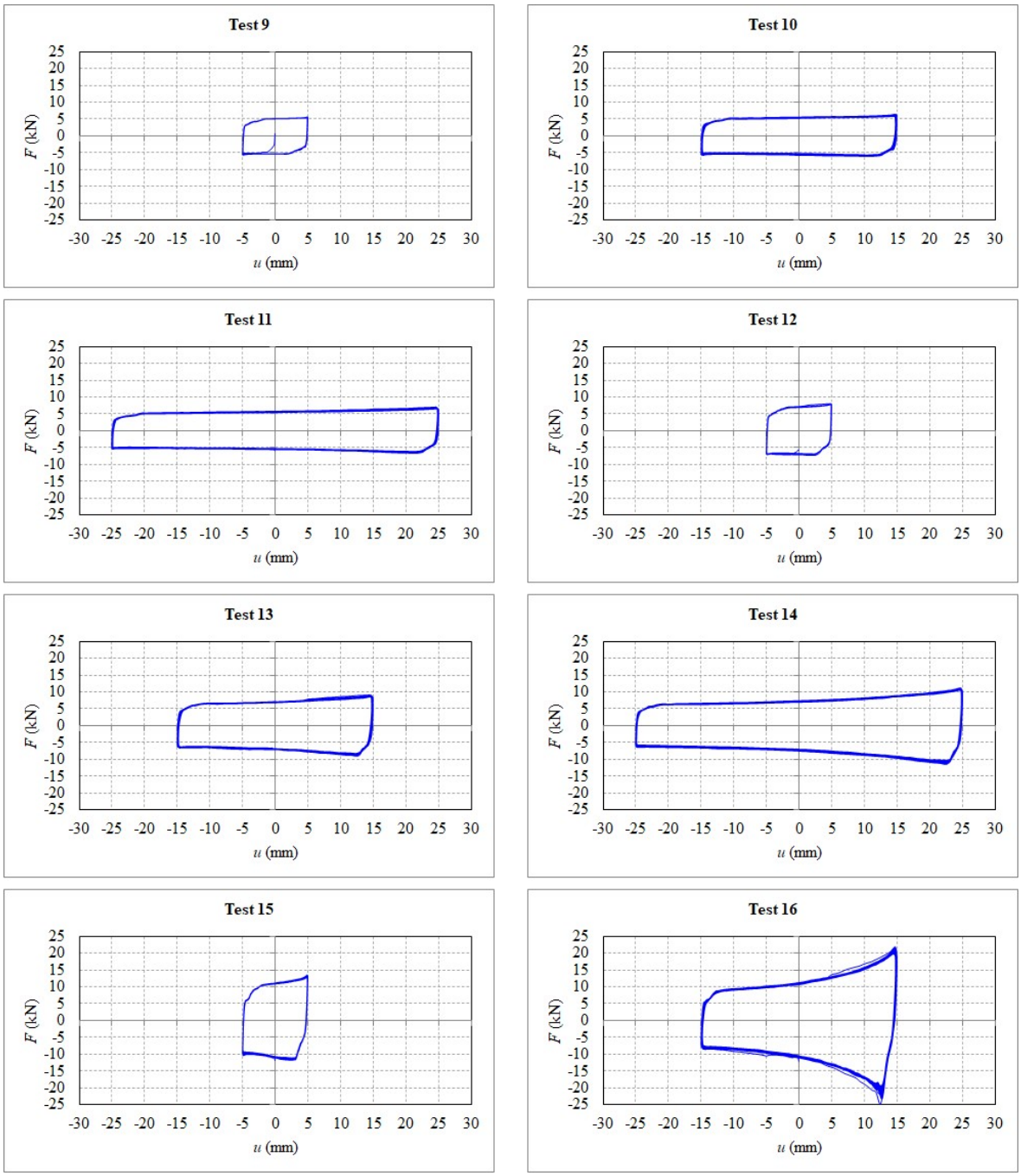

Figure 2.8. Force-displacement plots for Group 2 tests.

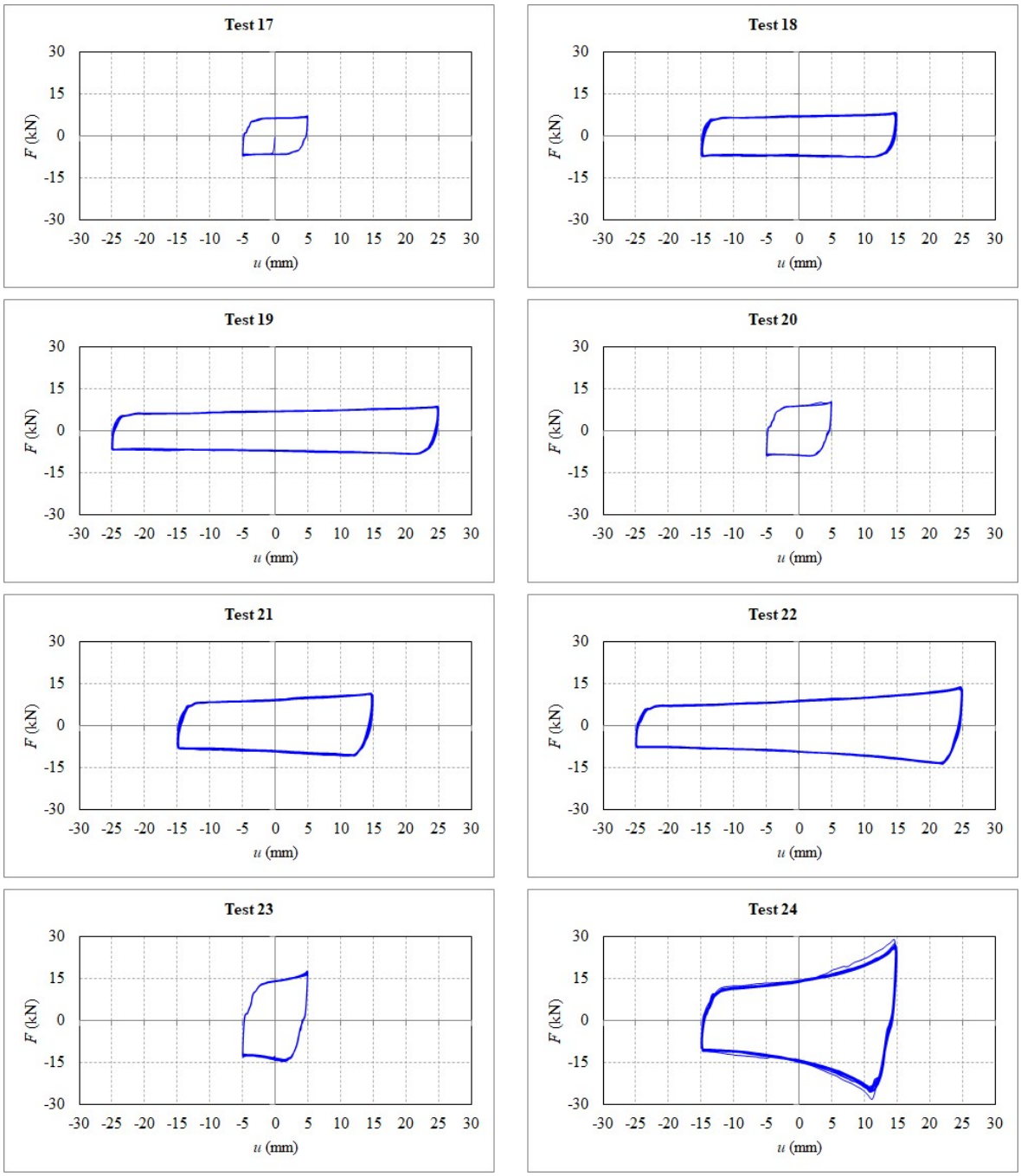

Figure 2.9. Force-displacement plots for Group 3 tests.

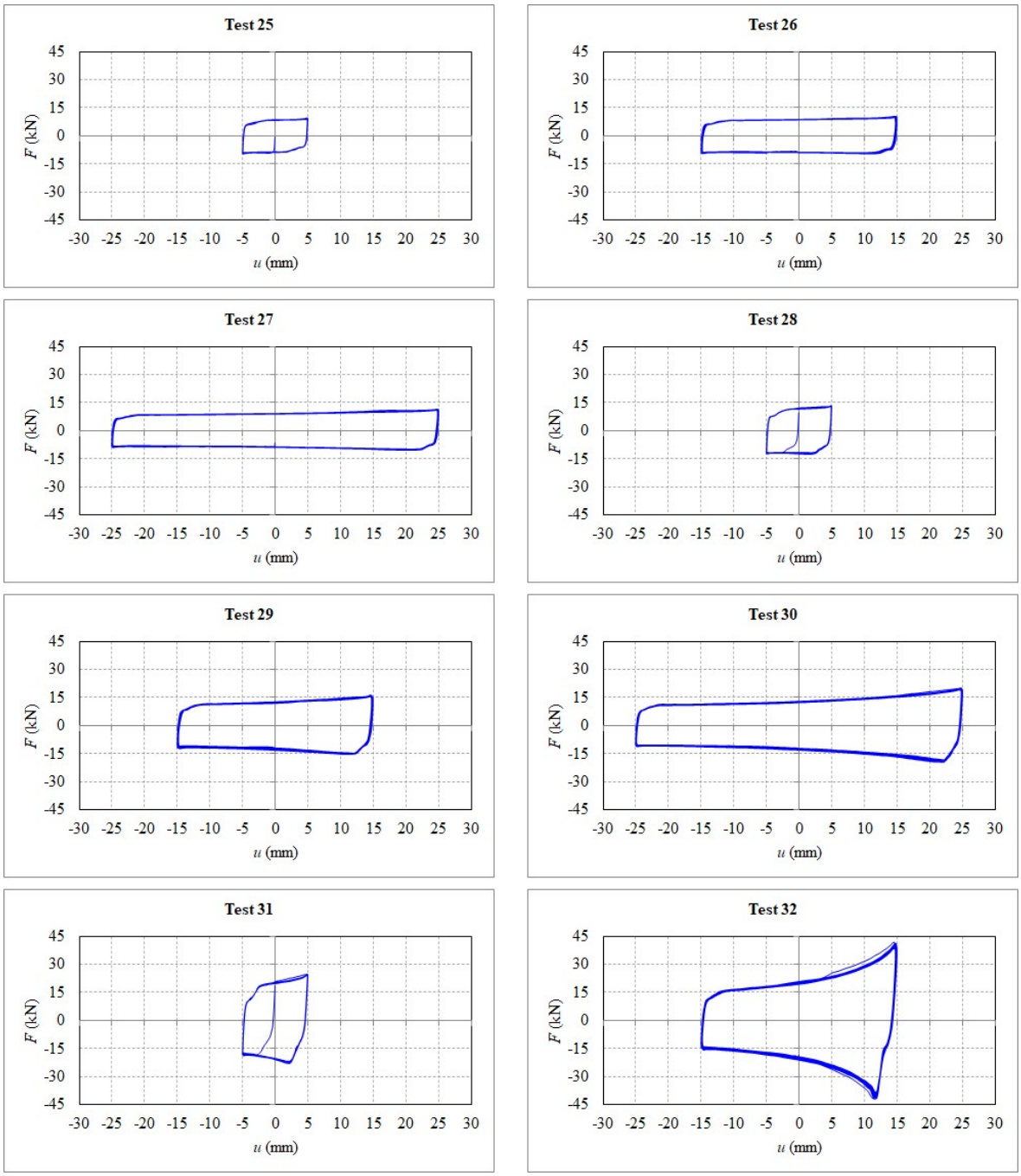

Figure 2.10. Force-displacement plots for Group 4 tests.

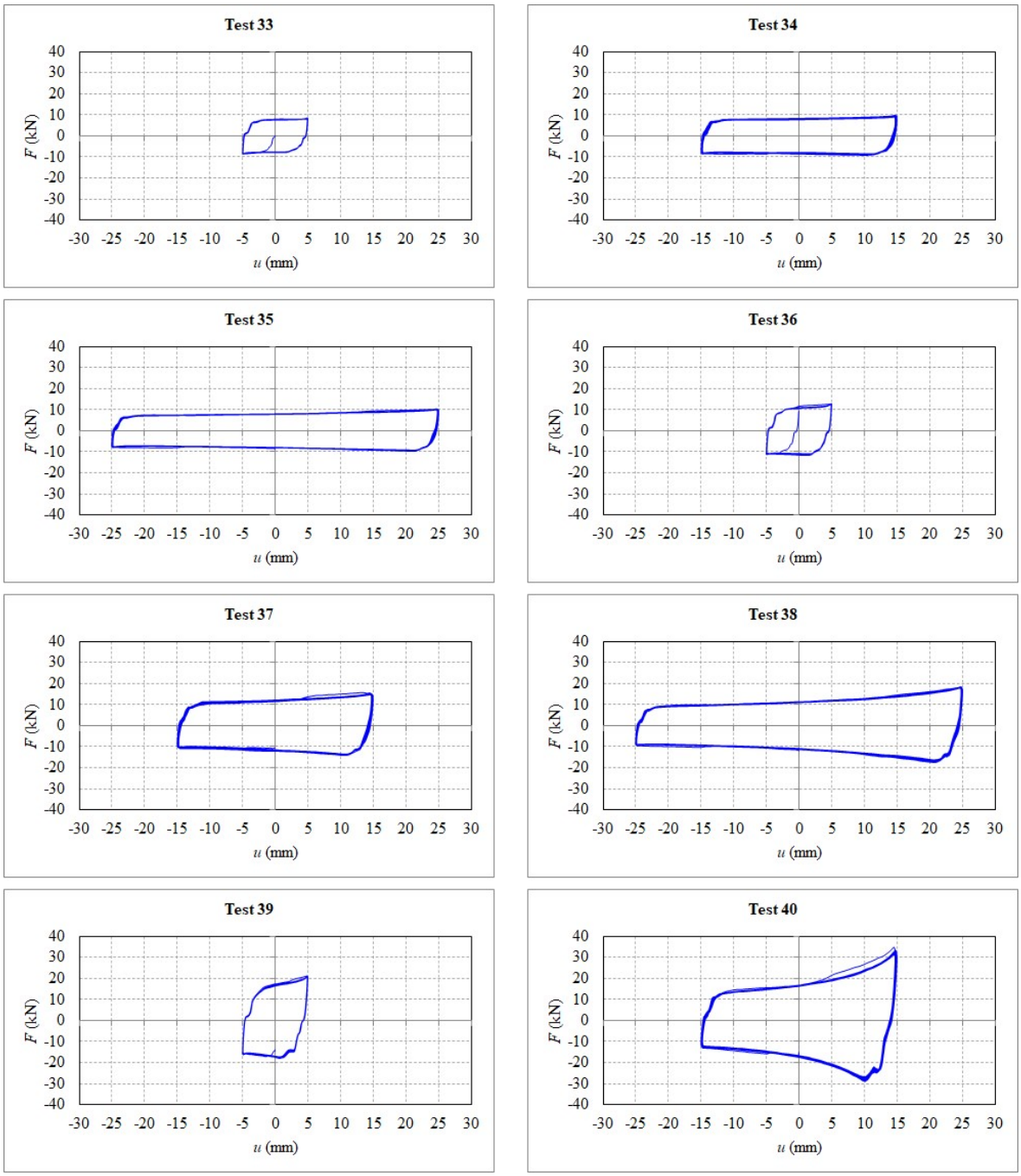

Figure 2.11. Force-displacement plots for Group 5 tests.

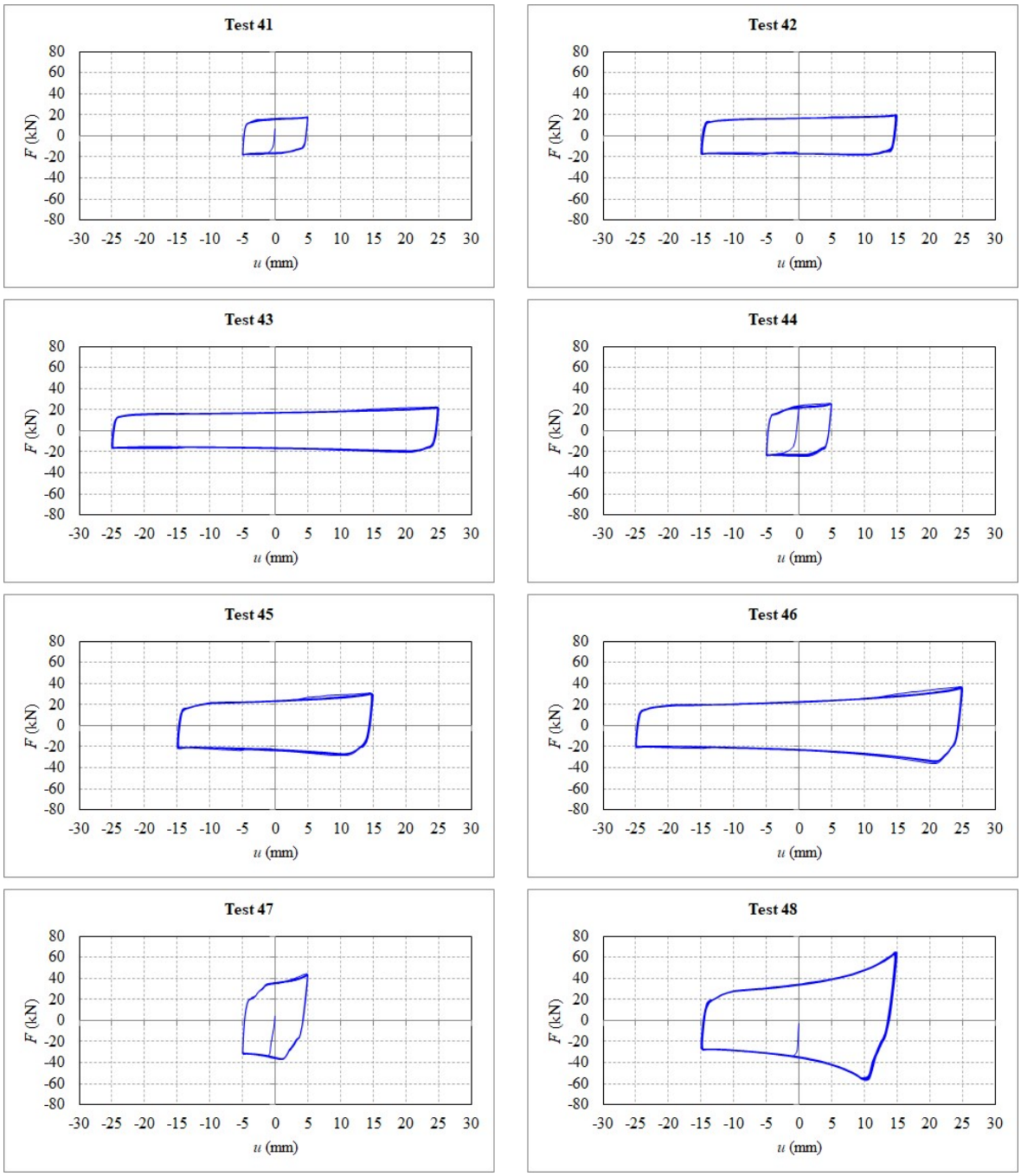

Figure 2.12. Force-displacement plots for Group 6 tests.

2.3.4. Force Capacity

Figure 2.13 shows the maximum reactions recorded throughout the response histories for the tests, which is an indicator of the force capacity of the damper mechanism. The sensitivity of the response to the initial angle θ_i is also observed in terms of force capacity F_{max}. For u_{max}=15mm, when the initial angle is decreased from 22.5 degrees to 15 degrees, the force capacity increases more than twice for all groups. For example, for Group 6, the force capacity for Test 45 is 30.8 kN, whereas the force capacity for Test 48 is 65.0 kN.

A reduction of initial angle from 30 degrees to 22.5 degrees, however, has a much smaller effect on force capacity. For example, comparing Test 42 and Test 45, it can be seen that the force capacity is increased roughly 50% (20.1 kN vs 30.8 kN). This complies with the nonlinear sensitivity of the damper response to the change in initial angle.

The effect of applying bolt torques at top and bottom joints in addition to the middle joint has the effect of increasing force capacity. However, this effect is slightly different than the theoretically expected effect of doubling the force capacity. A comparison of Group 5 and Group 6 results, for example, shows that the force capacity is increased 1.87 times for the case in which θ_i=15 degrees (Test 40 vs Test 48). However, the ratio of force capacity for Test 32 and Test 24 is 1.44. As can be observed, as the amount of applied bolt torque increases, the ratio of force capacity gets closer to the theoretical value of 2. This is due to the fact that the amount of bolt torque applied to the prototype damper mechanism was limited by the force capacity of the test machine. For smaller values of bolt torques, the friction force was not distributed uniformly along the interface. This caused a deviation from the expected theoretical result.The amplification effect of initial angle is also demonstrated in displacement amplitude u_{max}. As u_{max} gets larger, the force capacity of the damper increases significantly for the case in which initial angle is 15 degrees. For large initial angle, the response is not sensitive to the displacement amplitude.

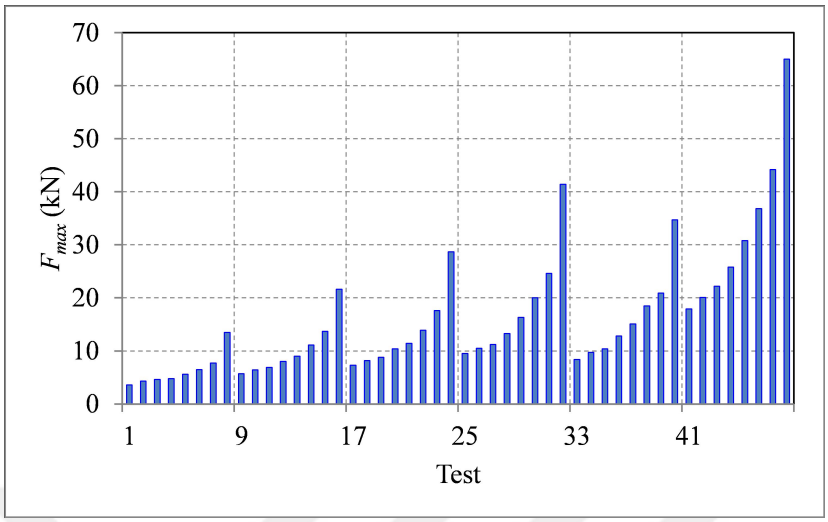

Figure 2.13. Force capacity results for tests.

2.3.5. Initial Stiffness

Figure 2.14 shows $k_{eff,ave}$, the initial stiffness values calculated as an average of 30 full cycles for all tests.

Decreasing initial angle θ_i significantly increases initial stiffness of the damper mechanism. For example, average initial stiffness values for for Test 45 and Test 48 are 1749 kN/m and 3103 kN/m, respectively. The values of $k_{eff,ave}$ for Test 29 and Test 32 are 937 kN/m and 1867 kN/m, respectively. This indicates that the stiffness of the damper is almost doubled when the initial angle is decreased from 22.5 degrees to 15 degrees.

Applying torque at top and bottom joints also increases the initial stiffness of the damper. For example, average initial stiffness values for for Test 38 and Test 46 are 558 kN/m and 1131 kN/m, respectively. The values of $k_{eff,ave}$ for Test 40 and Test 48 are 1523 kN/m and 3103 kN/m, respectively. This shows that applying bolt torques at top and bottom joints of the damper in addition to the middle joint effectively doubles its initial stiffness.

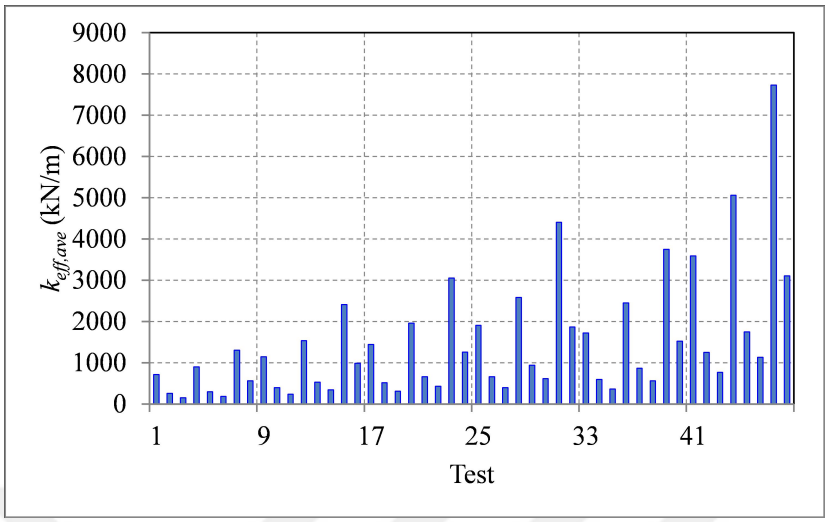

Figure 2.14. Results of average initial stiffness for tests.

2.3.6. Area of the Hysteresis Loop

Figure 2.15 shows the results for the area of the hysteresis loop, which is an indicator of the energy dissipated by the damper mechanism.

The effect of initial angle θ_i on area of hysteresis loop W_D is different than its effect on force capacity. For example, W_D for Test 45 and Test 48 is 1344 kNmm and 2027 kNmm, respectively. This means that when the initial angle is decreased from 22.5 degrees to 15 degrees, the area of the hysteresis loop is increased only 50%, whereas the increase in force capacity was more than 100%. This is a result of the exponential nature of the damper response. The maximum force capacity at the given displacement amplitude is a measure of the reaction which is recorded for that amplitude. The area of the hysteresis loop is the total area under the loop. Since the force-displacement response does not have a constant slope, the increase in closed loop area is smaller than the increase in force capacity.

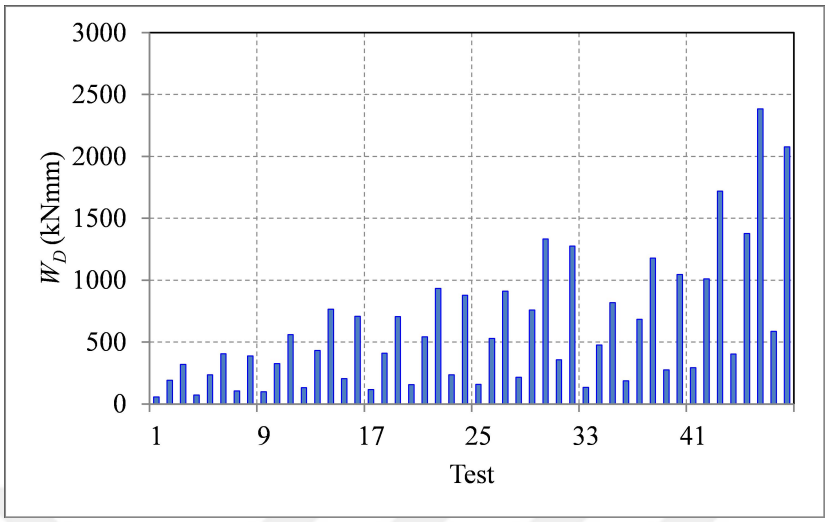

Figure 2.15. Results of area of the hysteresis loop for tests.

2.3.7. System Adequacy of the Damper Mechanism

FEMA-356 specifies that the effective stiffness and the area of the hysteresis loop for the prototype damper mechanism for any one cycle should not differ by more than ±15% from the average value obtained from all cycles in the test [4]. All 48 tests conducted on the damper mechanism satisfy this criterion, except for the first cycle in Test 3. Figure 2.16 through Figure 2.21 shows the effective stiffnesses calculated for all cycles for Group 1 through Group 6. Figure 2.22 through Figure 2.27 shows the areas of the hysteresis loop calculated for all cycles for Group 1 through Group 6. Red dashed lines in the figures represent the ±15% limits which are defined by FEMA-356 and the blue dashed line is the average of the tests.

These results indicate that there is no degradation in the behavior of the damper as number of cycles increase.

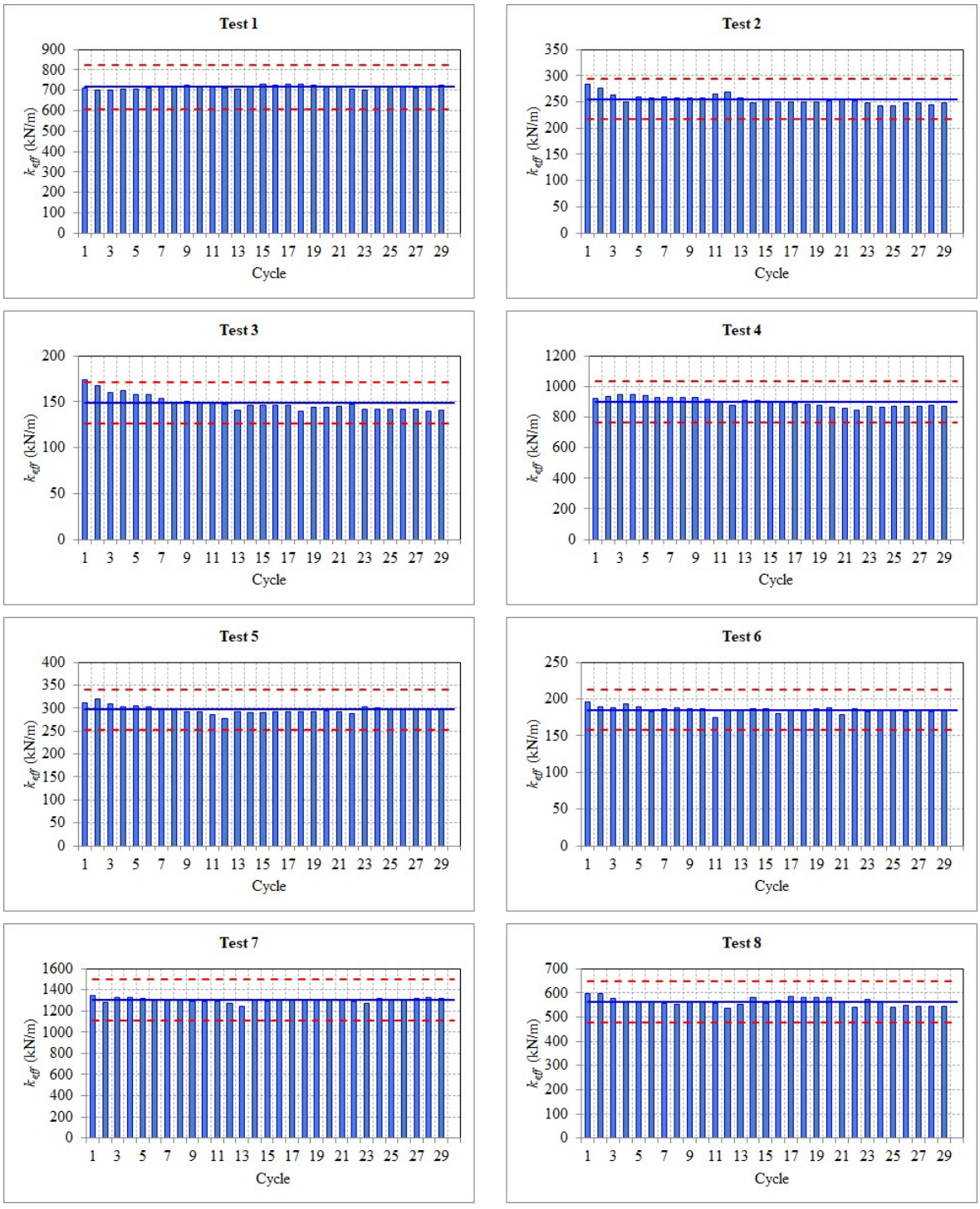

Figure 2.16. Initial stiffness values calculated for all cycles of Group 1 tests.

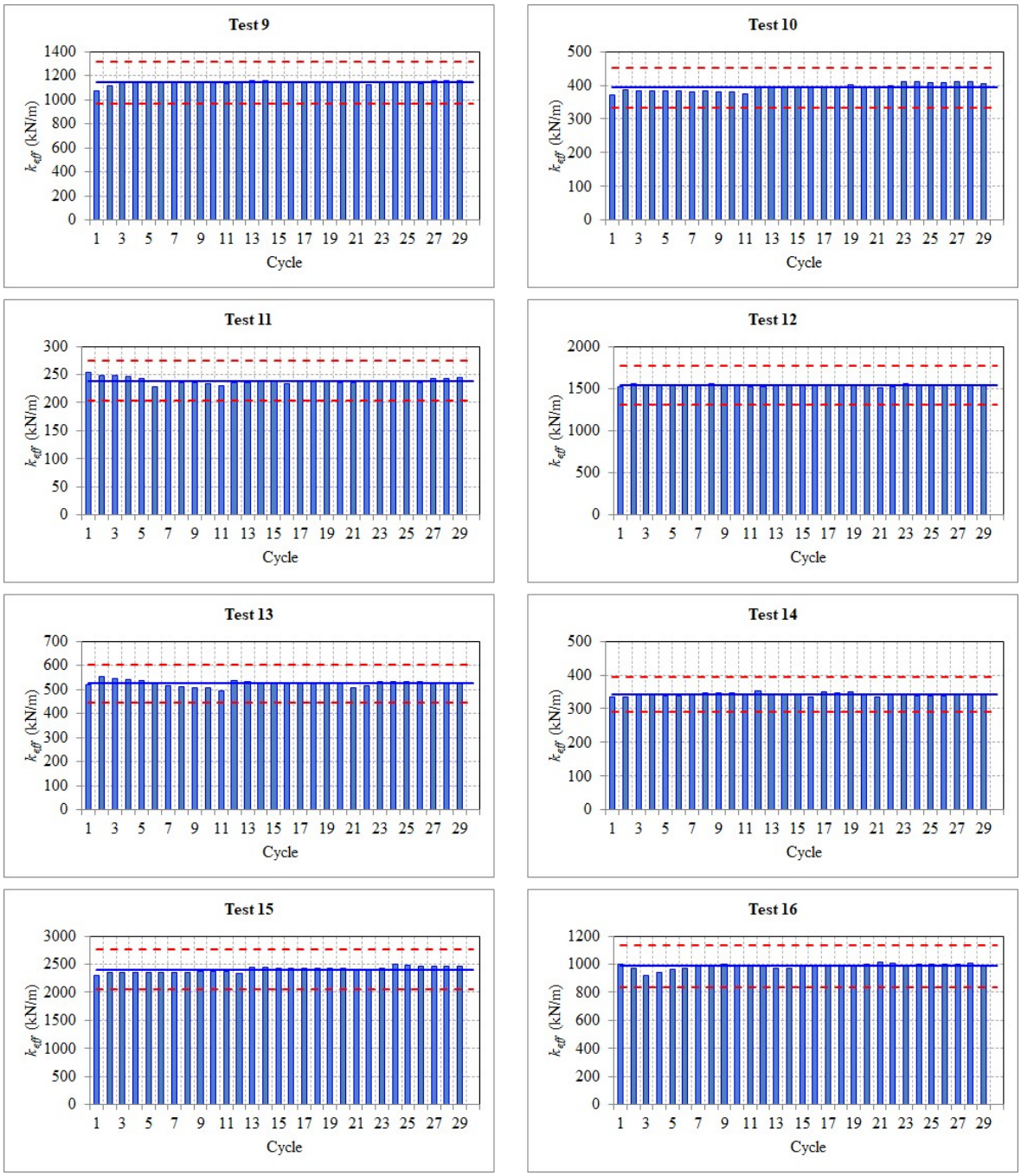

Figure 2.17. Initial stiffness values calculated for all cycles of Group 2 tests.

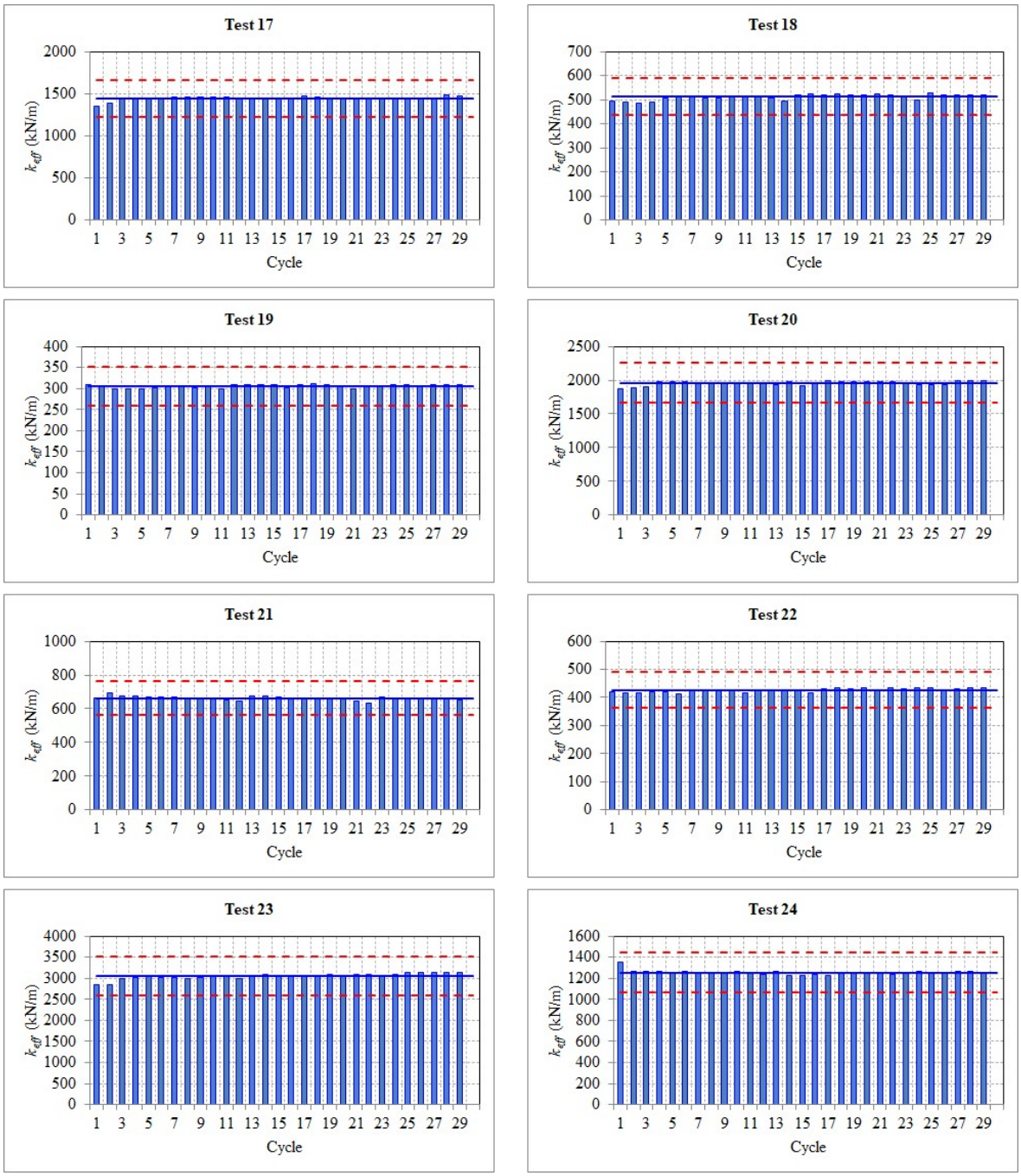

Figure 2.18. Initial stiffness values calculated for all cycles of Group 3 tests.

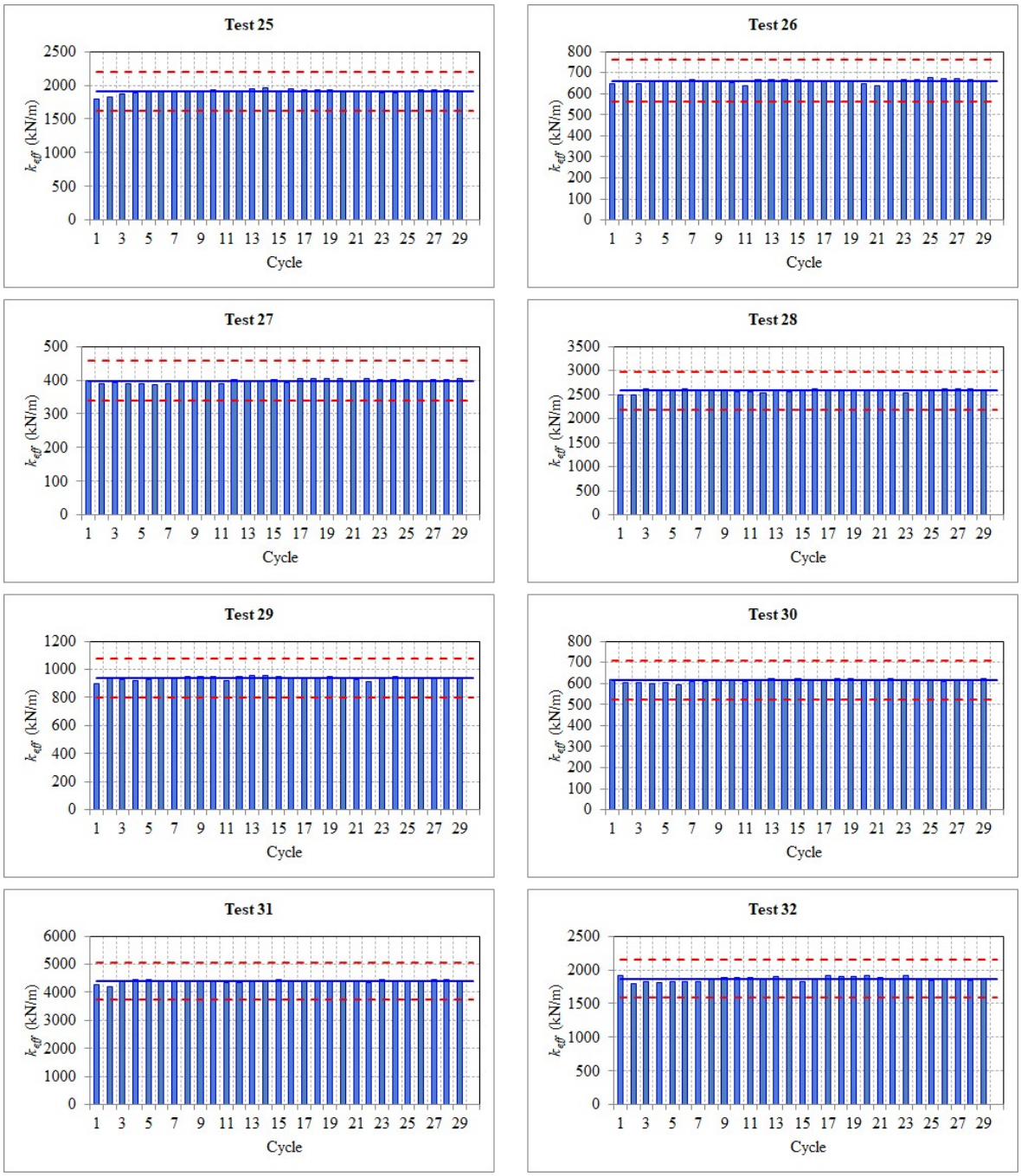

Figure 2.19. Initial stiffness values calculated for all cycles of Group 4 tests.

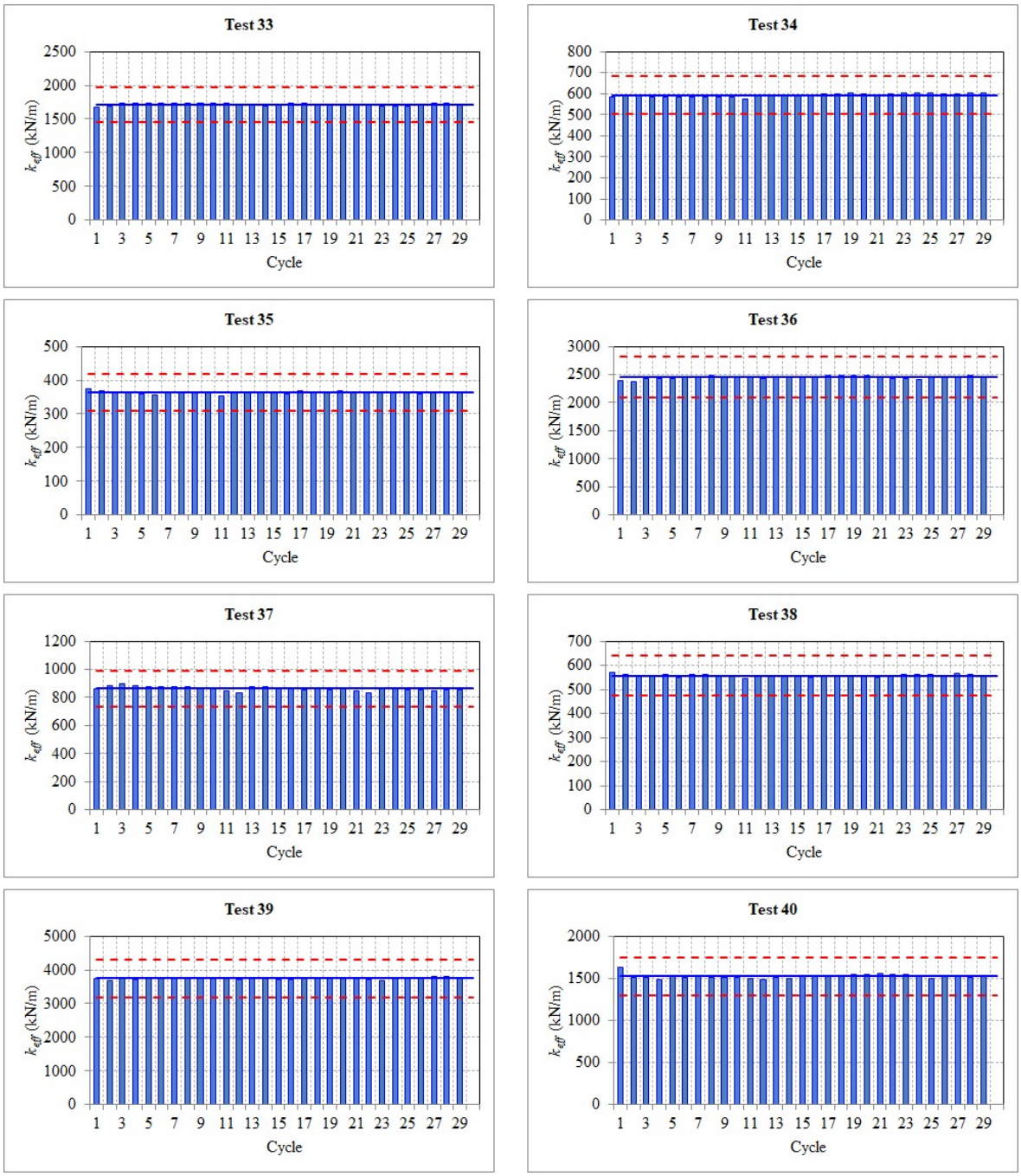

Figure 2.20. Initial stiffness values calculated for all cycles of Group 5 tests.

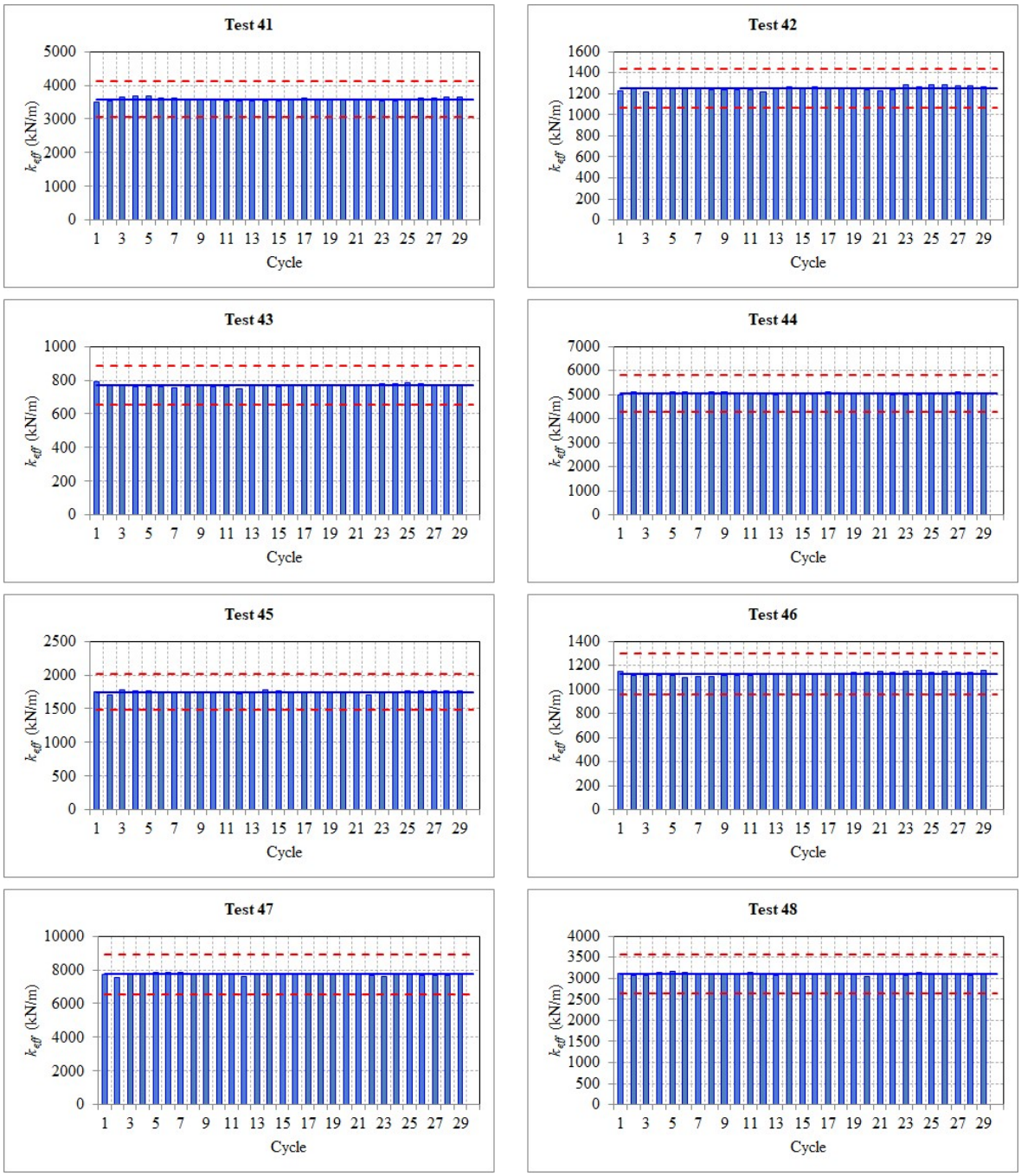

Figure 2.21. Initial stiffness values calculated for all cycles of Group 6 tests.

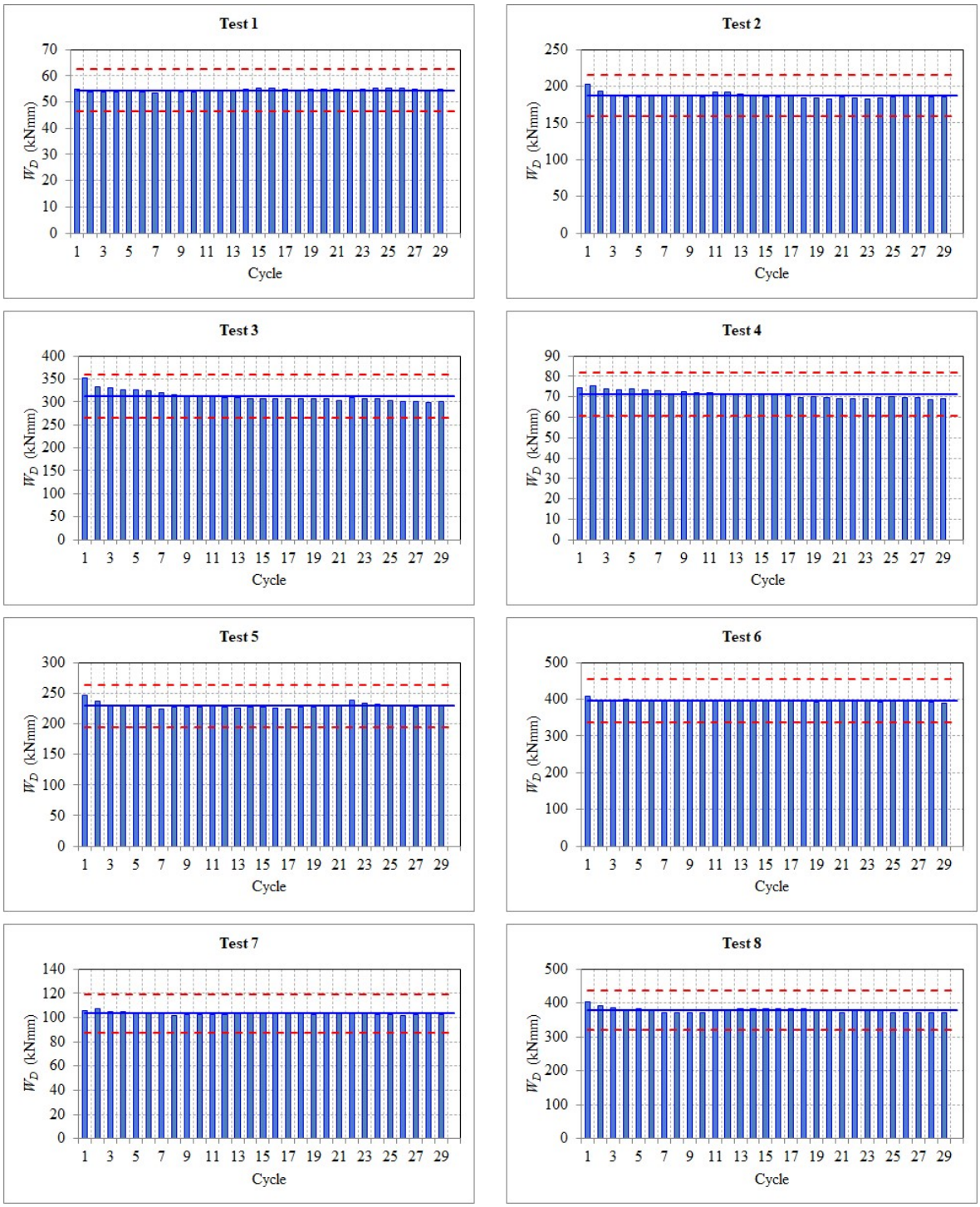

Figure 2.22. Area of the hysteresis loop values calculated for all cycles of Group 1 tests.

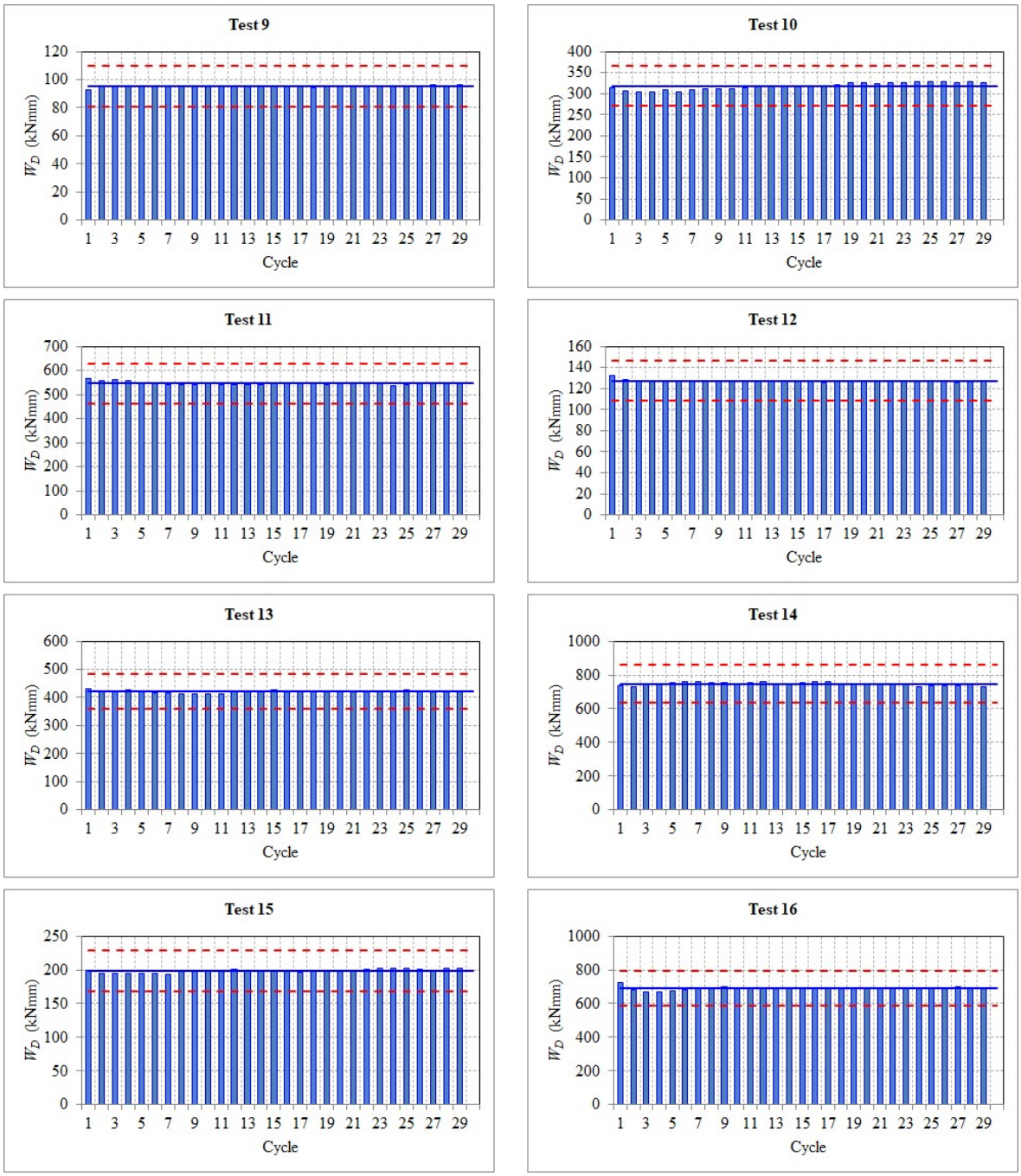

Figure 2.23. Area of the hysteresis loop values calculated for all cycles of Group 2 tests.

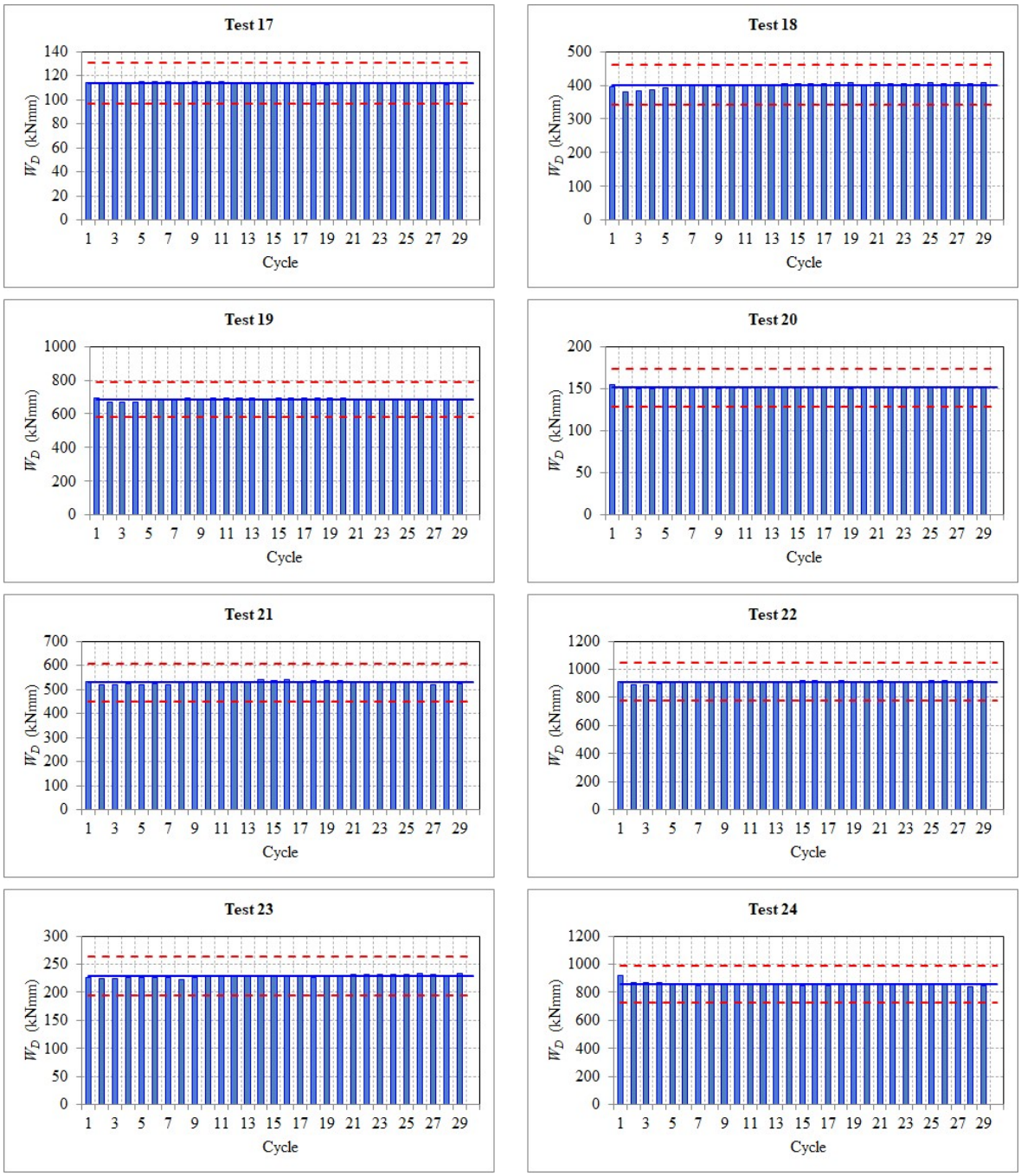

Figure 2.24. Area of the hysteresis loop values calculated for all cycles of Group 3 tests.

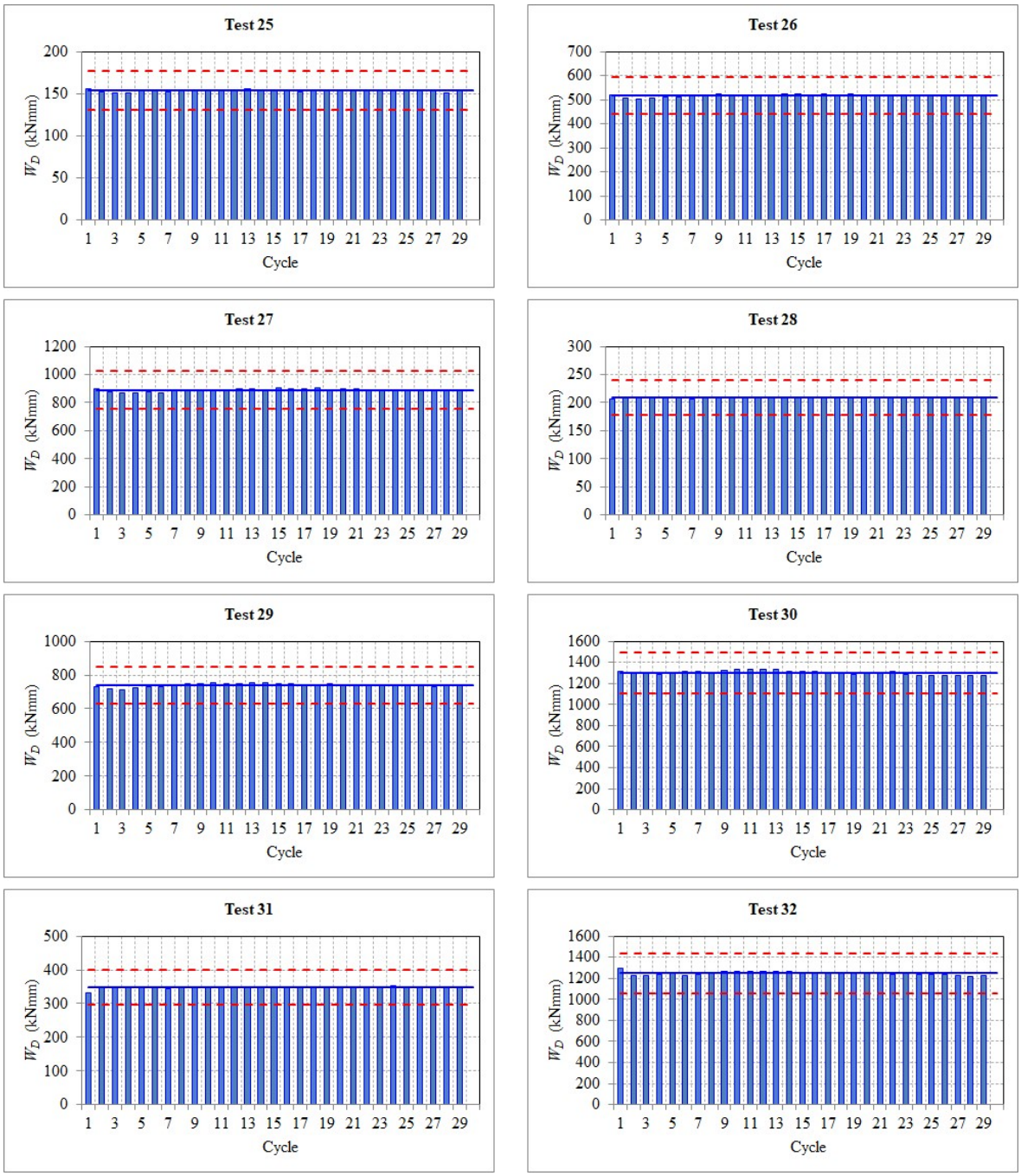

Figure 2.25. Area of the hysteresis loop values calculated for all cycles of Group 4 tests.

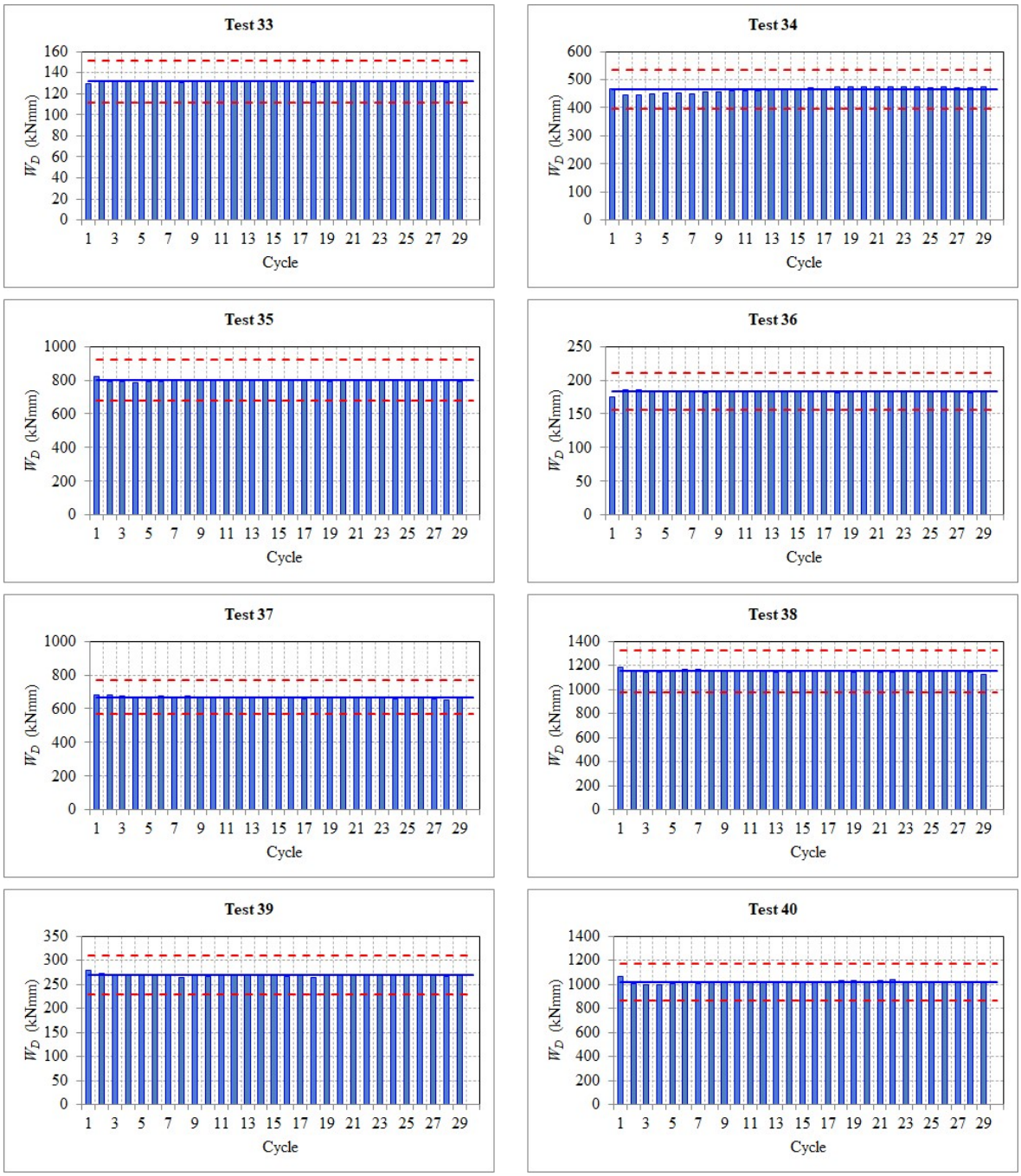

Figure 2.26. Area of the hysteresis loop values calculated for all cycles of Group 5 tests.

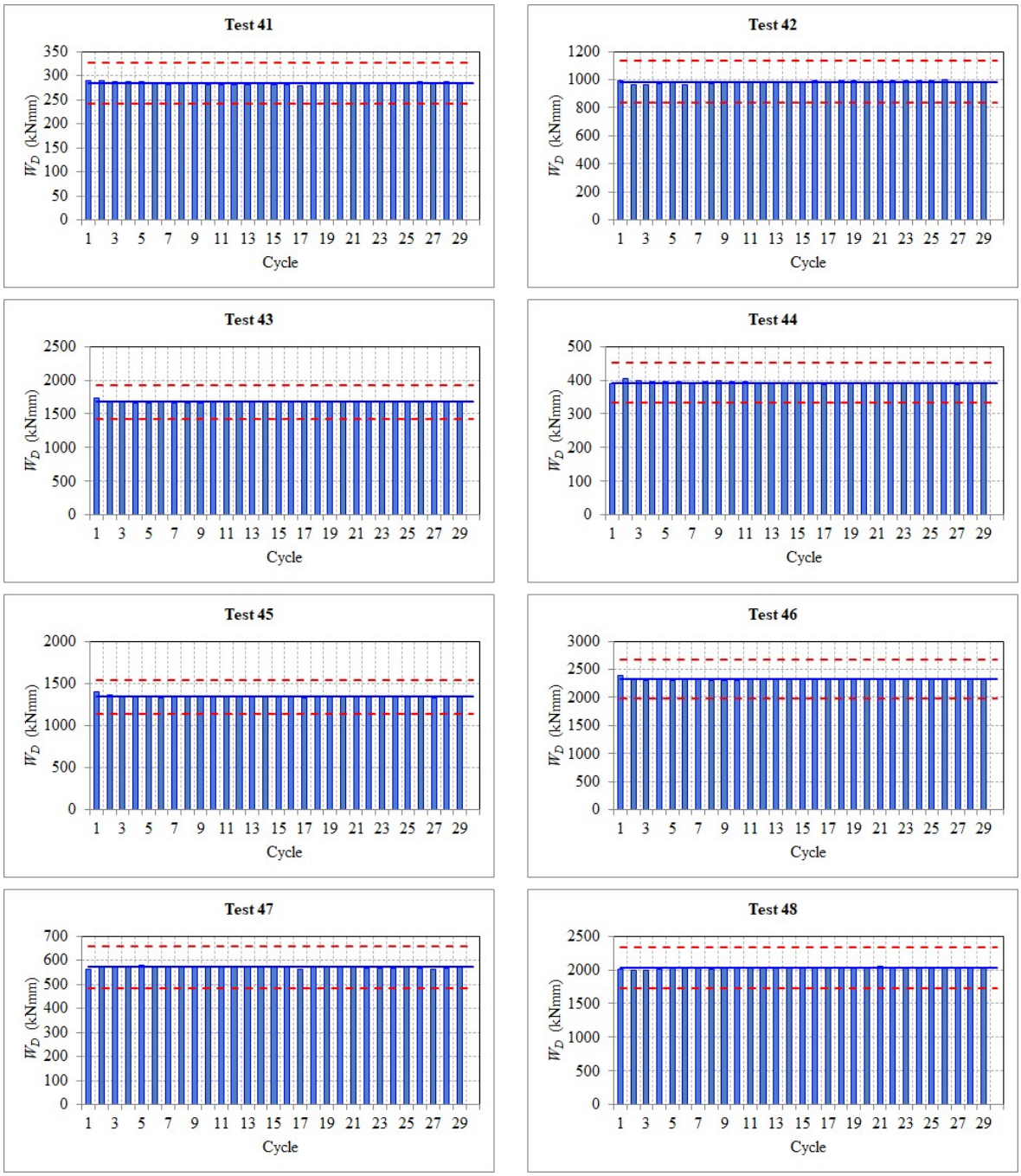

Figure 2.27. Area of the hysteresis loop values calculated for all cycles of Group 6 tests.

2.3.8. Condition of Prototype Damper Mechanism Components after the Test

Figure 2.28 through Figure 2.30 show the photographs of damper components taken after the experiments were conducted. Significant abrasion in the disks were not observed. Also, temperature increase in the joints during the measurements were on the order of a few degrees Celsius so thermal effects were negligible. On the other hand, as can be seen in Figures 2.28 and 2.30, abrasion is not uniformly distributed along the surface of the disks and plates, it is concentrated on particular locations. This implies that for cases in which bolt torque magnitude is small, friction occurs at particular locations in the interface and the uniform clamping pressure assumption may not be valid. Nevertheless, for large bolt torques, more uniform distribution of the clamping pressure is expected, hence experimental results are predicted to be in line with theory. It is worth mentioning, however, galvanic corrosion between aluminum alloy and steel surfaces is an issue that should be addressed.

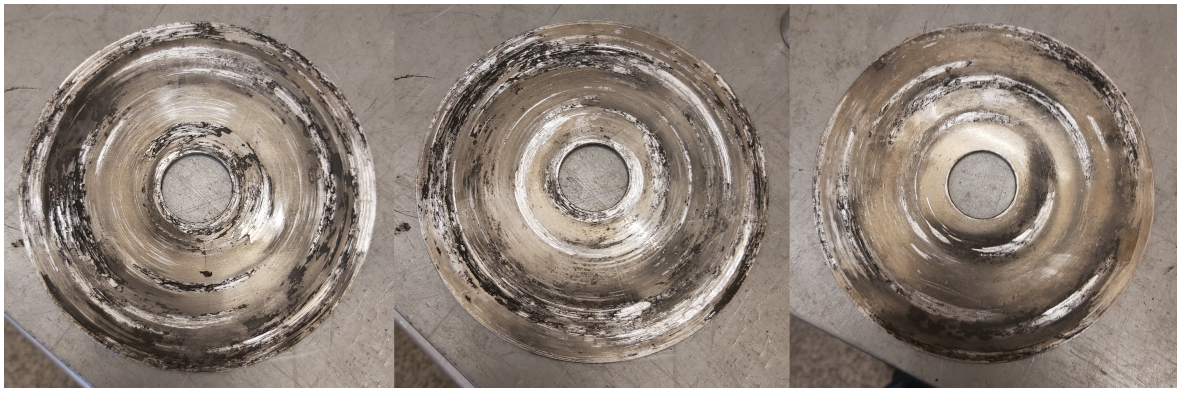

Figure 2.28. Aluminum alloy friction disks after the experiment.



Figure 2.29. Damper bolts after the experiment.



Figure 2.30. Damper plate friction surface experiment.

3. NUMERICAL STUDIES

The effect of the proposed damper on the response of precast post-tensioned concrete buildings were investigated by conducting numerical studies on beam-column sub-assemblies and example frames with and without the dampers. The adequacy of the numerical modeling principles for the prototype damper mechanism was verified comparing numerical results with experiment results. Furthermore, modeling principles that are required to represent the unique aspects of precast post-tensioned structures, such as gap-opening and unbonded nature of post-tensioning strands, were verified with comparing results of numerical studies performed by those from literature. This Chapter gives detailed information about numerical modeling principles, their verification and numerical studies done to investigate the effect of the proposed damper on precast post-tensioned concrete sub-assemblies and frames.

3.1. Principles and Verification of Numerical Model of the Damper Mechanism

The numerical model of the damper mechanism was created in OpenSEES (Open Source Earthquake Engineering Software), a finite-element based software that is suitable for modeling of such systems. The modeling principles are shown in Figure 3.1. The top plate that connects two identical damper components was modeled using a rigid link. The damper plates were modeled using inelastic steel fiber elements. The connection of the components to the bottom part of the test machine was represented by fixed supports. The joints of plates at which relative rotation and friction occurs were modeled by zero-length elements. At these joints, two seperate nodes, each representing ends of damper plates, were defined with identical coordinates. Their translation relative to each other was kinematically constrained in X and Y axis direction. For the rotation about Z axis, a zero-length element with a nonlinear moment-rotation behaviour was assigned. The nonlinear behaviour of the zero-length element was defined by the moment at which relative rotation occurs.

This moment, designated T_{fr} in Figure 3.1, is defined as

$$T_{fr} = \frac{2}{3}\pi\mu np(r_2^3 - r_1^3), \tag{3.1}$$

where T_{fr} is the moment at which rotation (sliding) begins, μ is the coefficient of friction between the materials at the joint interface, n=2 is the number of friction surfaces at the joint, p is the compressive stress at the joint interface and r_2=150mm and r_1=30mm are the outer and inner radii of the joint interfaces, respectively.

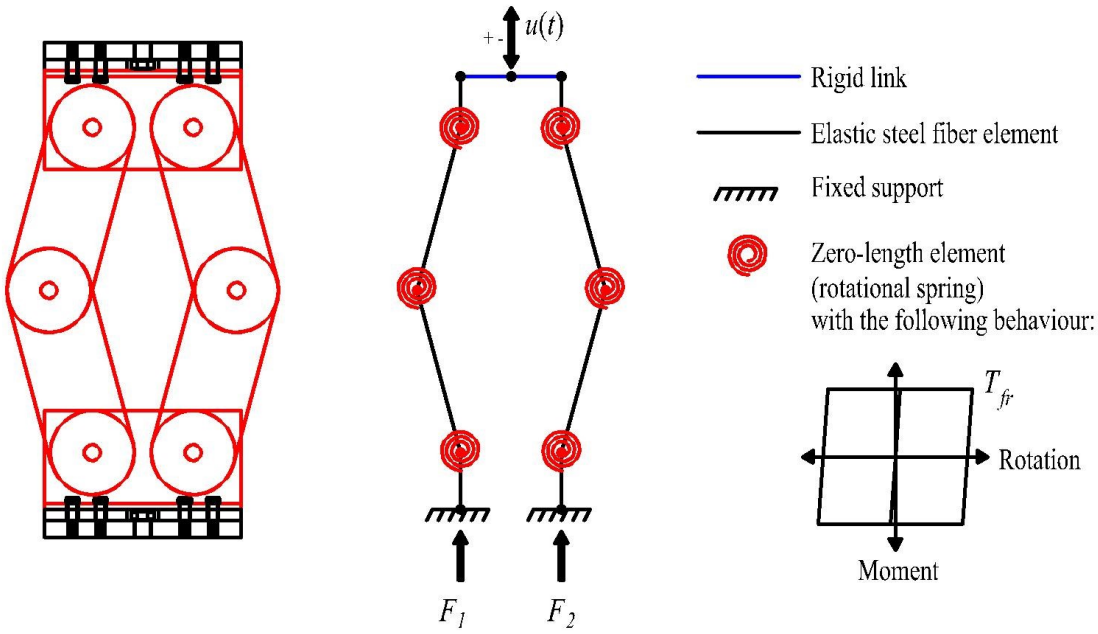

Figure 3.1. Modeling principles for the damper mechanism.

The relation between the bolt torques applied to the damper mechanism in the experiment and the compressive stress at the joint p is expressed as

$$p = \frac{2N_{blt}}{\pi(r_2^2 - r_1^2)}, \tag{3.2}$$

where N_{blt} is the normal force applied on the interface by the bolt.

The normal force applied on the interface by the bolt is defined as

$$N_{blt} = \frac{T_{blt}}{Kd}, \tag{3.3}$$

where T_{blt} is the bolt torque applied, K is a constant which is equal to 0.20 and d is the diameter of the bolt which is 30 mm.

The numerical analyses of the damper mechanism were done in two stages. In the first stage, force-displacement response was obtained taking coefficient of friction μ in Equation 3.1 equal to 1. For each test, the coefficient of friction μ was calculated as the ratios of the forces at which the plot intersects the positive y-axis for the experiment result and the numerical result from Stage 1. In the second stage, the μ value calculated was substituted in Equation 3.1 to obtain the numerical analysis results. This process is explained in Figure 3.2 for results of Test 27.

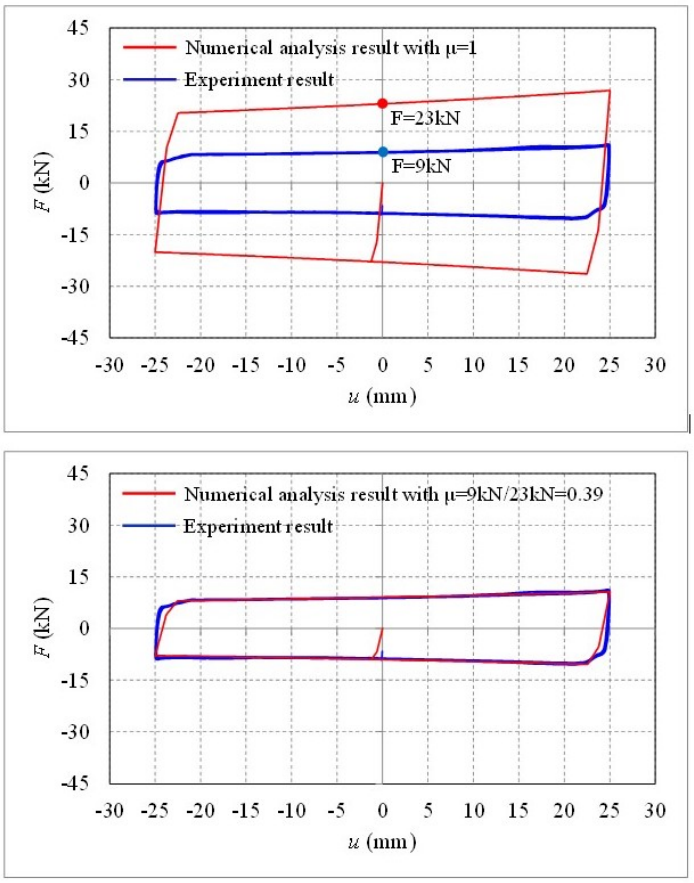

Figure 3.2. Determination of μ for Test 27.

Table 3.1 shows coefficient of friction (μ) values, along with the T_{fr} values calculated for all 48 tests using Equation 3.1.

Table 3.1. Coefficient of friction (μ) and T_{fr} values

Test	μ	$T_{blt,m}$	$T_{blt,tb}$	$T_{fr,m}$	$T_{fr,tb}$	Test	μ	$T_{blt,m}$	$T_{blt,tb}$	$T_{fr,m}$	$T_{fr,tb}$
		Nm	Nm	kNm	kNm			Nm	Nm	kNm	kNm
1	0.51	25	0	0.2	0.0	25	0.37	50	50	0.3	0.3
2	0.56	25	0	0.2	0.0	26	0.39	50	50	0.3	0.3
3	0.57	25	0	0.2	0.0	27	0.39	50	50	0.3	0.3
4	0.58	25	0	0.2	0.0	28	0.40	50	50	0.3	0.3
5	0.53	25	0	0.2	0.0	29	0.43	50	50	0.4	0.4
6	0.52	25	0	0.2	0.0	30	0.43	50	50	0.4	0.4
7	0.57	25	0	0.2	0.0	31	0.46	50	50	0.4	0.4
8	0.56	25	0	0.2	0.0	32	0.47	50	50	0.4	0.4
9	0.46	25	25	0.2	0.2	33	0.34	100	0	0.6	0.0
10	0.49	25	25	0.2	0.2	34	0.36	100	0	0.6	0.0
11	0.50	25	25	0.2	0.2	35	0.35	100	0	0.6	0.0
12	0.48	25	25	0.2	0.2	36	0.38	100	0	0.7	0.0
13	0.48	25	25	0.2	0.2	37	0.40	100	0	0.7	0.0
14	0.49	25	25	0.2	0.2	38	0.38	100	0	0.7	0.0
15	0.51	25	25	0.2	0.2	39	0.39	100	0	0.7	0.0
16	0.51	25	25	0.2	0.2	40	0.38	100	0	0.7	0.0
17	0.58	50	0	0.5	0.0	41	0.36	100	100	0.6	0.6
18	0.62	50	0	0.5	0.0	42	0.37	100	100	0.6	0.6
19	0.62	50	0	0.5	0.0	43	0.37	100	100	0.6	0.6
20	0.59	50	0	0.5	0.0	44	0.40	100	100	0.7	0.7
21	0.63	50	0	0.5	0.0	45	0.40	100	100	0.7	0.7
22	0.61	50	0	0.5	0.0	46	0.38	100	100	0.7	0.7
23	0.64	50	0	0.5	0.0	47	0.41	100	100	0.7	0.7
24	0.65	50	0	0.6	0.0	48	0.39	100	100	0.7	0.7

The average value for μ for the first 24 tests (Groups 1, 2 and 3) is 0.55 and for the second set of 24 tests (Groups 4, 5 and 6) is 0.39. The discrepancy between

these two sets is likely a result of small bolt torques applied in the first set. Because of the small bolt torques, the friction forces at the interface are not distributed uniformly, thus preventing an accurately predictable response. The average values of μ for the two sets of experiments comply very well with previous research conducted on aluminum alloy-steel friction surfaces. Latour et al., for example, specify a value of approximately 0.60 for low torque cases and a value of approximately 0.40 for higher torque cases [53]. Hereby, it should be noted that the bolt torques applied to the prototype damper mechanism were limited by the vertical force capacity of the testing machine (100 kN).

Figure 3.3 through Figure 3.8 shows comparison of numerical results and experimental results for representative tests using the coefficient of friction values presented in Table 3.1. It can be seen that numerical results represent the behavior significantly well.

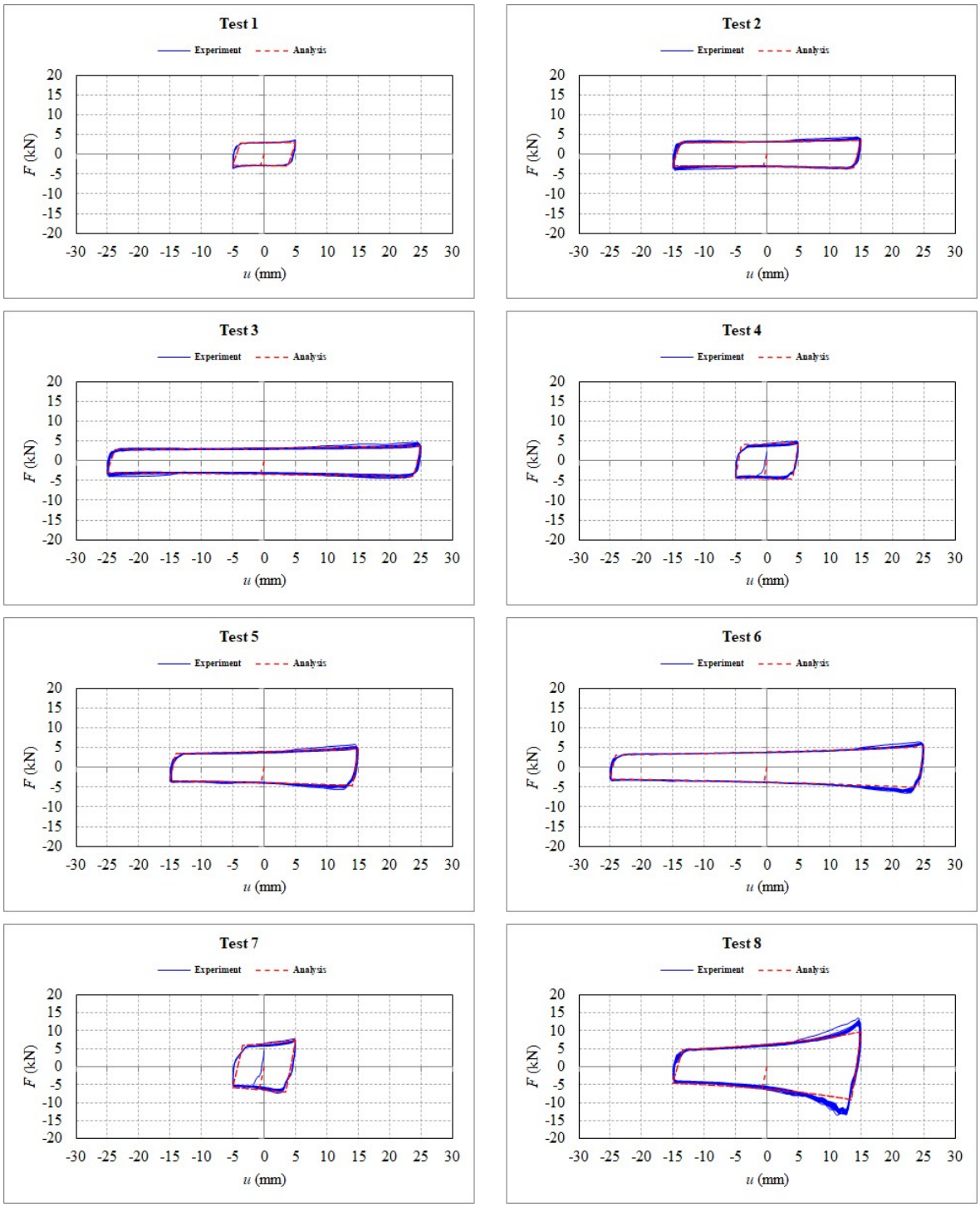

Figure 3.3. Comparison of experimental and numerical results for Group 1 tests.

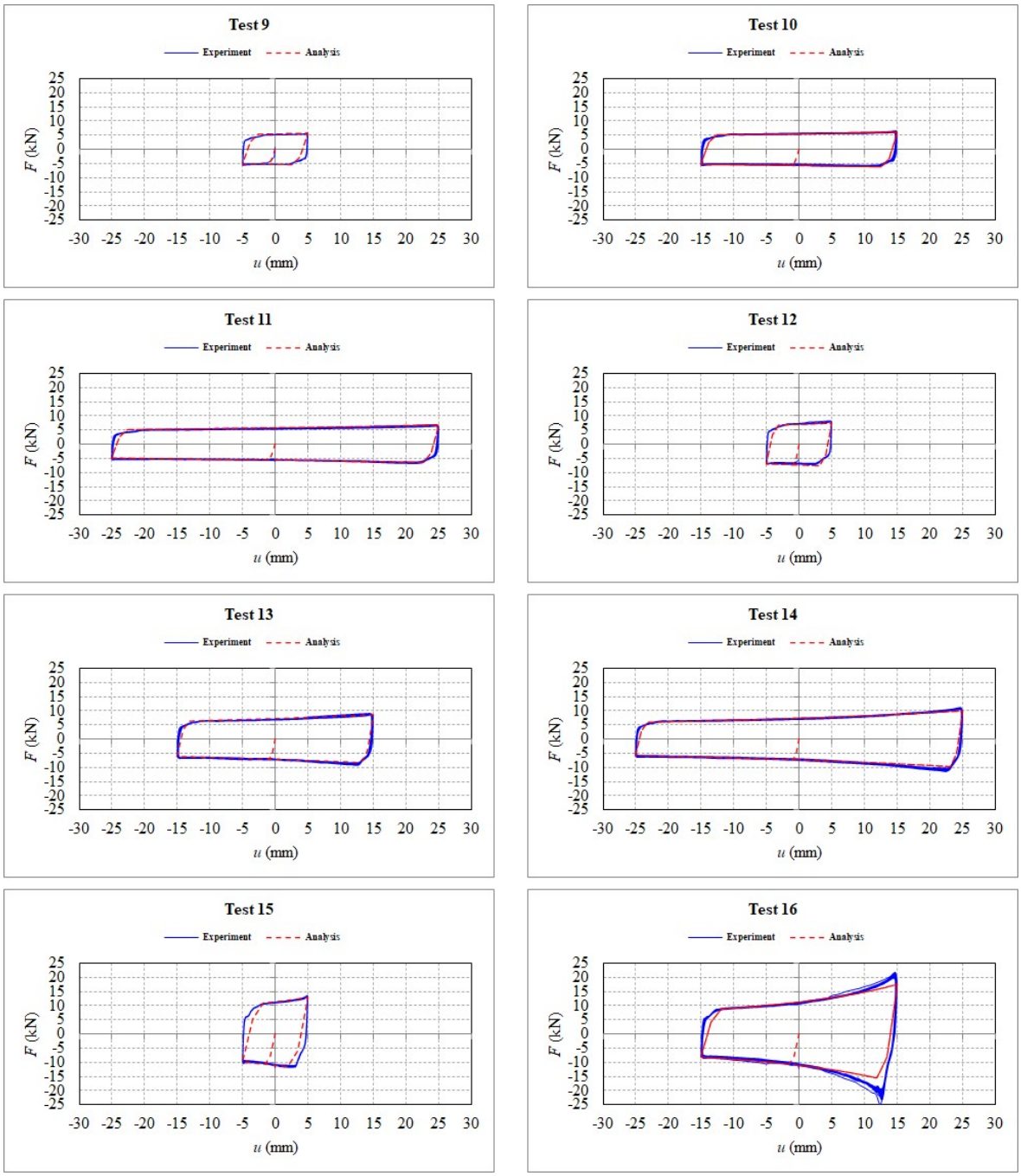

Figure 3.4. Comparison of experimental and numerical results for Group 2 tests.

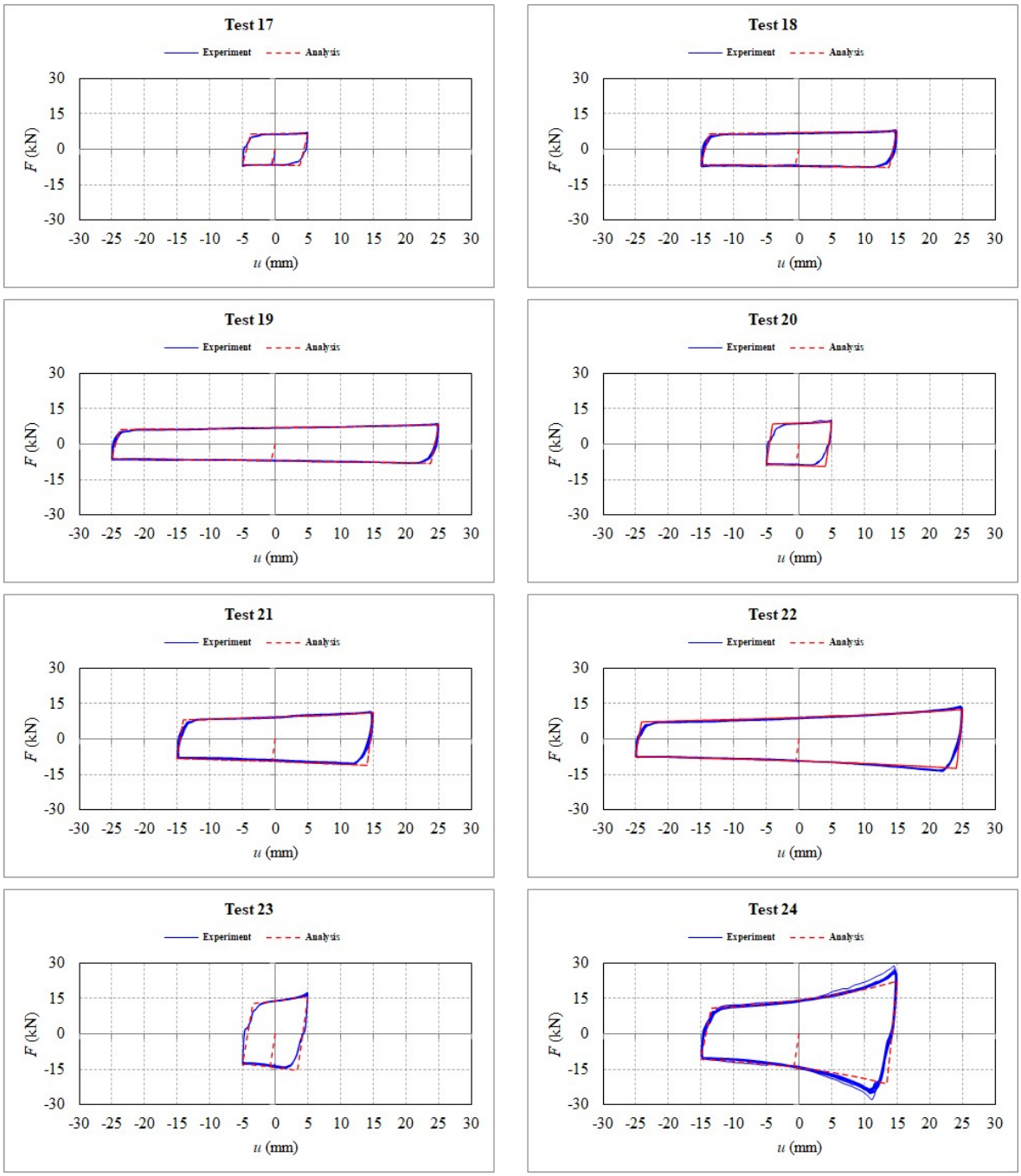

Figure 3.5. Comparison of experimental and numerical results for Group 3 tests.

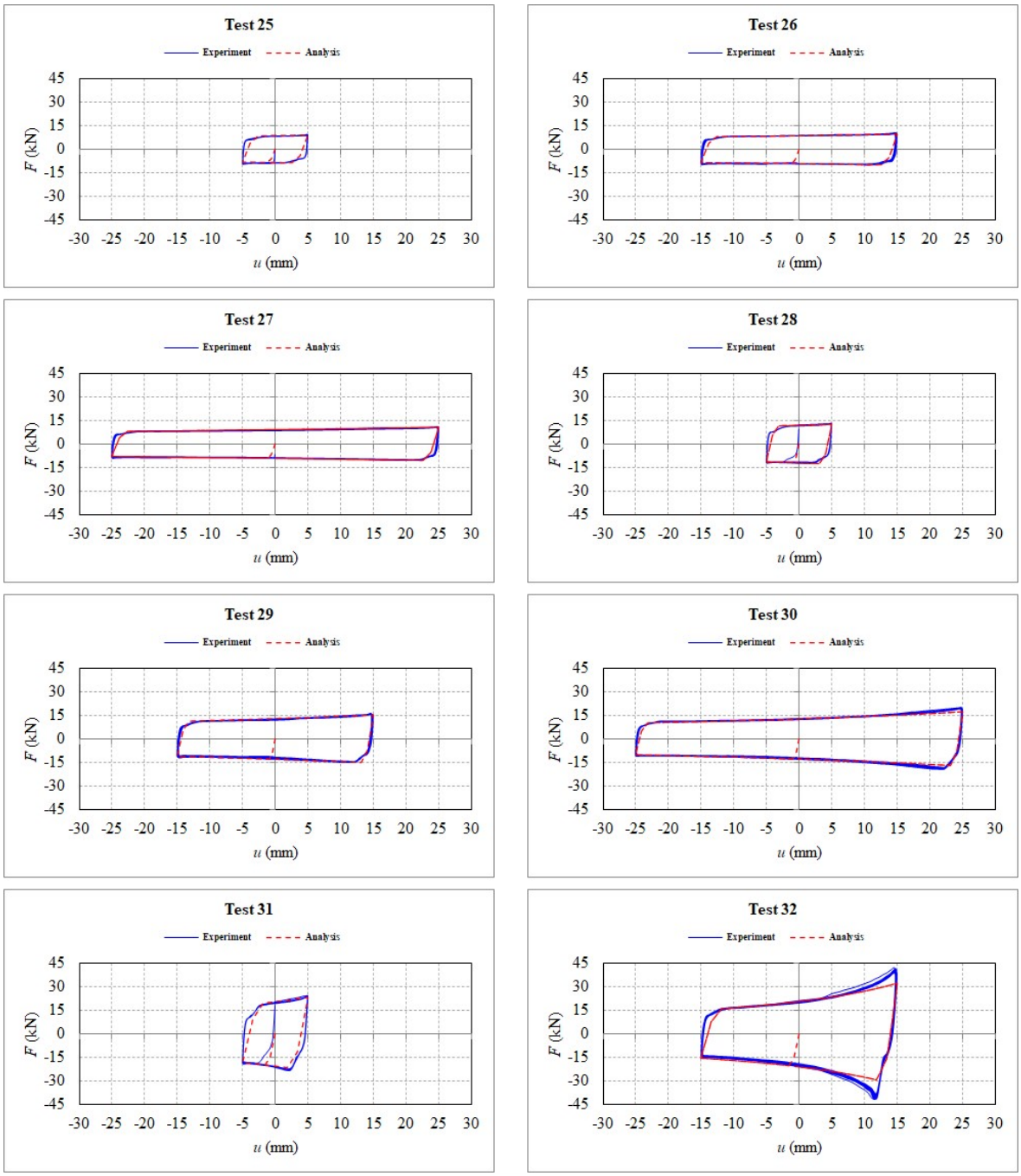

Figure 3.6. Comparison of experimental and numerical results for Group 4 tests.

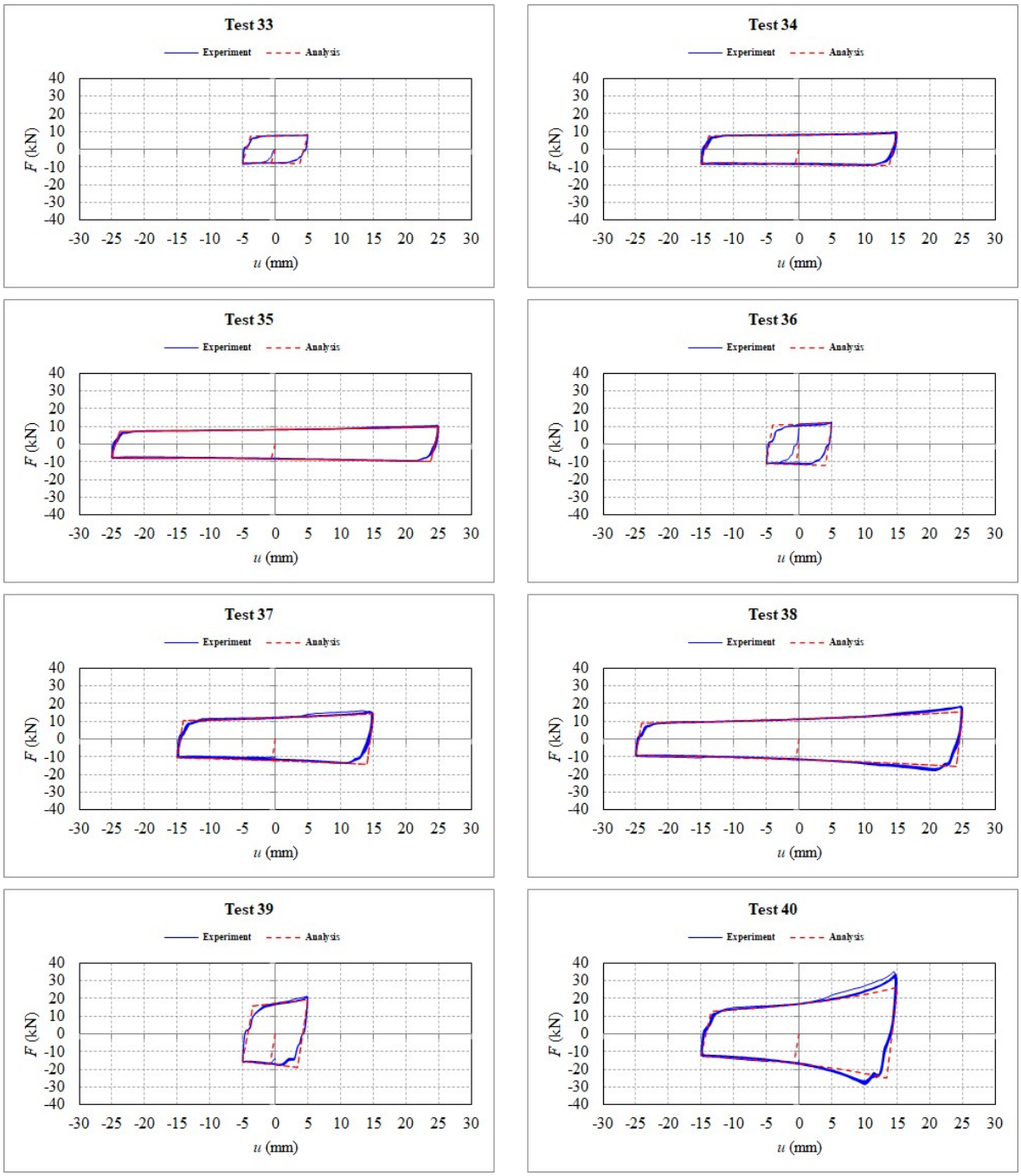

Figure 3.7. Comparison of experimental and numerical results for Group 5 tests.

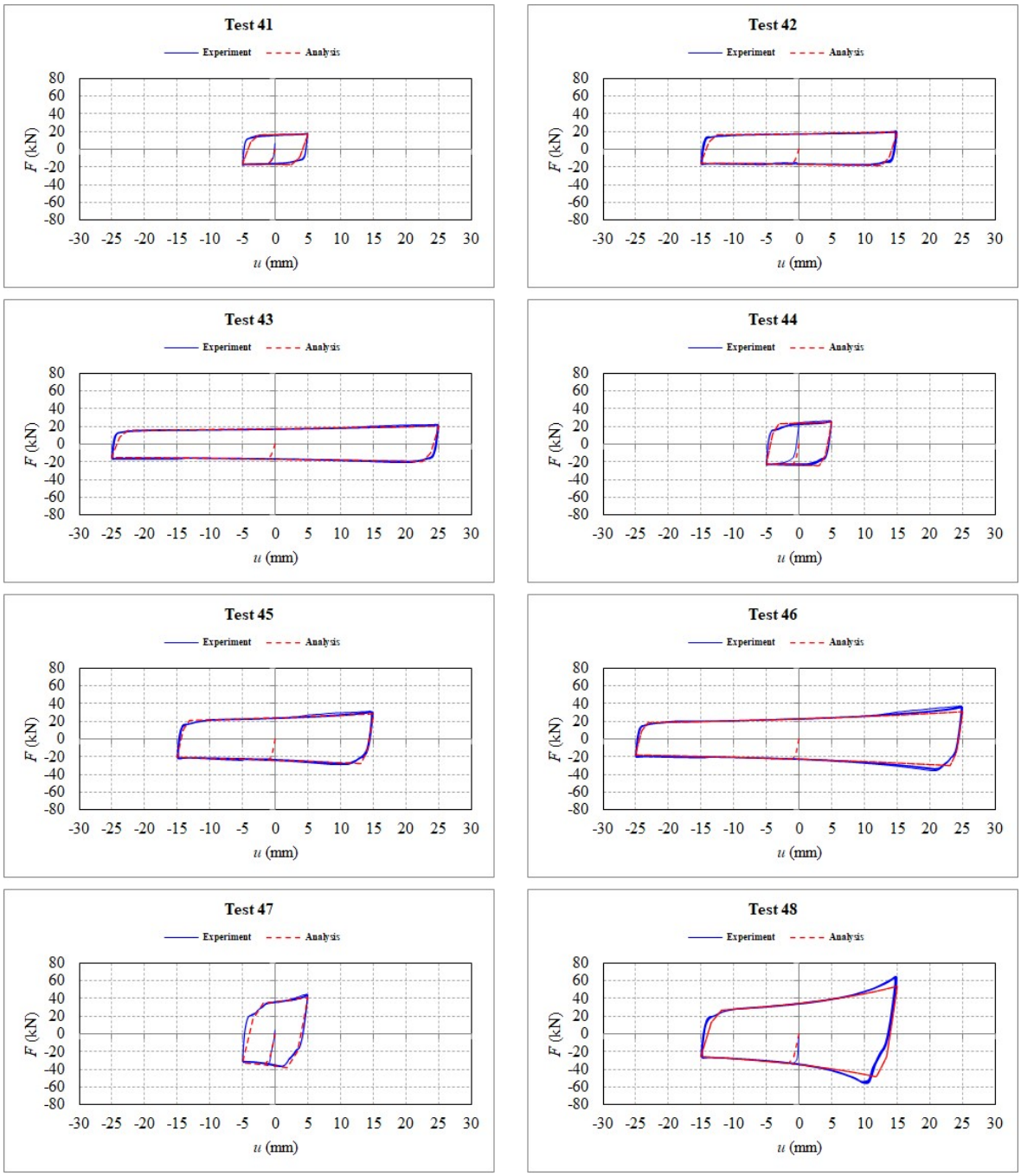

Figure 3.8. Comparison of experimental and numerical results for Group 6 tests.

3.2. Sub-Assembly Level Analyses

The effect of the proposed damper mechanism on the behaviour of precast post-tensioned concrete systems was analytically investigated incorporating the numerical model for the damper mechanism described in Section 3.1 in the numerical model for these systems. This section describes the modeling principles for precast post-tensioned concrete sub-assemblies and the results of the analyses conducted to investigate the effect of proposed dampers on them.

3.2.1. Principles and Verification of Numerical Model

The precast post-tensioned concrete sub-assembly that was used to investigate the effect of the proposed damper mechanism was modeled in OpenSEES (Open Source Earthquake Engineering Software), as was the case for simulating the experimental response of the damper mechanism.

Figure 3.9 shows the numerical modeling principles used in this study to investigate precast post-tensioned concrete sub-assemblies. These principles, outlined in detail by Morgen and Kurama [21] for Drain2DX, were adapted to be used in OpenSEES.

The precast beams and columns are modeled using "*dispBeamColumn*" elements. These elements are by definition based on displacement formulation, and consider the spread of plasticity along the element. These elements consist of segments of fiber sections, each fiber containing a uniaxial material, an area and a location. The uniaxial materials are defined according to their cyclic nonlinear behaviour. The *Concrete02* (linear tension-softening) model for concrete is used for definition of concrete material of precast members. This model is shown in Figure 3.10. The longitudinal mild steel rebars at precast concrete sections were modeled using *Steel01*, a bilinear steel material object with kinematic hardening. The confinement effect of transverse rebars were taken into account by defining confined uniaxial nonlinear concrete behaviour for fibers inside these rebars.

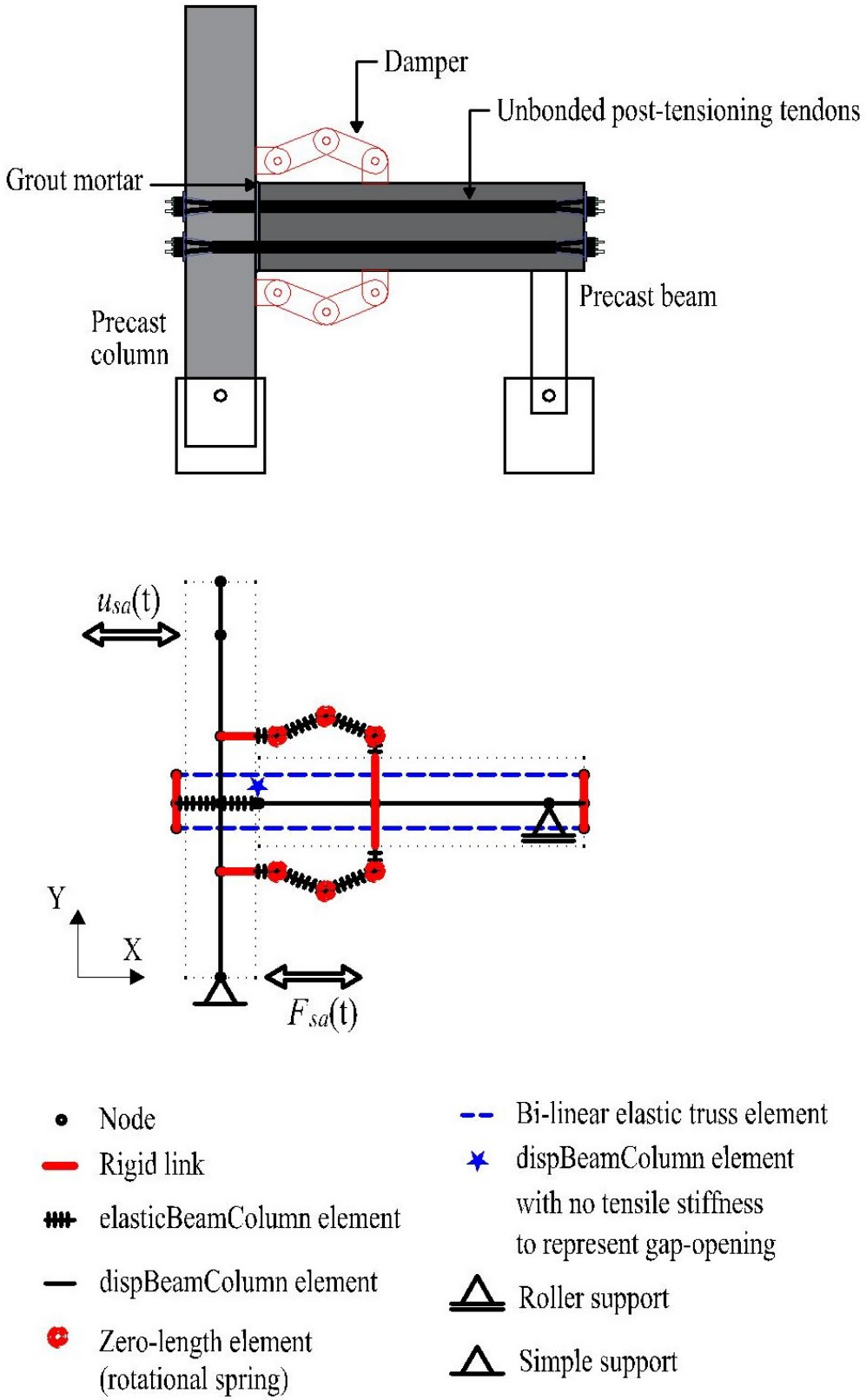

Figure 3.9. Numerical modeling principles for Ertas sub-assembly for verification.

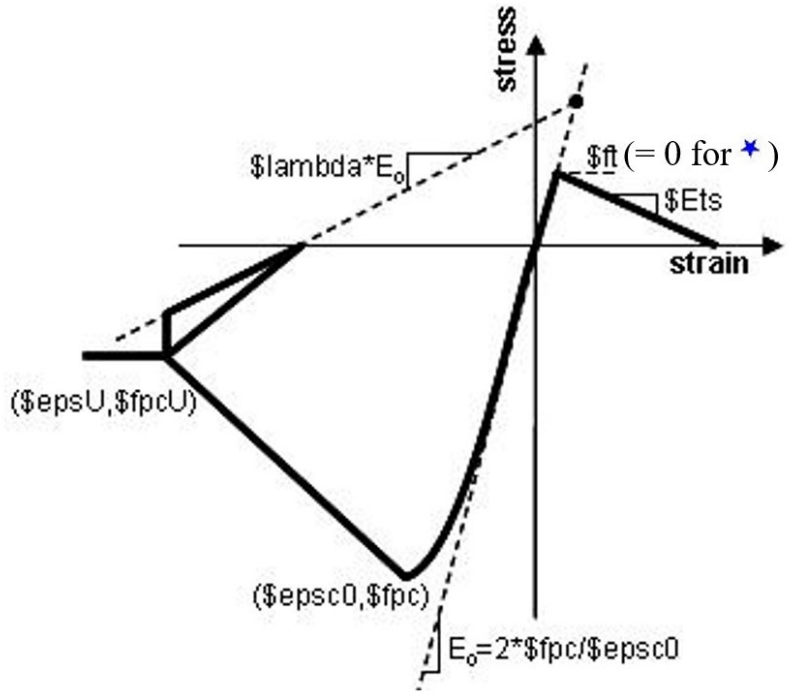

Figure 3.10. Concrete model used in OpenSEES.

The gap-opening mechanism that occurs at the beam-column joint was modeled by defining a displacement-based beam-column element of 20 mm length in which the concrete material used in the fibers has zero tensile stiffness and strength (shown with a $\star$ in Figure 3.9). This short element was followed by the precast beam, in which concrete material has tensile stiffness and strength.

Since continuity of beam element across the column is imperative to represent anchorage of post-tensioning tendons at their ends and the contact at which joint gap opening occurs, these parts were modeled using "*elasticBeamColumn*" elements. These elements were in a way rigid links that provide continuity throughout the frame.

The post-tensioning tendons are modeled using "*Truss*" elements, using "*Elastic-MultiLinear*" material, for which behaviour is by definition nonlinear but elastic. The stress-strain relation for 270K (f_{up}=1860MPa) prestressing steel, shown in Figure 3.11, is defined for this material. To represent the initial jacking stress, the elastic multi-linear material is assigned to "*InitStressMaterial*", with the initial stress defined as the percentage of ultimate strength of prestressing steel. This initial stress is shown with

a dashed line in Figure 3.11. The unbonded nature of tendons are represented by not constraining them kinematically to beam or column elements along their length. The anchorage of tendons at their ends are modeled by kinematically constraining them to the relevant beam joints.

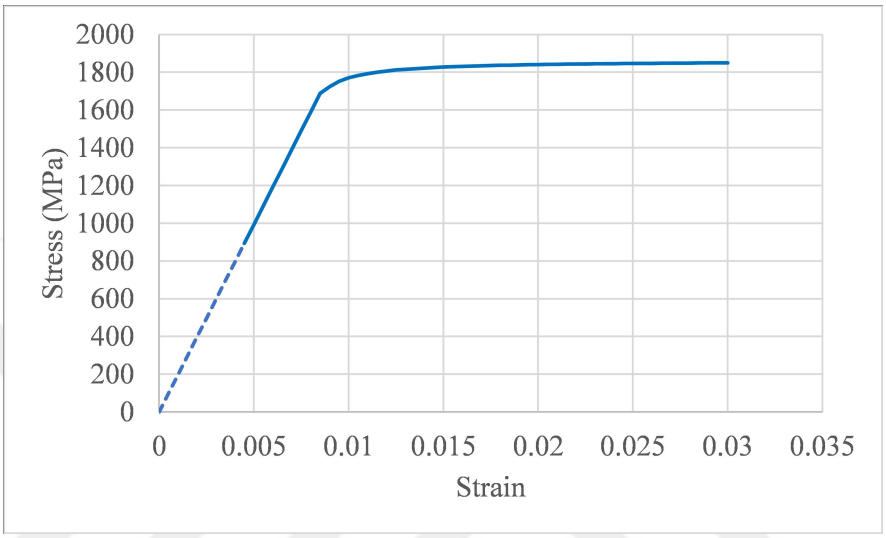

Figure 3.11. Stress-strain curve for prestressing steel.

The damper mechanism was modeled using the principles explained in detail in Section 3.1. The damper plates were modeled as single "*elasticBeamColumn*" elements, defining sum of plate thicknesses at the damper component as the thickness of the single element. Necessary checks for strength of the damper mechanism were done using the internal forces obtained from the analyses. The friction at the interface was defined using the calculations outlined in Section 3.1. The damper was kinematically constrained to the relevant nodes at beams and columns by rigid links.

The numerical analysis is conducted by subjecting the relevant column node to a displacement protocol, designated as $u_{sa}(t)$ in Figure 3.9. The horizontal reaction at the bottom of the column, $F_{sa}(t)$, is recorded. Then story drift, $\delta_{sa}(t)$, is calculated and the δ_{sa} vs F_{sa} plot is drawn. This process is explained in more detail in next section.

To verify the accuracy of the modeling principles, the experiment results published by Ertas for his test specimen [54] was used as reference. Figure 3.12, in which all dimensions are in mm, shows the experiment setup used by Ertas. The post-tensioning

tendons were placed at mid-height of the beam. There were totally 6 tendons with 0.5" diameter used, each with a cross-sectional area of 98 mm^2. The tendons were of 270K low relaxation type. The initial jacking stress for the tendons was 40% of the ultimate strength of prestressing steel. The compressive strength for concrete material used in precast members was 60 MPa. Two ϕ20 mild steel rebars were used at top and bottom parts of the precast beam, not protruding from the joint.

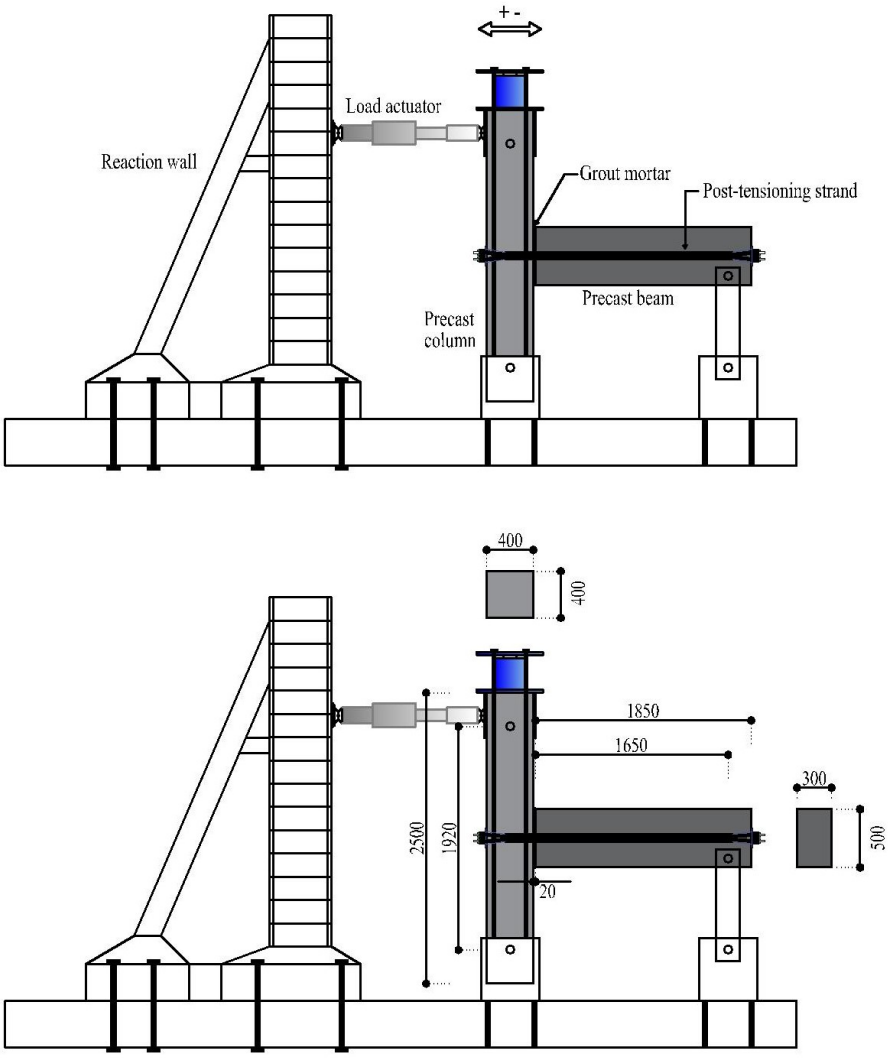

Figure 3.12. Experiment sub-assembly of Ertas used for verification of numerical modeling principles [54].

Figure 3.13 shows the δ_{sa} vs F_{sa} plots obtained from experiment by Ertas and from numerical analysis performed using the principles explained in this study. It can be

observed that the numerical principles represent the behavior of precast post-tensioned concrete sub-assemblies very well.

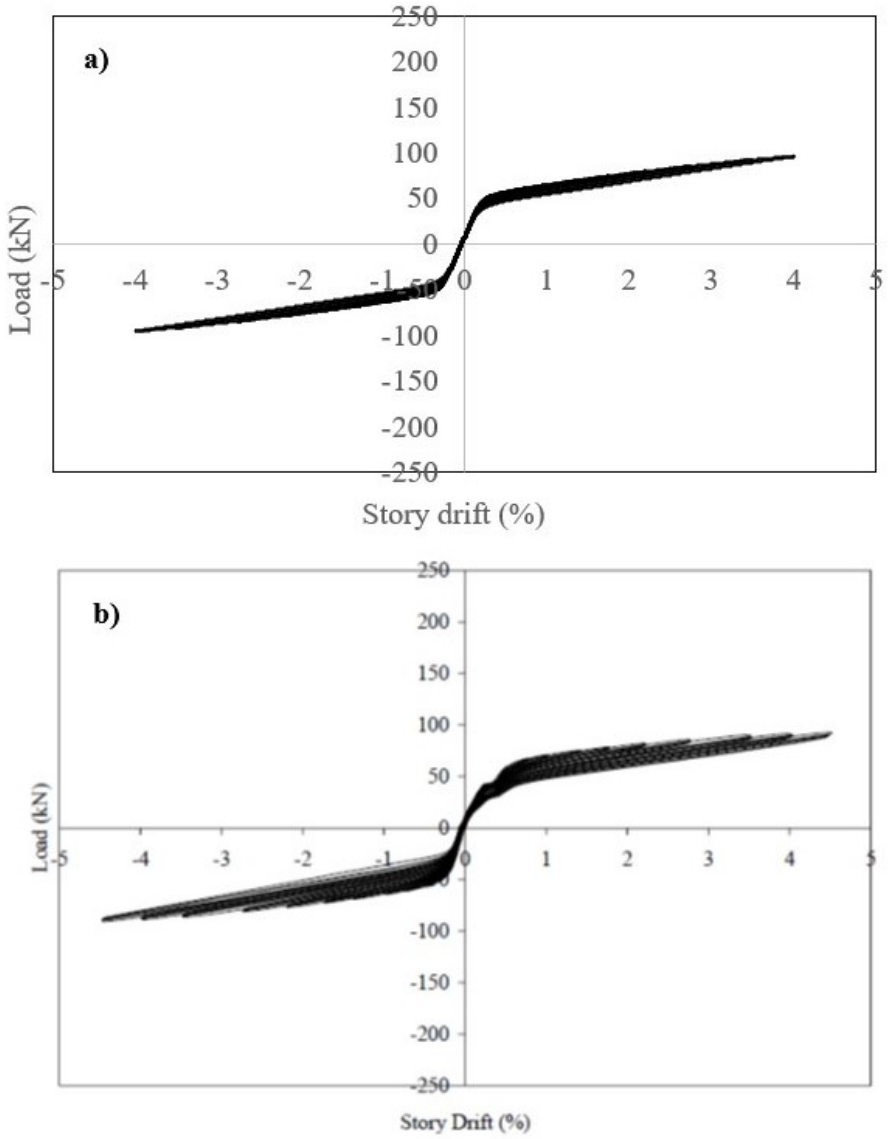

Figure 3.13. Comparison of a) Numerical results and b) Experiment results for Ertas sub-assembly [54].

3.2.2. Sub-assembly Analysis Parameters

In order to investigate the effect of the proposed damper mechanism on the response of precast post-tensioned concrete structures, one lateral load bearing exterior frame of a typical precast residential building was taken as reference. This frame is

described in detail in Section 3.3.2. The evaluation of the sub-assembly tests were done according to ACI T1.1-01, American Concrete Institute's *Acceptance Criteria for Moment Frames Based on Structural Testing* [55]. The dimensions for the sub-assembly investigated in this section were determined using the principle of possible contra-flexure points of the frame under seismic loads. The column element was cut from its mid-height, whereas the beam element was cut from one third of its clear length. Figure 3.14, in which all dimensions are in mm, shows details for the sub-assembly used for parametric numerical analyses.

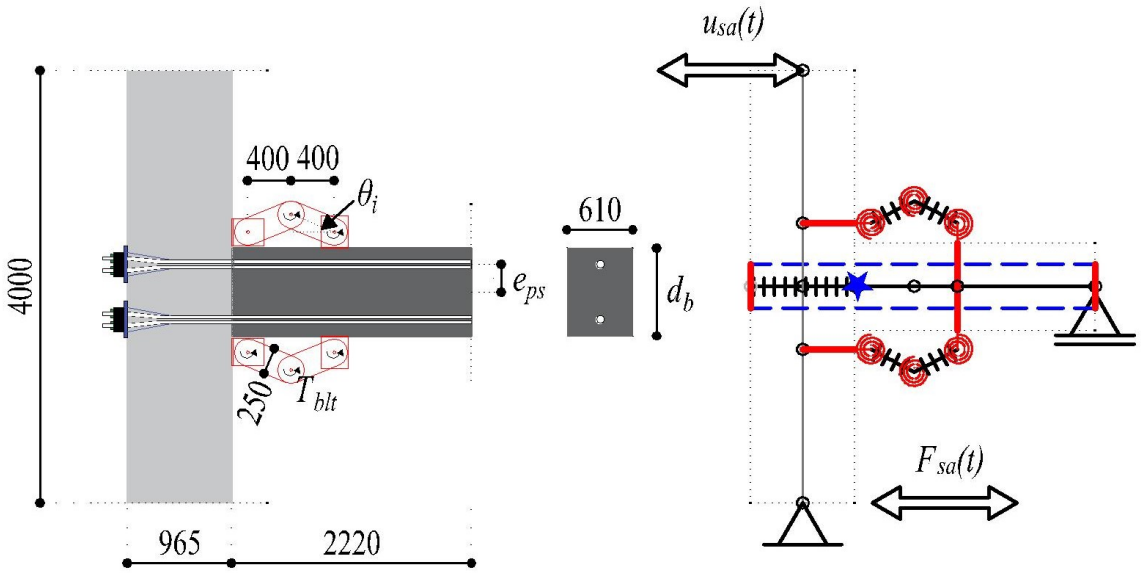

Figure 3.14. Sub-assembly used in numerical analyses.

The test parameters with which the sub-assembly tests were performed are shown in Table 3.2. The tests are classified according to five groups. Group 0 constitutes the base tests, Test 1 being the sub-assembly without damper and Test 2 being the sub-assembly with the damper with reference parameters. Group 1 has varying values for initial angle θ_i, Group 2 has varying values for bolt torque T_{blt}, Group 3 has varying values for total area of post-tensioning tendons A_{ps}, Group 4 has varying values for beam depth d_b and Group 5 has varying values for tendon eccentricity e_{ps}. It should be noted that the bolt torques T_{blt} are defined to all joints of the damper mechanism.

Table 3.2. Parameters for sub-assembly tests

SU	θ_i	T_{blt}	T_{fr}	A_{ps}	d_b	e_{ps}	Group
	deg	Nm	kNm	mm^2	mm	mm	
0	22.50	0	0.0	1400	810	0	0
1	22.50	200	9.0	1400	810	0	
2	30.00	200	9.0	1400	810	0	1
3	26.25	200	9.0	1400	810	0	
4	18.75	200	9.0	1400	810	0	
5	15.00	200	9.0	1400	810	0	
6	22.50	50	2.2	1400	810	0	2
7	22.50	100	4.5	1400	810	0	
8	22.50	300	13.5	1400	810	0	
9	22.50	400	18.0	1400	810	0	
10	22.50	200	9.0	840	810	0	3
11	22.50	200	9.0	1120	810	0	
12	22.50	200	9.0	1680	810	0	
13	22.50	200	9.0	1960	810	0	
14	22.50	200	9.0	1400	610	0	4
15	22.50	200	9.0	1400	710	0	
16	22.50	200	9.0	1400	910	0	
17	22.50	200	9.0	1400	1010	0	
18	22.50	200	9.0	1400	810	305	5
19	22.50	200	9.0	1400	810	230	
20	22.50	200	9.0	1400	810	155	
21	22.50	200	9.0	1400	810	80	

One thing to note is that bolt torques T_{blt} are defined in the analysis in terms of T_{fr} using Equation 3.1. The displacement protocol, $u_{sa}(t)$, is defined in the numerical computer model in terms of relative story drift $\delta_{sa}(t)$. The sub-assembly has been subjected to story drifts of ±0.15%, ±0.20%,±0.25%,±0.35%,±0.50%, ±0.75%, ±1.00%,

±1.40%, ±1.75%, ±2.20%, ±2.75%, ±3.50% and ±4.00%. This protocol is shown in Figure 3.15. The story drift $\delta_{sa}(t)$ is expressed as

$$\delta_{sa}(t) = \frac{u_{sa}(t)}{L_c}. \tag{3.4}$$

In this expression, L_c is the vertical distance between the application of displacement and the column support, which is equal to 4000 mm for the sub-assembly.

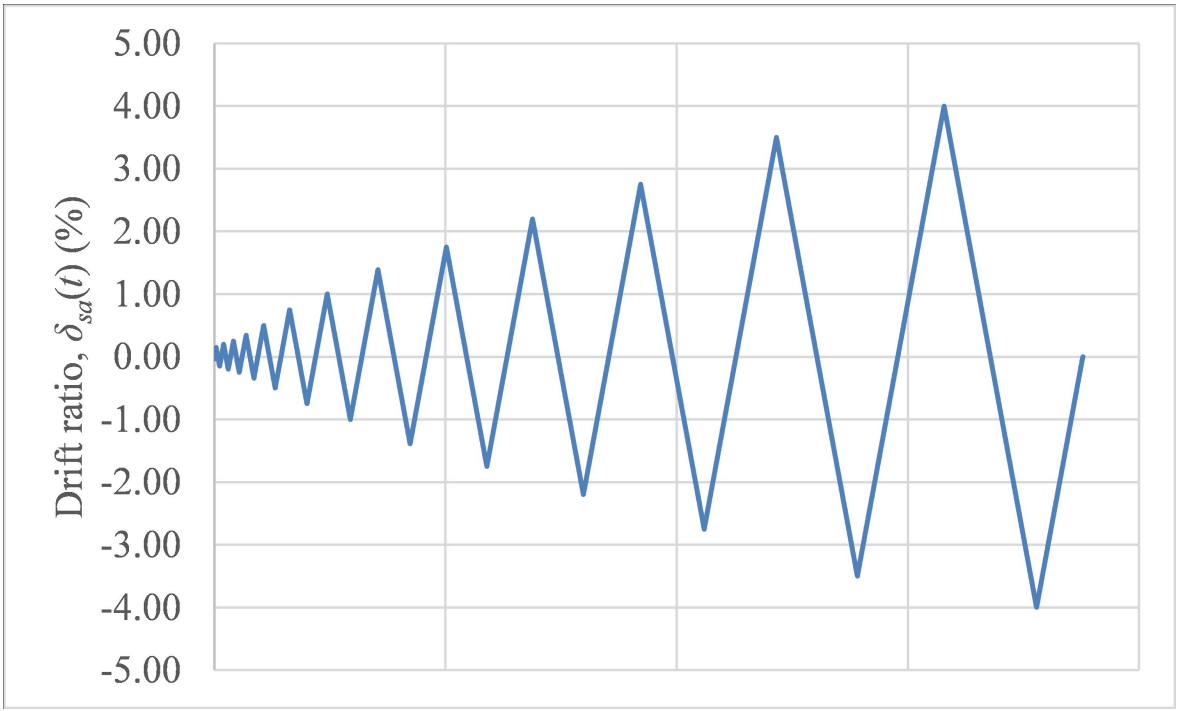

Figure 3.15. Drift ratio protocol applied to the sub-assembly.

The response parameters according to which the sub-assemblies were evaluated are force capacity F_{sa} and relative energy dissipation ratio β. These parameters were calculated for each of the drift ratio values the sub-assembly is subjected to, and an i is added at the end of the parameter to indicate that it is calculated for drift ratio i. For example, $\beta_{4.00}$ is the β value calculated for the hysteresis loop for ±4.00% drift demand. Force capacity F_{sa} is by definition the horizontal force reaction at the bottom of the column for the relevant drift ratio.

Relative energy dissipation ratio β is a term defined in ACI T1.1-01 [55] and is an indicator of the hysteretic energy dissipation capacity of the structural system. It is

calculated as the ratio of the area enclosed within the hysteresis loop to the area inside the parallelogram which is defined by the initial stiffness of the system in positive and negative directions. It is illustrated in Figure 3.16 and is expressed as

$$\beta_i = \frac{A_h}{(F_1 + F_2)(\theta_1' + \theta_2')} \tag{3.5}$$

where β_i is the relative energy dissipation ratio for drift ratio i, A_h is the area of the hysteresis loop, F_1 and F_2 are peak lateral resistance for positive and negative loading, respectively, and θ_1 and θ_2 are drift ratios for zero lateral load for unloading at positive and negative initial stiffnesses, respectively. It is imperative to point out that the initial stiffness is that of the first drift ratio, not initial stiffness of the cycle of drift ratio for which β is calculated. ACI T1.1-01 specifies that for a structural system to be deemed sufficient, the relative energy dissipation ratio β should be greater than equal to 0.125 for drift ratio level at which acceptance is sought, but not less than ±3.50%.

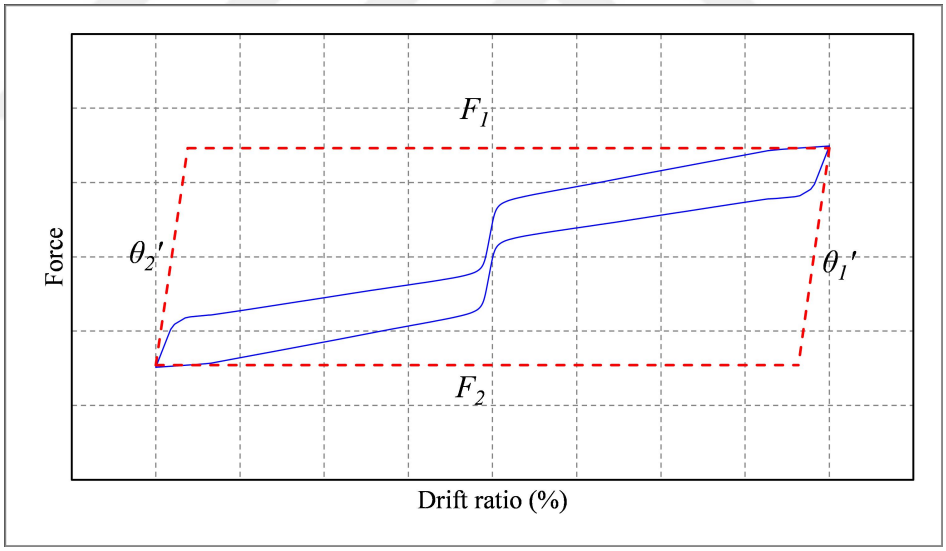

Figure 3.16. Relative energy dissipation ratio β.

3.2.3. Force-Drift Ratio Plots

The force vs. drift ratio plots of the sub-assemblies obtained from numerical analyses are shown in Figure 3.17 and Figure 3.18.

The effect of test parameters can be visualized by observing force vs. drift ratio plots. For example, increasing bolt torque (SU6 through SU9) has the obvious effect of increasing area of the hysteresis loop. Decreasing initial angle θ_i while all other parameters are the same (SU2 through SU5) increases the area of the hysteresis loop significantly. It is worth noting that the stiffness of the sub-assembly, which in other cases reduces due to post-tensioning strands exceeding limit of proportionality after 3.00% drift, does not decrease for the case in which θ_i=15 degrees (SU5), due to the contribution of damper's stiffness. Increasing the eccentricity e_{ps} of the post-tensioning strands causes them to exceed the limit of proportionality for smaller drifts. This is expected since placing the strands closer to extreme fibers of the beam imposes greater strain demands on them for a given story drift. Another important point to stress is that in none of the sub-assemblies the self-centering behaviour of precast post-tensioned concrete systems is compromised. This is evident since there is no residual strains even after ±4.00% drift ratio cycle.

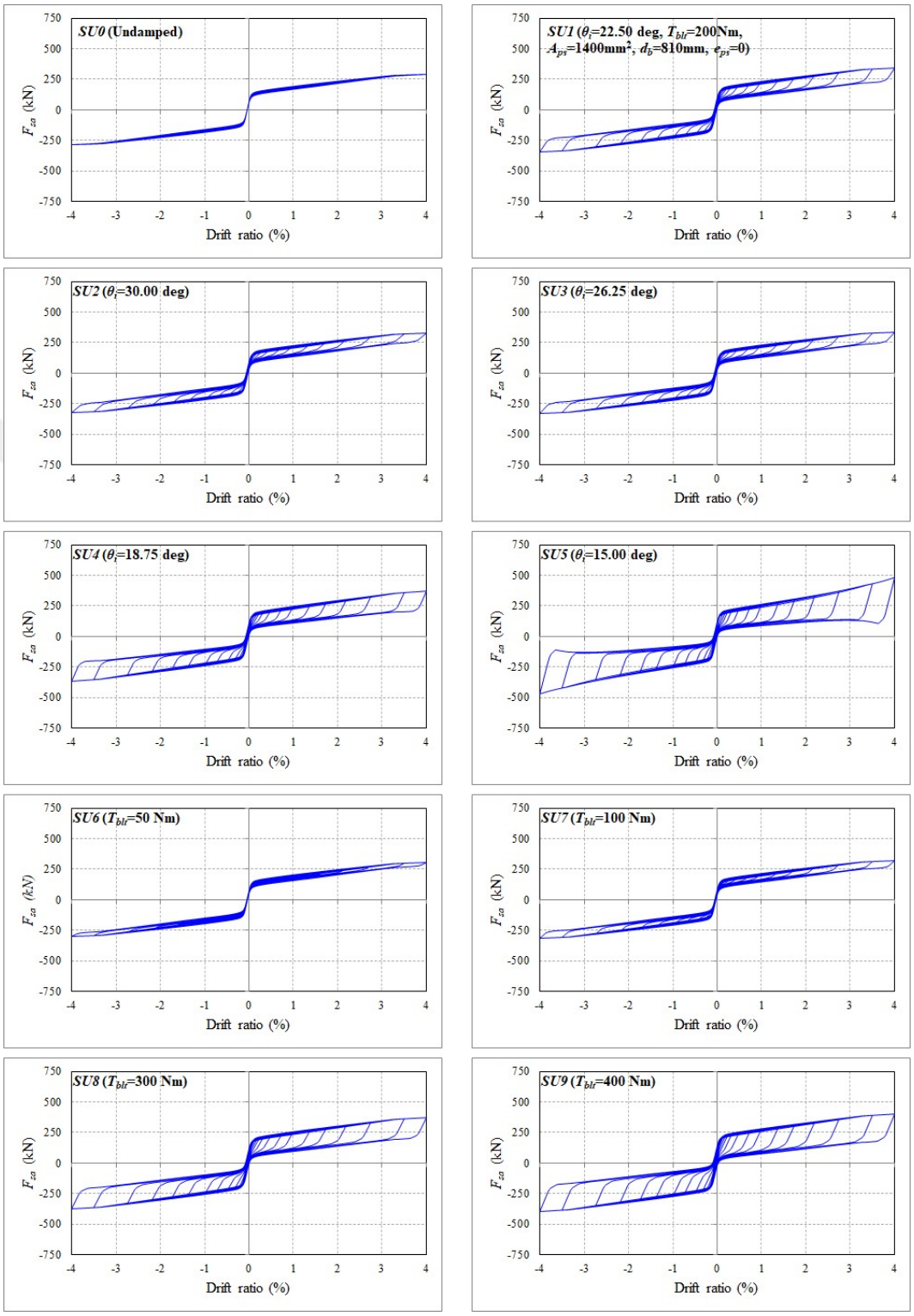

Figure 3.17. Force vs. drift ratio plots for sub-assembly 0 through 9.

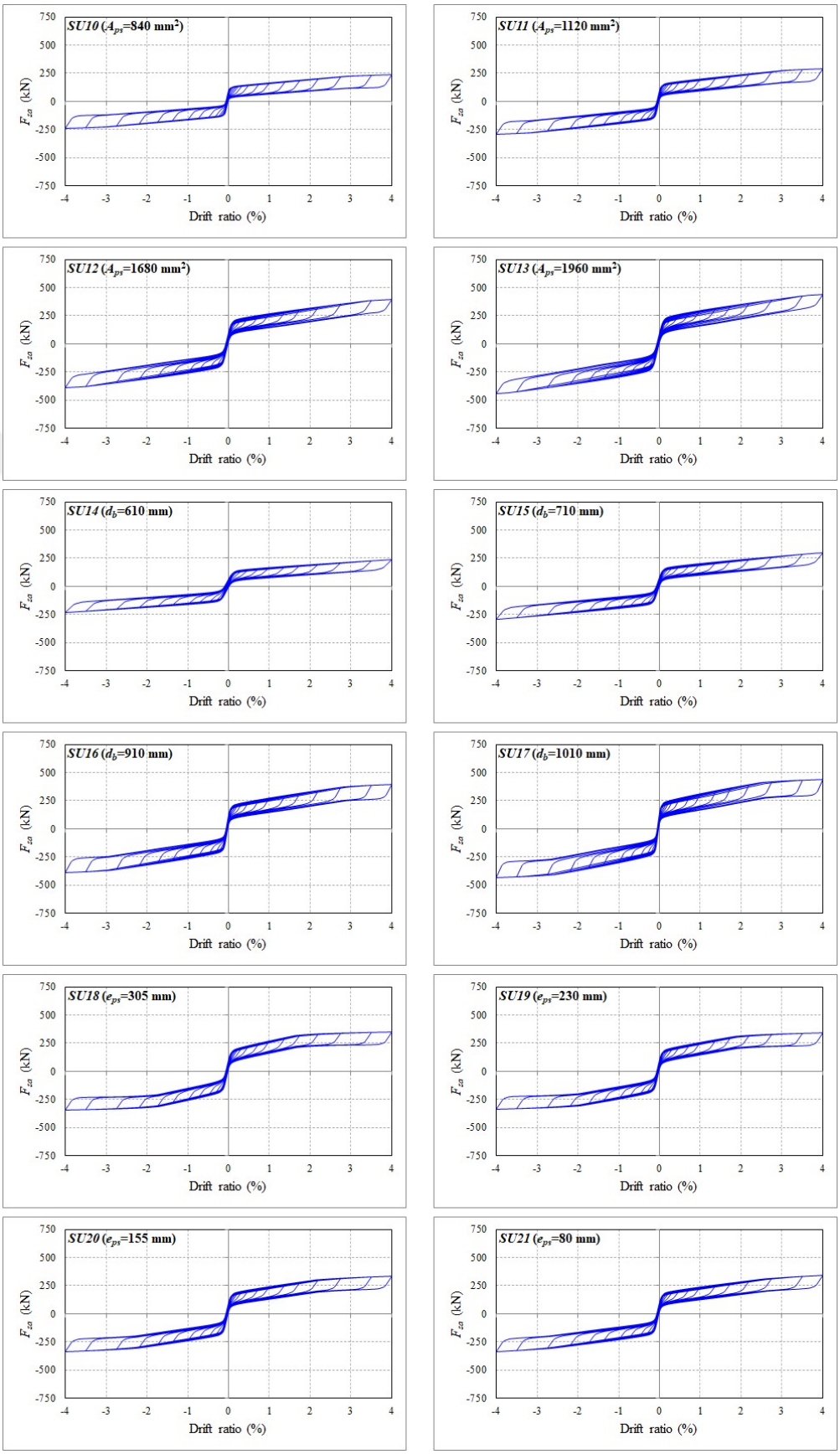

Figure 3.18. Force vs. drift ratio plots for sub-assembly 10 through 21.

3.2.4. Force Capacity

Table 3.3 shows force capacity values for representative drift ratio levels obtained from numerical analyses.

Table 3.3. Force capacity F_{sa} for sub-assemblies

SU	Force capacity, F_{sa} (kN)							Group
	±0.20%	±0.50%	±1.00%	±1.75%	±2.20%	±3.50%	±4.00%	
0	147	165	189	221	239	282	288	0
1	186	205	230	264	284	331	340	
2	176	196	220	253	271	315	322	1
3	181	200	224	258	276	322	328	
4	193	213	239	275	296	351	364	
5	204	225	254	297	324	419	469	
6	157	175	199	232	250	294	301	2
7	166	185	210	242	261	306	313	
8	206	226	252	286	306	357	366	
9	226	246	273	309	330	382	393	
10	132	144	161	184	198	227	233	3
11	160	176	196	226	242	281	287	
12	210	234	263	301	322	380	389	
13	233	261	293	335	359	422	436	
14	133	149	163	183	194	223	234	4
15	160	177	196	222	237	278	290	
16	212	235	266	309	333	379	386	
17	238	265	303	356	385	423	430	
18	194	222	263	315	326	339	343	5
19	190	215	249	296	312	329	334	
20	188	210	239	279	301	325	332	
21	186	206	233	268	289	327	336	

Drift ratio vs. force capacity plots are presented in Figure 3.19 to interpret the effect of test parameters. A general observation of the results shows that the force capacity of precast post-tensioned systems is sensitive to the test parameters investigated in this study. Plot for Group 1 sub-assemblies is a very clear demonstration of the amplification effect of small initial angle θ_i. For θ_i=30 degrees to θ_i=18.75 degrees (SU2 to SU4), the change in force capacity is not dramatic. For example, decreasing θ_i from 30 degrees (SU2) to 18.75 degrees (SU4) increases F_{sa} only 11% for 3.50% drift ratio (315kN vs. 351kN). However, a further decrease of initial angle to 15 degrees (SU5) increases the force capacity 33% (315kN vs. 419kN). The effect of initial angle on force capacity is even larger for 4.00% drift ratio, in which decreasing θ_i from 30 degrees to 15 degrees increases F_{sa} by 45% (322kN vs. 469kN).

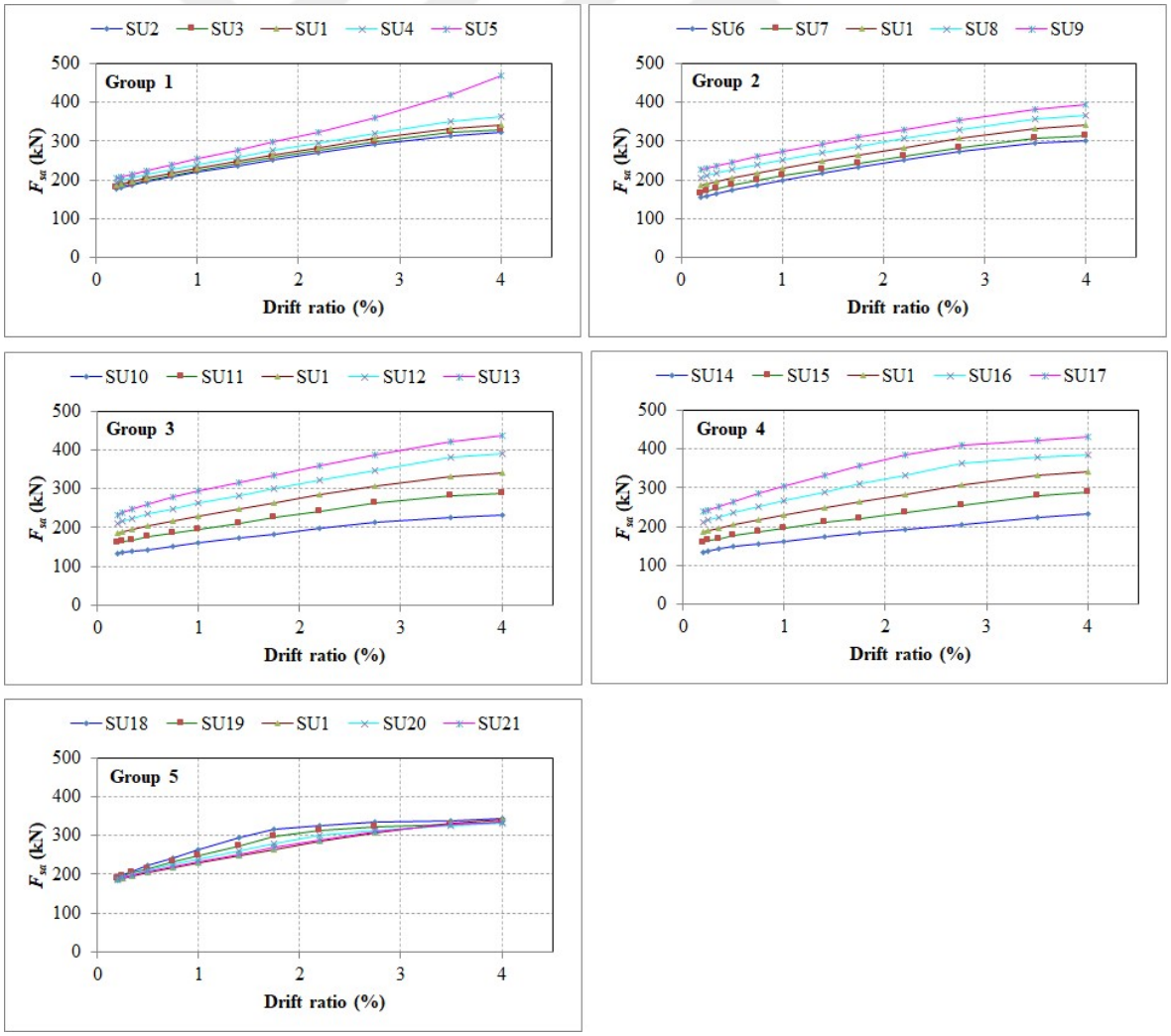

Figure 3.19. Force capacity vs. drift ratio plots.

Another important consequence of using damper mechanism on response of the sub-assembly can be observed on the behaviour after post-tensioning strands reach limit of proportionality. The post-tensioning tendons reach limit of proportionality for all sub-assemblies of Group 1 at approximately 3.30% drift demand. This is manifested both in force vs. drift ratio plots in Figure 3.17 and force capacity vs drift ratio plots in Figure 3.19. After the tendons reach limit of proportionality, there is a visible decrease in the stiffness of the system. However, this reduction in stiffness gets smaller as initial angle is decreased, with the stiffness even increasing for the case in which initial angle is 15 degrees (SU5).

Increasing bolt torque T_{blt} has the expected consequence of increasing force capacity F_{sa}. For example, increasing bolt torque from 50Nm (SU6) to to 200Nm (SU1) increases the force capacity 14% (250kN vs. 284kN) for 2.20% drift ratio. Increasing bolt torque further to 400Nm (SU9) increases force capacity by 32% (250kN vs. 330kN). One important thing to note here is that the correlation between force capacity and bolt torque is not linear, in other words changing the bolt torque value does not cause the same change in force capacity. This is obvious since force capacity is not solely dependent on contribution from damper mechanism, it is also a function of post-tensioning tendon forces.

Group 3 results indicate the effect of total post-tensioning strand cross-sectional area A_{ps} on force capacity F_{sa}. Post-tensioning strand area has significant effect on force capacity. For example, increasing A_{ps} from 840mm^2 (SU10) to 1960mm^2 (SU13) increases force capacity by 82% (198kN vs. 359kN) for 2.20% drift ratio. This is expected since a significant part of force capacity is provided by the post-tensioning strands. One thing to note is that in the numerical analyses conducted in this study, force capacity F_{sa} is more sensitive to A_{ps} than it is to bolt torque T_{blt}. This is due to the fact that the contribution of the damper mechanism to force capacity is limited by self-centering requirements.

Increasing beam depth d_b has the expected effect of increasing force capacity F_{sa} of the system. Increasing the eccentricity e_{ps} also increases the force capacity F_{ps}. This

is due to the fact that as eccentricity of the tendons increase, the moment arm of the tendon forces at the joint interface also increases, thereby providing more force capacity to the system. However, it is crucial to note that the effect of increasing eccentricity gradually decreases as drift ratio increases. This is a consequence of post-tensioning tendons exceeding limit of proportionality at smaller drift ratios, since strain demand imposed on them are higher when they are placed closer to extreme beam fibers. For example, increasing e_{ps} from 0 (SU1) to 305mm (SU18) increases force capacity 15% for 2.20% drift ratio (284kN vs. 326kN). However, for 3.50% drift ratio, the force capacity is almost the same (331kN vs. 339kN).

3.2.5. Relative Energy Dissipation Ratio

Relative energy dissipation ratios are given in Table 3.4. Results are classified in six groups according to parameters.

Table 3.4. Relative energy dissipation ratio β for sub-assemblies

SU	Relative energy dissipation ratio, β								Group
	0.20%	0.50%	1.00%	1.75%	2.20%	3.50%	4.00%	Avg	
0	0.003	0.004	0.004	0.006	0.007	0.011	0.006	0.010	0
1	0.118	0.191	0.189	0.175	0.168	0.155	0.150	0.164	
2	0.053	0.134	0.141	0.133	0.128	0.118	0.112	0.115	1
3	0.081	0.159	0.162	0.151	0.145	0.133	0.128	0.136	
4	0.172	0.232	0.224	0.207	0.199	0.186	0.182	0.203	
5	0.238	0.285	0.271	0.253	0.244	0.229	0.222	0.255	
6	0.044	0.061	0.058	0.054	0.053	0.052	0.047	0.057	2
7	0.076	0.110	0.106	0.098	0.095	0.089	0.084	0.097	
8	0.140	0.252	0.255	0.239	0.229	0.211	0.206	0.216	
9	0.149	0.300	0.310	0.292	0.282	0.259	0.254	0.256	
10	0.156	0.259	0.263	0.244	0.234	0.217	0.214	0.224	3
11	0.130	0.216	0.217	0.202	0.193	0.178	0.175	0.186	
12	0.113	0.174	0.169	0.157	0.151	0.139	0.133	0.150	
13	0.112	0.162	0.155	0.144	0.138	0.129	0.121	0.141	
14	0.139	0.234	0.228	0.213	0.205	0.187	0.178	0.198	4
15	0.122	0.207	0.205	0.191	0.183	0.167	0.159	0.177	
16	0.118	0.180	0.177	0.163	0.157	0.148	0.146	0.156	
17	0.118	0.172	0.167	0.154	0.149	0.147	0.143	0.151	
18	0.116	0.180	0.168	0.148	0.146	0.148	0.147	0.152	5
19	0.117	0.184	0.176	0.158	0.153	0.153	0.151	0.157	
20	0.118	0.188	0.183	0.167	0.159	0.155	0.153	0.161	
21	0.118	0.190	0.187	0.173	0.165	0.156	0.152	0.163	

Table 3.4 shows relative energy dissipation ratio β values for representative drift ratio levels obtained from numerical analyses. Drift ratio vs. relative energy dissipation ratio plots are presented in Figure 3.20 to interpret the effect of test parameters. As can be seen in Figure 3.20, relative energy dissipation ratio β is sensitive to the test parameters investigated in this study, with the exception of tendon eccentricity e_{ps}, for which the reason is explained further in this section. One general thing to note is that the β value tends to increase up to the drift value of 0.50%, after which it starts to decrease. This is due to the fact that elastic bending of the column member is more dominant on the behavior of the system up to roughly 0.50% drift demand. This phenomenon is demonstrated in detail in the next section of this document.

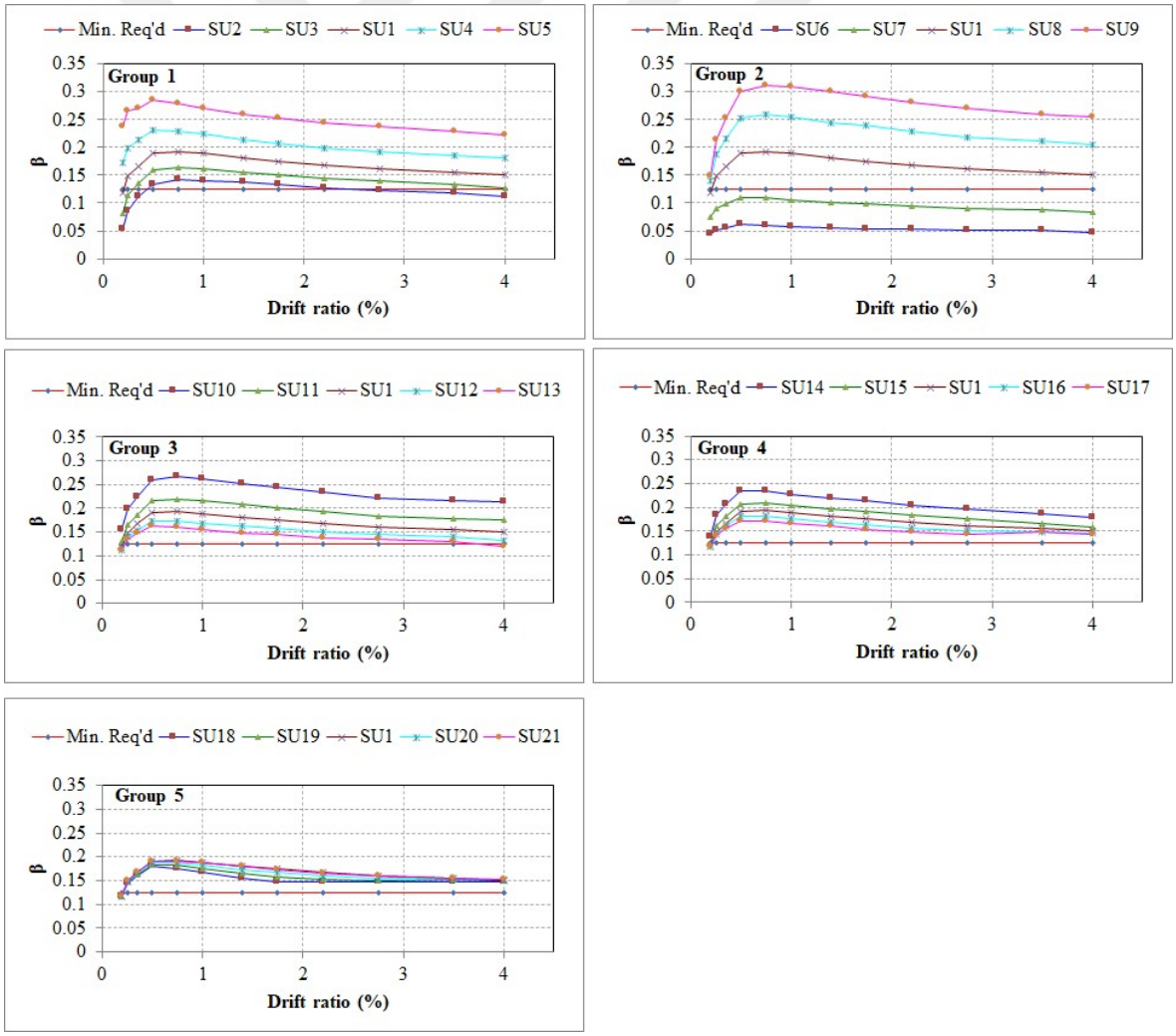

Figure 3.20. Force capacity vs. relative energy dissipation ratio plots.

Precast post-tensioned concrete sub-assembly without damper (SU0) has very small relative energy dissipation ratio β, way below the minimum requirement of 0.125

for 3.50% drift demand. This is consistent with the argument made in the previous sections of this thesis that these systems have very limited energy dissipation capacity due to lack of hysteretic energy dissipation and the elastic behavior of post-tensioning tendons which are the primary element in response.

The effect of initial angle θ_i on energy dissipation capacity can be observed in Group 1 results. Decreasing θ_i from 30 degrees (SU2) to 15 degrees (SU5) increases average relative energy dissipation ratio β by 121% (0.115 vs. 0.255). The correlation between relative energy dissipation ratio and initial angle is not linear, it is exponential. In other words, as the initial angle gets smaller, the sensitivity of relative energy dissipation ratio on initial angle increases. For example, decreasing θ_i by 3.75 degrees from 30 degrees (SU2) to 26.25 degrees (SU3) increases average β value only 19% where the same change from 18.75 degrees (SU4) to 15 degrees (SU5) increases average β value 26%.

Relative energy dissipation ratio β tends to decrease after a level of drift ratio level, which is 0.50% in most cases. This is due to the fact that the rate of increase in the area enclosed by the parallelogram defined by initial stiffness is larger than the rate of increase in the hysteresis loop as drift ratio demand gets larger. This phenomenon can be visually observed in Figure 3.21, where the area of the hysteresis loop and the area enclosed by the parallelogram for 1.00% and 4.00% drift values can be seen.

Another observation to make is that relative energy dissipation ratio of sub-assemblies with small initial angles (SU4, SU5) is large even for small drift ratio demands. For example, for 0.50% drift ratio level, β value for sub-assembly with θ_i (SU5) is equal to 0.285, which is more than twice the minimum requirement of 0.125. This is another advantage of amplification effect of small initial angle, which contributes dramatically to the energy dissipation capacity of the system even for light-moderate earthquake levels, thus further decreasing displacement demands.

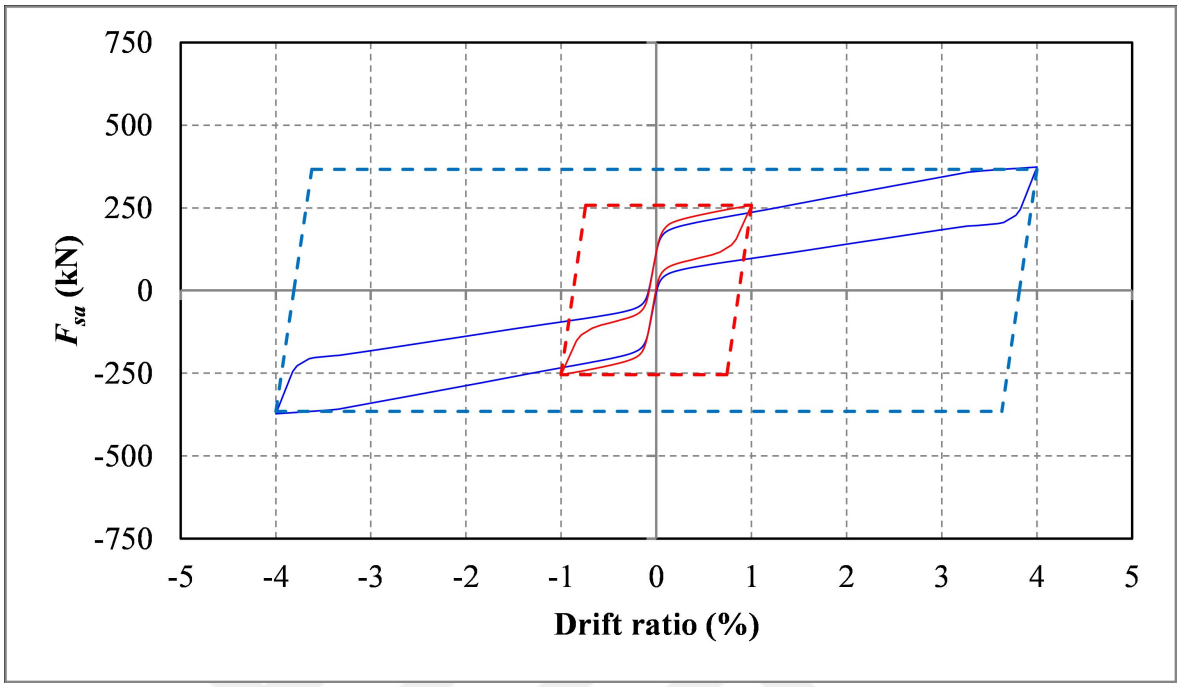

Figure 3.21. Comparison for β at 1.00% and 4.00% drift ratios for SU8.

3.2.6. Post-Tensioning Tendon Stresses

Figure 3.22 and Figure 3.23 show the stress at the post-tensioning tendons as a function of drift ratio. It should be noted that the tendons for which stress is calculated are the ones placed at bottom part of the beam for Group 5 sub-assemblies. The post-tensioning tendons exceed limit of proportionality at drift ratio of 3.30% for Group 0, Group 1, Group 2 and Group 3. After this stage, there is a significant decrease at stiffness of the system, which is most clearly observed for the force vs. drift ratio plot for the sub-assembly without damper (SU0), since there is no contribution from the damper to compensate for the loss in stiffness. For Group 4 sub-assemblies (SU14-SU17), as the beam depth increases, the drift level at which tendons exceed limit of proportionality decreases. This is due to the fact that as beam depth increases, the moment arm of tendon location increases, thus imposing more strain demand on the tendons for same drift ratio. For Group 5 sub-assemblies (SU18-SU21), there is a similar trend. As eccentricity of the tendons increases, the strain demand also increases, with the result of tendon exceeded limit of proportionality at a lower level of drift ratio.

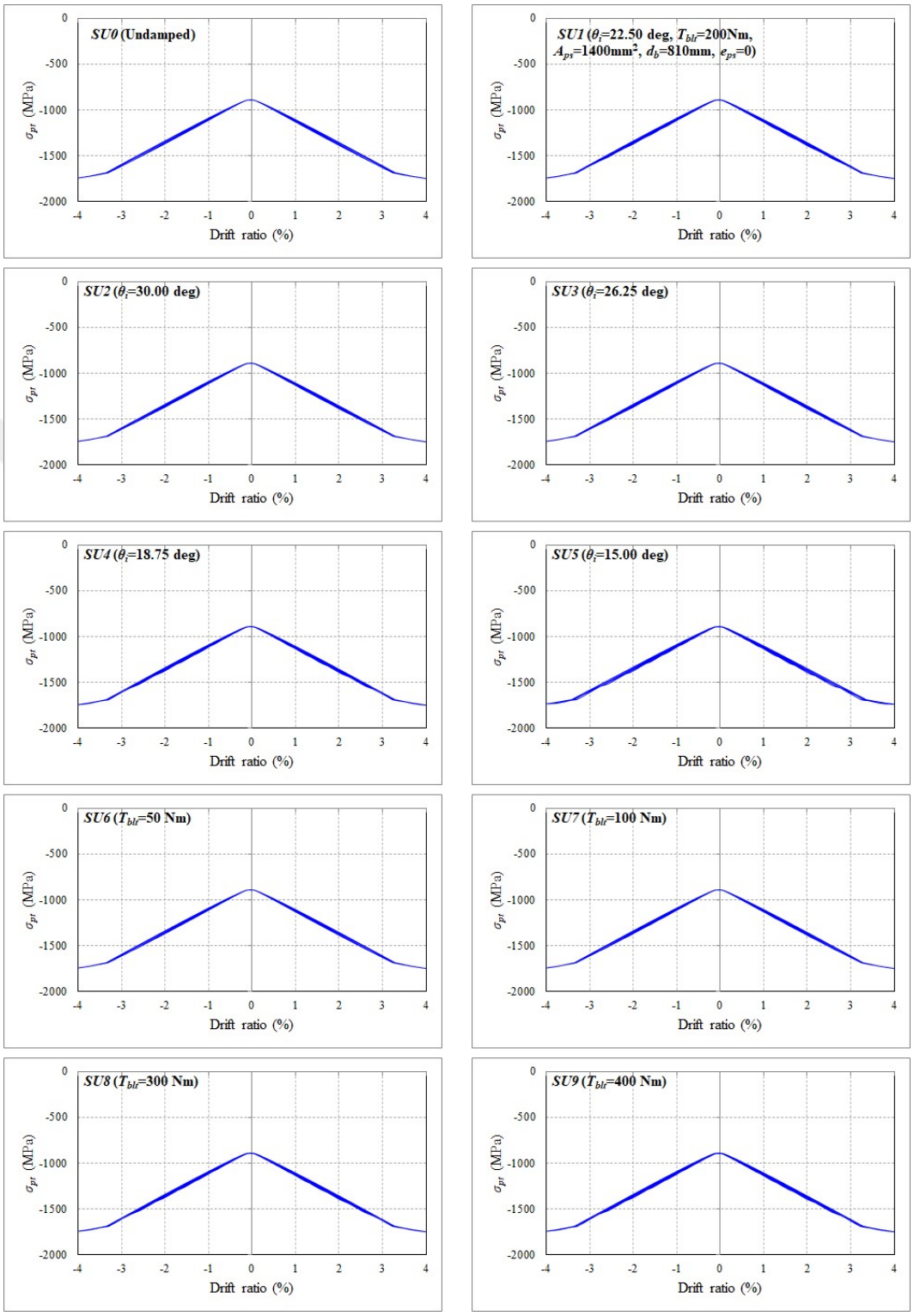

Figure 3.22. Post-tensioning stress vs. drift ratio plots for sub-assembly 0 through 9.

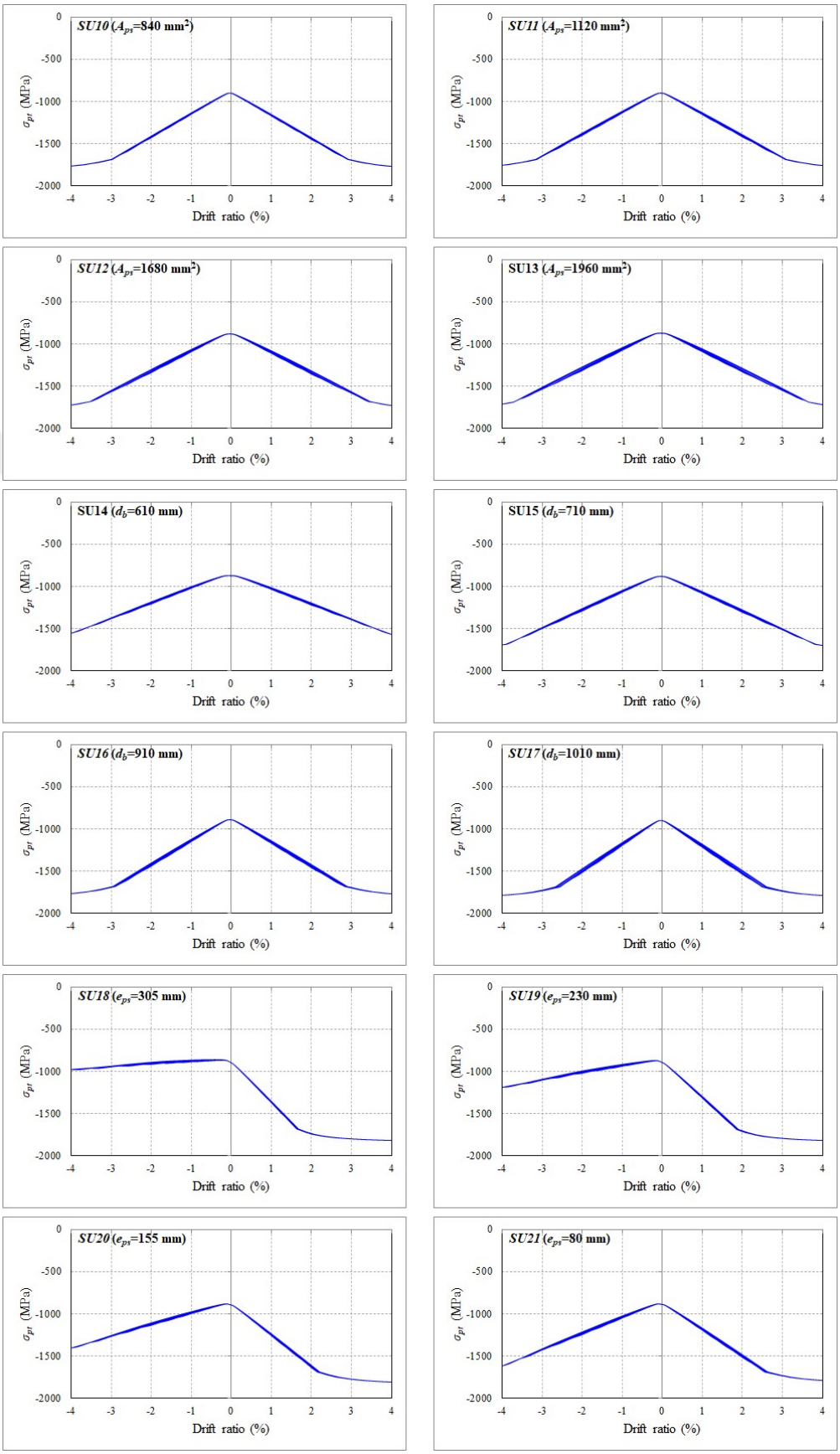

Figure 3.23. Post-tensioning stress vs. drift ratio plots for sub-assembly 10 through 21.

3.2.7. Damper Forces

Results for damper forces are shown in this section. These results demonstrate the relation between the parameters and the damper forces.

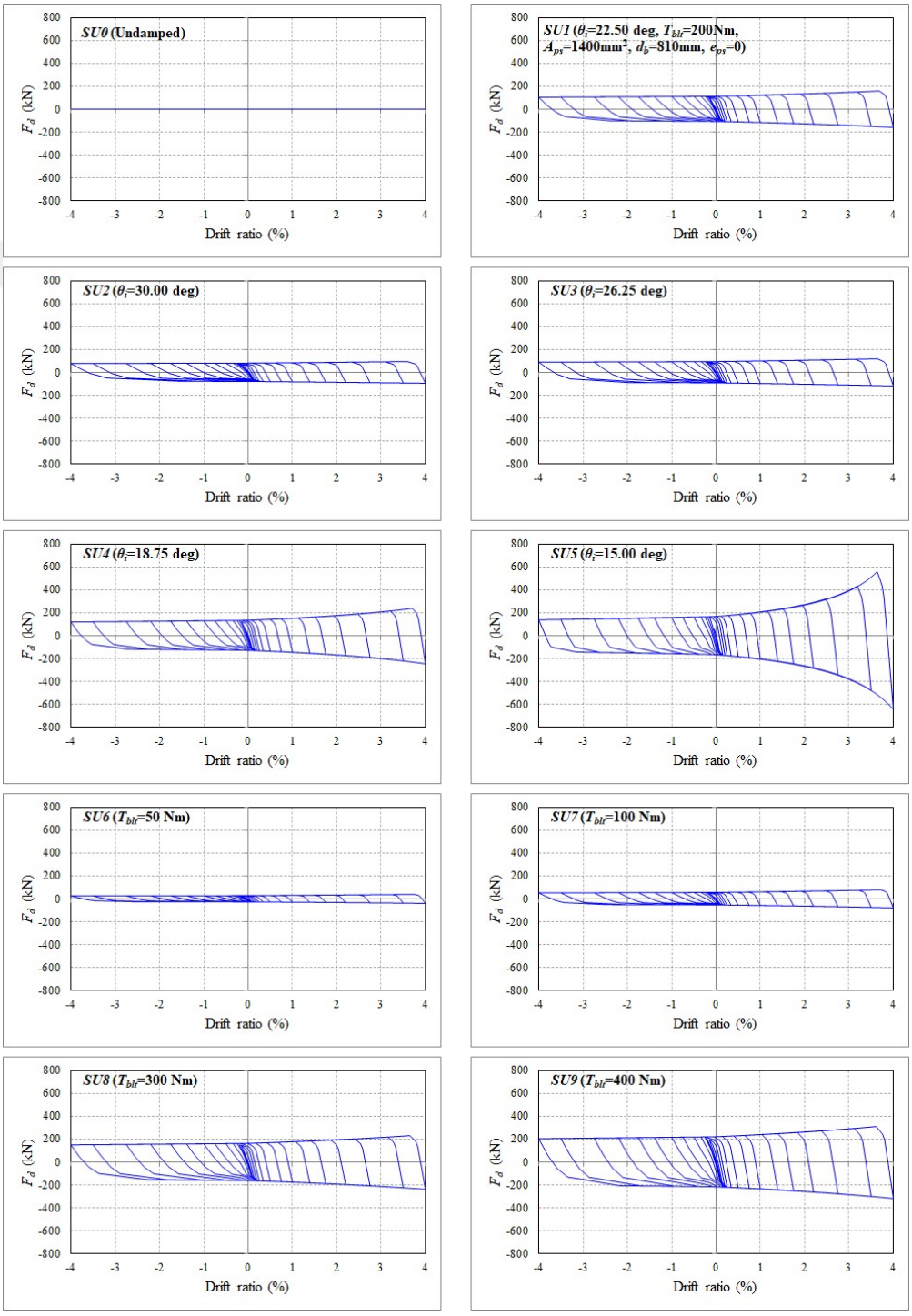

Figure 3.24. Damper force vs. drift ratio plots for sub-assembly 0 through 9.

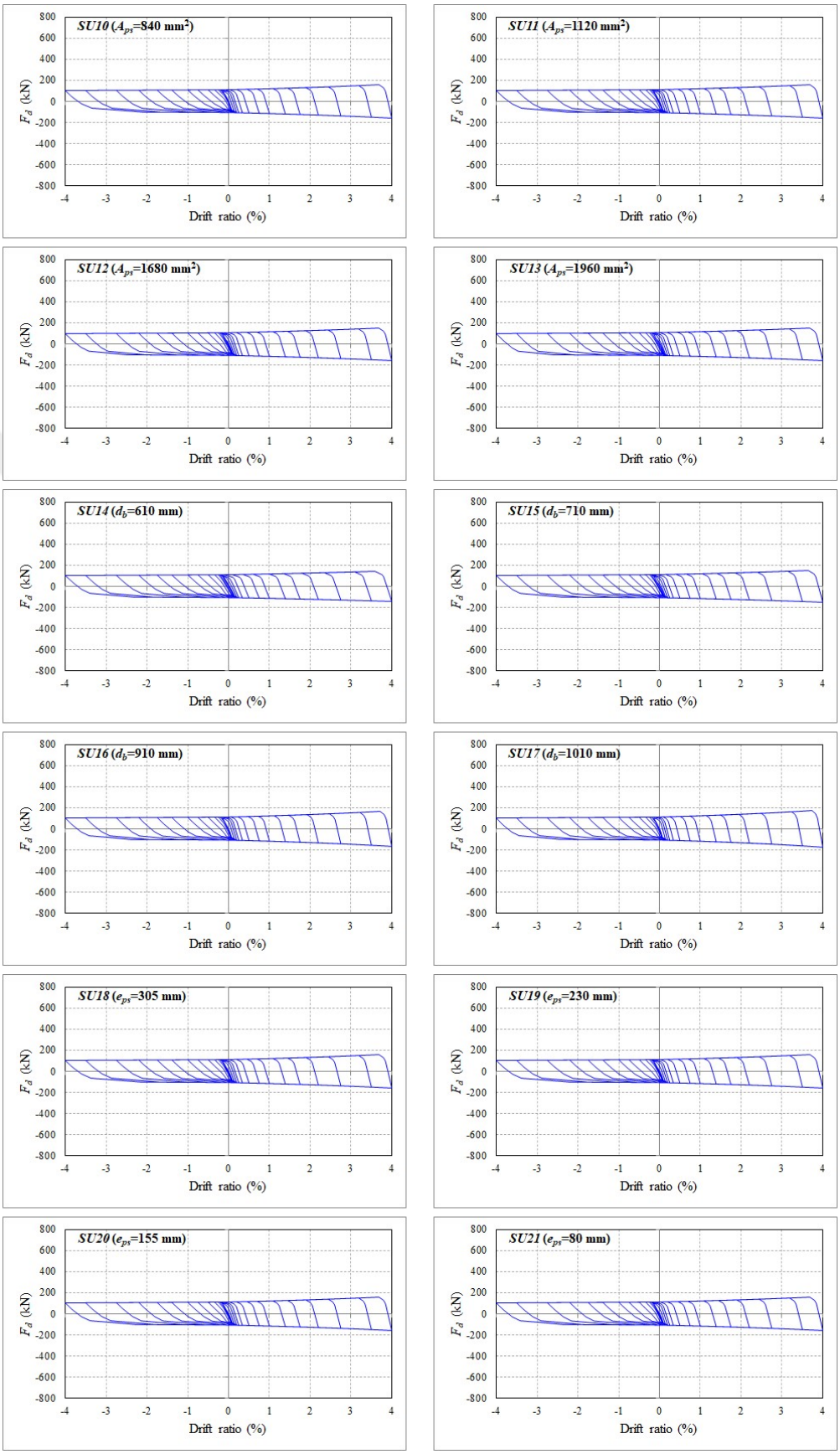

Figure 3.25. Damper force vs. drift ratio plots for sub-assembly 10 through 21.

3.3. Frame-Level Analyses

In order to investigate the effect of the proposed damper mechanism on the cyclic response of precast post-tensioned concrete structural buildings, numerical analyses are conducted on parametric frames. The properties of the frame used in the analyses are taken from [21], in which Morgen and Kurama perform parametric analyses on the frame. The exterior load-bearing frame of a typical precast office building in the East-West direction, which is the reference frame for the numerical analyses, is shown in Figure 3.26. All dimensions in the figure are in millimeters.

The building has four lateral load resisting frames at its parameters, two in East-West direction and two in North-South direction. The investigated frame is the East-West direction frame. The lateral load resisting system consists of precast concrete columns and precast concrete beams connected with unbonded post-tensioning tendons anchored at ends of the frame. Precast concrete double Tees constitute the gravitational load bearing system. There is also a layer of topping concrete with 64mm thickness. The columns have depth of 965mm and width of 710mm. The width of beams is 610mm for all stories. The depth of beams is 1220mm for first and second stories, 1015mm for third and fourth stories, 810mm for fifth and sixth stories.

A total of six frames are investigated in this study. F_0 is the frame in which no damper mechanism is used. F_{st} is the "strengthened" F_0 by addition of 40 couples of damper mechanisms. $F_{20D\text{-}1/4}$ is the frame with 20 damper couples which is designed to have a relative energy dissipation ratio β of approximately 0.250 for $\pm$3.50% roof drift. $F_{40D\text{-}1/4}$ and $F_{40D\text{-}1/8}$ are the frames with 40 damper couples which is designed to have a relative energy dissipation ratio β of approximately 0.250 and 0.125 for $\pm$3.50% roof drift, respectively. The post-tensioning tendons and damper bolt torques of frames except for F_{st} are designed so that they have similar force capacities for 0.50% roof drift. A "damper couple" indicates two dampers placed symmetrically at top and bottom parts of the beam. F_{hyb} is the 'hybrid' frame in which additional mild steel rebars are used at top and bottom parts of the beams. The damper configurations for the investigated frames are shown in Figure 3.27.

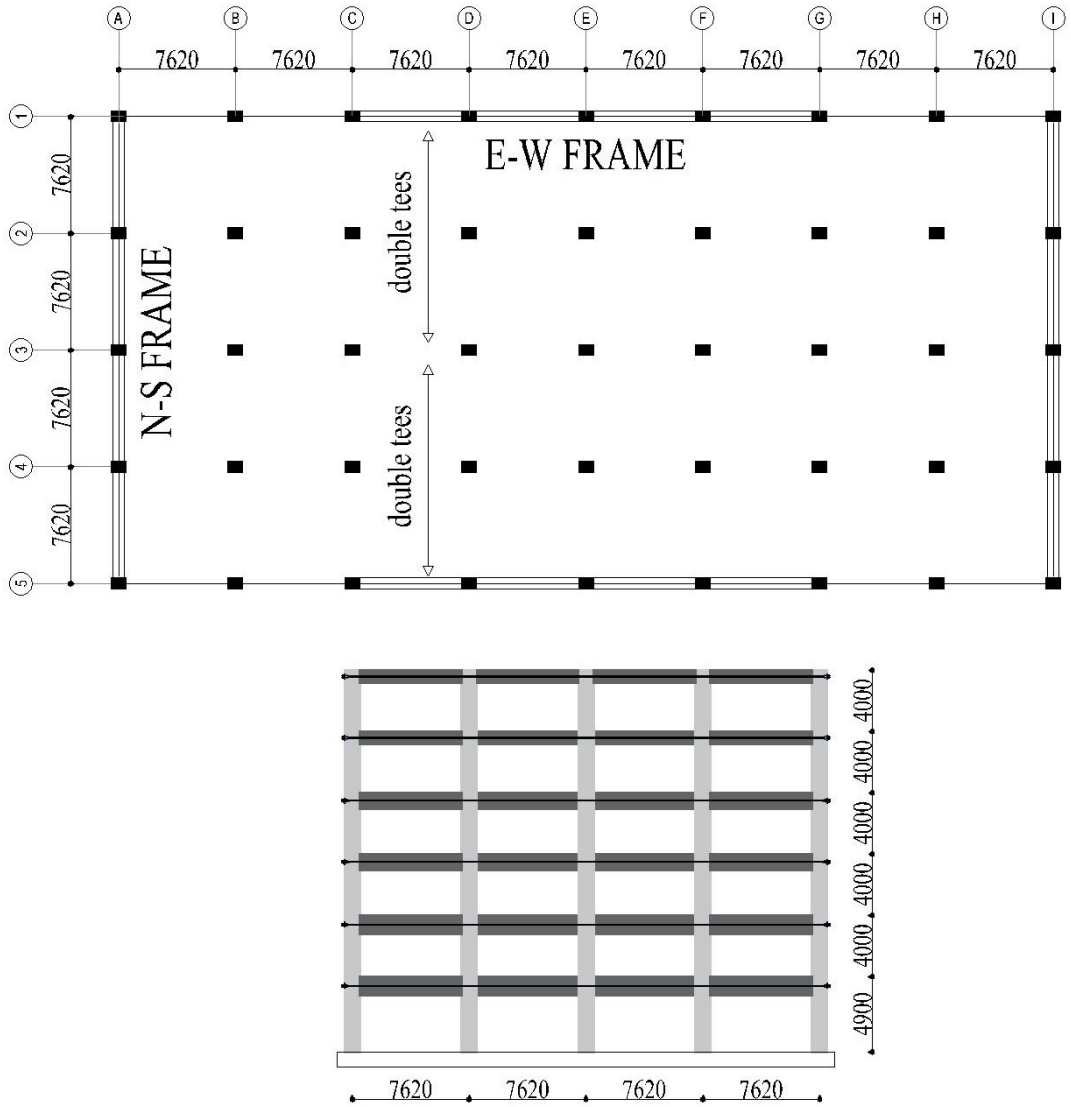

Figure 3.26. Plan of the prototype building and section of the analyzed frame.

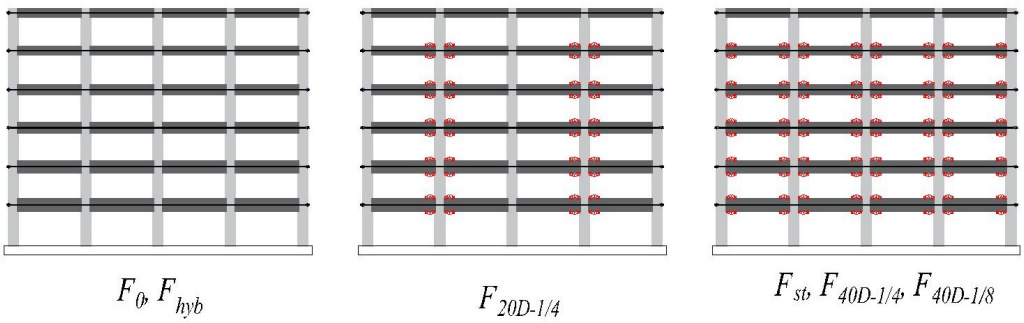

Figure 3.27. Damper configurations for investigated frames.

The parameters for the investigated frames are shown in Table 3.5. The post-tensioning tendons for all the frames are placed at mid-height of the beam. The post-tensioning tendon areas and the damper bolt torques are designed to achieve force capacities that are similar for 0.50% roof drift ratio demand. For hybrid frame F_{hyb} in which mild steel rebars are used at top and bottom parts of beam-column joints in addition to post-tensioning tendons placed at mid-height of the beam, the total area of the mild steel rebars are 0.5% of the cross-sectional area of the beam at the relevant joint.

Table 3.5. Analysis parameters for investigated frames

Floor	1	2	3	4	5	6
Member dimensions (mm)						
Columns	710/965					
Beams	610/1220	610/1220	610/1015	610/1015	610/810	610/810
Post-tensioning tendon area A_{ps} (mm^2)						
F_0	7942	7024	7264	5174	3304	1490
F_{st}	7942	7024	7264	5174	3304	1490
$F_{20D\text{-}1/4}$	4901	4615	4639	3523	2378	1490
$F_{40D\text{-}1/4}$	4520	4200	4463	3161	2081	1490
$F_{40D\text{-}1/8}$	6026	5600	5950	4214	2936	1490
F_{hyb}	4218	3920	4165	2950	1942	1490
Damper bolt torques T_{blt} (Nm)						
F_0	0	0	0	0	0	0
F_{st}	1587	1508	1349	1111	714	0
$F_{20D\text{-}1/4}$	4232	4020	3598	2962	1904	0
$F_{40D\text{-}1/4}$	2116	2010	1799	1481	952	0
$F_{40D\text{-}1/8}$	265	251	224	185	120	0
F_{hyb}	0	0	0	0	0	0

The bolt torques values shown in Table 3.5 are defined in analysis as T_{fr}, as was the case in numerical analyses for the damper mechanism and sub-assemblies. The details of the damper mechanism used in the analyses are shown in Figure 3.28, in which all dimensions are shown in millimeters. The damper mechanism consists of 30mm thick and 250mm wide plates, connected using bolts with diameter of 36mm. The initial angle θ_i is 15 degrees.

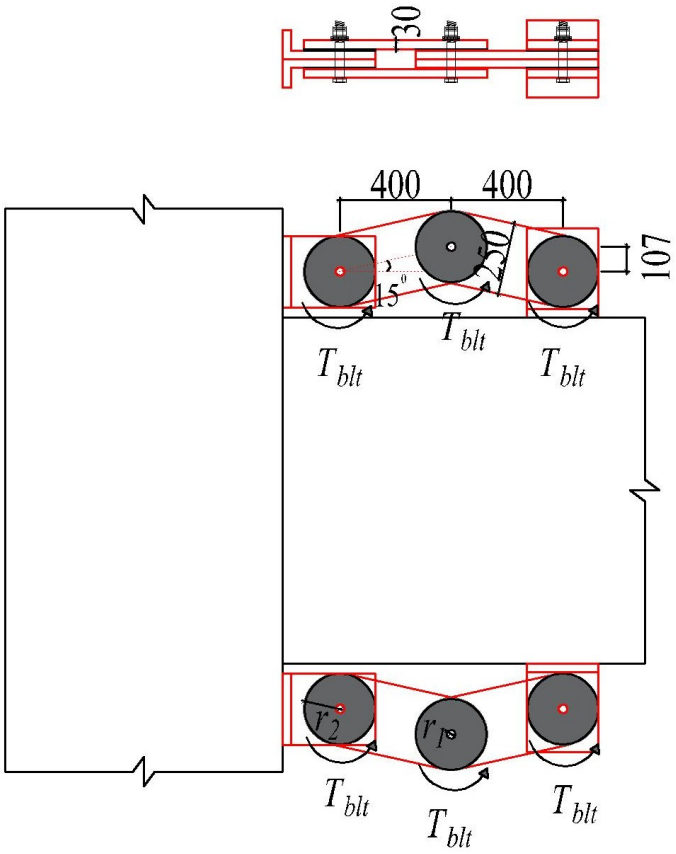

Figure 3.28. Details for damper mechanism used in frame analyses.

An example calculation for T_{fr} using bolt torque T_{blt}=2116Nm using Equation 3.1, Equation 3.2 and Equation 3.3, is made as

$$N_{blt} = \frac{2116\text{Nm}}{(0.20)(0.036\text{m})} = 293.9\text{kN},$$

$$p = \frac{2\text{x}293888\text{N}}{\pi(125\text{mm}^2 - 18\text{mm}^2)} = 12.23\text{MPa},$$

$$T_{fr} = \frac{2}{3}\pi(0.40)(2)(12.23\text{MPa})(125\text{mm}^3 - 18\text{mm}^3) = 40\text{kNm}.$$

3.3.1. Principles and Verification of Numerical Model

The numerical modeling principles for the frame is the same with sub-assemblies, with the exception of gravitational loadings applied to the joints of the beam. Since OpenSEES does not support distributed loading, gravitational loads due to dead and live loads are applied to the defined nodes of the beam, taking into account the load span between those nodes. The numerical modeling principles for the frame are outlined in Figure 3.29.

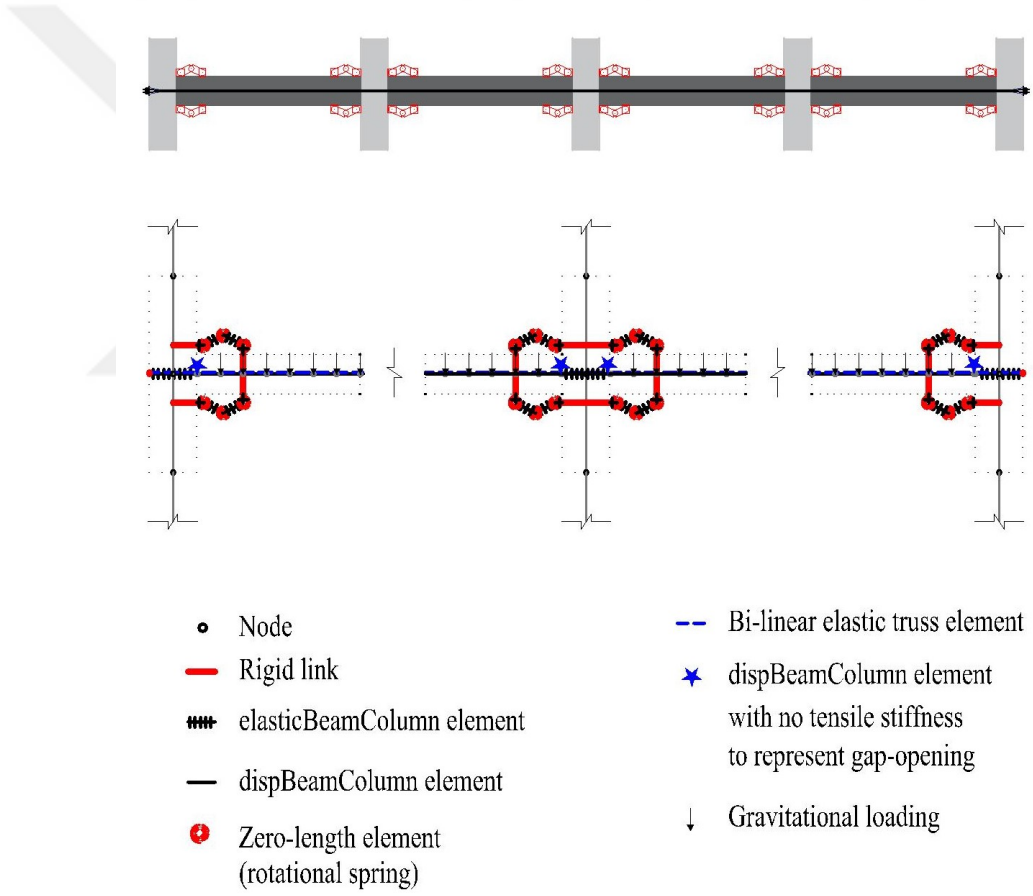

Figure 3.29. Numerical modeling principles for the frames.

The aforementioned numerical modeling principles are verified with results from Morgen and Kurama [21] and shown in Figure 3.30. It can be seen that the results are very close to eachother.

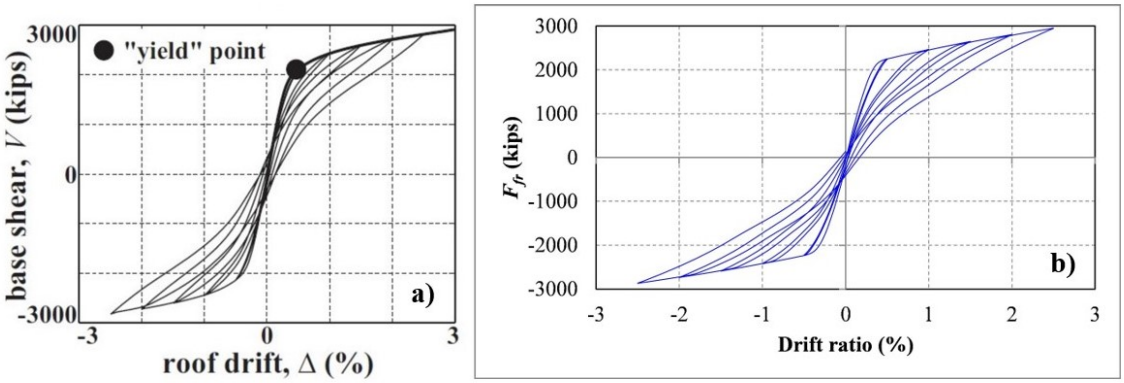

Figure 3.30. Comparison of frame results for a) Morgan and Kurama [21] b) this study.

3.3.2. Frame Analysis Parameters

The response parameters with which the frames are evaluated are the same as those for sub-assembly analyses, namely base shear F_{fr} and relative energy dissipation ratio β, with the exception of labeling, in which frames are labeled with the subscript $_{fr}$ rather than $_{sa}$.

The roof of the frame is subjected to a cyclic displacement protocol that corresponds to ±0.50%, ±1.00%, ±2.00% and ±3.50% drift ratios δ_{fr}, respectively.

An additional indicator of energy dissipation capacity, equivalent viscous damping is also calculated for frame-level analyses. The equivalent viscous damping ξ_{eq}, defined by Chopra [2], is illustrated in Figure 3.31 and is expressed as

$$\xi_{eq} = \frac{A_h}{4\pi A_{so}}, \tag{3.6}$$

where ξ_{eq} is the viscous damping and A_{so} is the strain energy which is expressed as

$$A_{so} = \frac{k_{in}\delta_{fr}^2}{2}. \tag{3.7}$$

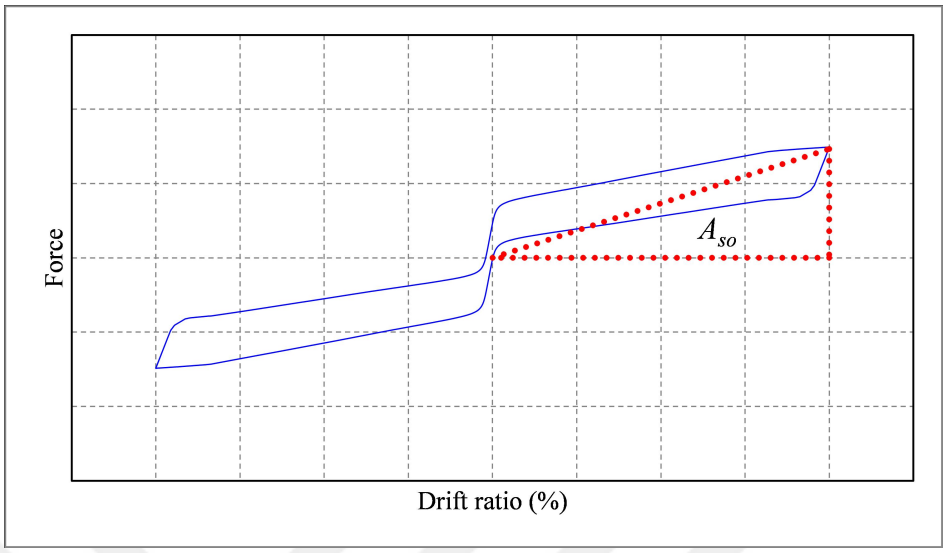

Figure 3.31. Equivalent viscous damping ξ_{eq}.

3.3.3. Base Shear

Table 3.6 shows the base shear values calculated for the frames. Figure 3.32 shows the base shear F_{fr} vs roof drift δ_{fr} plots.

Table 3.6. Base shear values

Base shear, F_{fr} (kN)				
Roof drift, δ_{fr} (%)	+0.50%	+1.00%	+2.00%	+3.50%
F_0	10798	12163	13934	15851
F_{st}	12303	14240	16391	19814
$F_{20D\text{-}1/4}$	10908	12231	14121	17565
$F_{40D\text{-}1/4}$	10410	11706	14091	18440
$F_{40D\text{-}1/8}$	10247	11413	13313	15828
F_{hyb}	10534	11845	13217	14441

The base shear values for F_0, $F_{20D\text{-}1/4}$, $F_{40D\text{-}1/4}$, $F_{40D\text{-}1/8}$ and F_{hyb} are similar except for 3.50% roof drift, which was the intended result of the preliminary design. At 3.50% drift, the base shear for $F_{20D\text{-}1/4}$ and $F_{40D\text{-}1/4}$ are 11% and 16% larger than F_0, respectively. This is because the post-tensioning tendons exceed limit of proportionality

and the stiffness of the frame without damper (F_0) decreases, which was the case observed in sub-assembly analyses. The stiffness of the damper mechanism prevents a significant reduction in global stiffness of the frames after this stage, which is observed in $F_{20D\text{-}1/4}$ and $F_{40D\text{-}1/4}$. The base shear for $F_{40D\text{-}1/4}$ at drift ratio 3.50% is 5% larger than $F_{20D\text{-}1/4}$. This is because at $F_{20D\text{-}1/4}$ the damper mechanisms are not placed at all joints, and as a result when the strain at post-tensioning tendons exceed limit of proportionality the stiffness reduction is more significant.

The addition of damper mechanisms to F_0 increases base shear by 14% for +0.50% roof drift, 17% for +1.00% roof drift, 18% for +2.00% roof drift and 25% for +3.50% roof drift. This is another demonstration of the contribution of dampers to the frame after post-tensioning tendons exceeding limit of proportionality. It can be observed in Figure 3.32 that for all the frames, the residual displacement is tolerable after ±3.50% roof drift demand.

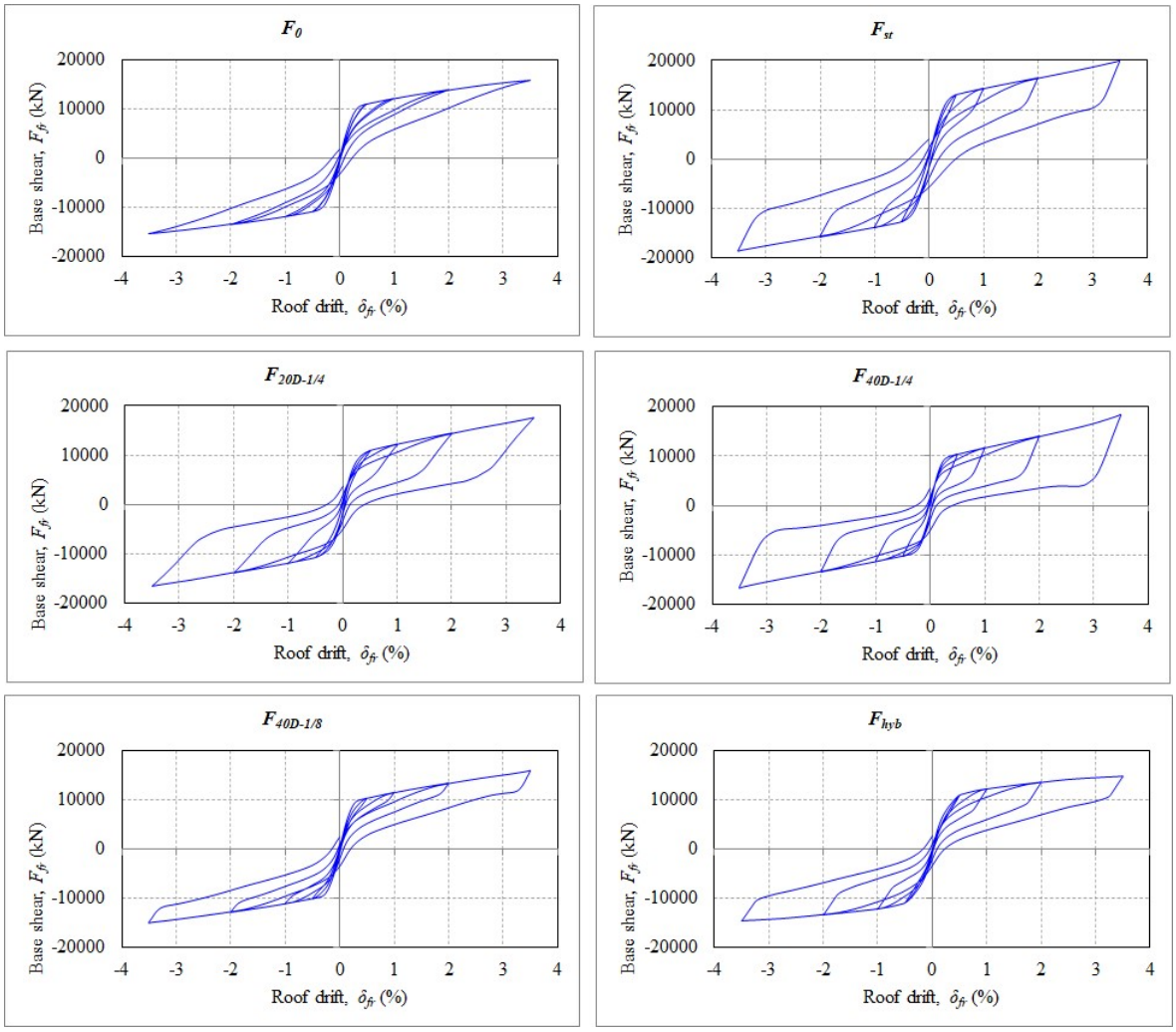

Figure 3.32. Base shear vs roof drift plots for the frames.

3.3.4. Energy Dissipation Parameters

Table 3.7 shows the relative energy dissipation ratio β and equivalent viscous damping ratio ξ_{eq} values calculated for the frames.

Table 3.7. Energy dissipation values for frames

Relative energy dissipation ratio, β					
Roof drift, δ_{fr} (%)	±0.50%	±1.00%	±2.00%	±3.50%	Avg
F_0	0.085	0.073	0.096	0.104	0.090
F_{st}	0.203	0.205	0.225	0.235	0.217
$F_{20D\text{-}1/4}$	0.126	0.195	0.238	0.249	0.202
$F_{40D\text{-}1/4}$	0.234	0.253	0.267	0.274	0.257
$F_{40D\text{-}1/8}$	0.130	0.114	0.133	0.149	0.131
F_{hyb}	0.099	0.164	0.213	0.223	0.175
Equivalent viscous damping ratio, ξ_{eq}					
Roof drift, δ_{fr} (%)	±0.50%	±1.00%	±2.00%	±3.50%	Avg
F_0	0.028	0.034	0.051	0.059	0.043
F_{st}	0.061	0.090	0.117	0.128	0.099
$F_{20D\text{-}1/4}$	0.045	0.093	0.129	0.139	0.101
$F_{40D\text{-}1/4}$	0.086	0.122	0.143	0.149	0.125
$F_{40D\text{-}1/8}$	0.047	0.055	0.072	0.084	0.064
F_{hyb}	0.033	0.076	0.115	0.128	0.088

The undamped frame F_0 does not satisfy the minimum requirement of 0.125 for relative energy dissipation ratio β for all drift ratios. This is an indicator of insufficient energy dissipation capacity of precast post-tensioned concrete structural systems. All other frames with the damper mechanisms satisfy the minimum requirement of β for all roof drift ratios, except for ±1.00% drift ratio for $F_{40D\text{-}1/8}$. The frames with 40 damper couples, F_{st}, $F_{40D\text{-}1/4}$ and $F_{40D\text{-}1/8}$, have larger relative energy dissipation ratios for ±0.50% roof drift ratio compared with the frame with 20 damper couples, $F_{20D\text{-}1/4}$. As roof drift ratio reaches ±2.00%, the β values of the damped frames gets closer to each other. This is another indicator of the amplifying effect of the proposed

damper, since as the imposed displacement on the dampers gets larger, the effect of the dampers on the energy dissipation capacity increases. Since the bolt torque for $F_{20D\text{-}1/4}$ is significantly larger, as the relative rotation demand on its joints increase, its contribution to the force capacity of the system exponentially increases. Hence, the relative energy dissipation ratio gets closer to F_{st} and $F_{40D\text{-}1/4}$. The average β value is largest for $F_{40D\text{-}1/4}$. This is because for smaller roof drift demands, more dampers contribute to energy dissipation for $F_{40D\text{-}1/4}$ compared with $F_{20D\text{-}1/4}$ (0.257 vs. 0.202). The reason $F_{40D\text{-}1/4}$ has larger average β value than F_{st} (0.257 vs. 0.217) is because according to the design, the percentage of contribution of dampers to behaviour of the system is larger for $F_{40D\text{-}1/4}$.

The equivalent viscous damping contribution of $F_{40D\text{-}1/4}$ is the largest, whereas $F_{20D\text{-}1/4}$ and F_{st} have almost the same average ξ_{eq} values. The rapid increase in equivalent viscous damping for $F_{20D\text{-}1/4}$ after $\pm 0.50\%$ roof drift is consistent with β results.

3.3.5. Post-Tensioning Tendon Forces

Figure 3.33 through Figure 3.37 show the plots for post-tensioning tendon forces F_{pt} as a function of roof drift for all 6 stories of the frames. It can be seen that the force at post-tensioning tendons F_{pt} exceeds limit of proportionality at most cases. This is consistent with the results of base shear, for which the stiffness of the frames changed due to the reduced stiffness of the tendons. The roof drift at which this happens changes for each story, because the strain demand imposed by roof drift on the tendons change. As the story height increases, the strain demand increases, and consequently the post-tensioning tendon exceeds limit of proportionality at an earlier stage of roof drift. For example, for $F_{40D\text{-}1/4}$, the stress at tendons exceed limit of proportionality at 2.60% roof drift for second and third stories, 2.35% roof drift for fourth story, 2.20% roof drift for fifth story and 1.95% roof drift for sixth story.

Another parameter that effects the roof drift ratio at which the tendon stresses exceed limit of proportionality is the existence of dampers and the bolt torques. For example, for fifth story, σ_{pt} exceeds limit of proportionality at 2.65% for F_0, at 2.85%

for F_{st}, at 2.45% for $F_{20D\text{-}1/4}$ and at 2.20% for $F_{40D\text{-}1/4}$. The reason that strengthening the frame with dampers (F_0 vs. F_{st}) delays the tendons to exceed limit of proportionality is that the existence of the dampers reduces the amount of gap opening at the joints caused by roof drift. This is an important result since the dampers do not only contribute to energy dissipation and force capacity, but also ensure more efficient use of post-tensioning tendons. This effect, however, cannot be observed in comparison of $F_{20D\text{-}1/4}$ and $F_{40D\text{-}1/4}$, in which the use of more dampers causes the tendons to reach limit of proportionality at an earlier stage. This is due to the fact that although the amount of dampers decrease in $F_{20D\text{-}1/4}$, the bolt torques applied are significantly larger, hence providing significant stiffness and "attracting" loads. As a consequence the relative rotation of the damper at $F_{20D\text{-}1/4}$ are larger, thus the smaller roof drift at which tendons exceed limit of proportionality. This phenomenon is further explained in the next section.

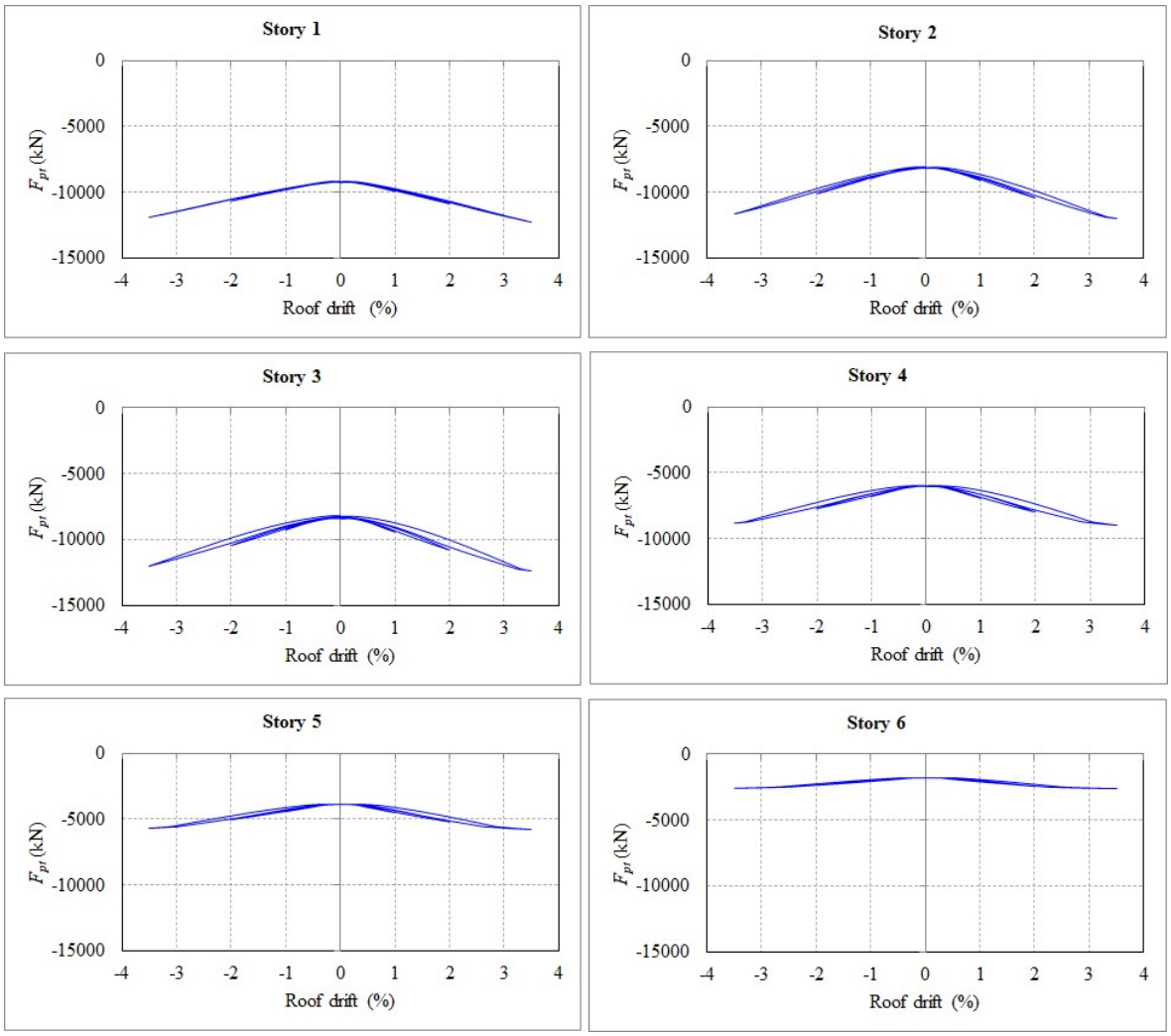

Figure 3.33. Post-tensioning forces for F_0.

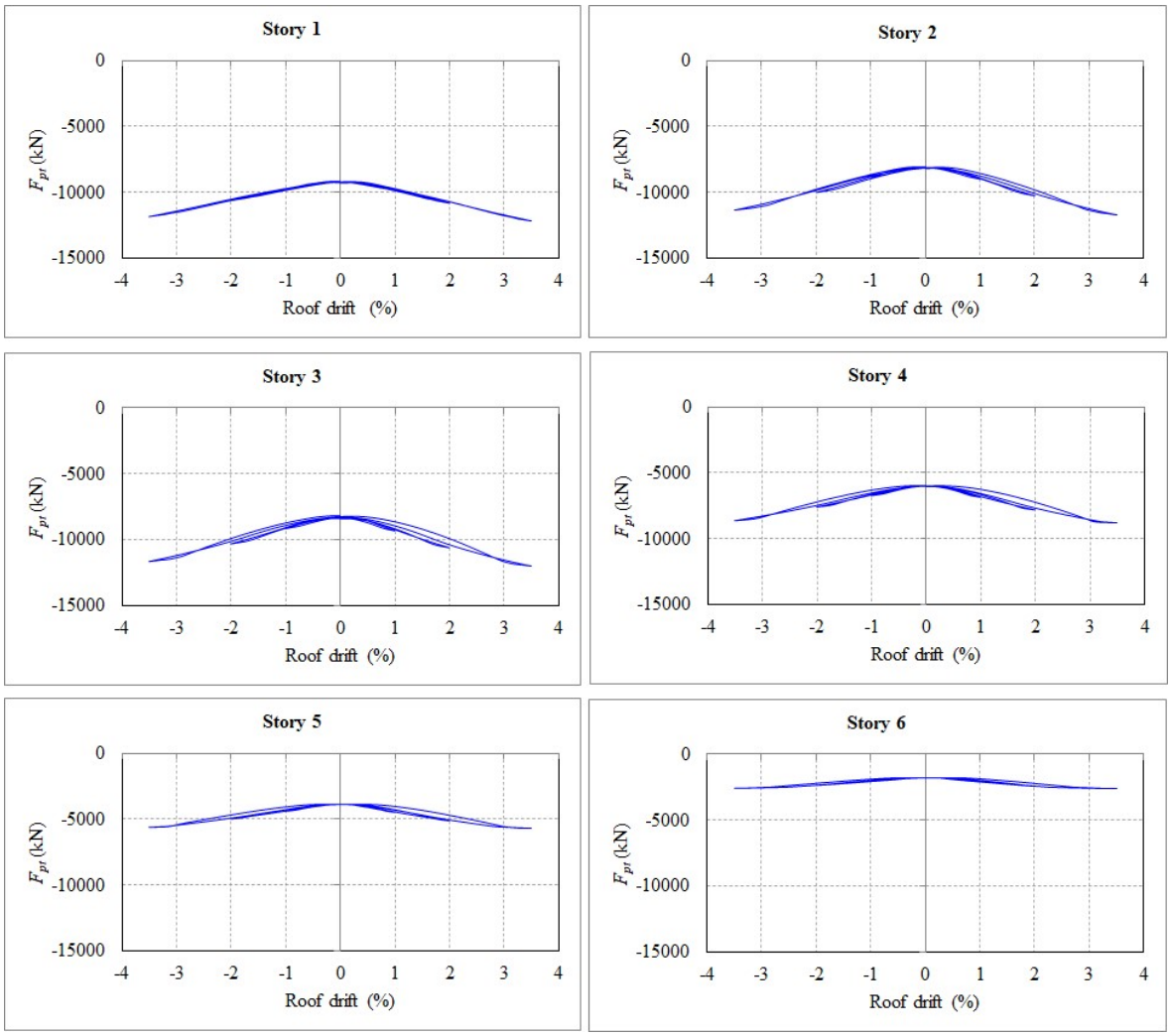

Figure 3.34. Post-tensioning forces for F_{st}.

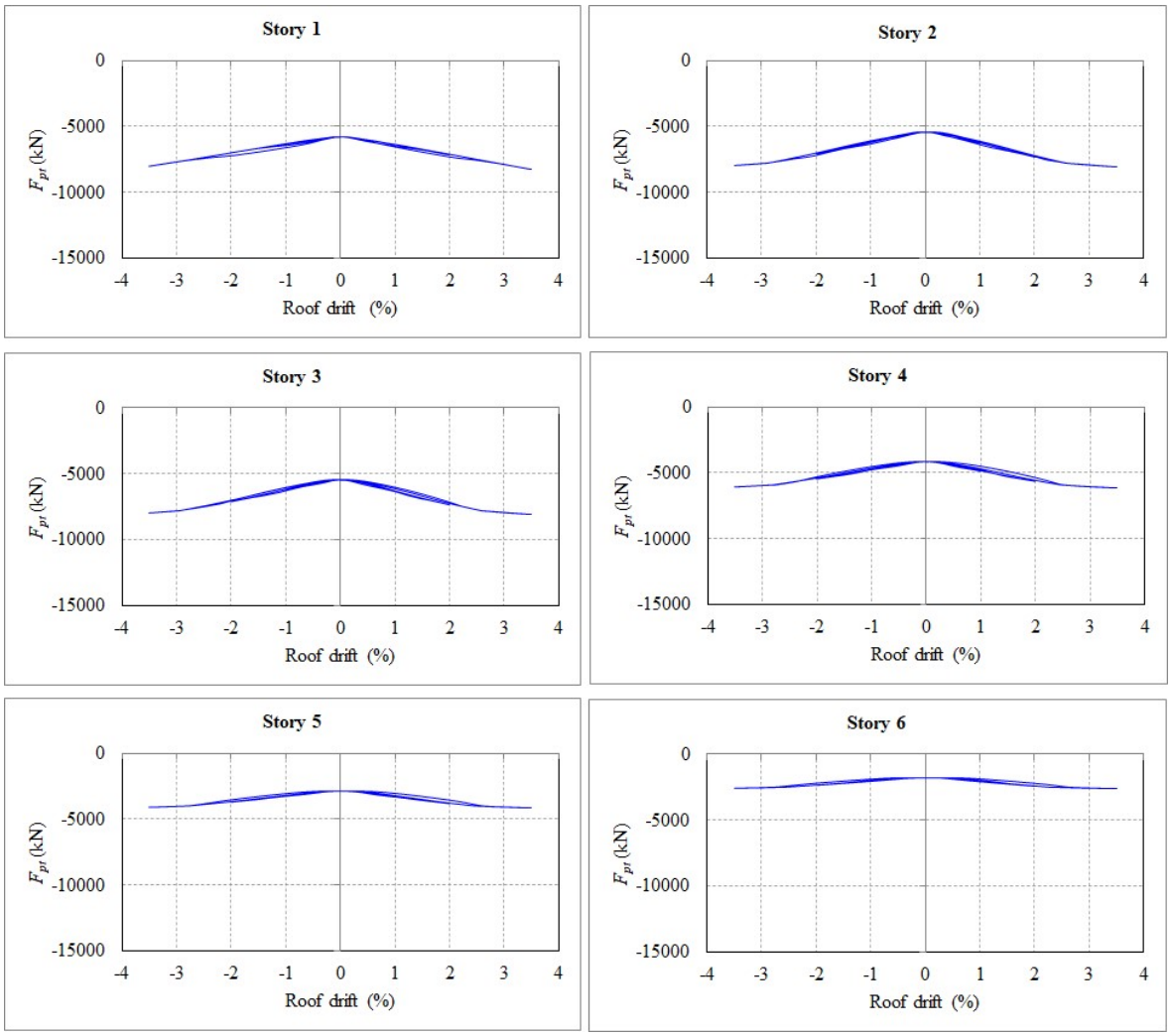

Figure 3.35. Post-tensioning forces for $F_{20D\text{-}1/4}$.

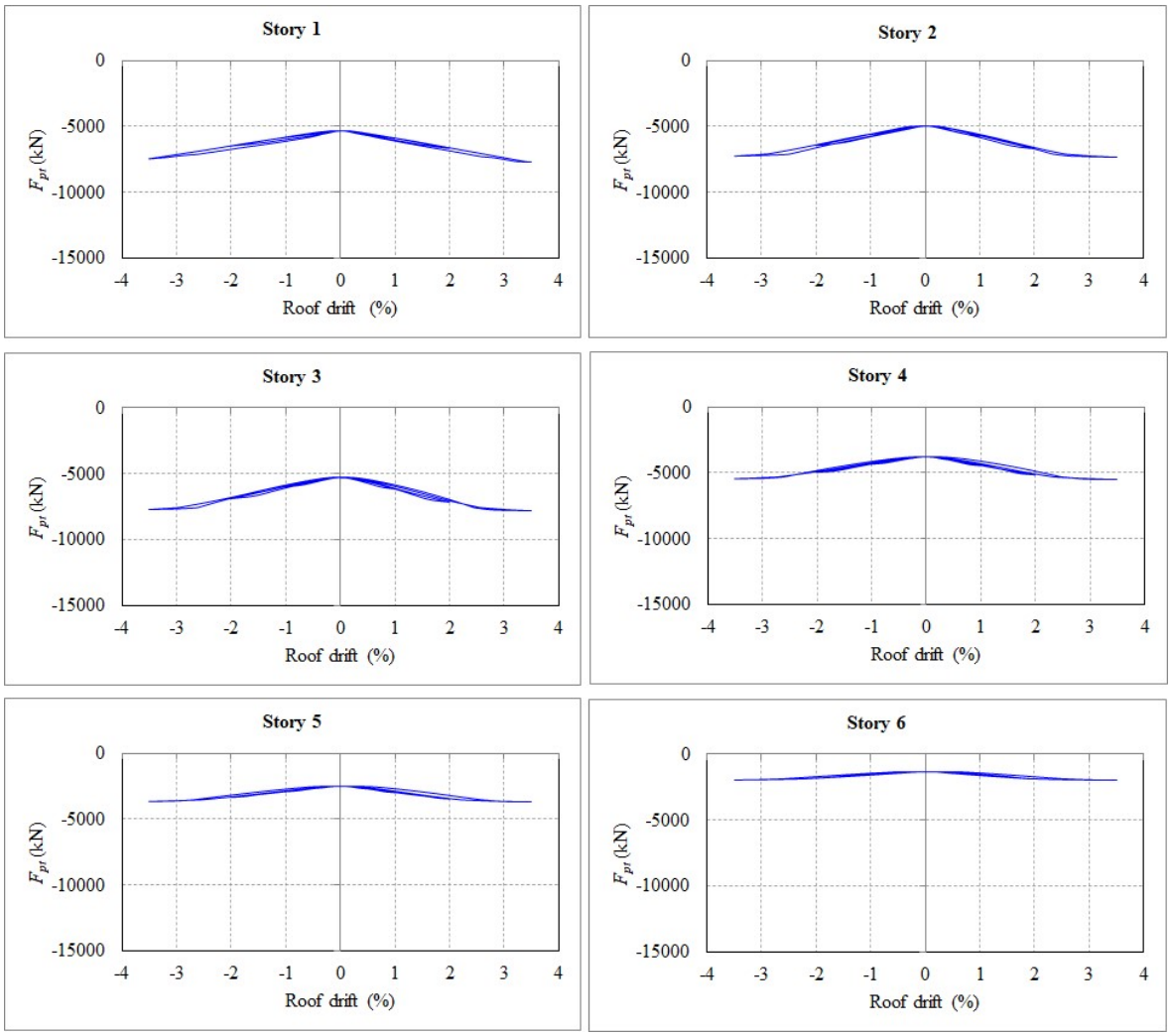

Figure 3.36. Post-tensioning forces for $F_{40D\text{-}1/4}$.

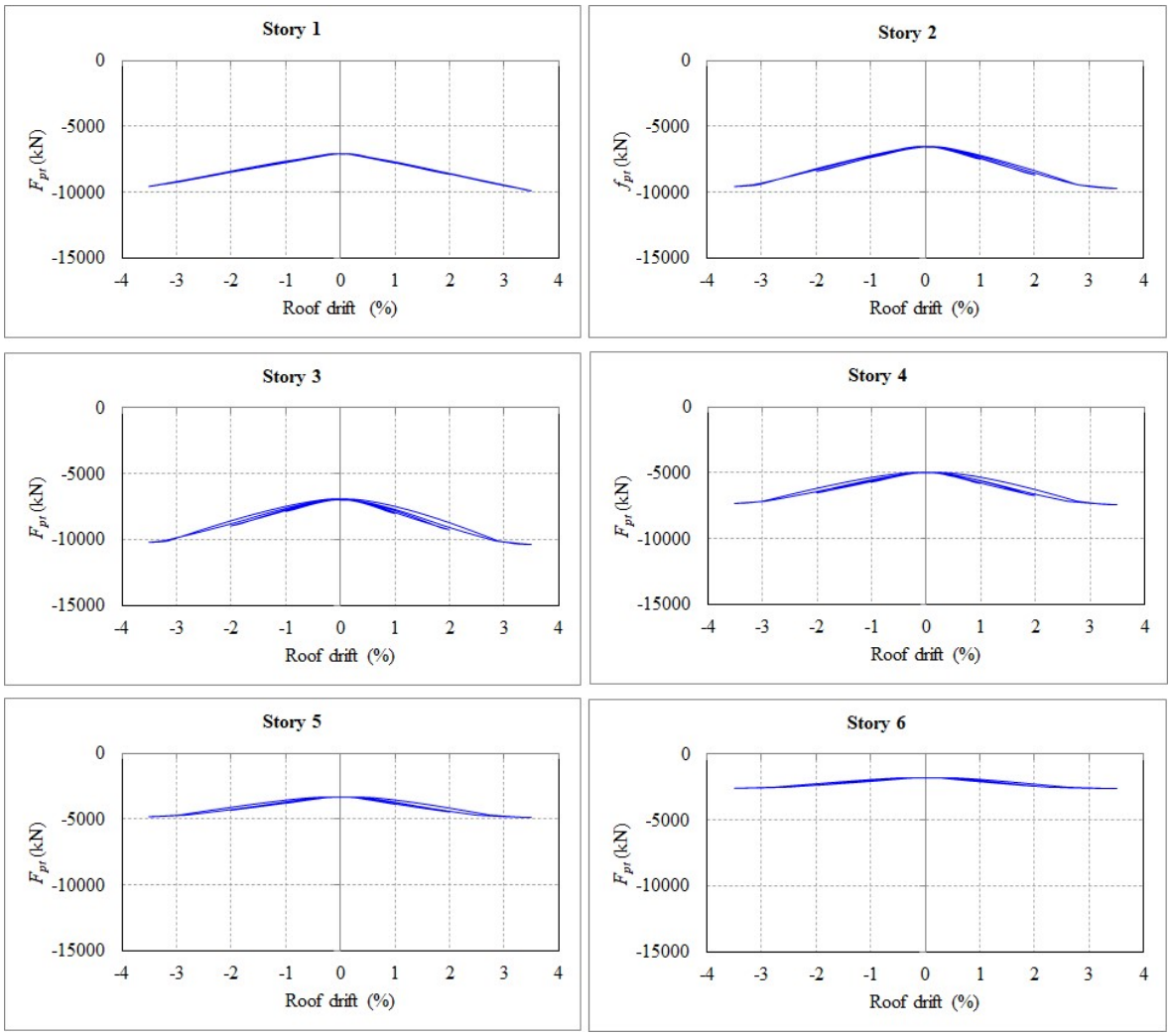

Figure 3.37. Post-tensioning forces for $F_{40D\text{-}1/8}$.

3.3.6. Damper Forces

Figure 3.39 through Figure 3.42 show the plots for damper forces F_d as a function of roof drift for 5 stories of the frames at which dampers are used. The damper force F_d indicates the horizontal force that is transfered by the lower left unit of damper to the second column. Since the initial angle θ_i is small, the vertical damper force is negligibly small.

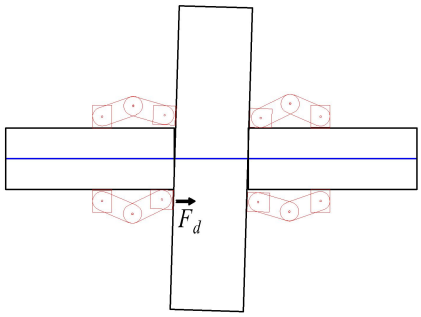

Figure 3.38. Damper force F_d.

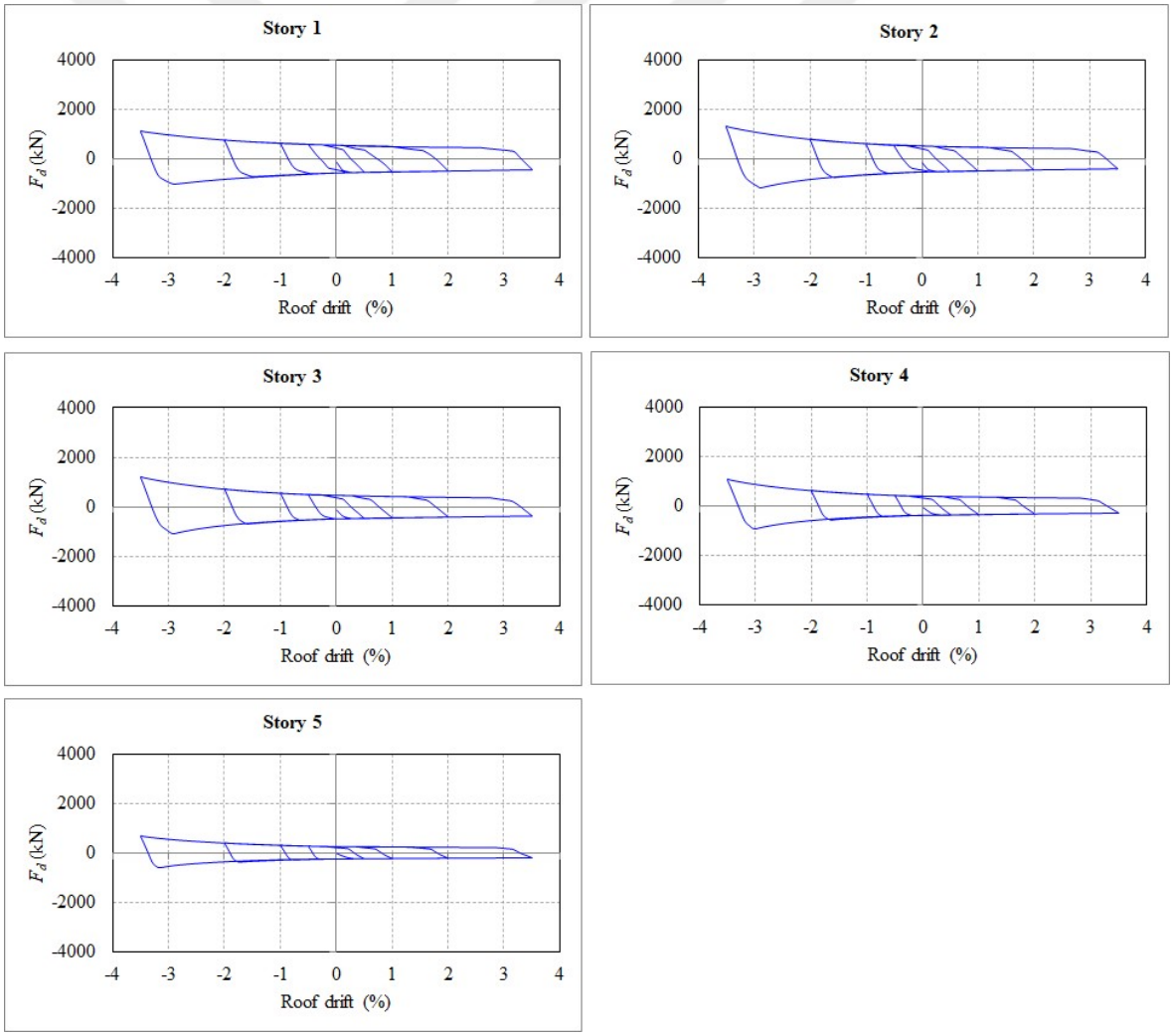

Figure 3.39. Damper forces for F_{st}.

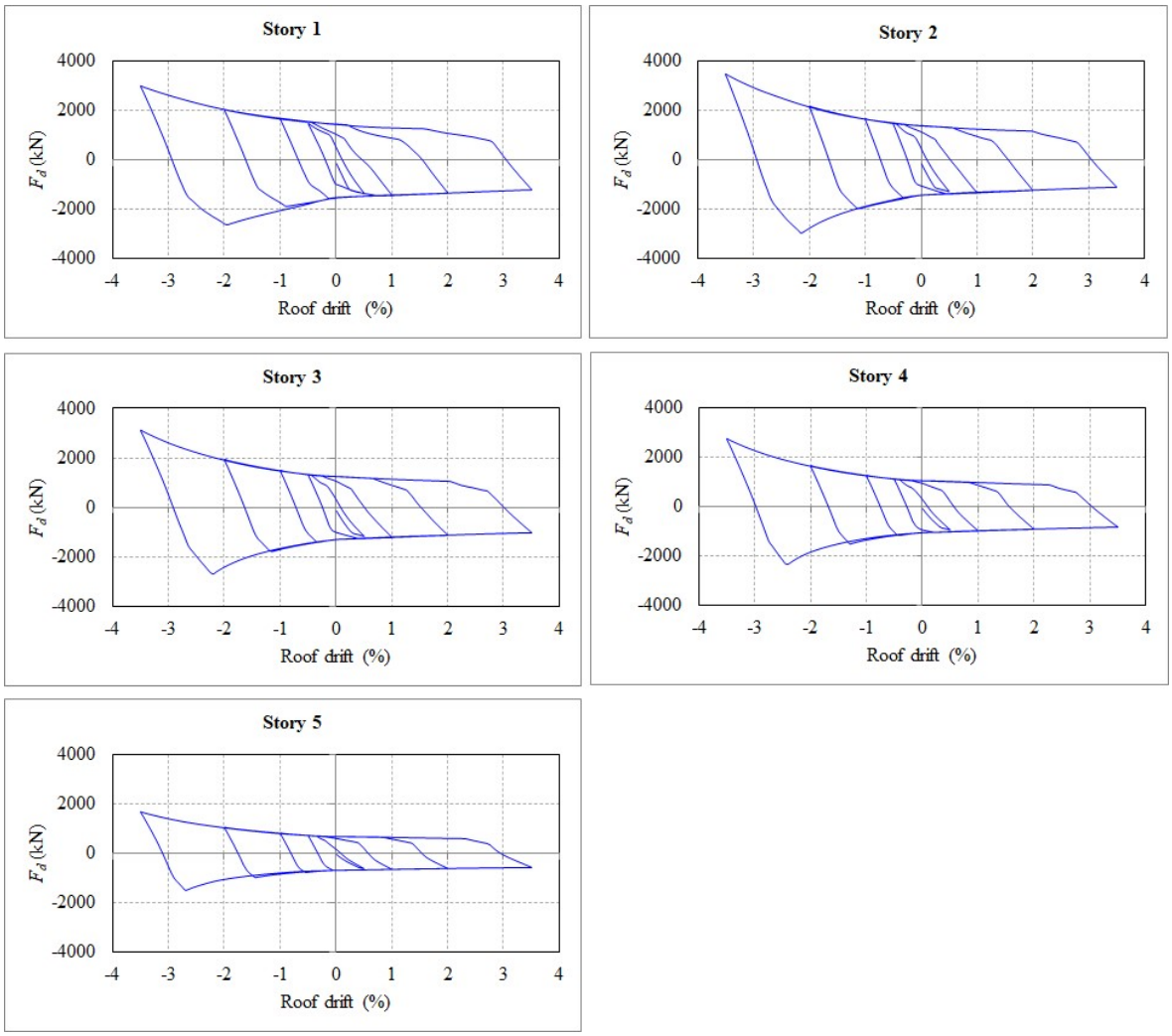

Figure 3.40. Damper forces for $F_{20D\text{-}1/4}$.

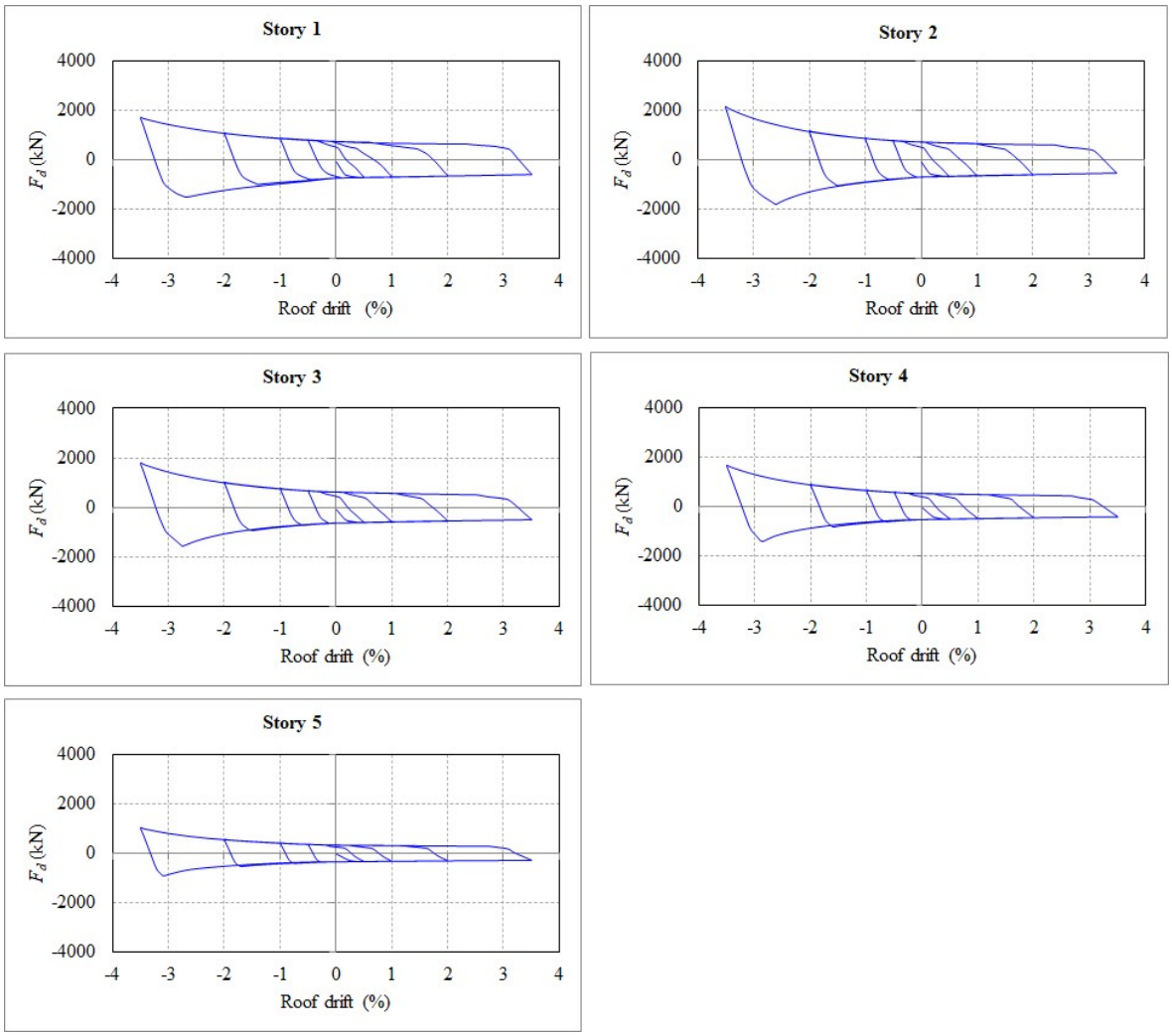

Figure 3.41. Damper forces for $F_{40D\text{-}1/4}$.

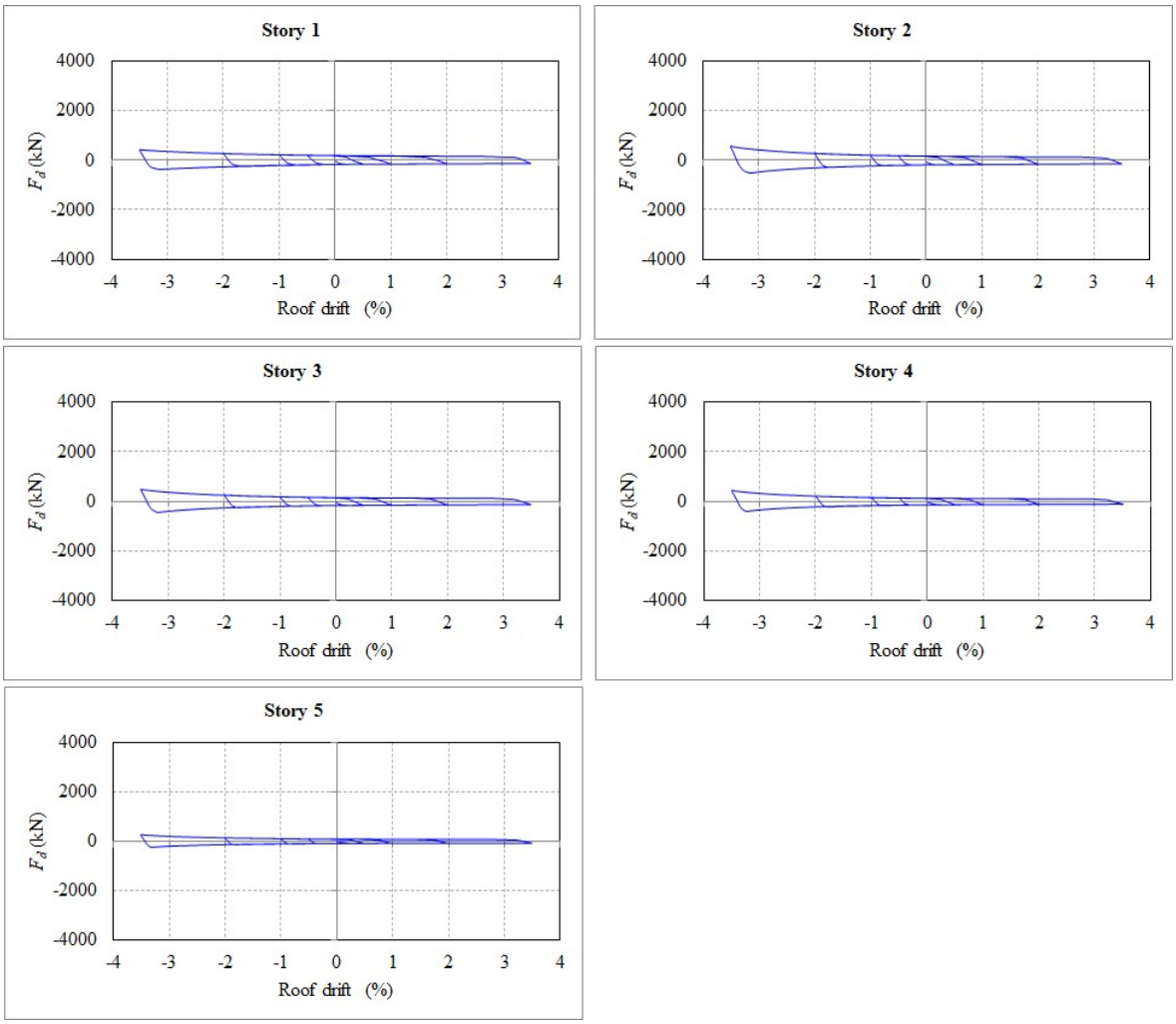

Figure 3.42. Damper forces for $F_{40D\text{-}1/8}$.

The plots for damper force are consistent with the results obtained from damper mechanism and sub-assembly level analyses. As the bolt torques applied increase, the hysteresis loop of the damper increases. Furthermore, as the roof drift increases, the force acting on the damper exponentially increases.

3.4. Time-History (Dynamic) Analyses

In order to investigate the effect of the proposed dampers on the dynamic behavior of precast post-tensioned structures, dynamic response of the frames subjected to earthquake records are obtained. The frames chosen for the analyses are the frame without dampers F_0, the strengthened version of this frame F_{st} and the frame with 40 couples of dampers with a target energy dissipation ratio of 1/8, $F_{40D-1/8}$.

The results obtained from free vibration analyses of these frames are shown in Table 3.8. T_N is natural vibration period and U_X is the modal mass participation ratio for X direction. It can be observed that the change in natural vibration period of the frame with the addition of the dampers is negligible. This indicates that the dampers do not affect the initial stiffness of the frames significantly, thus not causing the frames to be subjected to larger base shears.

Table 3.8. Natural vibration periods (T_N) of the frames

		Mode 1	Mode 2	Mode 3	Mode 4	Mode 5
F_0	T_N (sec)	0.80 sec	0.28 sec	0.16 sec	0.11 sec	0.08 sec
	U_X (%)	86.3	10.4	2.3	0.7	0.2
F_{st}	T_N (sec)	0.76 sec	0.27 sec	0.15 sec	0.10 sec	0.08 sec
	U_X (%)	86.7	10.2	2.2	0.7	0.2
$F_{40D-1/8}$	T_N (sec)	0.77 sec	0.27 sec	0.16 sec	0.10 sec	0.08 sec
	U_X (%)	86.2	10.5	2.3	0.7	0.2

A total of twelve acceleration histories from six past earthquakes are chosen for dynamic analyses of these frames. For each earthquake, two horizontal components perpendicular to each other are applied (East-West, North-South directions). The earthquakes used in time-history analyses are listed in Table 3.9. The acceleration histories and elastic spectra for each record are shown in Figure 3.43 and Figure 3.44.

Table 3.9. Earthquakes used in time-history analyses

No	Location	Direction	Year	Magnitude	Depth(km)	PGA(g)
1	Coyote Lake, USA	E-W	1979	5.7	8.0	0.422
2	Coyote Lake, USA	N-S	1979	5.7	8.0	0.319
3	Düzce, Türkiye	E-W	1999	7.1	14.0	0.404
4	Düzce, Türkiye	N-S	1999	7.1	14.0	0.515
5	Erzincan, Türkiye	E-W	1992	6.7	9.0	0.496
6	Erzincan, Türkiye	N-S	1992	6.7	9.0	0.387
7	Imperial Valley, USA	E-W	1979	6.5	10.0	0.447
8	Imperial Valley, USA	N-S	1979	6.5	10.0	0.449
9	Kobe, Japan	E-W	1995	6.9	17.9	0.483
10	Kobe, Japan	N-S	1995	6.9	17.9	0.464
11	Loma Prieta, USA	E-W	1989	6.9	17.5	0.559
12	Loma Prieta, USA	N-S	1989	6.9	17.5	0.368

The acceleration histories of the earthquakes are scaled with the principle that the average value of the elastic spectrum for all the earthquakes within the range of $0.2T_N$ and $1.5T_N$, where T_N is the first natural vibration period of the frame, is not smaller than the elastic response spectrum of the frame for the given seismicity. The scale factor is found as 1.458 and the spectra are shown in Figure 3.45.

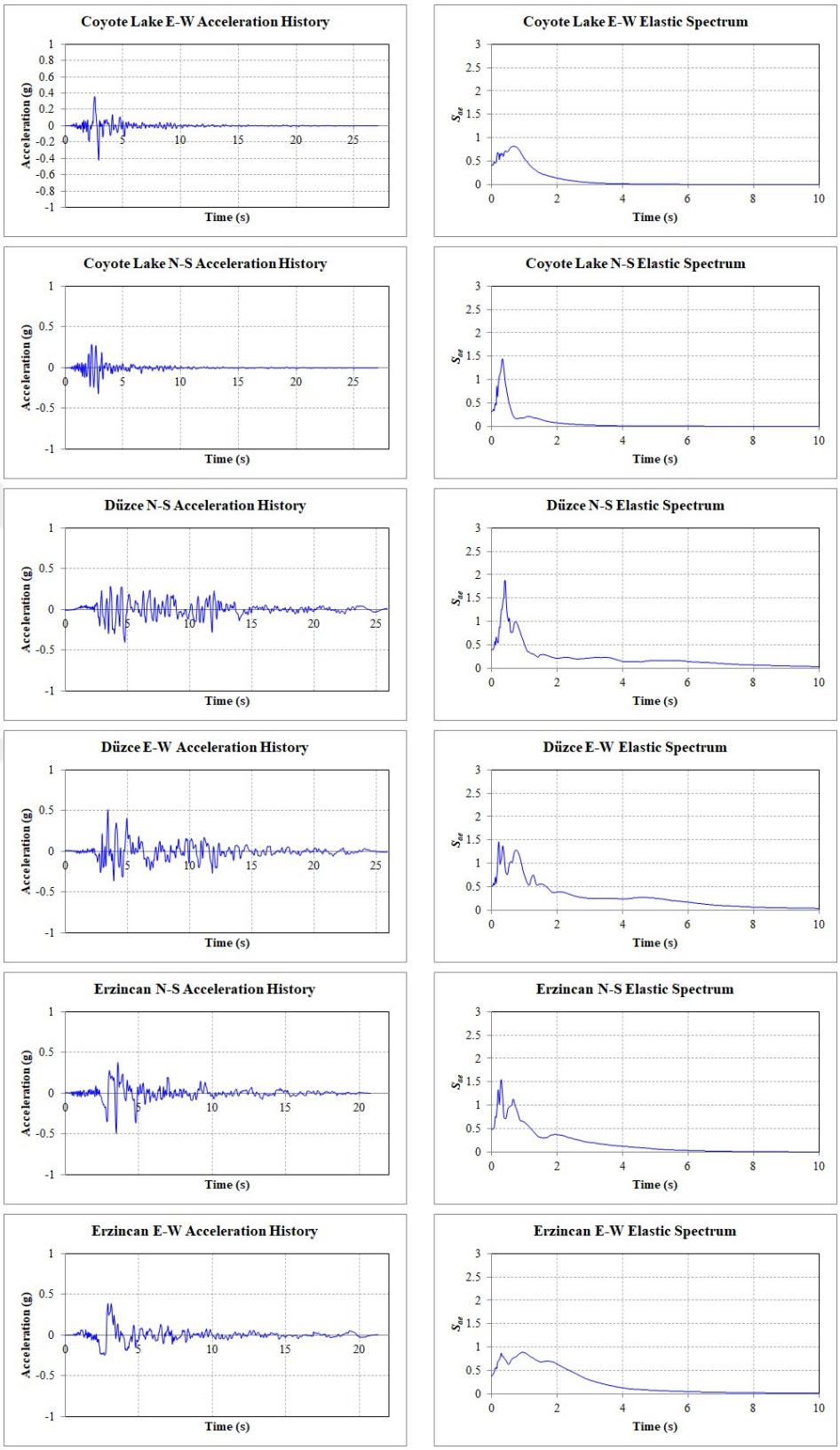

Figure 3.43. Acceleration history and elastic spectra for Coyote Lake, Düzce and Erzincan earthquakes.

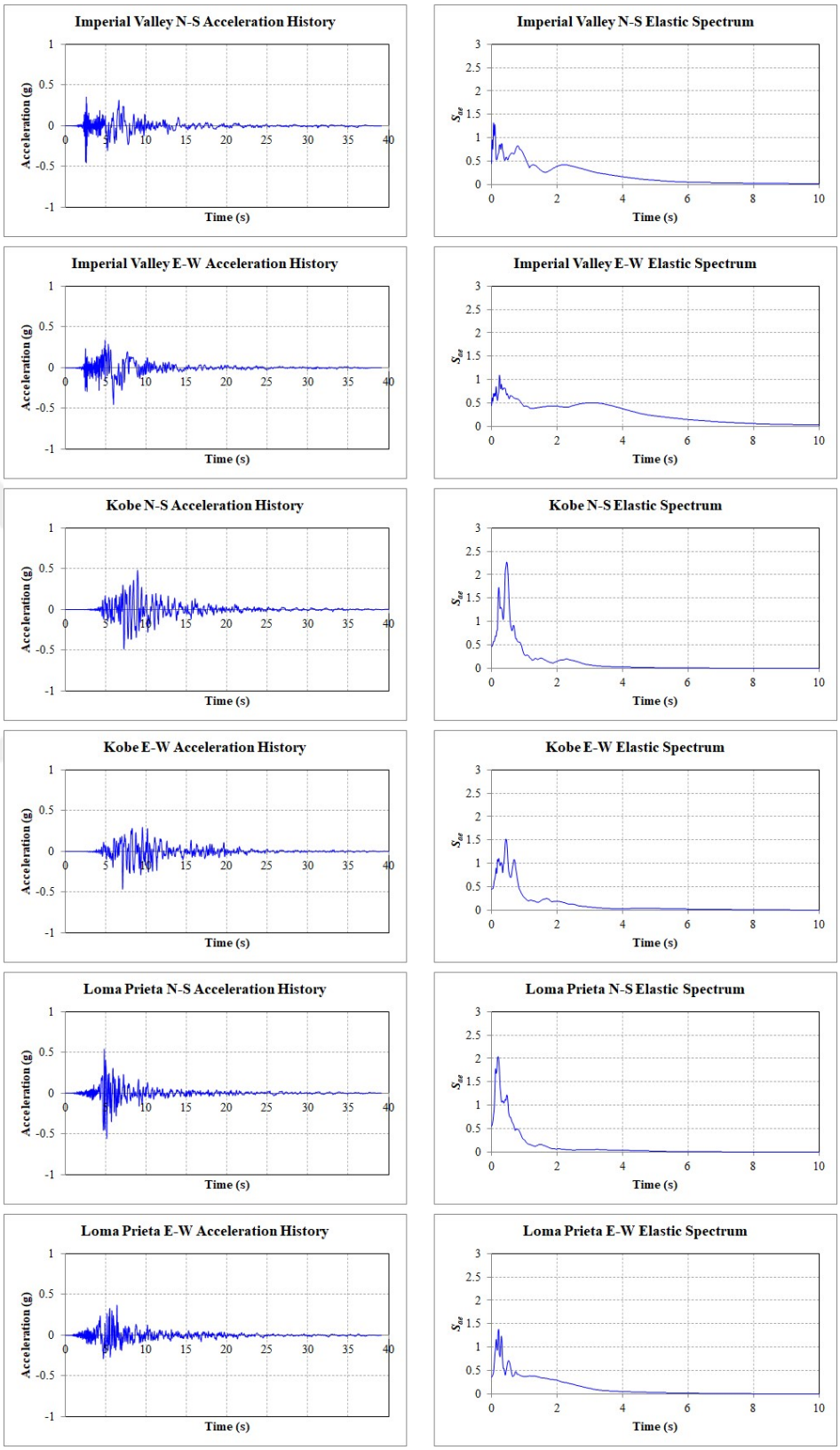

Figure 3.44. Acceleration history and elastic spectra for Imperial Valley, Kobe and Loma Prieta earthquakes.

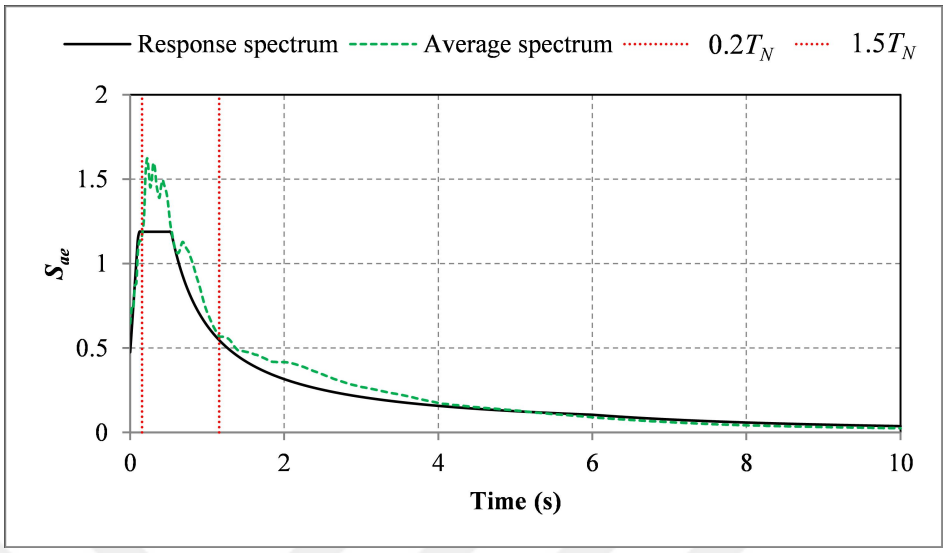

Figure 3.45. Scaling of acceleration histories of earthquakes.

The maximum story drifts obtained from dynamic analyses for the twelve acceleration records and their average values are shown in Table 3.11 through Table 3.13. The comparison of the story drifts undergone by the three frames are summarized in Table 3.10. For each frame in Table 3.10, 'Ave' indicates the average drift value for twelve records, 'Max' indicates the drift value for the record with the largest effect (Erzincan (E-W)). Base shear values obtained from dynamic analyses for the twelve acceleration records and their average values are shown in Table 3.14.

Table 3.10. Comparison of story drifts (%)

		1	2	3	4	5	6	Roof
F_0	Ave	1.42	1.17	1.00	0.85	0.71	0.54	0.90
	Max	3.89	2.93	2.19	1.61	1.09	0.81	2.12
F_{st}	Ave	1.35	1.00	0.82	0.70	0.61	0.46	0.81
	Max	3.53	2.33	1.64	1.17	0.85	0.64	1.75
$F_{40D-1/8}$	Ave	1.28	1.05	0.90	0.78	0.67	0.49	0.84
	Max	3.44	2.57	1.92	1.39	0.96	0.69	1.87

Table 3.11. Maximum story drifts for F_0 (%)

	1	2	3	4	5	6	Roof
Coyote Lake (N-S)	1.59	1.38	1.16	0.92	0.69	0.50	1.04
Coyote Lake (E-W)	0.48	0.34	0.28	0.46	0.60	0.51	0.32
Düzce (N-S)	0.88	0.77	0.86	0.87	0.83	0.65	0.75
Düzce (E-W)	2.12	1.76	1.37	1.04	0.82	0.62	1.27
Erzincan (N-S)	1.48	1.40	1.15	0.86	0.66	0.48	0.83
Erzincan (E-W)	3.89	2.93	2.19	1.61	1.09	0.81	2.12
Imperial Valley (N-S)	1.58	1.26	0.96	0.87	0.73	0.55	0.94
Imperial Valley (E-W)	1.76	1.37	1.01	0.77	0.61	0.45	1.00
Kobe (N-S)	0.76	0.69	0.78	0.67	0.59	0.48	0.59
Kobe (E-W)	0.68	0.55	0.73	0.79	0.70	0.52	0.61
Loma Prieta (N-S)	0.68	0.65	0.64	0.58	0.64	0.50	0.55
Loma Prieta (E-W)	1.10	0.92	0.80	0.68	0.57	0.40	0.75
Average	**1.42**	**1.17**	**1.00**	**0.85**	**0.71**	**0.54**	**0.90**

Table 3.12. Maximum story drifts for F_{st} (%)

	1	2	3	4	5	6	Roof
Coyote Lake (N-S)	1.47	1.09	0.89	0.73	0.59	0.44	0.88
Coyote Lake (E-W)	0.43	0.26	0.24	0.32	0.40	0.34	0.23
Düzce (N-S)	0.89	0.81	0.85	0.84	0.76	0.59	0.77
Düzce (E-W)	2.12	1.56	1.17	0.88	0.75	0.58	1.17
Erzincan (N-S)	1.56	1.19	0.92	0.70	0.56	0.40	0.91
Erzincan (E-W)	3.53	2.33	1.64	1.17	0.85	0.64	1.75
Imperial Valley (N-S)	1.51	1.05	0.88	0.77	0.65	0.48	0.86
Imperial Valley (E-W)	1.65	1.17	0.85	0.67	0.55	0.42	0.90
Kobe (N-S)	0.94	0.69	0.59	0.54	0.60	0.48	0.58
Kobe (E-W)	0.54	0.54	0.69	0.70	0.61	0.44	0.58
Loma Prieta (N-S)	0.63	0.49	0.53	0.53	0.52	0.40	0.48
Loma Prieta (E-W)	1.00	0.73	0.63	0.56	0.48	0.34	0.63
Average	**1.35**	**1.00**	**0.82**	**0.70**	**0.61**	**0.46**	**0.81**

Table 3.13. Maximum story drifts for $F_{40D-1/8}$ (%)

	1	2	3	4	5	6	Roof
Coyote Lake (N-S)	1.44	1.20	1.00	0.83	0.66	0.47	0.94
Coyote Lake (E-W)	0.44	0.30	0.26	0.37	0.46	0.37	0.28
Düzce (N-S)	0.85	0.76	0.85	0.87	0.81	0.61	0.75
Düzce (E-W)	1.94	1.63	1.29	1.00	0.80	0.59	1.20
Erzincan (N-S)	1.41	1.25	1.04	0.81	0.63	0.44	0.95
Erzincan (E-W)	3.44	2.57	1.92	1.39	0.96	0.69	1.87
Imperial Valley (N-S)	1.42	1.12	0.91	0.84	0.71	0.53	0.87
Imperial Valley (E-W)	1.57	1.25	0.93	0.74	0.60	0.42	0.93
Kobe (N-S)	0.78	0.65	0.66	0.61	0.59	0.48	0.55
Kobe (E-W)	0.50	0.51	0.69	0.73	0.66	0.47	0.58
Loma Prieta (N-S)	0.60	0.55	0.52	0.50	0.56	0.42	0.45
Loma Prieta (E-W)	0.98	0.81	0.70	0.63	0.54	0.38	0.67
Average	**1.28**	**1.05**	**0.90**	**0.78**	**0.67**	**0.49**	**0.84**

Table 3.14. Base shear values (kN) obtained from dynamic analyses.

	F_0	F_{st}	$F_{40D-1/8}$
Coyote Lake (N-S)	20052	20271	19670
Coyote Lake (E-W)	13164	12538	12326
Düzce (N-S)	16587	17324	16770
Düzce (E-W)	22080	22812	21533
Erzincan (N-S)	19533	20838	19601
Erzincan (E-W)	27131	27236	26219
Imperial Valley (N-S)	20178	20574	19698
Imperial Valley (E-W)	20855	21052	20184
Kobe (N-S)	15454	17397	15694
Kobe (E-W)	14723	14081	12985
Loma Prieta (N-S)	14738	14770	13912
Loma Prieta (E-W)	17682	17843	17291
Average	**18515**	**18894**	**17990**

Although modern specifications do not specify seismic performance requirements for structural systems in terms of story drift, FEMA-356 [4] outlines typical values to illustrate the structural response. For concrete frames, FEMA-356 Table C1-3 defines maximum 1.00% drift for *Immediate Occupancy Performance Level*, maximum 2.00% drift for *Life Safety Performance Level* and maximum 4.00% drift for *Collapse Prevention Performance Level*.

As can be seen in Table 3.12, the addition of dampers did not have a significant effect on the average roof drift value for twelve records. However, the maximum roof drift value of the undamped frame F_0 for Erzincan (E-W) record is notably reduced by the dampers. For this event F_0, with a roof drift of 2.12%, is in *Collapse Prevention Performance Range*. With the addition of dampers, the roof drift is reduced to 1.75% and 1.87% for F_{st} and $F_{40D1/8}$, respectively, indicating that the frame is in *Life Safety Performance Range*. The fact that the average roof drift is smaller than 1.00% but the maximum roof drift is larger than 2.00% shows that the dampers' effectiveness increases as the drift demand increases. This is further illustrated by the fact that the reduction of average drifts by addition of dampers is at level of 10% where the same reduction for maximum (Erzincan (E-W)) case is at level of 20% for most stories.

As can be seen, there is no significant increase in the base shear imparted on the frame by the earthquakes with the addition of dampers, with a slight reduction for the case of $F_{40D-1/8}$. This further demonstrates the fact that the reduction in story drifts by the addition of dampers is not a result of stiffening of the frame, but a result of additional energy dissipation capacity provided by the friction mechanism that occurs at damper joints.

4. ANALYTICAL MODEL

In order to formulate the behaviour precast post-tensioned concrete structural systems with the proposed dampers, analytical modeling principles were established. This Section describes in detail these principles.

4.1. Analytical Model of the Damper

Analytical model of the damper mechanism was created using work-energy method and verified with experiment results. As the damper is displaced with an amount of u, the six joints of the damper at which friction resistance T_{fr} exists rotate relative to each other with an amount $\Delta\theta_j$. The total work done by the friction resistances at these joints are equal to the work done by force F which is required displace the damper with an amount of u. This model is illustrated in Figure 4.1 and is defined as

$$F(t)\Delta u(t) = \Sigma T_{fr,j}\Delta\theta_j(t), \tag{4.1}$$

where $F(t)$ is the vertical force required at the top to displace the damper an amount of $\Delta u(t)$ at stage t, $T_{fr,j}$ is the friction torque at joint j and $\Delta\theta_j(t)$ is the relative rotation at joint j for the given $\Delta u(t)$. The force is calculated by imposing displacement Δu, and finding relative rotation at each joint by kinematics. Then the right-hand side of the equation (total work done by relative rotation at joints) is calculated and divided by $u(t)$ to find force $F(t)$.

Since the damper mechanism is symmetric in the model, the work done by one of the units is equal to the work done by the other unit. Therefore, using kinematics to find the change in angles θ_1, θ_2 and θ_3 is sufficient to solve the work-energy equation. Furthermore, the change in θ_1 is equal to the change in θ_3. In light of the explanations made above, Equation 4.1 can be rewritten as

$$F(t)\Delta u(t) = 2(T_{fr,1}\Delta\theta_1(t) + T_{fr,2}\Delta\theta_2(t) + T_{fr,3}\Delta\theta_3(t)). \tag{4.2}$$

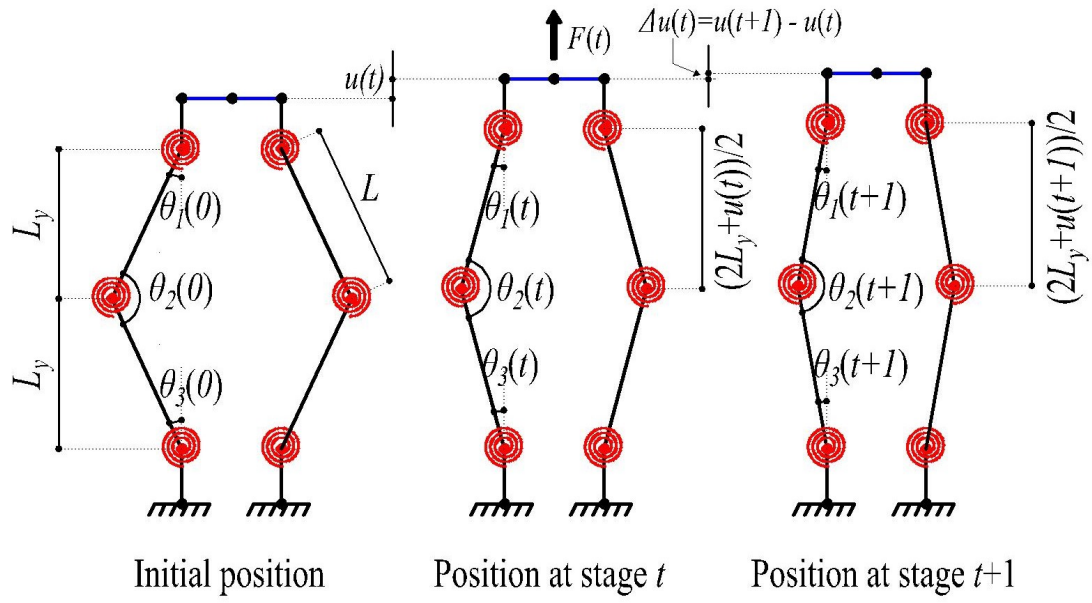

Figure 4.1. Analytical model for the damper.

The changes in θ_1, θ_2 and θ_3 due to displacement Δu are calculated as

$$\Delta\theta_1(t) = \Delta\theta_3(t) = cos^{-1}\left(\frac{2L_y + u(t) + \Delta u(t)}{2L}\right) - cos^{-1}\left(\frac{2L_y + u(t)}{2L}\right), \quad (4.3)$$

$$\Delta\theta_2 = -(\Delta\theta_1 + \Delta\theta_3) = -2\Delta\theta_1. \quad (4.4)$$

The force $F(t)$ required to displace the damper an amount of $\Delta u(t)$ is expressed as

$$F(t) = \frac{2(T_{fr,1} + 2T_{fr,2} + T_{fr,3})(cos^{-1}(\frac{2L_y+u(t)+\Delta u(t)}{2L}) - cos^{-1}(\frac{2L_y+u(t)}{2L}))}{\Delta u(t)}. \quad (4.5)$$

The force F vs displacement u plot for the damper tests 43 and 48 in Chapter 2 was obtained using Equation 4.5 and verified using experiment results. The comparison can be seen in (Figure 4.2). It should be noted that in order to compare the results, the vertical force F found in Equation 4.1 has been multiplied by -1 to convert it to the force reaction measured for the tests at the bottom of the damper mechanism.

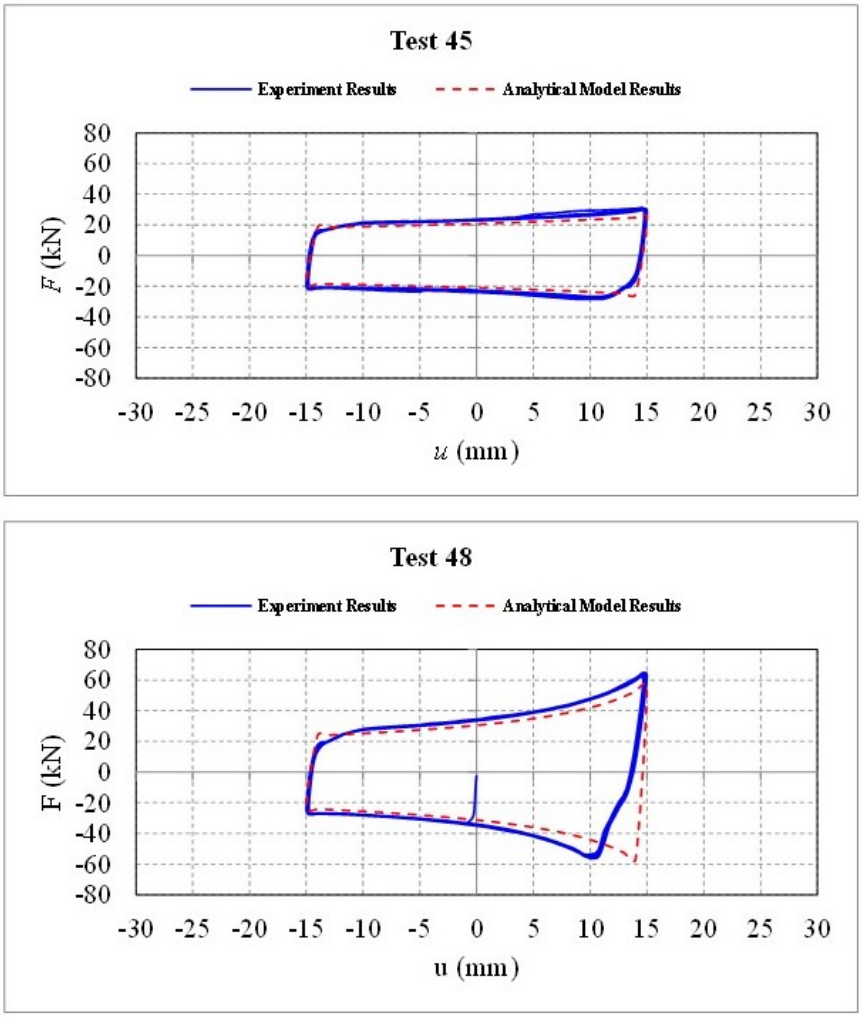

Figure 4.2. Verification of analytical model for the damper.

To illustrate why the relation between $F(t)$ and $u(t)$ is exponential as initial angle θ_i decreases, the total relative rotation $\Sigma\Delta\theta_j$ as a function of θ_i is plotted in Figure 4.3 for a displacement amplitude of 15 mm. It can be observed that as the initial angle of the damper decreases, the total relative rotation that occurs at the joints exponentially increases. This is due to the motion amplification phenomenon that is provided by small initial angle.

Furthermore, Figure 4.3 illustrates the unsymmetric nature of the damper in terms of positive and negative displacement. As the imposed displacement $u(t)$ is positive (upwards), the damper angle decreases, hence the relative rotation of the joints

increase exponentially. As $u(t)$ is negative (downwards), however, the damper angle decreases, and the relative rotation for the same amplitude of displacement decreases. This causes the damper to behave unsymmetrically with regards to the displacement direction.

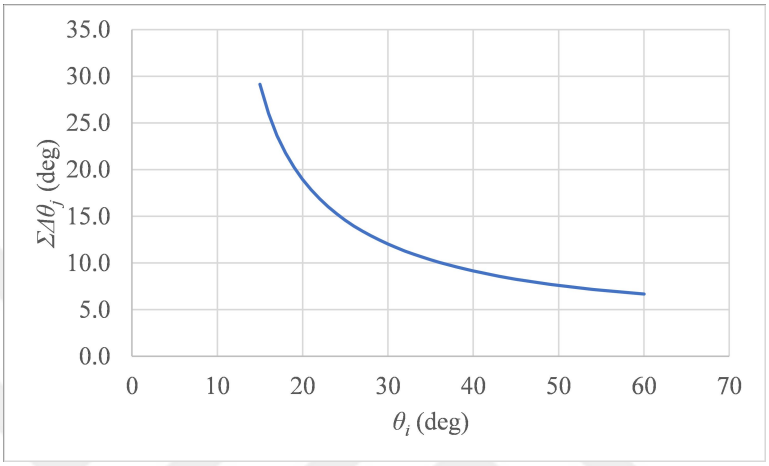

Figure 4.3. Initial angle vs. total relative rotation plot for fixed axial displacement of one end of the mechanism.

Kinematics can also be used to determine the initial angle θ_i for which the damper will 'lock itself' for a given displacement amplitude u_{max}. This is also called the toggle position. This case happens when the damper links constitute a straight line, in other words when θ_1 is 0 degrees. (Figure 4.4)

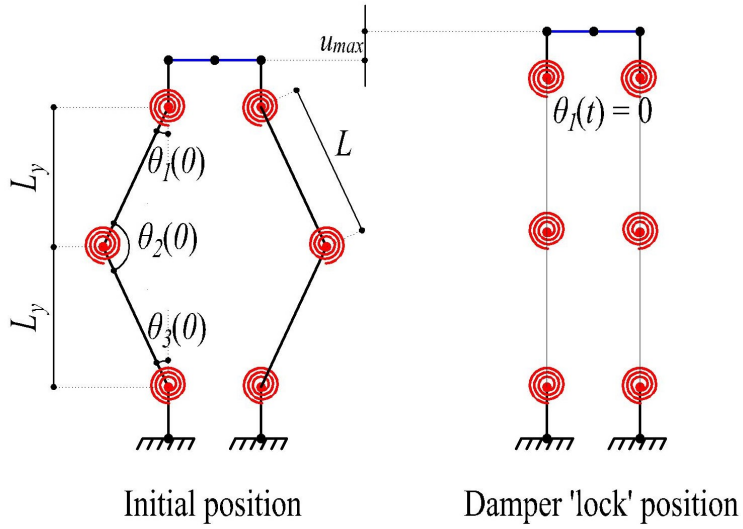

Figure 4.4. Damper "lock" position.

The smallest initial angle θ_i at which the damper locks itself for a given displacement amplitude u_{max} is expressed as

$$\theta_i = cos^{-1}(\frac{2L - u_{max}}{2L}). \tag{4.6}$$

A plot of u_{max} and the initial angle θ_i at which the damper locks itself for the imposed u_{max} can be seen in Figure 4.4 for the damper specimen of the tests (L=300mm).

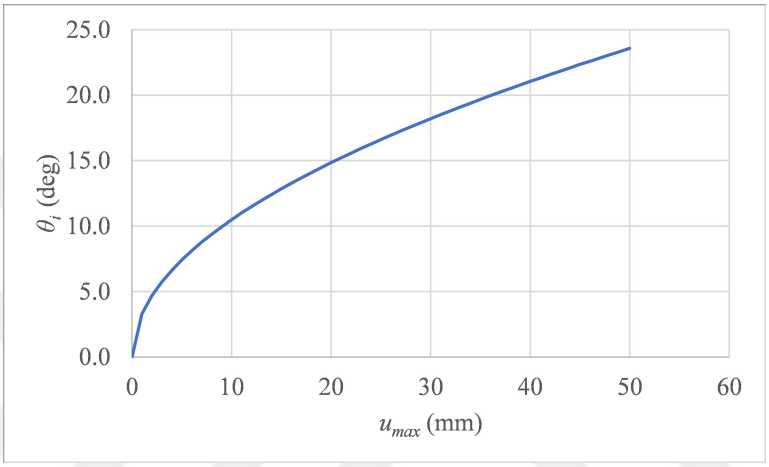

Figure 4.5. Plot of the initial angle at which damper locks itself for imposed u_{max}.

4.2. Analytical Model of the Sub-Assembly

The work-energy method used in damper analytical model was adapted to the sub-assembly to formulate the analytical model for precast post-tensioned concrete systems. The force vs drift ratio relation for the sub-assembly is obtained by imposing a horizontal displacement u_{sa} to the relevant joint of the column and solving the work-balance equation which equates the work done by u_{sa} to the sum of works done by the moment acting at the joint, the relative rotations of damper friction surfaces and the internal strain energy in the beam and column due to elastic bending. The work balance equation is defined as

$$F_{sa}u_{sa} = M_{jo}\theta_{jo} + \Sigma T_{fr,j}\Delta\theta_j + \int M_{col}\phi_{col} + \int M_{beam}\phi_{beam}, \tag{4.7}$$

where F_{sa} is the force required to displace the top node of the column an amount of u_{sa}, M_{jo} is the moment acting on the beam-column joint, θ_{jo} is the rotation at the beam-column joint, $T_{fr,j}$ is the friction torque at joint j of the damper, $\Delta\theta_j$ is the

relative rotation at joint j of the damper, M_{col} and M_{beam} is the moment acting on the column and beam and ϕ_{col} and ϕ_{beam} is the elastic curvature of the column and beam.

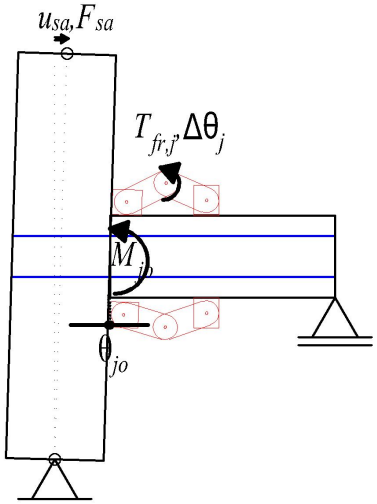

Figure 4.6. Analytical model.

The equilibrium at the beam-column joint is determined by imposing a joint rotation θ_{jo} which is equal to the drift ratio δ_{fr}. A value is assumed for concrete compressive block depth c_c. The concrete compressive reaction force F_c is found by determining the strain at the extreme fiber and calculating stresses using Mander's model [56]. It is important to indicate that the extreme concrete compressive strain is determined using relations developed by Pampanini [57], since there is no "strain compatibility" in the joint. The strain demands on the post-tensioning tendons are determined by calculating the elongation at the tendon level due to gap opening. The strains are calculated taking into account the unbonded length of the tendons. The stress is calculated using the stress-strain relation of prestressing steel, after adding the additional strain due to gap opening to the initial jacking strain of the steel. This process is repeated until a compressive block depth c_c value that satisfies joint equilibrium is found. Finally, the moment at joint M_{jo} is calculated using the forces at equilibrium.

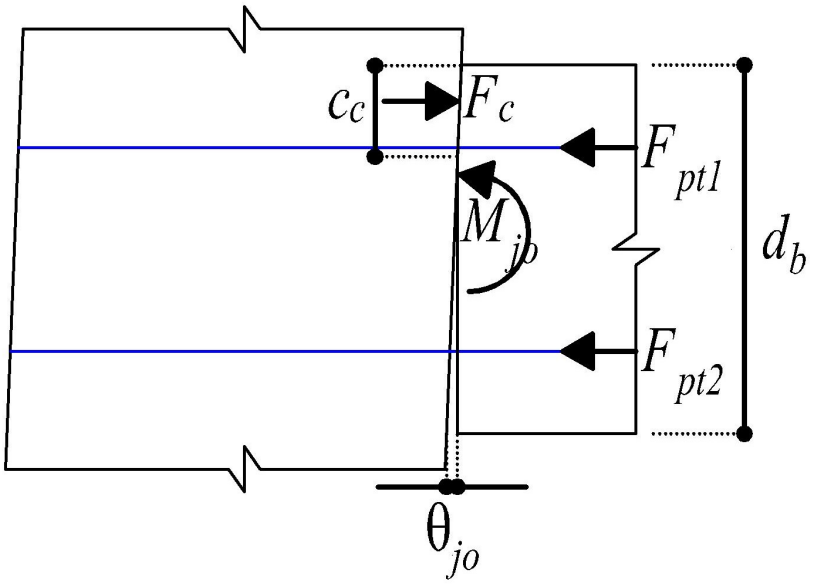

Figure 4.7. Beam-column joint equilibrium.

The rotations at damper joints are found by kinematics. For each damper unit (the one at the top and the one at the bottom), the principle of "vector loop" [58] is used by taking the bottom node of column as the origin and forming a 4-bar mechanism. Vector A and vector C are virtual vectors from the origin to the end joints of the damper mechanism. Vector B and D represent the damper plates. This is shown in Figure 4.8 for upper damper unit and in Figure 4.2 for lower damper unit. After the joint locations are found, the relative rotations of the joints are calculated. The drift ratio vs force graphs are plotted for the sub-assemblies studied in Section 3.2 using the analytical model described above. These plots, shown in Figure 4.10, constitute the "backbone curve" of the cyclic drift ratio vs. force plots for the sub-assemblies. The relation with which the joint locations are to be found is expressed as

$$\overline{A}cos\alpha_A + \overline{B}cos\alpha_B = \overline{C}cos\alpha_C + \overline{D}cos\alpha_D, \tag{4.8}$$

$$\overline{A}sin\alpha_A + \overline{B}sin\alpha_B = \overline{C}sin\alpha_C + \overline{D}sin\alpha_D. \tag{4.9}$$

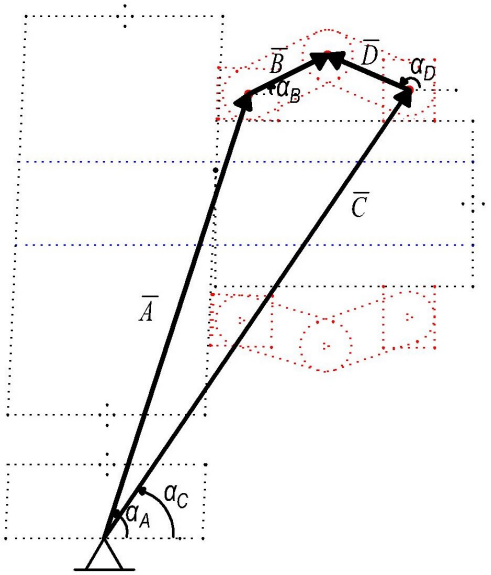

Figure 4.8. Vector loop for upper damper unit.

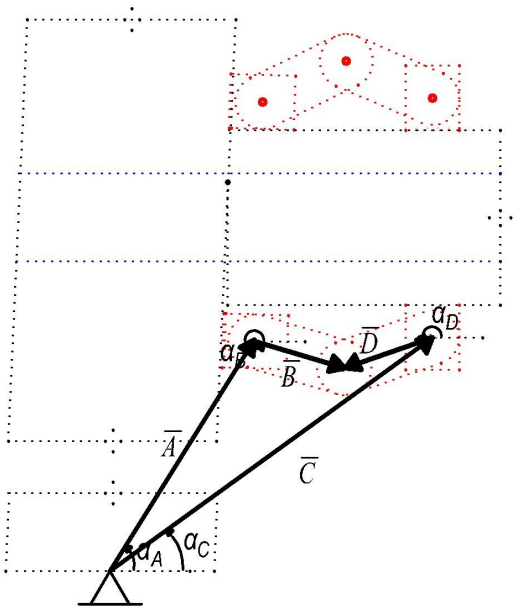

Figure 4.9. Vector loop for lower damper unit.

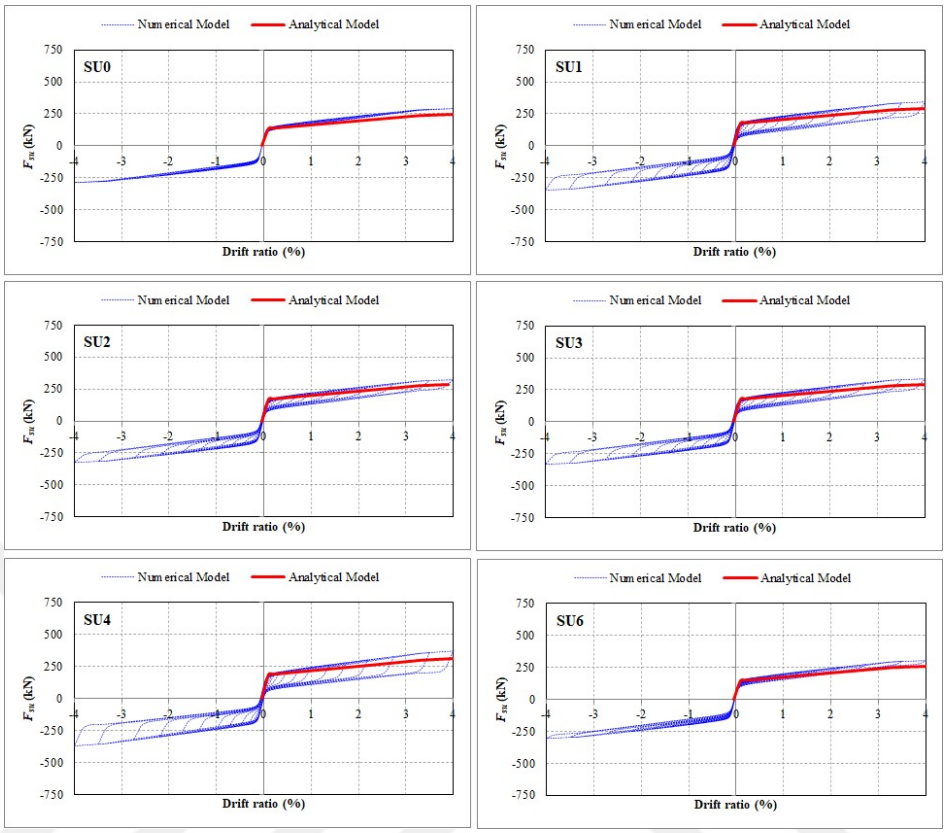

Figure 4.10. Verification of sub-assembly analytical model.

5. SUMMARY AND CONCLUSIONS

A novel damper mechanism that works with principle of rotational friction was proposed. The novelty of the damper stems from two major aspects. The plates of the mechanism are placed in such a composition that the initial angle is small. This improves energy dissipation capacity and force capacity of the damper significantly. The reason that small initial angle is not used in previously proposed dampers is that they are used predominantly in chevron braces that span diagonally in frame bays. This imposes larger displacement demands on the device and causes the damper to "lock" after the angle reaches a certain value. The second novel aspect of the proposed damper is that bolt torques are applied at all joints. Previously proposed dampers have bolt torques at middle joints only. It is assumed that this is because of installation issues.

It was argued that the damper mechanism is particularly effective for precast post-tensioned structures in which the seismic behaviour is governed by a gap-opening mechanism at beam-column joints. The dampers are designed to be placed at the joints and to take advantage of this gap-opening. The small initial angle of the dampers is used to amplify the displacements imposed on the joints and dissipate energy by rotational friction.

Experiments were conducted on the proposed damper mechanism to investigate the performance with respect to force capacity and energy dissipation capacity. The test parameters were initial angle, displacement amplitude, bolt torque values at the middle joint and at top and bottom joints. Experiment results releaved that small initial angle dramatically increased force capacity and energy dissipation capacity. Increasing bolt torques had a linear effect on increasing force and energy capacities if the torques are not very small. For small torque values, the uniform clamping pressure at the interface of the friction disks are not satisfied. Furthermore, applying bolt torque at top and bottom joints also increased performance of the damper. Results showed the exponential increase in force and energy dissipation capacities for small initial angle.

Numerical modeling of the dampers were conducted in OpenSEES. Numerical analyses were conducted on damper, sub-assembly and frame levels and the modeling principles were validated by experimental and analytical results.

Results of analyses performed on exterior precast beam-column sub-assemblies showed that small initial angle was very effective in improving force capacity and energy dissipation capacity of these systems. Increasing bolt torques also had the expected effect of increasing system performance. Sub-assembly behaviour was also sensitive to the test parameters studied, namely post-tensioning tendon area, beam depth and tendon eccentricity.

Numerical analyses were also conducted on four frames to study the effect of the proposed dampers on a global perspective. The small initial angle proved to enhance force capacity and energy dissipation capacity of the frames significantly. A dramatic increase in energy dissipation capacity was observed in the precast post-tensioned frame strengthened with the proposed dampers. Furthermore, the force capacity added by the dampers to the structure enabled to achieve very similar base shear values with F_0, using 38% less post-tensioning tendons for $F_{20D-1/4}$, 43% less post-tensioning tendons for $F_{40D-1/4}$ and 24% less post-tensioning tendons for $F_{40D-1/8}$.

Dynamic analyses were performed on representative frames to investigate the effect of the dampers on the dynamic response of precast post-tensioned concrete structures. It was observed that the addition of dampers do not increase the base shear imparted on the frame by the earthquakes. Furthermore, reduction in story drifts were provided by the dampers. This reduction without an increase in base shear indicated that the damper contributes to the energy dissipation capacity of the frame without altering the free vibration behavior.

Analytical model of the damper mechanism and sub-assemblies with the damper mechanism were created using virtual work method and showed satisfactory consistency with numerical and experimental results.

Although the proposed damper mechanism is particularly effective when they are placed at joints of precast post-tensioned concrete structures, they can also be used in other structural systems. The compact nature of the damper mechanism enables architectural and structural flexibility to the designer. Furthermore, the novel design stemming from small initial angle and bolt torques applied at all joints, that previously proposed dampers lack, increases the performance of the mechanism dramatically.

REFERENCES

1. Cross, H., "Essays by Hardy Cross", 1921, `https://engineering.purdue.edu/`, accessed on November 12, 2022.

2. Chopra, A. K., *Dynamics of Structures: Theory and Applications to Earthquake Engineering*, Pearson Prentice Hall, New Jersey, USA, 1995.

3. *Türkiye Bina Deprem Yönetmeliği: Deprem Etkisi Altında Binaların Tasarımı için Esaslar*, Ankara, 2018.

4. FEMA, *Prestandard and Commentary for The Seismic Rehabilitation of Buildings*, Washington DC, 2000.

5. Pacific, C., "The Precast Hybrid Moment System", 2011, `https://clarkpacific.com/products/`, accessed on December 21, 2022.

6. Cheok, G. and W. Stone, "Performance of 1/3-Scale Model Precast Concrete Beam-Column Connections Subjected to Cyclic Inelastic Loads", *National Institute of Standards and Technology*, 1993.

7. Priestley, N., S. Sritharan, J. Conley and S. Pampanin, "Preliminary Results and Conclusions from the PRESSS Five-Storey Precast Concrete Test Building", *PCI Journal*, Vol. 44, No. 6, pp. 42–67, 1999.

8. Kato, H., Y. Ichisawa, K. Takamatsu and N. Okamoto, "Earthquake Response of an Eleven Story Precast Prestressed Concrete Building by Substructure Pseudo Dynamic Test", *12th World Conference on Earthquake Engineering*, Auckland, New Zealand, 2000.

9. Wada, A., H. Sakata, K. Nakano, Y. Matsuzaki, K. Tanabe and S. Machida, "Study on Damage Controlled Precast-Prestressed Concrete Structure with P/C

MILD PRESS JOINT", *Proceedings of the 2nd Federation of Concrete International Congress*, Naples, Italy, 2006.

10. Lee, D. and D. Taylor, "Viscous Damper Development and Future Trends", *Structural Design of Tall Buildings*, Vol. 10, No. 5, pp. 311–320, 2001.

11. Makris, N., "Viscous Heating of Fluid Dampers. I: Small Amplitude Motions", *Journal of Engineering Mechanics*, Vol. 124, No. 11, 1998.

12. Cahalarca, B., A. Filiatraut and D. Perrone, "Parametric Study and Prediction Models of the Seismic Response of Single-Degree-of-Freedom Structural Systems Equipped with Maxwell Material Fluid Viscous Dampers", *Structures*, Vol. 43, pp. 388–406, 2022.

13. Lobo, R., J. Bracci, K. Shen, A. Reinhorn and T. Soong, "Inelastic Response of Reinforced Concrete Structures with Viscoelastic Braces", *Earthquake Spectra*, Vol. 9, No. 3, pp. 419–446, 1993.

14. Lin, W., C. Yu, M. Tsai, Y. Chang, S. Peng and S. Wang, "Hysteretic Behaviour of Viscoelastic Dampers Subjected to Damage During Seismic Loading", *Journal of Building Engineering*, Vol. 53, 2022.

15. Kam, W., S. Pampanin, A. Palermo and A. Carr, "Self-Centering Structural Systems with Combination of Hysteretic and Viscous Energy Dissipations", *Earthquake Engineering and Structural Dynamics*, pp. 1083–1108, 2010.

16. Black, C., N. Makris and I. Aiken, "Component Testing, Stability Analysis and Characterization of Buckling-Restrained Braces", *Pacific Earthquake Engineering Research Center Technical Report*, 2002.

17. Wu, C., Q. Zhang, W. Huang, S. Zhang and X. Xu, "Cyclic Behaviour of Metallic Damper Connected Reinforced Concrete Beam-Column Joint with an Opening in Slab", *Journal of Building Engineering*, Vol. 60, 2022.

18. Koshikawa, T., H. Kadowaki and M. Matsumora, "Energy Dissipation Efficiency of Unbonded Post-Tensioned Precast Concrete Beam-Column Connections with Beam-End Dampers", *Proceedings of the 15th World Conference on Earthquake Engineering*, Lisbon, Portugal, 2012.

19. Pall, A. and C. Marsch, "Seismic Response of Friction Damped Brace Frames", *Journal of Structural Division*, Vol. 108, pp. 1313–1323, 1982.

20. Grigorian, C., T. Yang and E. Popov, "Slotted Bolted Connection Energy Dissipators", *Earthquake Spectra*, Vol. 9, No. 3, pp. 491–504, 1993.

21. Morgen, B. and Y. Kurama, "Friction-Damped Unbonded Post-Tensioned Precast Concrete Moment Frame Structures for Seismic Regions", *Structural Engineering Research Report, University of Notre Damme*, 2007.

22. Xu, G. and J. Ou, "Seismic Performance of Combined Rotational Friction and Flexural Yielding Metallic Dampers", *Journal of Building Engineering*, Vol. 49, 2022.

23. Symans, M., F. Charney, A. Whittaker and M. Constantinou, "Energy Dissipation Systems with Seismic Applications: Current Practice and Recent Developments", *Journal of Structural Engineering*, Vol. 134, No. 1, pp. 3–21, 2008.

24. Soong, T. and G. Dargush, *Passive Energy Dissipation Systems in Structural Engineering*, John Wiley and Sons, New Jersey, USA, 1997.

25. Mualla, I., "Experimental Evaluation of New Friction Damper Device", *Proceedings of the 12th World Conference on Earthquake Engineering*, Auckland, New Zealand, 2000.

26. Mualla, I. and B. Belev, "Performance of Steel Frames with a New Friction Damper Device Under Earthquake Excitation", *Engineering Structures*, Vol. 24, pp. 365–371, 2002.

27. Liao, W., I. Mualla and C. Loh, "Shaking-Table Test of a Friction-Damped Frame Structure", *The Structural Design of Tall and Special Buildings*, Vol. 13, No. 1, pp. 45–54, 2004.

28. Amiri, J., M. Naghipoor and S. Jalali, "Performance of Rotational Friction Damper (RFD) in Steel Frames", *14th World Conference on Earthquake Engineering*, Beijing, China, 2008.

29. Sanati, M., S. Khadem, S. Mirzabagheri, H. Sanati and M. Khosravieh, "Performance Evaluation of a Novel Rotational Damper for Structural Reinforcement Steel Frames Subjected to Lateral Excitations", *Earthquake Engineering and Engineering Vibration*, Vol. 13, 2014.

30. Shirkhani, A., I. Mualla, N. Shabakhty and S. Mousavi, "Behaviour of Steel Frames with Rotational Friction Dampers by Endurance Time Method", *Journal of Conctructional Steel Research*, Vol. 107, pp. 211–222, 2015.

31. Jarrahi, H., A. Asadi, M. Khatibinia and S. Etedali, "Optimal Design of Rotational Friction Dampers for Improving Seismic Performance of Inelastic Structures", *Journal of Building Engineering*, Vol. 27, 2020.

32. Jensen, M., "Experimental Evaluation of a Friction Damper Device", *Technical University of Denmark*, 2009.

33. Chen, W. and H. Hao, "Numerical Study of Blast-Resistant Sandwich Panels with Rotational Friction Dampers", *International Journal of Structural Stability and Dynamics*, Vol. 13, No. 6, 2013.

34. Javidan, M. and J. Kim, "Seismic Retrofit of Soft-First-Storey Structures Using Rotational Friction Dampers", *Journal of Structural Engineering*, Vol. 145, No. 12, 2019.

35. Zareian, M., M. Esfahani and A. Hosseini, "Experimental Evaluation of Self-

Centering Hybrid Coupled Wall Subassemblies with Friction Dampers", *Engineering Structures*, Vol. 214, 2020.

36. Veismoradi, S., S. Yousef-beik, P. Zarnani and P. Quenneville, "Development and Parametric Story of a New Self-Centering Rotational Friction Damper.", *Engineering Structures*, Vol. 235, 2021.

37. Sui, W., X. Wang and Z. Wang, "Experimental Study on Mechanical Properties of the Steel Friction Pads Used in a Rotational Friction Damper", *Structures*, Vol. 29, pp. 1808–1818, 2021.

38. Javidan, M. and J. Kim, "A Rotational Friction Damper-Brace for Seismic Design of Resilient Framed Structures", *Journal of Building Engineering*, Vol. 51, 2022.

39. Hwang, J., J. Kim and Y. Kim, "Rotational Inertia Dampers with Toggle Bracing for Vibration Control of a Building Structure", *Engineering Structures*, Vol. 29, pp. 1201–1208, 2007.

40. Mirtaheri, M., A. Zandi, S. Samadi and H. Samani, "Numerical and Experimental Study of Hysteretic Behaviour of Cylindirical Friction Dampers", *Engineering Structures*, Vol. 33, pp. 3647–3656, 2011.

41. Constantinou, M., P. Tsopelas, W. Hammel and A. Sigaher, "Toggle-Brace Damper Seismic Energy Dissipation Systems", *Journal of Structural Engineering*, Vol. 127, No. 2, pp. 105–112, 2000.

42. Jae-Seung, H., K. Jinkoo and Y. Kim, "Rotational Inertia Dampers with Toggle Bracing for Vibration Control of a Building Structure", *Engineering Structures*, Vol. 29, pp. 1201–1208, 2007.

43. Y., R. and A. Reinhorn, "Design of Amplified Structural Damping Using Optimal Considerations", *Journal of Structural Engineering*, Vol. 129, No. 10, pp. 1422–1427, 2003.

44. R., Z., H. He, D. Weng, H. Zhou and S. Ding, "Theoretical Analysis and Experimental Research on Toggle-brace-damper System Considering Different Installation Modes", *Scientia Iranica*, Vol. 19, No. 6, pp. 1379–1390, 2012.

45. S., B. and J. Bolander, "Amplification System for Supplemental Damping Mechanisms in Seismic Applications", *Journal of Structural Engineering*, Vol. 131, No. 6, p. 979, 2005.

46. Huang, H., "Efficiency of the Motion Amplification Mechanism with Viscous Dampers and its Application in High Rise Buildings", *Earthquake Engineering and Engineering Vibration*, Vol. 8, pp. 521–536, 2009.

47. Londono, J., S. Neild and D. Wagg, "Using a Damper Amplification Factor to Increase Energy Dissipation in Structures", *Engineering Structures*, Vol. 84, pp. 162–171, 2015.

48. Ozden, S. and O. Ertas, "Behaviour of Unbonded, Post-tensioned, Precast Concrete Connections with Different Percentages of Mild Steel Reinforcement", *PCI Journal*, Vol. 52, No. 2, pp. 32–44, 2007.

49. Kurama, Y. and B. Morgen, "A Friction Damper for Post-tensioned Precast Concrete Moment Frames", *PCI Journal*, Vol. 49, No. 4, pp. 112–133, 2004.

50. Marriott, D., S. Pampanin, A. Palermo and D. Bull, "Shake-Table Testing of Hybrid Post-Tensioned Precast Wall Systems with Alternative Dissipating Solutions", *Proceedings of the 14th World Conference on Earthquake Engineering*, Beijing, China, 2008.

51. Li, Z., Y. Qi and J. Teng, "Experimental Investigation of Prefabricated Beam-to-Column Steel Joints for Precast Concrete Structures Under Cyclic Loading", *Engineering Structures*, Vol. 209, pp. 1–16, 2020.

52. Wang, H., E. Marino, P. Pan, H. Liu and X. Nie, "Experimental Study of a

Novel Precast Prestressed Reinforced Concrete Beam-to-Column Joint", *Engineering Structures*, Vol. 156, pp. 68–81, 2018.

53. Latour, M., V. Piluso and G. Rizzano, "Experimental Analysis on Friction Materials for Supplemental Damping Devices", *Construction and Building Materials*, Vol. 65, pp. 159–176, 2014.

54. Ertas, O., *Ductile Beam-Column Connections in Precast Concrete Moment Resisting Frames*, Ph.D. Thesis, Boğaziçi University, 2005.

55. *American Concrete Institute (ACI) T1.1-01: Acceptance Criteria for Moment Frames Based on Structural Testing*, Washington DC, 2001.

56. Mander, J., M. Priestley and R. Park, "Theoretical Stress-Strain Model for Confined Concrete", *ASCE Journal of Structural Engineering*, Vol. 114, No. 8, 1988.

57. Vernu, S. and S. Sritharan, "Section, Member and System Level Analysis for Precast Concrete Hybrid Frames", *Iowa State University Technical Report*, 2004.

58. Eckhardt, H. D., *Kinematic Design of Machines and Mechanisms*, McGraw-Hill Professional, New York City, 1998.

59. Segui, W. T., *Steel Design, Fourth Edition*, Thomson, Michigan, 2007.

60. *PCI Design Handbook: Precast and Prestressed Concrete, Eighth Edition*, New Jersey, 2021.

APPENDIX A: DAMPER DESIGN

The design procedure for the proposed dampers is described in this section. The damper device is designed according to the sufficiency of the steel plates and the connections. In addition, the anchorage of the dampers to precast concrete beams and columns is discussed.

The unfavorable case for the steel plates are combined effects of axial compression and moment. The unfavorable case for the other design situations are when tensile force acting on the damper is maximum, which happens when the damper angle is smallest. Since these two cases occur at different stages, the design will be made according to these different stages. Figure A.1 shows the internal forces acting on the critical section of damper device. M_d is the moment acting on the damper, N_{d2} is the compressive force acting on the damper for steel plate design and N_{d1} is the tensile force acting on the damper for bolt shear and bearing check and anchorage design.

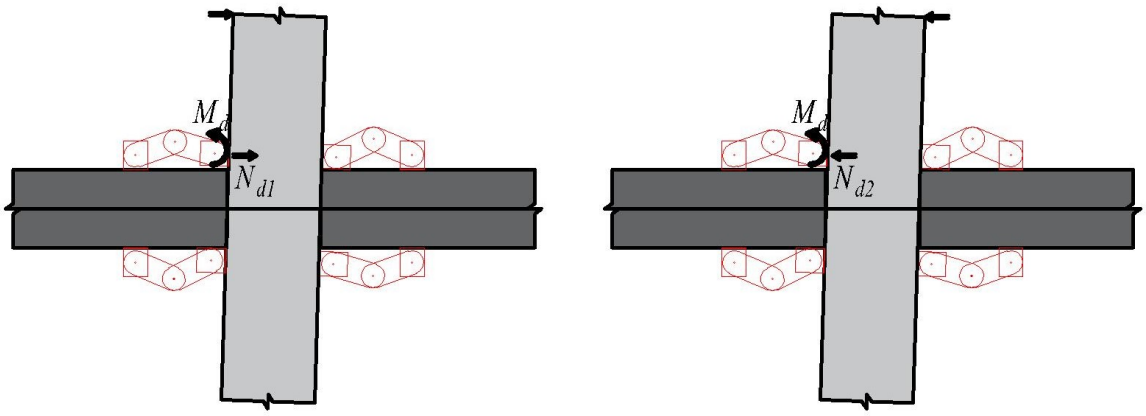

Figure A.1. Internal forces acting on the damper.

The sufficiency of the damper plates under the combined effect of normal force and moment, the bolt shear strength and connection bearing strength are checked. The transfer of damper forces to precast concrete beams and columns are also ensured by designing the anchorage of the damper device to the precast members. In anchor-

age design, steel strength, concrete breakout and concrete pullout failure modes are checked. The design procedure for the damper device is outlined as follows:

1. Obtain N_{d1}, N_{d2} and M_d values from analysis

2. Check adequacy of the steel damper plate [59]. This check is defined as

$$\frac{P_u}{2\phi_c P_n} + \frac{M_u}{\phi_b M_n} \leq 1.0, \tag{A.1}$$

where P_u is the axial load acting on the section, $\phi_c P_n$ is the available strength in axial compression for the section, M_u is the amplified acting moment and $\phi_b M_n$ is the maximum moment capacities for the section.

3. Check bolt design shear strength [59]. This check is defined as

$$\phi R_n = 0.75 F_{nv} A_b \geq N_{dbo}, \tag{A.2}$$

where R_n is the nominal shear strength of the bolt, F_{nv} is the nominal shear stress, A_b is the cross-sectional area of the unthreaded part of the bolt and N_{dbo} is the shear force acting on the bolt.

4. Check connection bearing strength [59]. This check is defined as

$$\begin{aligned} 1.2 L_c t F_u &\geq N_{dbe}, \\ 2.4 d t F_u &\geq N_{dbe}. \end{aligned} \tag{A.3}$$

where L_c is clear distance in the direction parallel to the applied load, t is the thickness of the connected part, F_u is the ultimate tensile stress of the connected part, d is the diameter of the bolt and N_{dbe} is the force acting on the bearing surface.

5. Check steel strength for the anchorage [60]. This check is defined as

$$\phi N_s = 0.75 n_{st} A_{se} f_{ut} \geq N_{d1}, \tag{A.4}$$

where N_s is the nominal tensile strength of an anchorage based on steel capacity, n_{st} is the number of headed struts in the anchorage assembly, A_{se} is the nominal area of the headed-stud shank and f_{ut} is the specified steel strength of the stud steel.

6. Check concrete breakout failure for the anchorage [60]. This check is defined as

$$\phi N_{cb} = 0.75 C_{bs} A_N C_{crb} \psi_{ed,N} \psi_{ec,N} \geq N_{d1}, \tag{A.5}$$

where N_{cb} is the nominal concrete breakout capacity, C_{bs} is the breakout strength

coefficient, A_N is the projected surface area for a stud of group of studs, C_{crb} is the cracking factor, $\psi_{ed,N}$ is the modification for edge distance and $\psi_{ec,N}$ is the eccentricity factor.

7. Check concrete pullout failure for the anchorage [60]. This check is defined as

$$\phi N_{ph} = n_{st}(0.70)11.2A_{brg}f'_cC_{crp} \geq N_{d1}, \tag{A.6}$$

where A_{brg} is the bearing area of the stud head in tension, f'_c is concrete compressive strength and C_{crp} is pullout cracking coefficient.

The design procedure summarized above is demonstrated with an example, taking into consideration internal forces resulting from analysis of $F_{40D-1/8}$ in Section 3.3. The design axial tensile force N_{d1} is 428 kN, the design axial compressive force N_{d2} is 394 kN and the design moment M_d is 10 kNm. Figure A.2 shows the internal forces acting on the damper, according to which design of the damper device and its anchorage to the precast member is demonstrated. The structural steel is St37 grade and the bolt is 8.8 grade M36. Steps 2 through 4 are related to the design of damper device and step 5 is related to anchorage of damper forces to the precast members. The steel struts for the anchorage of the damper are continues from one anchorage plate to the anchorage plate on the other hand in order to prevent concrete pullout and breakout failures. For this reason, step 6 and step 7 in the procedure is not calculated.

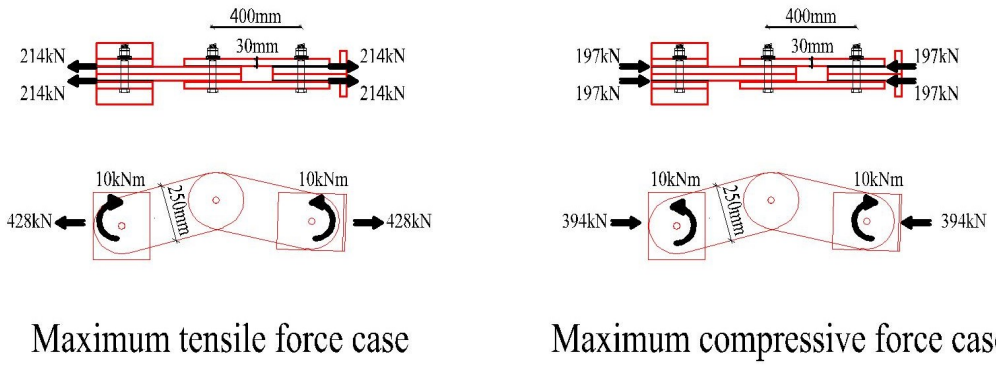

Figure A.2. Internal forces acting on the damper plate for maximum tensile force case.

1. N_{d1}, N_{d2} and M_d values are obtained from analysis as 428 kN, 394 kN and 10 kNm, respectively.

2. Check adequacy of the steel damper plate.

$$\frac{P_u}{2\phi_c P_n} + \frac{M_u}{\phi_b M_n} = \frac{197\text{kN}}{2\text{x}1680\text{kN}} + \frac{10\text{kNm}}{63\text{kNm}} = 0.22 < 1.00.$$

3. Check bolt design shear strength.

$$0.75F_{nv}A_b = 0.75\text{x}414\text{MPax}1018\text{mm}^2 = 316\text{kN} > N_{dbo} = 214\text{kN}.$$

4. Check connection bearing strength.

$$1.2L_c t F_u = 1.2\text{x}107\text{mmx}30\text{mmx}370\text{MPa} = 1426\text{kN} > N_{dbe} = 214\text{kN},$$

$$2.4dtF_u = 2.4\text{x}36\text{mmx}30\text{mmx}370\text{MPa} = 959\text{kN} > N_{dbe} = 214\text{kN}.$$

The transfer of damper forces to precast concrete structural members is ensured by designing the anchorage of the damper to these members. Since the critical case for anchorage design is the case at which tensile forces are transferred, the anchorage of the damper device to the precast column is demonstrated here. The anchorage consists of steel plates and steel struts which are embedded in precast concrete column in production. (Figure A.3)

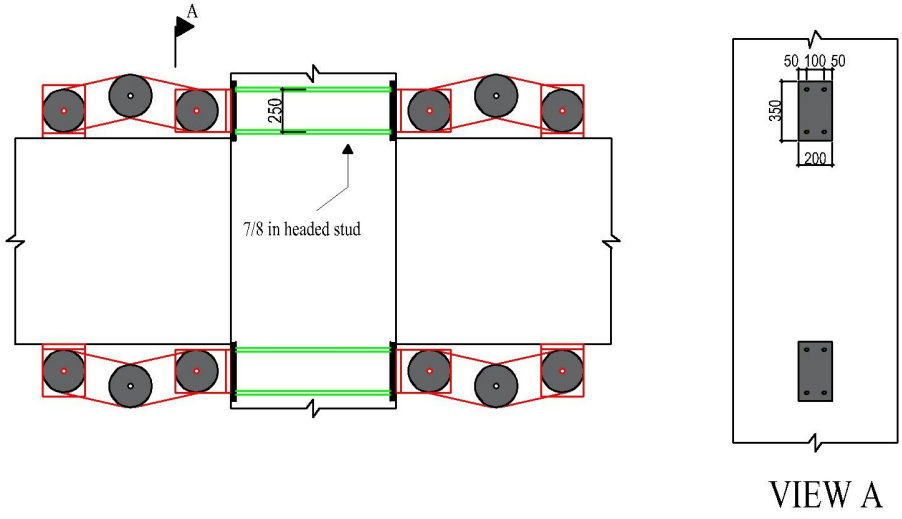

Figure A.3. Anchorage of damper to precast column.

5. Check steel strength for the anchorage.

$$0.75n_{st}A_{se}f_{ut} = 0.75\text{x}4\text{x}387\text{mm}^2\text{x}448\text{MPa} = 520\text{kN} > N_{d1} = 428\text{kN}.$$

APPENDIX B: COPYRIGHTS FOR FIGURES

In this section, copyrights obtained for relevant figures are presented. Figures for which information is not shown here are created by the author and within the scope of "valid publishing policy for the reuse of the text and graphics produced by the author".

Thomas Klemens <tklemens@pci.org>
To: Ata Kulaksizoglu

Wed, Feb 1 at 7:01 PM

Dear Mr. Kulaksizoglu:

Please consider this email your permission to use the figures you have described from several issues of *PCI Journal, as noted below*. We simply request that you note the source of the images.

Permission is granted to use the following:

Figure 2 and Figure 16 from Priestley, N., S. Sritharan, J. Conley and S. Pampanin, "Preliminary Results and Conclusions From the PRESSS Five-Story Precast Concrete Test Building," *PCI Journal* 44, no. 6 (November-December 1999): pages 44 and 54. https://doi.org/10.15554/pcij.11011999.42.67.

Figure 4 from Ozden, S. and O. Ertas, "Behavior of Unbonded, Post-Tensioned, Precast Concrete Connections with Different Percentages of Mild Steel Reinforcement," *PCI Journal* 52, no. 2 (March-April 2007): page 36. https://doi.org/10.15554/pcij.03012007.32.44.

Please contact me with any other questions. Thank you.

Thomas Klemens, PE
Director, Publications
Precast/Prestressed Concrete Institute
8770 W. Bryn Mawr Ave., Suite 1150
Chicago, IL 60631 USA
(312) 583-6773 (Direct)

Figure B.1. Copyrights obtained from PCI

This is a License Agreement between AHMET ATA KULAKSIZOGLU/BOGAZICI UNIVERSITY ("User") and Copyright Clearance Center, Inc. ("CCC") on behalf of the Rightsholder identified in the order details below. The license consists of the order details, the Marketplace Order General Terms and Conditions below, and any Rightsholder Terms and Conditions which are included below.

All payments must be made in full to CCC in accordance with the Marketplace Order General Terms and Conditions below.

Order Date	09-Jan-2023	Type of Use	Republish in a thesis/dissertation
Order License ID	1309063-1	Publisher	PERGAMON
ISSN	0141-0296	Portion	Chart/graph/table/figure

LICENSED CONTENT

Publication Title	Engineering structures	Rightsholder	Elsevier Science & Technology Journals
Article Title	Experimental investigation of prefabricated beam-to-column steel joints for precast concrete structures under cyclic loading	Publication Type	Journal
		Start Page	110217
		Volume	209
Date	01/01/1978		
Language	English		
Country	United Kingdom of Great Britain and Northern Ireland		

REQUEST DETAILS

Portion Type	Chart/graph/table/figure	Distribution	Worldwide
Number of Charts / Graphs / Tables / Figures Requested	2	Translation	Original language of publication
		Copies for the Disabled?	No
Format (select all that apply)	Print, Electronic	Minor Editing Privileges?	No
Who Will Republish the Content?	Academic institution	Incidental Promotional Use?	No
Duration of Use	Life of current edition	Currency	USD
Lifetime Unit Quantity	Up to 499		
Rights Requested	Main product		

NEW WORK DETAILS

Figure B.2. Copyrights obtained from Engineering Structures